

# **Design of Triphenylamine Derivatives for Organic Electronics Applications: Synthesis, Photophysics and Device Studies**

by

**SHIBNA BALAKRISHNAN**

**10CC17A39003**

A thesis submitted to the  
Academy of Scientific & Innovative Research  
for the award of the degree of  
DOCTOR OF PHILOSOPHY  
in  
SCIENCE

Under the supervision of  
**Dr. JOSHY JOSEPH**



**CSIR-National Institute for Interdisciplinary  
Science and Technology (CSIR-NIIST),  
Thiruvananthapuram – 695 019**



Academy of Scientific and Innovative Research  
AcSIR Headquarters, CSIR-HRDC campus  
Sector 19, Kamla Nehru Nagar,  
Ghaziabad, U. P. – 201 002, India

**August 2023**



**Dedicated**  
**to** **Achan, Amma**  
**Reji and Kuttu**

# National Institute for Interdisciplinary Science and Technology (CSIR-NIIST)



Council of Scientific & Industrial Research (CSIR)  
Industrial Estate P. O., Trivandrum - 695 019  
Kerala, INDIA

Dr. Joshy Joseph  
Principal Scientist & Associate Professor  
Chemical Sciences and Technology Division


Tel: +91-471-2515 476  
Fax: +91-471-2491 712  
E-mail: joshyja@gmail.com, joshy@niist.res.in

August 3, 2023

## CERTIFICATE

This is to certify that the work incorporated in this Ph.D. thesis entitled, "*Design of Triphenylamine Derivatives for Organic Electronics Applications: Synthesis, Photophysics and Device Studies*", submitted by *Ms. Shibna Balakrishnan* to the Academy of Scientific and Innovative Research (AcSIR) in fulfilment of the requirements for the award of the Degree of *Doctor of Philosophy in Sciences*, embodies original research work carried out by the student. We further certify that this work has not been submitted to any other University or Institution in part or full for the award of any degree or diploma. Research materials obtained from other sources and used in this research work have been duly acknowledged in the thesis. Images, illustrations, figures, tables etc., used in the thesis from other sources, have also been duly cited and acknowledged.

  
03/08/2023  
**Shibna Balakrishnan**

  
03.08.2023  
**Dr. Joshy Joseph**  
(Supervisor)

## STATEMENTS OF ACADEMIC INTEGRITY

I Shibna Balakrishnan, a Ph.D. student of the Academy of Scientific and Innovative Research (AcSIR) with Registration No. 10CC17A39003 hereby undertake that, the thesis entitled "*Design of Triphenylamine Derivatives for Organic Electronics Applications: Synthesis, Photophysics and Device Studies*" has been prepared by me and that the document reports original work carried out by me and is free of any plagiarism in compliance with the UGC Regulations on "*Promotion of Academic Integrity and Prevention of Plagiarism in Higher Educational Institutions (2018)*" and the CSIR Guidelines for "*Ethics in Research and in Governance (2020)*".



03/05/2023

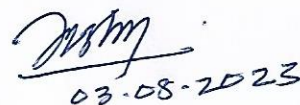
**Shibna Balakrishnan**

August 3, 2023

Thiruvananthapuram

---

It is hereby certified that the work done by the student, under my supervision, is plagiarism-free in accordance with the UGC Regulations on "*Promotion of Academic Integrity and Prevention of Plagiarism in Higher Educational Institutions (2018)*" and the CSIR Guidelines for "*Ethics in Research and in Governance (2020)*".



03-08-2023

**Dr. Joshy Joseph**

August 3, 2023

Thiruvananthapuram



## DECLARATION

I, Shibna Balakrishnan, AcSIR Registration No. 10CC17A39003 declare that my thesis entitled, "*Design of Triphenylamine Derivatives for Organic Electronics Applications: Synthesis, Photophysics and Device Studies*" is plagiarism-free in accordance with the UGC Regulations on "*Promotion of Academic Integrity and Prevention of Plagiarism in Higher Educational Institutions (2018)*" and the CSIR Guidelines for "*Ethics in Research and in Governance (2020)*".

I would be solely held responsible if any plagiarised content in my thesis is detected, which is violative of the UGC regulations 2018.



**Shibna Balakrishnan**

August 3, 2023

Thiruvananthapuram

## ACKNOWLEDGEMENTS

*I have great pleasure in expressing my deep sense of gratitude to Dr. Joshy Joseph, my thesis supervisor, for suggesting the research topic and for his constant guidance, endearing care, valuable support and encouragement, leading to the successful completion of this work.*

*I wish to thank Dr. C. Anandharamakrishnan, Director and Dr. A. Ajayaghosh, former Director of the CSIR-National Institute for Interdisciplinary Science and Technology, Thiruvananthapuram, for providing me the necessary facilities for carrying out the work.*

*My sincere thanks to:*

- *Dr. Vijayakumar C., Dr. Narayanan Unni K. N. and Dr. Hareesh U. S., Doctoral Advisory Committee (DAC) members for their informative discussions in the DAC meetings.*
- *Dr. V. Karunakaran, Dr. C. H. Suresh and Dr. R. Luxmi Varma, present and former AcSIR co-ordinators for the timely help and advice for the academic procedures of AcSIR.*
- *Dr. K. V. Radhakrishnan, Dr. P. Sujatha Devi, and Dr. R. Luxmi Varma present and former Heads, Chemical Sciences and Technology Division for their endless support.*
- *All the AcSIR faculty members of CSIR-NIIST for their help and support during the course work period.*
- *Dr. K. R. Gopidas, Dr. Biswapriya Deb, Dr. Jubi John, Dr. Sreejith Sankar, Dr. V. K. Praveen, Dr. Suraj Soman, Dr. Ishita Neogi, Dr. Adersh Asok, Dr. Sunil Varughese, Dr. K. Yoosaf, Dr. Rakhi R. B., Dr. E. Bhoje Gowd present and former, and all other scientists of the Chemical Sciences and Technology Division, for all the help and support extended to me.*
- *Prof. Dr. Atsushi Wakamiya, Dr. Richard Murdey, Dr. Minh Anh Truong and Dr. Tomoya Nakamura, Kyoto University, Japan for the Perovskite solar cell fabrication.*
- *Mr. Robert Philip, Mr. Kiran Mohan, Mr. Nidhin, Mr. Jerin, Mr. Merin, Mrs. Gayathri, Mr. Prasad, Mrs. Viji S. and Ms. Aswathi for the general help, Mrs. Saumini Mathew for NMR analysis, Mrs. Viji for HRMS data, Mr. Amal Raj for XRD analysis, and Mr. Peer Mohamed A. for XPS analysis.*

- *Mr. Vibhu Darshan, Mr. Vipin C. K., Ms. Ranjana Venugopal, Mr. Nayan Dev Madhavan, Dr. Shaiju, Ms. Krishna Priya, Ms. Sofi, Ms. Raji, Mr. Rishad, Ms. Anjali Sajeev, Mr. Shyam, Dr. Sumitha Paul, Dr. Gayathri, Dr. Vijitha and Dr. Nitha P. R. for helping me with the various experiments.*
- *Dr. Sreejith M., Dr. Sandeepa K. V., Dr. Silja Abraham, Dr. Shameel, Dr. Sajena K. S., Dr. Anjali B. R., Mr. Mathews K. Maniyani, Dr. Shanthi Krishna A., Dr. Samatha Mathew, Ms. Nishna N., Ms. Pavithra V. Prabhu, Ms. Anagha Thomas, Mr. Arjun V. Prakash, Ms. Aswathi H., Mr. Hrishikes A., Ms. Swathi Lakshmi, Mr. Robert Philip and all other former group members for their good cooperation and companionship in the lab.*
- *M. Sc. project students for all the help and love*
- *Indu, Susu, Sheba, Vishnu for their constant care, support, and affection throughout my stay at NIIST and Neethi, Vimal, Mani, Akshay, Rani, Kavya, Aneesha, Megha, Riya, Naveen, Vyshna Priya, Praveen, Anu, Alisha, Anisha, Greeshma and all other present and former members of CSTD & friends at CSIR-NIIST for their good companionship, care, love, and support throughout my PhD period.*
- *CSIR-JRF and SRF for financial assistance.*

*I am deeply indebted to my parents and my brother for their unconditional love, and unerring support in my life. I am deeply grateful to my partner Reji for all the patience, understanding, love and support. I would also like to extend my thanks and appreciation to all my teachers and friends for their help and support.*

***Shibna Balakrishnan***

## TABLE OF CONTENTS

Certificate		i
Statements of Academic Integrity		ii
Declaration		iii
Acknowledgments		iv
Table of Contents		vi
List of Abbreviations		ix
Preface		xiii
<b>CHAPTER 1</b>	<b>Triphenylamine based Molecules towards Organic Electronics Applications: An Overview</b>	<b>1-74</b>
1.1.	Abstract	1
1.2.	Introduction	3
1.3.	Triphenylamine: Structural and Electronic Properties	4
1.4.	Triphenylamine based Materials for Electrochromic Applications	8
1.4.1.	Electrochromism	8
1.4.2.	TPA based Small Molecules	15
1.4.3.	TPA Containing Polymers	18
1.5.	Triphenylamine based Materials as Hole Transporting/Injecting Layers	27
1.5.1.	Perovskite Solar Cells and TPA based Hole Transporting Materials	27
1.5.2.	Organic Light Emitting Diodes and TPA based Hole Transporting/Injecting Materials	39
1.6.	Cross-linkable Materials and their Organic Electronics Applications	45
1.6.1.	Hyper-cross-linking/Hyper-branching of Materials and their Organic Electronics Applications	53
1.7.	Objectives of the Present Investigation	56
1.8.	References	58
<b>CHAPTER 2</b>	<b>Effect of Hyper-crosslinking on the Electrochromic Device Properties of Carbazole-Diphenylamine Derivatives</b>	<b>75-124</b>
2.1.	Abstract	75
2.2.	Introduction	77
2.3.	Results and Discussion	84
2.4.	Conclusions	103



2.5.	Experimental Section	104
2.5.1.	Materials and Methods	104
2.5.2.	Electrolyte Preparation	105
2.5.3.	Electrochromic Device Fabrication	106
2.5.4.	Synthesis and Characterization of the Molecules	107
2.5.5.	NMR and ESI-HRMS Spectra of <b>C-OMe</b> , <b>C-Sty2</b> and <b>C-Sty3</b>	114
2.6.	References	118
<b>CHAPTER 3</b>	<b>Terpyridine Appended Tetraphenylethylene-Diphenylamine Derivatives and their Iron Metallo-polymers: Photophysical and Electrochromic Properties</b>	<b>125-170</b>
3.1.	Abstract	125
3.2.	Introduction	127
3.2.1.	The Randles-Sevcik Equation and Electrochemical Processes	133
3.3.	Results and Discussion	135
3.4.	Conclusions	155
3.5.	Experimental Section	156
3.5.1.	Materials and Methods	156
3.5.2.	Synthesis of Metallo-polymers	158
3.5.3.	Polymer Film Preparation	158
3.5.4.	Synthesis and Characterization of the Molecules	159
3.5.5.	NMR and Mass Spectra of <b>TPE-TPy4</b> and <b>TPE-TPy2</b>	164
3.6.	References	167
<b>CHAPTER 4A</b>	<b>Cross-linkable, Carbazole-Diphenylamine Derivatives as Dopant Free, Hole Transporting Materials for Perovskite Solar Cells</b>	<b>171-202</b>
4A.1.	Abstract	171
4A.2.	Introduction	173
4A.2.1.	Mixed Halide Hybrid Perovskites for Perovskite Solar Cells	176
4A.3.	Results and Discussion	180
4A.3.1.	Thermal, Photophysical and Electrochemical Properties	180
4A.3.2.	Photovoltaic Performance of Devices	185
4A.4.	Conclusions	195
4A.5.	Experimental Section	195
4A.5.1.	Materials and Methods	195
4A.5.2.	Preparation of $\text{Cs}_{0.05}\text{FA}_{0.80}\text{MA}_{0.15}\text{PbI}_{2.75}\text{Br}_{0.25}$ Solution	197

4.A.5.3.	p-i-n Device Fabrication	197
4A.6.	References	199
<b>CHAPTER 4B</b>	<b>TPE-Diphenylamine Derivatives as Solution- Processable Hole Injectors with Better Charge Balance for Organic Light Emitting Diodes (OLEDs)</b>	<b>203-224</b>
4B.1.	Abstract	203
4B.2.	Introduction	205
4B.2.1.	Charge Balance in OLEDs	206
4B.3.	Results and Discussion	209
4B.4.	Conclusions	219
4B.5.	Experimental Section	220
4B.5.1.	Materials and Methods	220
4B.5.2.	Device Fabrication	220
4B.6.	References	221
	Abstract of the Thesis	225
	List of Publications	227
	List of Posters Presented in Conferences	228

## LIST OF ABBREVIATIONS

Å	Angstrom
AFM	Atomic-force microscopy
AgCl	Silver(I) chloride
AIE	Aggregation induced emission
Ar	Argon
BaSO <sub>4</sub>	Barium sulphate
CB	Conduction band
CH <sub>2</sub> Cl <sub>2</sub>	Dichloromethane
CHCl <sub>3</sub>	Chloroform
CH <sub>3</sub> CN	Acetonitrile
cm	Centimetre
Conc.	Concentration
CDCl <sub>3</sub>	Deuterated chloroform
CV	Cyclic voltammetry
DCM	Dichloromethane
DFT	Density functional theory
DMF	Dimethylformamide
DMSO	Dimethyl sulfoxide
DSC	Differential scanning calorimetry
D-π-A	Donor-π-Acceptor
D-A-D	Donor- acceptor- donor
EEM	Excitation energy migration
equiv.	Equivalent
ESI	Electrospray ionization
EtOH	Ethanol
EtOAc	Ethyl acetate
EC	Electrochromic
ECD	Electrochromic device
E <sub>g</sub>	Band gap
<i>et al.</i>	Et alia
eV	Electron volt

FT-IR	Fourier transform-infrared
FTO	Fluorine doped Tin Oxide
H <sub>2</sub> O	Water
g	Gram
h	Hour
HOMO	Highest occupied molecular orbital
HRMS	High-resolution mass spectrometry
HTM	Hole transporting layer
HIL	Hole injecting layer
ICT	Internal charge transfer
$\epsilon$	Molar extinction coefficient
ITO	Indium doped tin oxide
IVCT	Intervalence charge transfer
IR	Infrared
K	Kelvin
KBr	Potassium bromide
KJ	Kilojoule
KI	Potassium iodide
KOH	Potassium hydroxide
K <sub>2</sub> CO <sub>3</sub>	Potassium Carbonate
LE	Locally excited
LUMO	Lowest unoccupied molecular orbital
LED	Light emitting diode
LiClO <sub>4</sub>	Lithium perchlorate
LiTFSI	Bis(trifluoromethane)sulfonimide lithium salt
M	Molar
MeOH	Methanol
MHz	Mega hertz
min	Minute
mL	Millilitre
mM	Millimolar
$\mu$ M	Micromolar
MV	Mixed valence
mol	Mole



m.p	Melting point
NaOH	Sodium hydroxide
Na <sub>2</sub> SO <sub>4</sub>	Sodium sulphate
nm	Nanometer
NaCl	Sodium chloride
NMR	Nuclear magnetic resonance
ns	Nanosecond
NREL	National Renewable Energy Laboratory
NiO	Nickel (II) oxide
NIR	Near infrared
OD	Optical density
OFET	Organic field-effect transistor
OPV	Organic photovoltaics
OLED	Organic light emitting diodes
PANI	Polyaniline
PB	Prussian blue
Pd(OAc) <sub>2</sub>	Palladium (II) acetate
PEDOT	Poly(3,4-ethylenedioxythiophene)
Pd(PPh <sub>3</sub> ) <sub>4</sub>	Tetrakis(triphenylphosphine)palladium(0)
PXRD	Powder X-ray diffraction
PMMA	Poly (methyl methacrylate)
$\Phi_F$	Quantum yields of fluorescence
ps	Picosecond
PVP	Poly(vinylpyrrolidone)
S	Second
SCLC	Space charge limited current
t	Time
T	Temperature
TBAPF <sub>6</sub>	Tetrabutylammonium hexafluorophosphate
TGA	Thermogravimetric analysis
THF	Tetrahydrofuran
TMS	Tetramethylsilane
TPA	Triphenylamine
TPE	Tetraphenylethylene

UV	Ultra Violet
UV-vis	Ultra Violet-visible
WAXD	Wide-angle X-ray scattering
WO <sub>3</sub>	Tungsten(VI) oxide
XRD	X-ray diffraction
$\delta$	Delta
$\Delta\lambda$	Change in wavelength
$\epsilon$	Molar extinction coefficient
$\lambda$	Wavelength
$\lambda_{em}$	Wavelength of emission
$\lambda_{ex}$	Wavelength of excitation
%	Percentage
$\tau$	Fluorescence lifetime
$\mu\text{L}$	Microliter
$\mu\text{M}$	Micromolar
$^{\circ}\text{C}$	Degree Celsius
2D	Two-dimensional

## PREFACE

In recent years, there has been a significant focus on organic electronics in both academic and industrial research and concerted efforts are in progress to advance the field by exploring new materials and improving their properties, including tunability, processability, efficiency and stability. Charge injection/transport materials and electroactive materials compatible with device fabrication conditions are essential components in many organic electronic devices such as electrochromic devices, Perovskite solar cells and organic light emitting diodes. Triarylamine derivatives in general demonstrate superior performance among several classes of materials used in organic electronics due to their favorable electron-donating properties, high thermal stability, tunable energy levels, versatility in molecular design, good film-forming properties, solution processability and cost-effectiveness. The design and development of new, triphenylamine-based charge transport materials and the investigation of the underlying principles related to their molecular design, film-forming ability, and application in organic electronics, are challenging but essential for further improvement in the device characteristics. The central focus of the current thesis is on the molecular design, synthesis, and structural role of triphenylamine-based materials in the development of solution-processable, solvent-resistant, and stable organic thin films for organic electronic devices such as electrochromic devices, Perovskite solar cells, and OLEDs.

The thesis is organised into four chapters, of which the **Chapter 1** provides an overview on triphenylamine based organic compounds, their synthesis, optical and electronic properties and classifications based on specific literature survey. It also discusses the role of triphenylamine derivatives as hole transporting and electrochromic materials in solar cells, OLEDs and electrochromic devices. This Chapter investigates the molecular design strategy, recent advancements and explores the potential of these materials as charge transporting materials in organic electronic devices. The design strategies and objectives of the thesis are also incorporated in this chapter.

In the **Chapter 2**, we discuss the EC properties of two carbazole-diphenylamine derivatives, **C-Sty2** and **C-Sty3**, with two and three thermally cross-linkable styryl units, respectively, following a donor- $\pi$ -donor (D- $\pi$ -D) design, where both the carbazole moiety and cross-linking styrene groups modulate the photophysical and EC properties. Both

styryl derivatives formed rigid, uniform, and transparent films with high solvent resistance and exhibited excellent thermal and electrochemical stability upon cross-linking. **C-Sty3**, with three cross-linkable styryl units, could form more extended cross-links, leading to hyper-cross-linked films with distinct, regular, and porous morphology compared to **C-Sty2**. The hyper-cross-linked films of **C-Sty3** demonstrated enhanced coloration efficiency, optical contrast, and open-circuit memory compared to **C-Sty2**. Electrochemical impedance spectroscopy analysis showed lower solution and charge-transfer resistances for hyper-cross-linked films of **C-Sty3**, indicating higher conductivity and ion diffusion compared to **C-Sty2**. Thus, a comparison of the EC properties of two polymers with the same electroactive groups reveals the significance of hyper-cross-linking in the EC properties of these cross-linked polymers. Furthermore, the EC properties of the hyper-cross-linked D- $\pi$ -D derivative, **C-Sty3**, were compared to those of previously reported molecules, demonstrating the importance of highly branched conducting polymers for EC applications.

Designing ligands with varying numbers of coordination sites can result in metallopolymers with linear and branched structures and these structural differences can have a significant impact on their thermal, morphological, and electrochromic characteristics. In this regard, in **Chapter 3**, two tetraphenylethylene-diphenylamine-terpyridine based ligands, **TPE-TPy2** and **TPE-TPy4**, having two and four terpyridine units attached to the diphenylamine moiety, were synthesised, and their photophysical, electrochemical, thermal, and metal interaction properties were investigated. The linear and hyperbranched Fe(II)-based metallopolymers were prepared by complexing Fe(II) salt with a 1:1 ratio of **TPE-TPy2** and a 2:1 ratio of **TPE-TPy4**, respectively. The obtained metallopolymers were fully characterized. Both the metallopolymer films on FTO showed a reversible colour change from dark greyish blue to yellow and purple to green for **TPE-TPy2-Fe** and **TPE-TPy4-Fe**, respectively. The spectroelectrochemistry of the films revealed concomitant changes corresponding to the oxidation of Fe(II) to Fe(III) and triphenylamine groups. Both the polymers demonstrated remarkable stability without significant transmittance loss for more than 300 switching cycles. Hyperbranched polymers of **TPE-TPy4-Fe** have electrochromic features predominantly due to triphenylamine oxidation including open circuit memory and near-infrared absorption. These hyperbranched polymers also exhibited better colouration efficiency

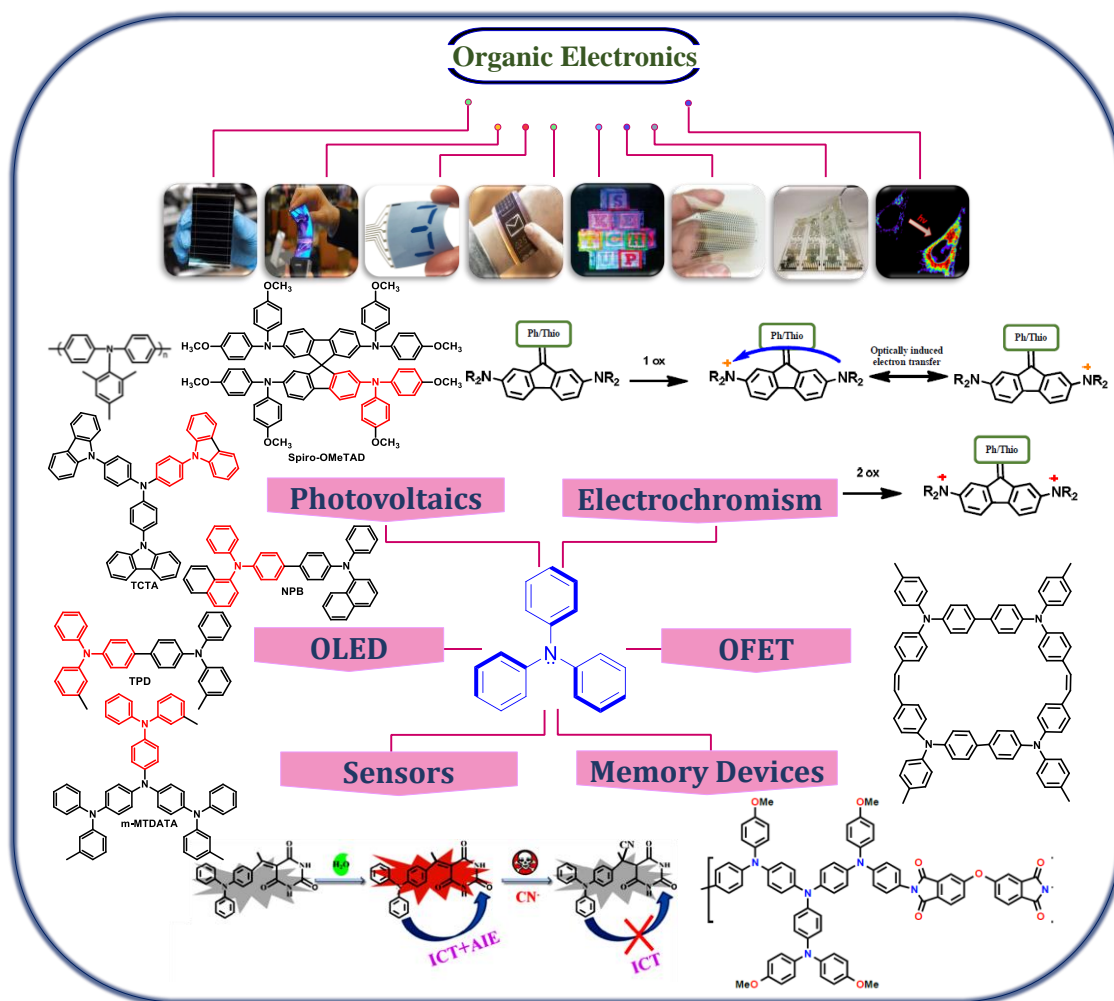


and shorter electrochromic switching time compared to linear metallopolymers of **TPE-TPy2-Fe**.

**Chapter 4A** of the thesis focuses on the application of previously discussed styrene attached carbazole-diphenylamine derivatives, **C-Sty2** and **C-Sty3** (Chapter 1) as thermally cross-linkable hole-transport materials for Perovskite solar cells. These molecules are specifically designed to exhibit thermal cross-linking properties, which allows for the formation of stable and durable hole-transporting layers in PSC devices. The performance of the PSC devices were optimized by varying several parameters, including weight percentage of the hole-transporting material, spin-coating speed (rpm), annealing time and annealing temperature. Optimized devices of **C-Sty3** and **C-Sty2** showed power conversion efficiencies (PCE) of 16.1% and 15.2%, respectively in comparison with the standard HTM, **PTAA** based device with PCE of 18.8%. This chapter highlights the influence of different parameters on device performance and demonstrates the potential of these materials to enhance the efficiency of PSCs through the formation of stable and conductive hole-transporting layers.

Charge injection and transport layers with optimum carrier transport properties are essential for stable and efficient OLED devices. In **Chapter 4B**, we report two tetraphenylethylene-diphenylamine derivatives, **TPOMe** and **TPOSt** having four and two methoxy substituents, respectively and explore their potential as solution processable hole injection layers (HILs) for OLEDs. Standard, Alq3-based green OLEDs with a simple device design were used to demonstrate the properties of the synthesized HILs, in comparison with a commercially available standard HIL, m-MTDATA. **TPOMe** based device exhibited a current efficiency of 4.2 cd/A, while **TPOSt** based device showed 3.81 cd/A at 10 mA/cm<sup>2</sup>. Both the above devices showed better performance compared to a control device fabricated with the standard HIL, m-MTDATA which showed a relatively lower current efficiency value (1.70 cd/A at 10 mA/cm<sup>2</sup>). Similarly, the maximum EQE of **TPOMe** (1.77%) and **TPOSt** (1.55%) were higher than that of the m-MTDATA based device (1.40%). Although m-MTDATA device has better luminance and hole mobility compared to **TPOMe** and **TPOSt** devices, the optimum charge balance in the latter devices lead to better current efficiency and EQE.

## Triphenylamine based Molecules towards Organic Electronics Applications: An Overview



### 1.1. Abstract

Organic materials have garnered a lot of attention in the past couple of decades, owing to advancements in material design and purification, which have strengthened material performance in various organic electronic devices. Weak van der Waals

interactions between individual molecules in organic materials enable the conservation of their characteristics in bulk, allowing organic material designs to be easily done at the molecular level. Organic photo- and electro-active materials, including small molecules, oligomers, and polymers have made their way into applications like organic light-emitting diodes, sensors, solar cells, photorefractive devices, organic field-effect transistors, and organic electrochromic devices due to their light weight and flexibility in forming low-cost, solution-processable thin films over a wide area and on flexible substrates. In this sense, triphenylamine derivatives with twisted molecular conformations and multiple amine centres have drawn specific interest as organic charge transport materials. The triphenylamine moiety acts as a good electron donor unit with easy oxidizability, hole mobility, and compatible energy levels, color tunability and redox stability enabling TPA derivatives to achieve the highest efficiency and performance among photovoltaics, OLEDs and electrochromic systems. The design and development of triphenylamine-based derivatives with features that could potentially enhance device performance are essential for improving the capabilities of organic materials for future applications. The current thesis examines the vital role that triphenylamine-based charge transport materials serve in optoelectronic applications and the principles underlying their molecular design. Synthesis of various triphenylamine derivatives, characterization, optoelectronic properties and investigation of their applications as electrochromic, hole transporting, and hole injecting materials in electrochromic devices, Perovskite Solar Cells (PSCs), and OLEDs, respectively are reported in the thesis. In this context, the current chapter provides an overview on molecular design and optoelectronic properties of triphenylamine derivatives with special focus on electrochromic, photovoltaic and OLED applications.

## 1.2. Introduction

In recent decades, organic materials have received a lot of attention as a result of developments in material design and purifying procedures. Organic light-emitting diodes (OLEDs), sensors, solar cells, photorefractive (PR) devices, and organic field-effect transistors (OFETs) are examples of the electrical, organic electronics and photonic devices that use these materials.<sup>1,2</sup> Organic materials have a number of benefits, especially their light weight, and flexibility, which facilitate the development of affordable, solution-processable thin films across large areas and on flexible substrates.<sup>3,4</sup> TPA derivatives, due to their efficient charge transport, thermal stability and tunable properties have allowed their function as organic charge transport materials and are used in devices as light emitters, electrochromics, hole transporting, and hole injecting materials.<sup>5</sup> To enhance the performance of electronic devices based on triphenylamine-based materials, researchers have explored various strategies like cross-linking, doping, molecular interface engineering etc. In recent studies, heat-induced cross-linking of styrene-based materials has been explored as a method to enhance their stability and charge transport properties in organic electronic devices. Approaches like hyper-cross-linking and hyper-branching have also been investigated to improve the mechanical and organic electronic properties of TPA-based materials. Triphenylamine-based compounds have shown great potential for application in electrochromic devices. Their ability to undergo reversible color changes when an electric field is applied makes them useful for displays and smart windows. As materials that transport or inject holes, TPA-based HTMs have utilized to increase the stability and performance of Perovskite solar cells and OLEDs. TPA is therefore a key component in organic electronic devices due to its outstanding charge



transport capabilities, variable energy levels, and stability. Continued research and development in this area has the potential to improve the performance and scope of these materials in future electronic technologies.

### **1.3. Triphenylamine: Structural and Electronic Properties**

For a wide range of organic electronic materials to be used in OLEDs, photovoltaics and electrochromic devices, certain material qualities are required, including high electronic-grade purity, suitable thermal stability, appropriate energy levels, non-crystalline or amorphous morphology when formed into thin films, and reversible electrochemical behavior. The electron-rich structural unit of triphenylamine can be incorporated in to the organic electronic materials like small organic molecules, organic polymers and metallopolymers for achieving the hole transporting and electrochromic behavior. Due to the steric hindrance caused by the bulky phenyl groups, the phenyl rings are forced to tilt or twist away from the plane defined by the nitrogen atom and its attached hydrogens typically more than<sup>6</sup> degrees. This tilting results in the propeller-like shape of the molecule with D<sub>3</sub> symmetry.

X-ray and computational analyses have unveiled certain structural characteristics in the neutral state of the compound.<sup>7</sup> These include an average C-N bond length measuring 1.42 Å, an optimal tilting of phenyl groups at a torsional angle of 42° relative to the CCCN plane and a C-N-C bond angle of 120° (Figure 1.1A).<sup>8</sup> The structure of triphenylamine molecule is shown in Figure 1.1B. The HOMO of the TPA is distributed all over the molecule, particularly on the N-atom (59% of unpaired electron is localized on the central nitrogen atom) and at the ortho- and para-positions of the phenyl carbon atoms, while it is less prominent at the meta-positions. The central nitrogen atom has no contribution to the LUMO (Figure 1.1C).

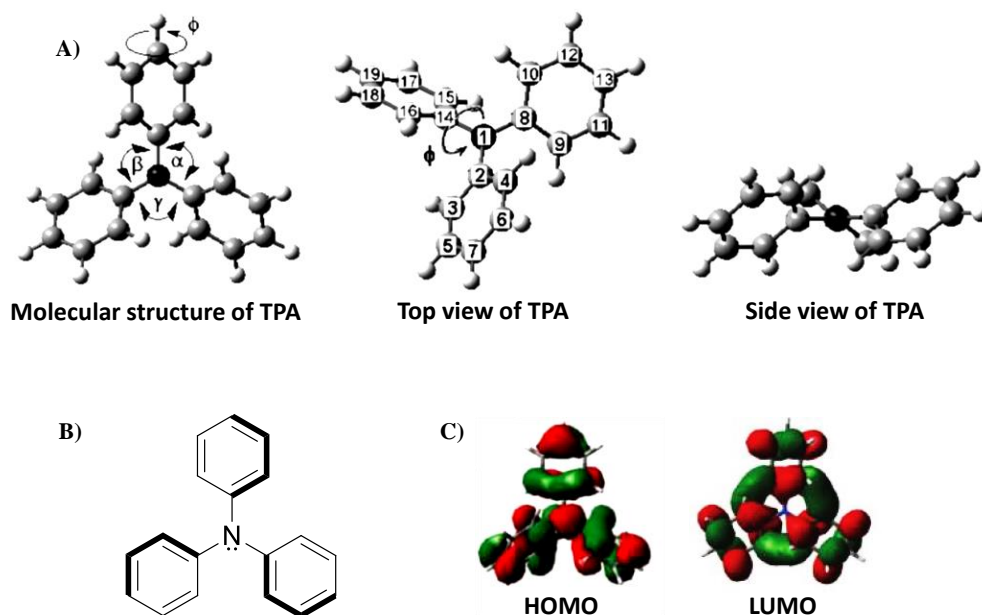


**Figure 1.1.** (A) Optimized molecular structure and top and side views of TPA; (B) Chemical structure of TPA and (C) HOMO-LUMO molecular orbitals for triphenylamine. (Adapted from reference 6 and 7)

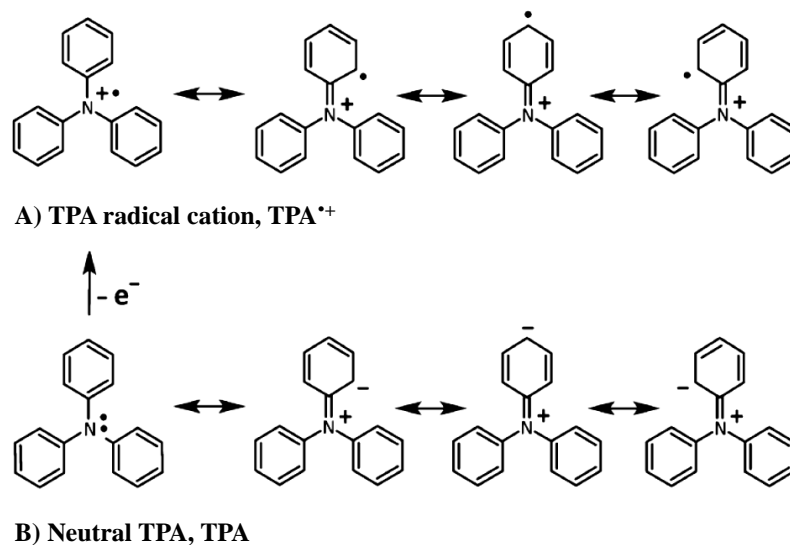


**Figure 1.2.** Resonance structures for (A)  $\text{TPA}^{\bullet+}$  and (B) neutral TPA. (Adapted from reference 9)

Radical cation also has a similar structure, with somewhat shorter CN bonds, a lower torsion angle, and the central NCCC atoms remaining planar.<sup>9</sup> Thus, the inner reorganization energy of the triphenylamine is lesser than many other redox systems. The distribution of the HOMO in the molecules indicates that the electrons in the lone

pair on the nitrogen atom are distributed almost all over the structure. Resonant Lewis structures can be employed to illustrate how the electron density is particularly strong on the *ortho*- and *para*- carbons of the phenyl ring, while the electron distribution is comparatively weaker on the *meta*- positions (Figure 1.2).<sup>10</sup>

TPA produces radical cation upon one electron oxidation which is unstable due to the high spin density at the *para*- position. Consequently, it undergoes an irreversible chemical process of dimerization to form tetraphenylbenzidine (**TPB**). Two radical cations of **TPA** (**TPA<sup>•+</sup>**) irreversibly combine to form **TPB<sup>2+</sup>** and the removal of two H<sup>+</sup> will result in the formation of stable and neutral benzidine. By introducing methoxy and tert-butyl groups in the *para*- position of triphenylamine, radical cations become incapable of electrochemical oxidation.<sup>11</sup>

Mixed valence systems refer to derivatives of TPA that contain more than one interconnected redox centers displaying distinct oxidation states. These systems enable the transfer of an electron or a hole through optical or thermal excitation. Robin and Day classified electron transfer interactions in bridged TPA compounds into three categories, considering two key factors: the degree of electronic coupling ( $H_{ab}$ ) between the two redox sites and the reorganization energy ( $\lambda$ ) involved with the transfer of electron between them. The magnitude of interaction or the electronic coupling is expressed as  $H_{ab}$  which is equal to  $\langle \Psi_a | H | \Psi_b \rangle$ , where H can be termed as molecular Hamiltonian and two localized states denoted as  $\Psi_a$  and  $\Psi_b$ .<sup>12</sup> According to the classification of Robin and Day in 1968, class I refers to no electronic coupling ( $H_{ab}=0$ ), i.e., the charge is completely localized so that redox couple act as separate entities. In class III, the opposite extreme is found, that is the interaction between the two centers is so great and strong electronic coupling results in uniform distribution of charge between the redox centers. The electronic coupling,  $2H_{ab}$ , of class III is

greater or equal to the reorganization energy ( $2H_{ab} \geq \lambda$ ). Class II systems exhibit a relatively low intermediate electronic coupling, resulting in the majority of the charge being localized in a specific redox center. However, this charge can still be transferred to another center. When the wave functions describing the two potential wells are mixed, new adiabatic potential energy surfaces are formed, characterized by an energy splitting of  $2H_{ab}$ .

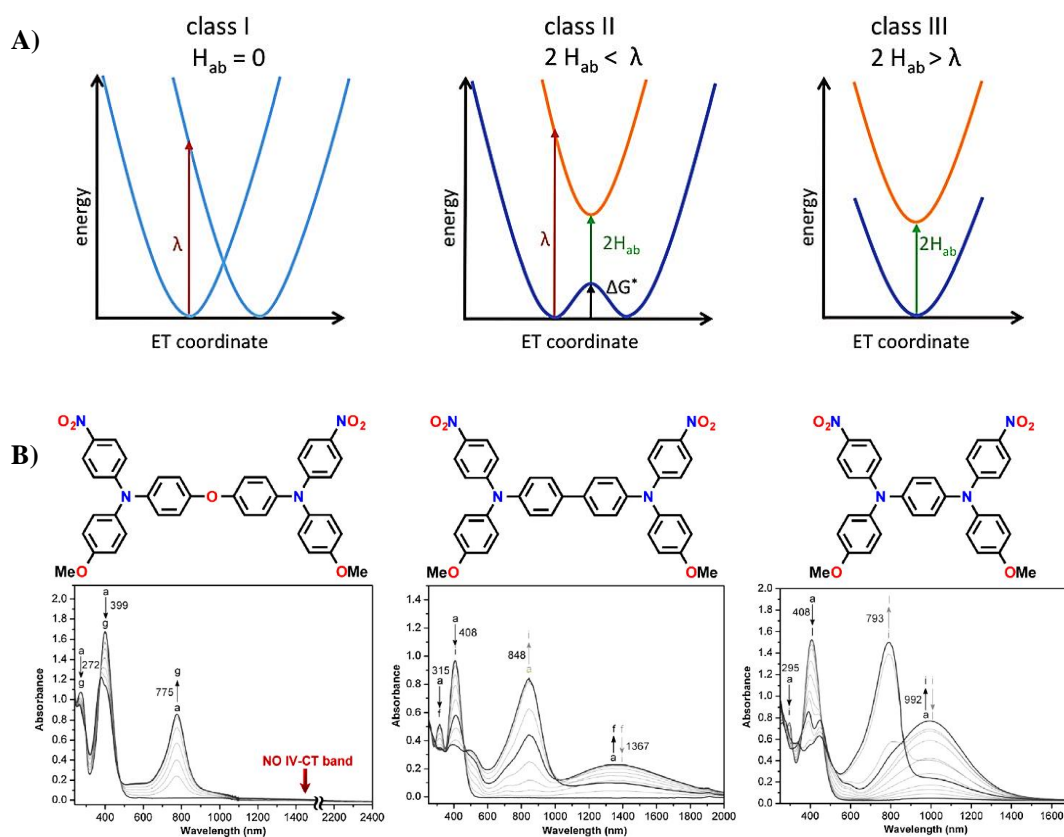


**Figure 1.3.** (A) Potential curves for the three Robin–Day classes and (B) Absorption spectra of representative compounds at various applied potential. (Adapted from reference 12 and 13).

In the potential energy diagram (Figure 1.3A) of class I compounds, the curves are not merged at all which represent the species as dissimilar and the reaction is unable to proceed whereas, class II and class III curves seem to merge because there the electron transfer is possible. Class II systems (electronic coupling,  $2H_{ab} < \lambda$ ) exhibit

a ground state potential energy curve characterized by a double-well structure, where two distinct reaction pathways can be formed. One pathway is associated with the absorption of light, while the other pathway is initiated by thermal processes. Such Franck-Codon transitions due to the optical excitation typically led to structureless broad bands in the near-infrared (NIR) region, which are denoted as intervalence charge transfer (IVCT) bands. In the case of class III systems, full mixing of two potential energy curves indicates there is no thermal activation barrier and no hump so that ions can freely transit between both states, which results in a very delocalized system. Usually, polymers bridged by ether linkage show separate redox centers having electrochemical properties and they fall into the class I category. A class III based tetraphenyl-*p*-phenylenediamine (TPPA)<sup>13</sup> and class II tetraphenylbenzidine (TPB)<sup>14</sup> exhibited IVCT bands in the near IR region (Figure 1.3B).

## **1.4. Triphenylamine based Materials for Electrochromic Applications**

### **1.4.1. Electrochromism**

The phenomenon of electrochromism has piqued the curiosity of many researchers due to its optical switching ability, which offers various options for energy-saving and color-tuning applications, such as smart windows, electronic papers, mirrors, sunglasses, display devices, etc.<sup>15-18</sup> Electrochromic devices have drawn a lot more attention since Deb displayed the first instances of the electrochromic phenomenon of tungsten trioxide (WO<sub>3</sub>). The WO<sub>3</sub> film exhibits a reversible color change, shifting from colorless to blue when subjected to a negative voltage. Furthermore, electrochromic device (ECD) using a thin film of WO<sub>3</sub>, which is widely recognized as the foundation of research in the field of electrochromism.<sup>19,20</sup> However, J.R. Platt created the term electrochromism in 1961 and stated that

“Theoretical considerations suggest that the absorption and emission spectra of certain dyes may be shifted by hundreds of angstroms upon application of a strong electric field. The effect could be called electrochromism, in analogy to thermochromism and photochromism”.<sup>21</sup>

Generally, ECD is a multilayer electrochemical device (Figure 1.4A), which includes two electrodes (FTO, ITO, carbon nanotubes, PET-ITO, graphene, carbon nanotubes, etc.), an electrochromic layer which is the active or core component that controls the EC performance and changes color when the reaction occurs and an ionically conductive electrolyte which can be liquid, semi-solid or solid doped with lithium salt, ammonium salt, or ionic liquid for balancing the carrier transportation from the active EC layer. An ion storage layer, which experiences reversible electrochemical oxidation (reduction) along with the reduction (oxidation) of the electrochromic layer in the device and ensures correct charge balance.

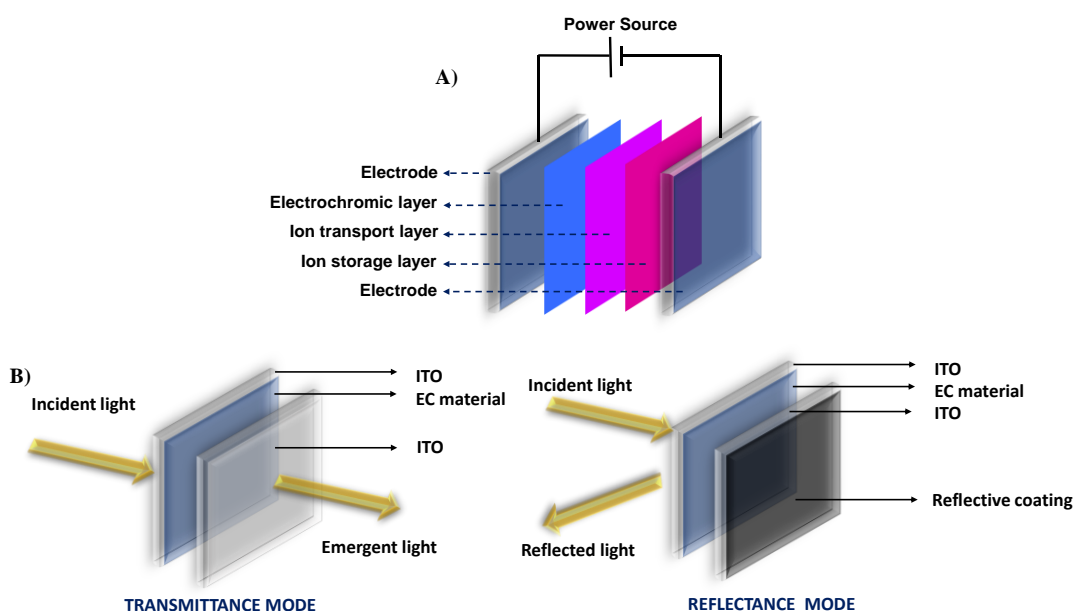


**Figure 1.4.** Representation of (A) general electrochromic device structure and (B) transmittance and reflectance mode electrochromic devices.

Depending on the type of application, structure of the ECD will be varied. ECDs are classified into two types: (i) absorptive/transmissive ECDs (smart windows and glasses) and (ii) absorptive/reflective ECDs (displays and auto-dimming car mirrors) on the basis of the structure and device modes of operations as shown in Figure 1.4B. In the transparent EC devices, two FTO/ITO coated glass substrates are used as electrodes and the transmittance mode of operation works. In the reflectance mode, the transparency of one electrode is maintained, whereas the other electrode is made reflective by coating it with aluminum, gold, or silver. Devices can also be grouped into inorganic (metal oxides, metal complexes, and metal/alloy), organic (small molecules, covalent organic frameworks, cross-linking molecules and polymers), metal-organic coordination complexes, and hybrid materials based on the electrochromic materials being used. Electrochromic device performance is determined by several device features such as;

**(i) Optical contrast:** The variation in transmittance between two different redox states of an electrochromic device. It is often reported as the percent transmittance change ( $\Delta\%T$ ) at a specified wavelength where the electrochromic material has the highest optical contrast.

**(ii) Coloration efficiency,  $\eta$ :** Ratio between the change in optical density ( $\Delta OD$ ) and the amount of electronic charge injected or ejected ( $Q_d$ ).

$$\eta = \frac{\Delta OD}{Q_d} = \log [T_b/T_c]/Q_d \quad \text{Equation 1.1}$$

where,  $\eta$  ( $\text{cm}^2/\text{C}$ ) is the coloration efficiency at a given wavelength and  $T_b$  and  $T_c$  are the percentage transmittance at bleached and coloured states, respectively.

**(iii) Response time/switching speed:** Time required for the electrochromic device to change from one color state to another (coloring/bleaching). Low response

time is required for applications such as switchable mirrors and dynamic displays. The response time of electrochromic materials is mainly dependent on factors such as the ionic conductivity of the electrolyte, ionic diffusion in the electro-active thin films, magnitude of the applied potential, thickness and morphology of the electrochromic film.

- (iv) ***Open-circuit memory***: Ability of the electrochromic material or device to maintain a given redox state even after the electric field is removed.
- (v) ***Cycle stability***: Measure of the device's ability to undergo repeated switching cycles without significant degradation. Irreversible redox reactions at extreme potentials, secondary reactions due to the presence of water or oxygen in the ECDs, and the resistive heating in the system will immensely contribute to the degradation process. A high cycle stability is essential for the long-term reliability of the device.
- (vi) ***Applied voltage required to switch***: Voltage that needs to be applied to the electrochromic device to induce the coloration or bleaching process. Lower applied voltages are preferred for energy-efficient operation.

Numerous EC materials have been extensively researched and are highly promising for their potential applications in the field of electrochromism. Among the building blocks available for fabricating the EC devices, triphenylamine (TPA) derivatives are developing vibrantly due to their excellent electron-donating nature with noticeable color changes and stable free radical formation. The propeller-shaped triphenylamine exhibits significant steric hindrance and benefits from hyper-conjugation electronic effects. These factors contribute to enhanced thermal and morphological stability, facilitating the formation of stable free radical cations and



improving hole mobility. Apart from that, synthetic accessibility and the possibility of tuning the electrochemical and photophysical properties also effectively enhanced the demand for these materials in the electrochromic research field.

In recent years, a great deal of focus has been placed on modifying the physical and chemical characteristics of various electrochromic materials in order to make them economically feasible. The use of composite materials to enhance electrochromic performance has become increasingly popular in the field of EC materials and applications. The fabrication strategy of using complementary color materials like viologen molecules as cathodic materials and tetra-*N*-phenyl-benzidine as anodic material<sup>22</sup>, Prussian white (PW) film and WO<sub>3</sub> nanosheets<sup>23</sup>, NiO and Prussian Blue<sup>24</sup> for achieving transparent to black EC switching are some examples. Similarly, combinations of metal electrodeposition and organic EC polymers<sup>25-27</sup>, combining electrically driven chemical-color changes with physical-color changes have been reported.<sup>28-30</sup> For example, Jianguo Mei's group demonstrated colloidal SiO<sub>2</sub> nanocrystals embedded into the electrolyte which can passively change the structural-color and actively control the light (color) under applied potential (Figure 1.5A).<sup>31</sup> Introduction of nanostructures in the active materials improve the EC properties due to their increased specific area and active sites.<sup>32-35</sup> ZnO nanofilms<sup>36</sup>, tungsten-bronze-like Nb<sub>18</sub>W<sub>16</sub>O<sub>93</sub><sup>37</sup>, free-standing 3D nanostructured polymers of PEDOT and its derivatives<sup>38</sup> and porous nanostructures such as, metal-organic frameworks<sup>6,39</sup>, covalent organic frameworks<sup>40,41</sup> and hydrogen-bonded organic frameworks<sup>42</sup> are some of the examples. A novel porous NiO@C thin film electrode was reported and it showed good electrical and ionic conductivity with fast switching speed and stability. The material was then applied as smart eyewear (Figure 1.5B).<sup>43</sup> In 2020, Masayoshi Higuchi reported a supramolecular metallopolymer of

Fe(II)/Os(II) EC material and displayed a flower pattern which displayed six multicolor image with the applied voltage and shown in Figure 1.5C.<sup>44</sup> In the research of Gerardo Hernandez-Sosa and group on a polymer called polyindenofluoren-8-tryarylamine polymer (PIF8-TAA), they demonstrated a dual-mode device that combines electrochromic and electrofluorochromic effects. This innovative device design offers a cost-effective solution for signage or advertising displays (Figure 1.5D).<sup>45</sup>

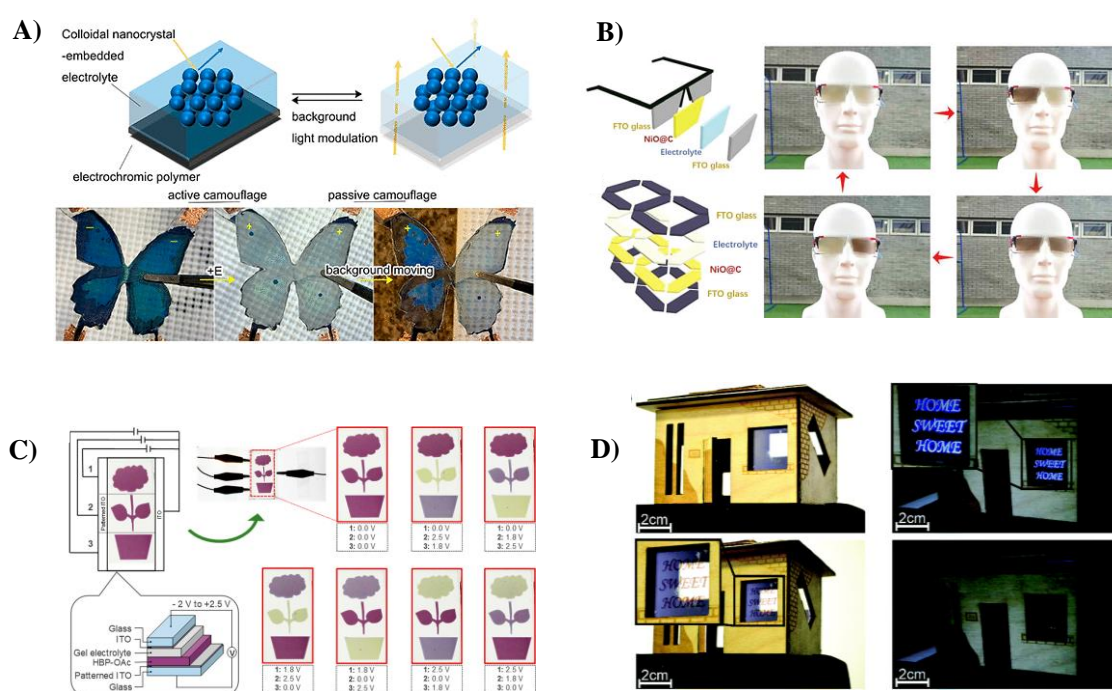


**Figure 1.5.** (A) Butterfly EC device showing color change for both active and passive camouflage; (B) NiO@C electrode-based EC devices for eye ware display; (C) Representation of structure and images of segmented EC display and (D) Application of EC/EFC dual-mode devices. (Adapted from reference 31, 43, 44 and 45)

Many attempts have been made to commercialize electrochromic materials (Figure 1.6). Auto-dimming rear-view mirror system for vehicles and dimmable windows for Boeing's New 777X based on electrochromic materials were created and made available by Gentex Corp. Electrochromic smart windows were first commercialized by Pilkington in 1998. Later Sage Electrochromics developed a smart

window called Sageglass, which is electronically tintable and today they possess the most advanced electrochromic glass services. Around the world, they have electrochromic glass installed in 700 projects including famous constructions like Frost School of Music Rooms (University of Miami), Museum of Science, Boston and Lawrence Berkeley Laboratory in Oakland, CA etc. NTERA's NanoChromics™ Ink-

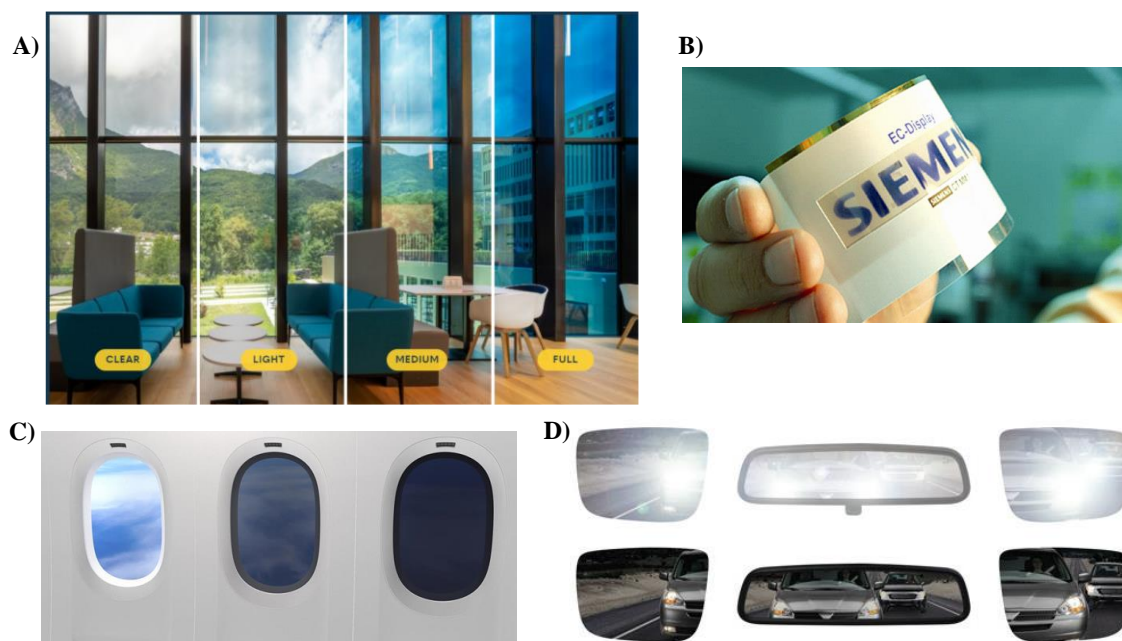


**Figure 1.6.** (A) Electrochromic window produced by SageGlass; (B) Printable and flexible electrochromic displays designed by Siemens; (C) Dimmable aircraft windows on the new Boeing 777X by Gentex Corporation and (D) Auto-dimming mirror system that eliminates virtually all rearview mirror glare.

technology enables the manufacturing of flexible printed electronic displays for smart cards, smart packaging, and smart objects. PPG Aerospace is a division of PPG Industries that specializes in aerospace coatings, sealants, and transparencies. PPG Aerospace has also made significant advancements in the field of electrochromic windows for aircraft. Their electrochromic windows, known as OPTICOR™, utilize a thin film of electrochromic material sandwiched between layers of glass. These windows can switch between clear and darkened states, allowing control over the

amount of light and heat entering the cabin. PPG Aerospace's electrochromic windows offer improved visibility, passenger comfort, and energy efficiency. They have been used in various commercial aircraft and have gained recognition in the aerospace industry.<sup>46</sup>

### 1.4.2. TPA based Small Molecules

Triarylamine based derivatives are considered as interesting anodic materials for both research and commercial electrochromic applications. While compared to inorganic materials, these materials exhibit advantages like good processability and color tunability through structural modifications. Good optical contrast, high coloration efficiency, and redox stability also make the organic molecules important candidates in the field. Oligomeric triarylamine derivatives possessing twisted molecular conformations and multiple centers have found extensive utility in many organic electronic applications as hole transporting materials, reductant and electrocatalysts etc.<sup>47-49</sup>

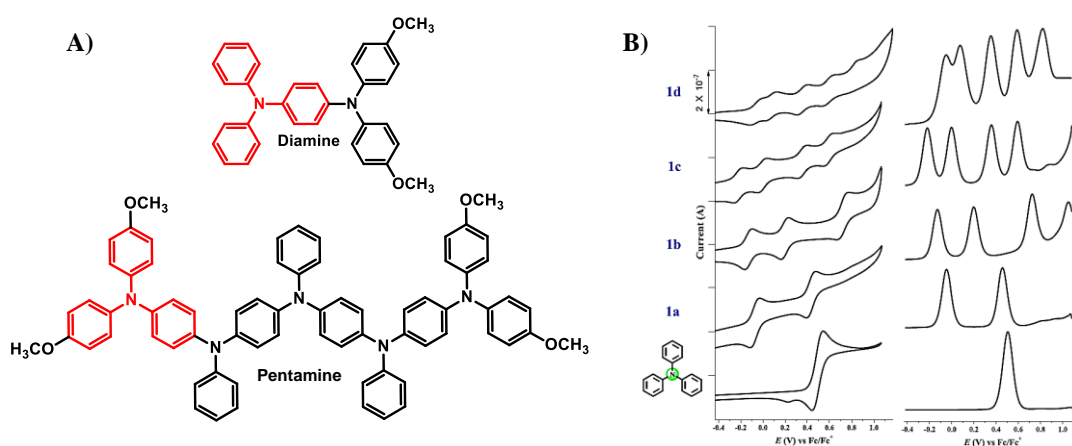


**Figure 1.7.** (A) Chemical structures of oligomeric triarylamine compounds having two and five TPA units and (B) CV and square-wave voltammograms of the oligomeric TPA derivatives and reference compound triphenylamine in  $\text{CH}_2\text{Cl}_2/\text{n-Bu}_4\text{NPF}_6$ . (Adapted from 49)

In 2017, Sheng-Hua Liu *et al.* reported a series of oligomeric triarylamine compounds by changing the number of TPA moieties from two (Diamine) to five (Pentamine) and studied the intramolecular electron transfer and their electrochromic behavior under different applied potentials.<sup>50</sup> The electrochemical results revealed well separated anodic oxidation processes for all molecules as shown in Figure 1.7. All the series of molecules displayed attractive switchable NIR absorption characteristics and different colors corresponding to their multistate redox potentials.

Six novel multi-chromic materials (NTBAs) are developed with a D-A structure, featuring nitrilotribenzoate as a catholically coloring material and TPA as an anodic material and a fluorescence quencher.<sup>51</sup> NTBAs showed multicolored electrochromism and electrofluorochromism. The monocationic radical formed from TPA oxidation caused the fluorescence-quenching. They found that the cyclic stability was more for the aryl substituents, which have an electron-donating group attached to them. Compounds with alkyl substituents showed the best performance with relatively better stability, coloration efficiency and electrofluorochromic properties.

Molecules that possess both photochromism and electrochromism together are not explored extensively. Akita *et al.* reported in 2008, a diarylethene (DAE) derivative which showed both photo and electrochromism simultaneously.<sup>52</sup> Another six novel DAE derivatives containing TPA moieties were synthesized and characterized by Xianggao Li's group (TPA-DAE), where the molecules demonstrated reversible photochromism at 302 nm UV irradiation. The fabricated electrochromic devices showed colorless to blue change with 8.6 s - 12.1 s duration for coloring and 8.9 s - 12.8 s for the corresponding bleaching process.<sup>53</sup> In 2019, a triphenylamine Schiff-base (TPASB) was introduced, which has both twisted intramolecular charge

transfer (TICT) and AIE properties.<sup>54</sup> TPASB has both electrochromic and photochromic properties and exhibits a yellow to tangerine color change at 2.5 V. The spectro-electrochemical analysis of the ECDs revealed that the IVCT band originated from the transfer of electrons between the nitrogen radical cation and the neutral nitrogen in the p-phenylenediamine segment. TPASB based device exhibited  $\Delta T_{\max}$  of 64.2% at 518 nm. A group of derivatives based on indolocarbazole-imidazole-triphenylamine were discovered to possess electrofluorochromic properties.<sup>55</sup> The fabrication of the devices involved sandwiching a mixture of compounds dissolved in an acetonitrile solution, along with 0.1 M  $\text{Bu}_4\text{NClO}_4$ , between two glass substrates coated with ITO. These devices exhibited distinct blue fluorescent switching characteristics when subjected to various applied voltages.

In 2019, Chu *et al.* have demonstrated new derivatives of TPA appended to AIEgens, triphenylethylene, and benzothiophene-1,1-dioxide with and without methoxy group attached to them, called TPE-TPA, TPE-TPAOMe, BTO-TPA, and BTO-TPAOMe.<sup>56</sup> Materials showed high quantum yield in solid state with good electro- and fluorochromic properties. Derivatives with methoxy groups showed better stability and lower oxidation potential. In this work they adopted a new cross-linking gel-type electrofluorochromic devices which can limit the restriction of intramolecular motion of AIEgen materials such that high fluorescent intensity can be observed. Heptyl viologen (HV) was also introduced in order to get better performance by reducing the working voltage and switching response time. Similarly, Guey-Sheng Liou and colleague reported TPA - Heptyl viologen based derivatives named NTPPA and NTPB prepared from Buchwald–Hartwig amination that showed both electrochromic and fluorochromic properties.<sup>57</sup> The EFC device with NTPB showed a high PL contrast ratio, low time for switching and very good stability. The ECDs displayed coloration

efficiency of  $210 \text{ cm}^2/\text{C}$  for NTPPA/HV (color change from a colorless state to a pale blue color) and  $287 \text{ cm}^2/\text{C}$  for NTPB/HV, which showed a color change from colorless to a dark blue-green color. In 2013, (4-(diphenylamino)phenyl)methyl phosphonic acid (DPP), an anodic EC material was reported by Mei Li and group.<sup>58</sup> ECD were fabricated with PC/EC/LiPF<sub>6</sub> electrolyte and a novel viologen derivative which is used as cathode material. The electrodes were surface modified by using the chemisorption method through phosphonic acid reaction with titanium dioxide. Device with these two electrodes demonstrated high contrast with the value of 63% at 670 nm and a long cyclic stability over 100k cycles. The structures of the above-mentioned molecules are shown in Figure 1.8.

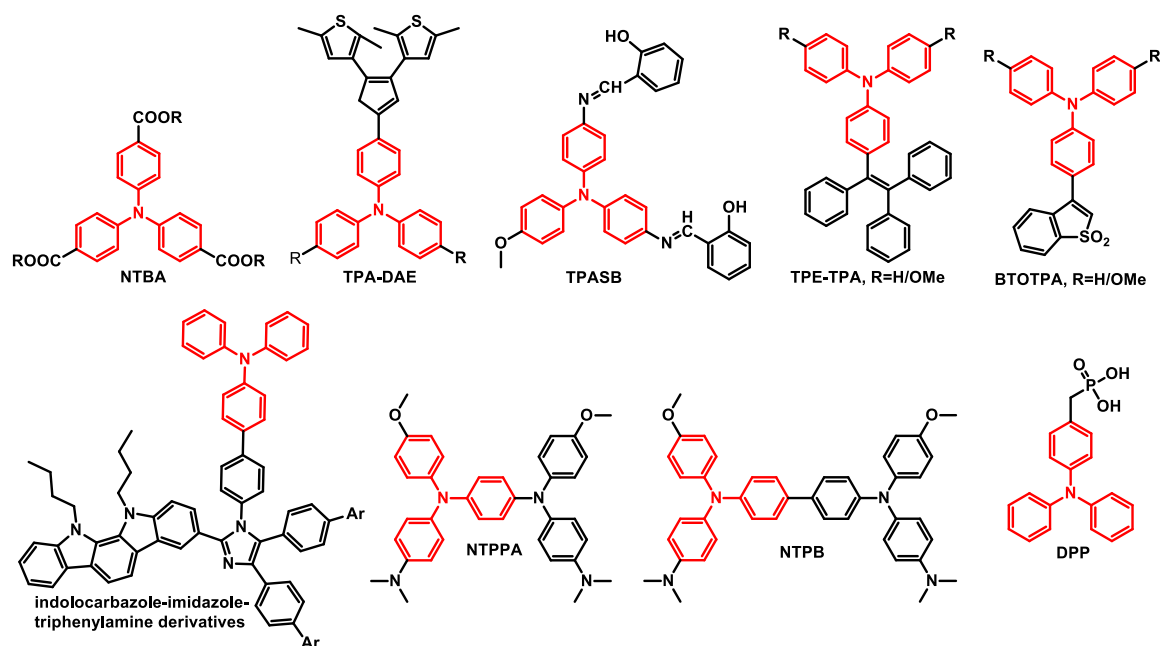


**Figure 1.8.** Chemical structures of some TPA based small molecules.

### 1.4.3. TPA Containing Polymers

The ability of charge conduction in conducting polymers arises from the delocalization of electrons in the conjugated polymeric chain, and the small bandgap ( $\sim 1.4 \text{ eV}$ ) allows low energy electronic transitions, which also enhances the electric conductivity. The oxidation of aromatic compounds such as thiophene, pyrrole,

aniline, furan, carbazole, azulene, indole, and their derivatives can lead to the formation of electroactive polymers. The properties like possible band gap tuning, fast switching, high coloration and multiple color tuning attract better attention towards conduction polymers (CP) over other inorganic polymers. Polymerization can be accomplished by different methods like thermal polymerization, electrochemical polymerization, UV irradiation, chemical synthesis etc.

Electrochemical polymerization or electropolymerization (EP) happens through the formation of cationic radical via oxidation of the monomer molecule coated on the substrates like FTO or ITO. EP offers the benefit of combining the synthesis and modification stages into a single procedure. The radical cation either reacts with the neighboring radical cation or with another monomer to form a polymer on the electrode.<sup>59</sup> In electrochemical polymerization processes, a three-electrode system is commonly employed. This system consists of three electrodes immersed in an electrolyte solution, and each electrode serves a specific purpose. The working electrode is where the polymerization happens. The choice of the working electrode material depends on the application and the specific polymer being synthesized. Inert metals (such as platinum, gold, or stainless steel), conducting glass (such as indium tin oxide, ITO), or carbon-based materials (such as glassy carbon or graphite) are frequently used as working electrodes. The reference electrode can be Ag/AgCl, and Pt is used as the counter electrode. The electropolymerization of the aniline forms PANI, which is non-conducting in its leucoemeraldine state and conducting in its emeraldine state.<sup>60</sup> Due to their good stability, conductivity and electronic properties, they have found applications in the field of organic electronics, especially in electrochromism. TPA attached molecules have been used as a polymerizing unit for the preparation of thin films since TPA can form aminium cation



that can create polymeric structure. Yu-Wu Zhong and his group have synthesized two star-shaped compounds having a pyrene core and four TPA units with (Compound 1; Figure 1.9) and without a phenyl linkage between the core and TPA moiety.<sup>61</sup> These compounds readily formed electropolymerized films on ITO substrates. The ECD fabricated with this molecule showed two step electrochromism in the NIR region.

In the year 2019, Deng *et.al* reported a 4-vinyltriphenylamine (VTPA), where the EC films with different thicknesses were prepared by electropolymerization method.<sup>62</sup> The cross-linked films were obtained by electropolymerization from a DCM solution containing 0.1M TBAP and 2.71 mg/mL PVTPA at 50 mV/s scan rate. They have tuned the thickness of the film by changing the polymerization time. For comparing the properties of the electropolymerized film, PVTPA compounds were spray coated on electrodes and then the devices were fabricated. The electropolymerized film-based device showed better cyclic stability and higher optical contrast than the others. Film with a thickness of 680 nm exhibited color changes from colorless to black with a 59.8% transmittance change in the 430-900 nm range. In a report by Shuai Li *et al.*, four TPA derivatives are discussed, which are D-A systems (nitrotriphenylamine) with different thiophene attached at the two *para*-positions of TPA and one site by an inactive unit ( methoxyl unit and cyano unit).<sup>63</sup> As a result, the polymerization site at the TPA moiety has shifted to thiophene unit, leading to an increased polymerization capability of the molecules. All polymers demonstrated high contrast ratios in the near IR region with fast switching times and excellent cyclic stabilities. In 2019, Cheng Zhang and group displayed another set of thiophene derivatives, TPAT and PHT, with TPA and phenyl core, respectively.<sup>61</sup> They prepared two bilayer polymer films during the ECP time with the compounds in the pTPAT/pPHT and pPHT/pTPAT sequential deposition order. The bilayer films

exhibited comparable optical contrast and cyclic stability to the single pTPAT films; however, they demonstrated a longer switching time. In the bilayer films, the presence of the pPHT layer functions as a barrier for charge transport, leading to a reduction in the hole-injection process. As a result, the influence of diffusion of ions and charge injection on the switching speed of electrochromic (EC) materials becomes apparent. A series of polymers derived from different TPA units and 2,5-dithienylpyrrole were designed and synthesized by Wen Wang *et al.* (2, 5-dithienylpyrrole, DTP Units) and their electropolymerization was done with Pt-counter electrode, ITO as working electrode, with 0.10 mol/L TBAP electrolyte. Among the polymers, TPA with single branched dithienylpyrrole showed better performance due to the reduced steric hindrance.<sup>64</sup> A recent study described the utilization of a pyrrole-based TPA derivative called *N*<sup>1</sup>,*N*<sup>4</sup>-bis(4-(1*H*-pyrrol-1-yl)phenyl)-*N*<sup>1</sup>,*N*<sup>4</sup>-diphenylbenzene-1,4-diamine (DPTPA) for electropolymerization, resulting in the formation of a polymer film.<sup>65</sup> The film displayed a range of six distinct colors, ranging from brown to blue, and exhibited high contrast levels of 41% at 852 nm and 52% at 617 nm. Additionally, the polymer film demonstrated rapid switching times and excellent stability. The structures of the above discussed materials are shown in Figure 1.9.

In 2015, Guey-Sheng Liou and group first reported a novel triphenylamine-imide derivative containing aromatic diamine, *N,N*-bis(4-aminophenyl)-*N',N'*-diphenyl-1,4-phenylenediamine and several tetracarboxylic dianhydrides units. The polymers formed transparent, tough, and flexible films by solution casting.<sup>66</sup> In the following years, several similar kind of derivatives of imide based polymers were reported as shown in Figure 1.10 and Figure 1.11.<sup>67-69</sup>



Similarly, numerous polyamide (PA) and TPA based systems have been reported till date, (Figure 1.12) for applications in the electrochromic field. The PAs showed high solubility, glass transition temperature, and stability. Polyamide-TPA based polymers which show NIR activity due to the IVCT happening from the strong electronic coupling also gained significant momentum. Novel starburst, NIR active TPA polymers were reported, which were prepared by phosphorylation polyamidation.<sup>70</sup> The ECD exhibited good electrochromic properties, indicating the potential for practical applications. There are many other classes of functional moieties incorporated with the triphenylamine unit and used for electrochromic applications, such as hydrazide, oxadiazole,<sup>71-74</sup> epoxy,<sup>75</sup> urethane,<sup>76,77</sup> benzoxazine<sup>78</sup> etc.

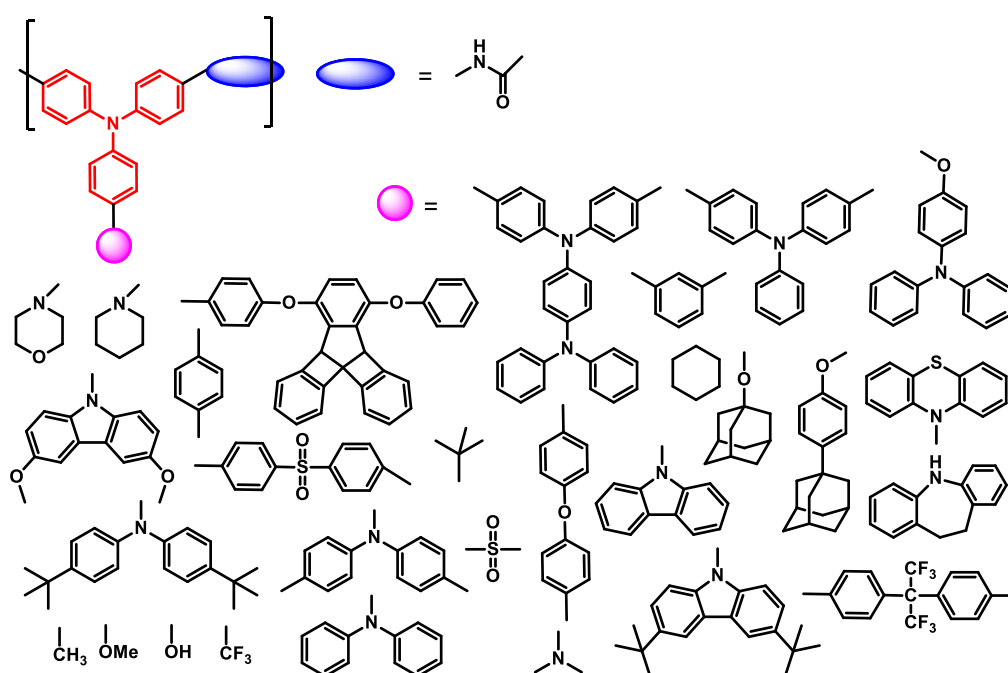


**Figure 1.12.** Chemical structures of the TPA based polyamides.

Metallopolymers comprising triphenylamine and terpyridine are a family of materials that have demonstrated potential for use in electrochromic applications. They offer several advantages like, multiple active sites, color tunability, extended

electrochromic memory, durability and NIR absorption. Tao *et al.* demonstrated the design and synthesis of six metallic terpyridine-based compounds with triphenylamine sides (Ligand L1 and Ligand L3), with the objective of increasing electrochemical polymerization and subsequently their open circuit memory and stability.<sup>79</sup> The complexes have four active polymerization sites and show discrete color variations throughout a voltage range of 0 V to 2 V. These polymer films (p-MLn) exhibited the tunability of electrochromic colors based on metal ion binding. Notably, the memory and stability of the triphenylamine-based ligands rely not only on their rigidity but also on their length. Cheng Zhang and group reported a star-shaped ligand named TPA-TPY, and successfully synthesized a Fe(II) metal complex nanosheet utilizing the liquid-liquid interface self-assembly method.<sup>80</sup> The resultant nanosheet had a thickness spanning hundreds of nanometers. The nanosheet displayed electrochromism when attached to an ITO glass substrate, changing from a purplish-red shade at 0 V to an orange-yellow shade at 1.4 V, and finally to green at 1.6 V. The optical contrast was also maintained at about 100% of its initial electrochemical activity across 500 cycles. Similarly, two trifunctional terpyridine-based triphenylamine derivatives were synthesized and their two Co(II) complex nanosheets were prepared by Wai-Yeung Wong and group.<sup>81</sup> They prepared low cost, easily processable nanosheets, with tunable structures. Metallo-polymeric films through the electropolymerization of two bisruthenium complexes  $[(Nptpy)_2Ru_2(tppyr)](PF_6)_2$  and  $[(Nptpy)_2Ru_2(tpb)](PF_6)_2$  were reported by Yao *et al.*<sup>82</sup> These polymers are composed of Nptpy, tppyr and tpb units. The films displayed four distinct anodic redox couples, corresponding to the stepwise oxidations of cyclometalated bisruthenium unit and triarylamine segments and demonstrated five-stage near-infrared electrochromism. Another liquid-liquid interface self-assembly

approach by mixing a water solution of Fe(II) metal ion with a star-shaped ligand (TBT) constituted of triphenylamine-substituted alkyl terpyridine in organic solvents was reported by Wong *et al.*<sup>83</sup> The incorporation of flexible alkyl arms within the structure resulted in films with outstanding flexibility and smooth surface. The film displayed color change from purple to yellow-green. The structures of the discussed molecules are given in Figure 1.13.

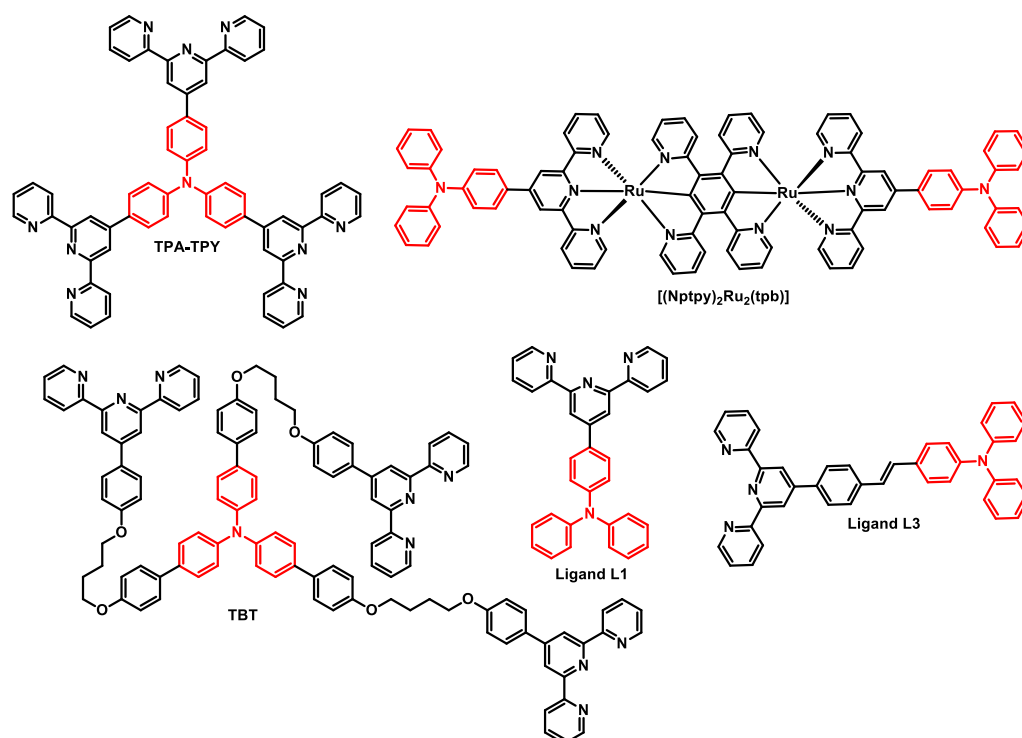


**Figure 1.13.** Triphenylamine-Terpyridine ligand structures.

Surface modified, self-assembled monolayer (SAMs) based thin films find applications in many fields and offer a versatile and powerful approach for film formation. On an ITO electrode surfaces, SAM of a ruthenium complex appended with a TPA and carboxylic acid moieties was effectively developed by Jiannian Yao and groups.<sup>84</sup> The developed films demonstrated three-color electrochromism under low voltage, strong NIR absorbance and excellent memory (Figure 1.14A). Similarly, two triphenylamine-carboxylic acid attached ruthenium complexes were synthesized by

Zhong *et al.*<sup>85</sup> A phenyl bridge separates the ruthenium ion and the amine site in complex 2, whereas a biphenyl bridge separates them in complex 4. Nanocrystalline TiO<sub>2</sub> films were produced on fluorine-doped SnO<sub>2</sub>/glass substrates to bind these complexes. Both films displayed two-step electrochromism in the NIR-region (Figure 1.14B).

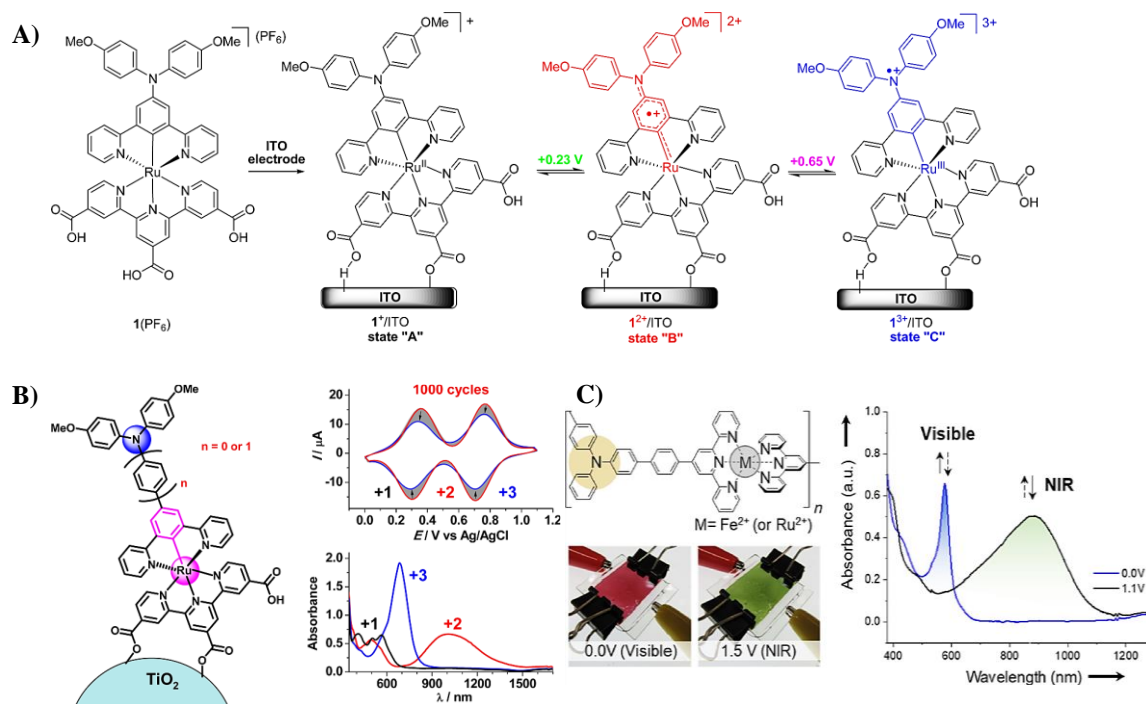


**Figure 1.14.** (A) Schematic diagram illustrating the SAM of the ruthenium complexes and their electrochromic states at different applied potentials; (B) Highly stable, NIR-active, TiO<sub>2</sub> films composed of nanocrystalline particles modified with ruthenium-amine conjugated complexes and (C) Structure of ditopic Ligand (LTPA) with NIR and visible electrochromism. (Adapted from reference 84, 85 and 86)

Two metallo-supramolecular polymers, namely polyFe-N and polyRu-N, were prepared by using the complexation of Fe(II) or Ru(II) ion with a ligand called LTPA and reported by Higuchi *et al.*<sup>86</sup> The polymers' UV-Vis spectra exhibited MLCT absorption in the visible range. From the CV experiment, two redox peaks at 0.5 V and 0.9 V corresponded to the TPA moiety and the metal oxidation, respectively were

revealed. Above 0.5 V, a new NIR absorption peak appeared attributed to the oxidation band of TPA moiety in the ligand (Figure 1.14C).

## **1.5. Triphenylamine based Materials as Hole Transporting/Injecting Layers**

A hole transporting layer (HTL) is a key component in organic electronics that promotes the transportation of positive charge carriers (holes) in an organic electronic device. It is used in organic electronic devices such as OLEDs, OPVs, and OFETs. The main function of an HTL is to efficiently transport the holes injected from the anode towards the active layer of the device or vice versa. The essential characteristics for an organic HTL/HIL are high hole mobility to allow rapid and efficient hole movement, properly aligned energy levels to facilitate effective charge injection and extraction, optical transparency in order to reduce the light absorption, good film-forming abilities for uniform and continuous layer of film formation, good chemical and thermal stability to maintain device stability and low cost. In the following sessions, we will discuss the specifics of several triphenylamine based hole-transporting materials and the way they are employed and affect the functionality of Perovskite Solar Cells and OLEDs.

### **1.5.1. Perovskite Solar Cells and TPA Based Hole Transporting Materials**

Solar cell technology has evolved through time, resulting in three generations that are; first-generation (crystalline silicon based solar cells), second-generation (thin-film solar cells from materials like amorphous silicon, CdTe and  $\text{CuIn}_x\text{Ga}_{(1-x)}\text{Se}_2$  etc.) and third-generation (DSSC, organic, Perovskite and polymer solar cells etc.). Third-generation solar cells have demonstrated a significant potential for higher efficiency and are the subject of intensive research and development. In the last few



decades, Perovskite Solar Cells (PSCs) have emerged as a capable and rapidly advancing solar technology in the field of photovoltaics. PSCs are manufactured using low-cost, solution-based techniques, making them suitable for flexible material applications and enabling cost-effective production. Furthermore, PSCs have the potential to attain greater efficiencies than Si solar cells due to their ideal band gap, which allows them to match the solar spectrum better. Perovskite materials are a type of materials that have a specific crystal structure called the Perovskite structure. The mineral Perovskite, with the chemical formula  $ABX_3$ , inspired the name of this structure.<sup>87</sup> The general formula for Perovskite material is  $ABX_3$ , where A and B represent cations of different sizes (A larger than B) and X represents an anion. The Perovskite crystal structure is an ideal cubic structure of corner-sharing  $BX_6$  octahedra, with the A cations occupying the spaces in between (Figure 1.15A).<sup>88</sup>

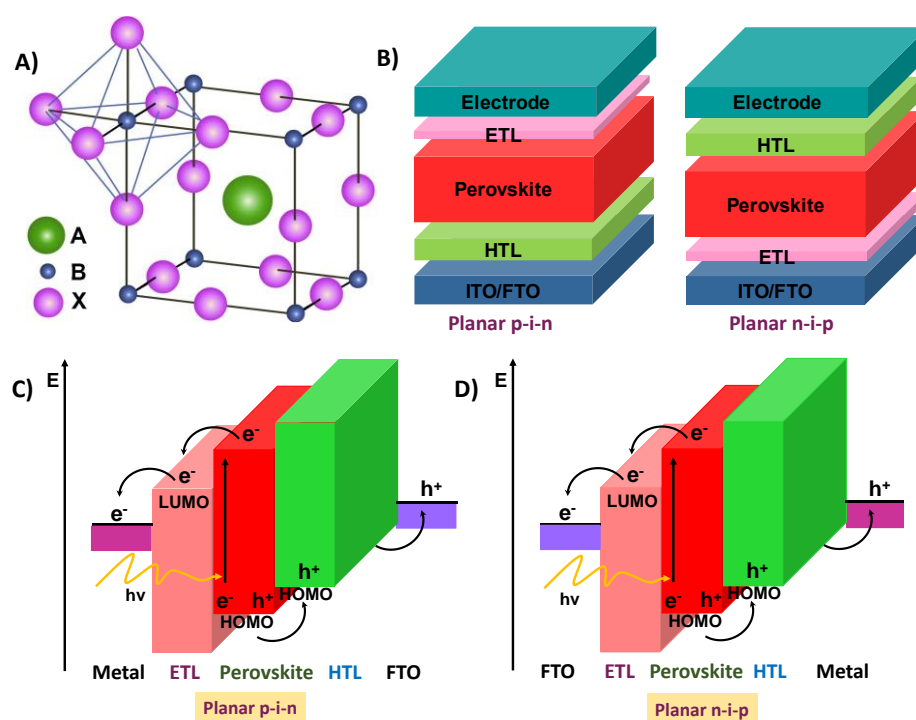


**Figure 1.15.** (A) The Perovskite crystal structure (Adapted from reference 88); (B) Planar p-i-n and n-i-p device architecture and (C) Planar p-i-n and (D) n-i-p device energy level diagram.

This arrangement creates a cubic lattice with a high degree of symmetry. In Perovskite solar cells, the most commonly studied Perovskite material is methylammonium lead iodide ( $\text{CH}_3\text{NH}_3\text{PbI}_3$ ). In this case, methylammonium (MA) acts as the A-site cation, lead (Pb) as the B-site cation, and iodine (I) as the X-site anion. Perovskite materials are used in solar cells due to their unique combination of properties that make them highly suitable for efficient light absorption and energy conversion. Some of the main reasons why Perovskite materials are employed in solar cells are its broad absorption spectrum comprising of a significant portion of the solar spectrum, including visible and near-infrared radiation; high charge carrier mobility which relates to how easily electrons and holes may travel across the material; long carrier diffusion length that can permit the charge to flow without recombining, enabling more charges to reach the corresponding electrodes and solution processability, which provides cost-efficient and scalable production of solar cells.

In 2009, Kojima *et al.* developed the first Perovskite solar cell (PSC) by substituting methylammonium lead iodide, a Perovskite absorber, for the dye ingredient in a traditional dye-sensitized solar cell (DSSC) design and achieved efficiency of 3.81%.<sup>89</sup> This revolutionary discovery launched the study of Perovskite solar cells and opened the door for the quick development of this technology. A Perovskite solar cell typically features numerous layers that function together to convert sunlight into electricity. The key components include, a transparent conductive oxide (TCO) layer on a substrate typically made of glass or a flexible material on that an electron transport layer (ETL) for electron transfer from the Perovskite absorber layer to the back electrode.  $\text{TiO}_2$ ,  $\text{ZnO}$ , derivatives of  $\text{C}_{60}$  are some examples of ETLs used. The Perovskite material is the absorber layer in a PSC. A hole transport layer (HTL) is coated over the active layer and then the metal contact

material as cathode material. Planar PSCs may be implemented in two ways: normal (n-i-p) or inverted (p-i-n). The position of the outermost transport material inside the device structure that interacts first with the incident light determines the architecture (Figure 1.15B). The selection between conventional and inverted structures is determined by a number of parameters, including aimed device performance, interface engineering, and the materials utilized. Both designs have been thoroughly researched and show promising results in terms of power conversion efficiency and stability. The working principle of a Perovskite solar cell (PSC) involves many steps. When sunlight (photons) strikes the PSC, the Perovskite material absorbs the light, causing excitons to form. At the interface between the Perovskite layer and the charge-transporting layers, excitons are separated into electrons and holes. The electrons then migrate to the ETL and the holes towards the HTL. The electrons and holes then reach their respective electrodes followed by that, through an external circuit recombination takes place and electric current generated. The energy band diagram of both p-i-n and n-i-p architecture are shown in Figure 1.15C.

Numerous organic hole transport materials with various electron donor components have been intensively explored for organic electronic devices. Carbazole, phenothiazine, pyrene, and triphenylamine (TPA) have emerged as actively researched organic HTMs, with many possibilities for improving device performance. TPA, a redox-active organic material, is widely utilized as an HTM in different organic electronic devices. HTMs containing TPA exhibit good hole transporting abilities due to the presence of nitrogen donor atoms and the structural features contribute thermal and morphological stabilities. Therefore, over the past decade, researchers have put a lot of time and effort towards developing facile synthetic methods for various TPA derivatives. The power conversion efficiency of 26% is the latest (2023)

and highest for a single junction Perovskite solar cell.<sup>90</sup> Seok and team successfully created an interlayer using Cl-bonded SnO<sub>2</sub> in combination with a Cl-containing Perovskite precursor (Alkylammonium chloride) between SnO<sub>2</sub> electron-transporting layer and a halide Perovskite light-absorbing layer. For the hole-transporting material (HTM), they utilized Spiro-OMeTAD.

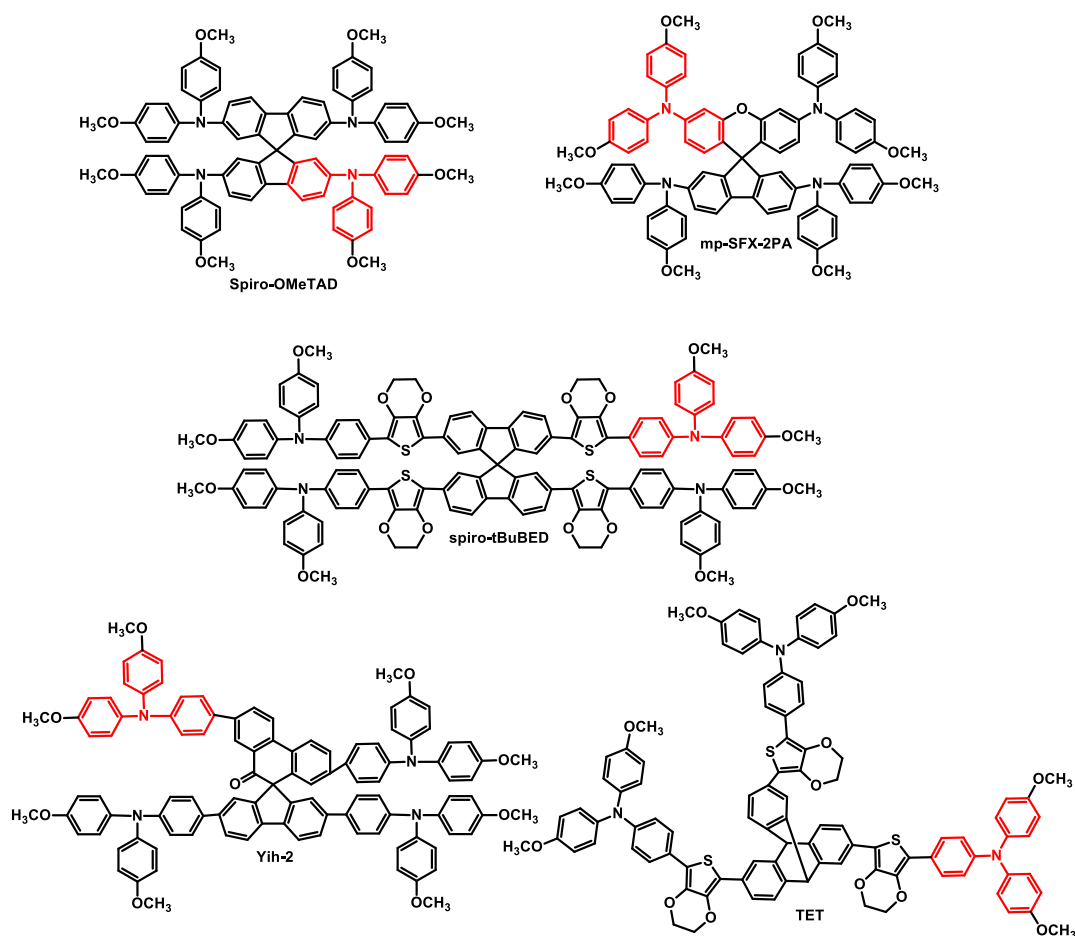


**Figure 1.16.** Chemical structures of triphenylamine based HTMs with spiro-structures.

The molecules with spiro structures containing TPA units are reported to have highest efficiency (Figure 1.16). Zhan *et al.* developed and synthesized four different hole transporting materials based on spiro[fluorene-9,9'-xanthene] (SFX). The devices outperformed the benchmark Spiro-OMeTAD-based control devices (15.5%) under the same circumstances, achieving power conversion efficiencies of up to

16.8% with very good stability.<sup>91</sup> Further with a mixed Perovskite layer, mp-SFX-2PA exhibited an improved PCE of 17.7%. Chang and group developed two donor-acceptor-donor type hole-transport materials using spiro[fluorene-9,9'-phenanthren-10'-one] core.<sup>92</sup> Compared to Spiro-OMeTAD, D-A-D HTMs (Yih-2) exhibited high resistance to moisture, increased production yield and comparable efficiency. Spiro-tBuBED, an efficient HTM based on spiro-bifluorene, showed a good power conversion efficiency of 18.6% when used in Perovskite solar cells without the use of a device pre-oxidation process that was once believed to be necessary.<sup>93</sup> Yuhao Sun and group developed a new derivative of Spiro-OMeTAD called TET, which showed high fill factor (>81%) and 18% efficiency with reduced cost (25 times lower than Spiro-OMeTAD).<sup>94</sup> Chemical structures of the above discussed spiro-based HTMs are shown in Figure 1.16.

Numerous papers discuss the use of low-molecular-weight materials with high efficiency that can be classified as linear HTMs. In 2017, Grätzel *et al.* reported two novel thiophene based hole-transporting materials, named Z25 and Z26, the latter is derived by introducing two double bonds into Z25.<sup>95</sup> Z26 demonstrated a remarkable PCE of 20.1%, comparable to the efficiency of 20.6% attained with SpiroOMeTAD. PSCs using Z26 also displayed greater stability than devices using Z25 and SpiroOMeTAD. Songyuan Dai and group demonstrated an easy method to create three Donor- $\pi$ -Donor, TPA-based HTMs with biphenyl, fluorene, or carbazole (H-Ca) linkers.<sup>96</sup> All novel compounds exhibited adequately matching HOMO levels with respect to Perovskite. The molecule developed with carbazole moiety demonstrated strong hole mobility and exhibited higher PCE% due to better hole extraction capacity at perovskite/HTM interface. In order to understand the structure and mechanism of electronic properties involved in HTMs, three specific molecular semiconductors,

namely Z1, Z2, and Z3 were designed.<sup>97</sup> According to comparative research, Z3, which has a perfectly oriented HOMO and excellent thin-film mobility, has a high potential for use in efficient Perovskite solar cells with PCE% of 20.84%. Grätzel *et al.* developed spiro-configured, HTM-1 composed of acridine-cyclopentadithiophene, with triarylamine moieties on either side.<sup>98</sup> A thin layer (40 nm) of HTM-1 in the PSC exhibited remarkable stability with PCE% of 21% and a fill factor value of 0.77. Chemical structures of above discussed linear HTMs are depicted in Figure 1.17.

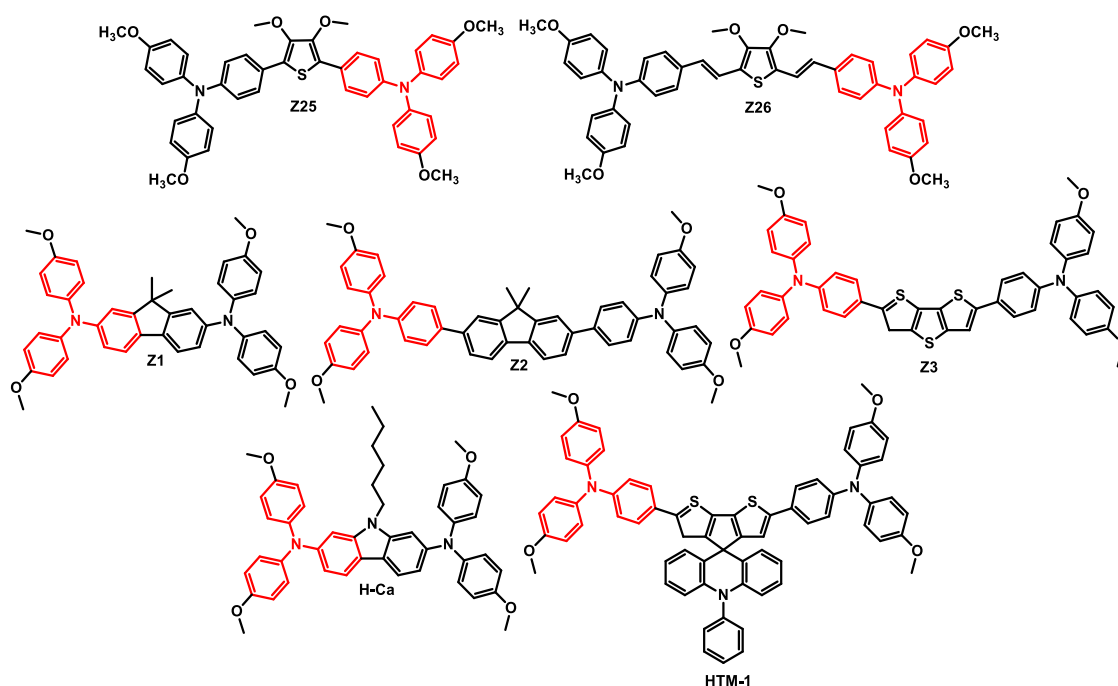


**Figure 1.17.** Chemical structures of triphenylamine based HTMs with linear structures.

HTM structural designs with star-shaped structures utilizing the triphenylamine core gathered considerable interest in the past decade (Figure 1.18). These novel designs attempt to improve the performance and stability of PSCs by utilizing the advantageous features of TPA as well as the structural benefits of star-shaped molecules. An innovative approach was developed by Falaras *et al.* which involved using an organic chromophore as an interlayer HTM, called D35 in

mesoporous PSCs.<sup>99</sup> They have achieved an 18.5% of PCE with high stability, retaining 83% of their initial efficiency after 37 days. Two novel HTMs from Nazeeruddin and group, based on isomeric forms of benzotrithiophene, were developed and named BTT-4 (three-armed) and BTT-5 (four-armed). They investigated the impact of isomerism in photophysical and electrochemical properties. PCE of 19.0% and 18.2% were achieved by using BTT-4 and BTT-5 as HTMs.<sup>100</sup>

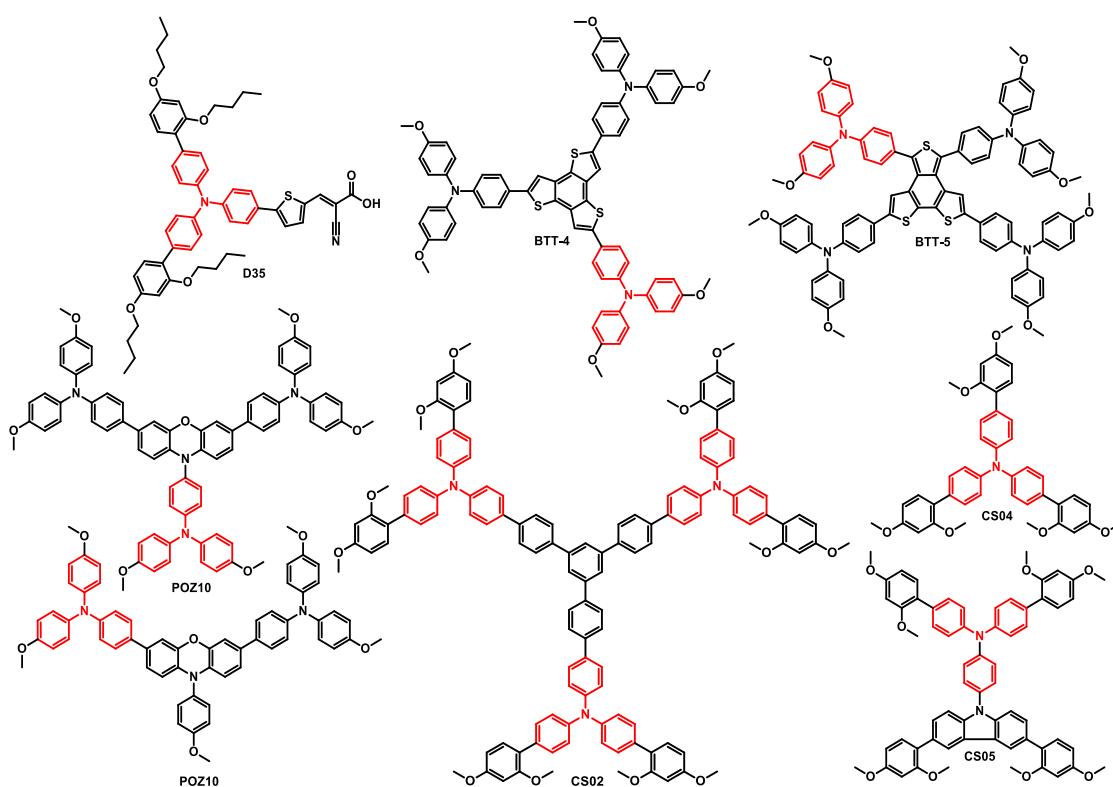


**Figure 1.18.** Star-shaped structures of HTMs containing TPA units.

Similarly, from the same group, three HTMs named CS02, CS04 and CS05 were reported.<sup>101</sup> CS05 achieved impressive efficiencies of 19.4% and proved that despite their comparable chemical and photophysical features, these HTMs have unique carrier recombination kinetics. Cheng Chen and group developed two phenoxazine based hole transport materials, POZ9 and POZ10.<sup>102</sup> The variations in the N-substitution on the phenoxazine core altered the PCE%. PSCs based on POZ10, contains three *N,N*-di-4-methoxyphenylamino units has achieved superior hole

transport capability and PCE of 19.4%. Chemical structures of star shaped HTMs are given in Figure 1.18.

As hole transport materials, star-shaped compounds with a tetra-arm structure have been developed and used (Figure 1.19). These compounds have a distinct star-like structure, with four arms extending from a central core. Yongfang Li *et al.* used silicon cores and triphenylamine branches and developed HTMs namely, Si-OMeTPA and SiTP-OMeTPA. Si-OMeTPA which demonstrated high thermal stability, crystallinity and hole mobility with 19.06 PCE% and outperformed the well-known PTAA.<sup>103</sup> Shao *et al.* displayed performances of two symmetric tetraphenylbutadiene derivatives called CJ-04 and CJ-03 and when CJ-03 was used as the HTM, the PCE increased to 20.06% while that of CJ-04 was 13.75% and the cost of preparing HTM-CJ-03 was only 23.1% of the price of Spiro-OMeTAD.<sup>104</sup>

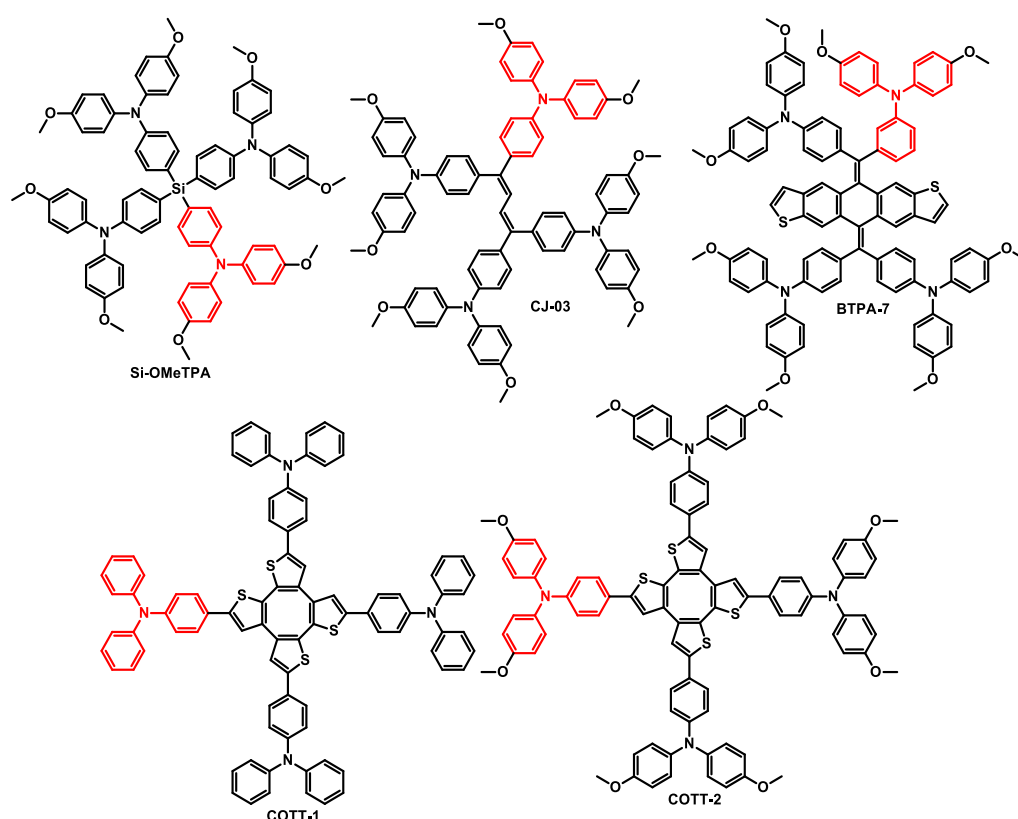


**Figure 1.19.** Star-shaped HTMs with tetra-arms and TPA units.



Liu *et al.* developed an HTM called BTPA-7 having anthradithiophene central core. The new HTM exhibited higher hole mobility, glass transition temperature and cost-effective synthesis, with 17.58% efficiency.<sup>105</sup> Luyao Zhao in 2019 reported two rigid three-dimensional HTMs with cyclooctatetrathiophene as the central component known as COTT-1 and COTT-2.<sup>106</sup> They tested the individual performances of the HTMs and achieved 8.4% and 17.7%, respectively. Further, they enhanced the PCE by employing one HTM as interfacial layer and the other as the hole transporting material. All the above discussed structures are shown in Figure 1.19.

In n-i-p perovskite devices, the hole transport material is placed on top of the perovskite layer. To ensure full coverage and protection of the rough perovskite surface and to prevent metal diffusion into the perovskite, a thick HTM film is required. In this configuration, high hole mobility becomes crucial for the HTM, alongside other essential characteristics like suitable energy levels, good solubility, smooth film morphology, and thermal stability. Spiro-OMeTAD, PEDOT:PSS, P3HT are some of the commonly used HTM in n-i-p perovskite solar cells, but it often needs to be doped with additives like t-BP, Li-TFSI, and cobalt complexes to enhance its performance due to its relatively low mobility. However, the hygroscopic nature of these dopants can negatively affect the device stability over time. On the other hand, in p-i-n perovskite devices, the HTM film can be much thinner since it is placed below the perovskite layer. Therefore, high mobility is not the primary concern in this configuration, but instead, properties like suitable energy levels and solvent resistance become essential. Polymeric materials such as dopant-free arylamine derivatives (e.g., PTAA and Poly-TPD) have gained popularity as HTMs in p-i-n structures due to their wide bandgaps, good hole mobility, thermal stability, and solution processability.<sup>107</sup> Their high solubility also proves advantageous during the

device fabrication process. The advancement of p-i-n perovskite solar cells indicates that they are approaching the performance levels of the best regular perovskite solar cells. Investigating the p-i-n configuration offers up new avenues for improving the efficiency and overall performance of perovskite solar cells. However, the solubility of hole transport materials (HTMs) may result in partial washing or etching when exposed to certain solvents used in subsequent fabrication steps, such as DMF and DMSO. Furthermore, the cost of manufacturing these materials may have an influence on their economic feasibility and appropriateness for large-scale applications. To address these issues, researchers widely employ cross-linking (detailed description is given in the section 1.6.) and self-assembled layer (SAM) techniques to develop stable HTM layers on substrates. These techniques enable effective hole extraction while also serving as a protective barrier, safeguarding the HTM from solvent-related degradation. The structures of the above discussed HTMs are given in Figure 1.20.

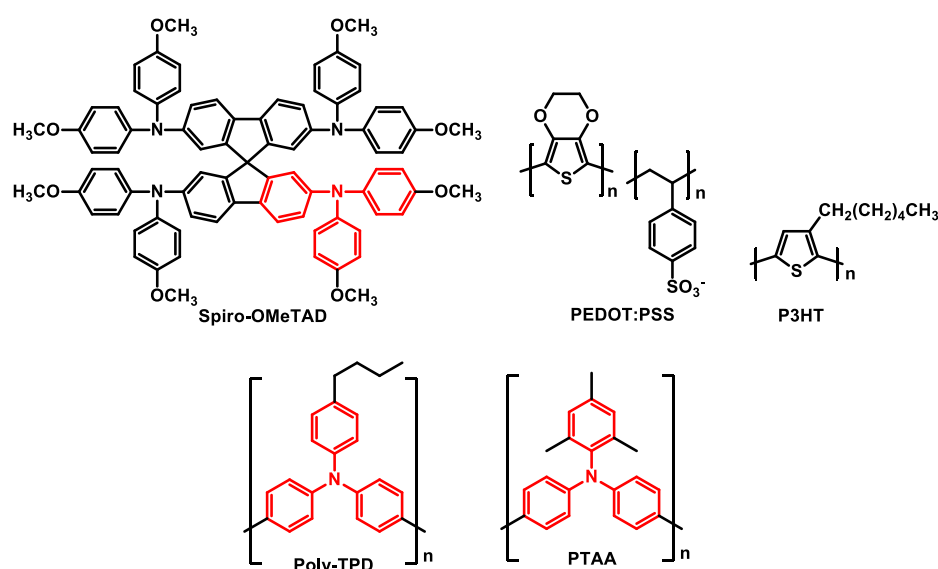


**Figure 1.20.** Commonly used and highly efficient HTMs for both p-i-n and n-i-p based Perovskite solar cells.

In 2023, Li *et al.* reported a modified Spiro-OMeTAD (Spiro-Acid) by introducing a carboxylic acid anchoring group, and demonstrated that Spiro-Acid can serve as an

efficient hole transport material without the need for dopants in p-i-n perovskite solar cells.<sup>108</sup> The solar cell based on the self-assembled Spiro-Acid showed comparable efficiency (18.15%) and remarkable fill factor of over 82%, when compared to devices using PTAA as the HTM. Additionally, device exhibited excellent long-term stability under illumination (Figure 1.21A).

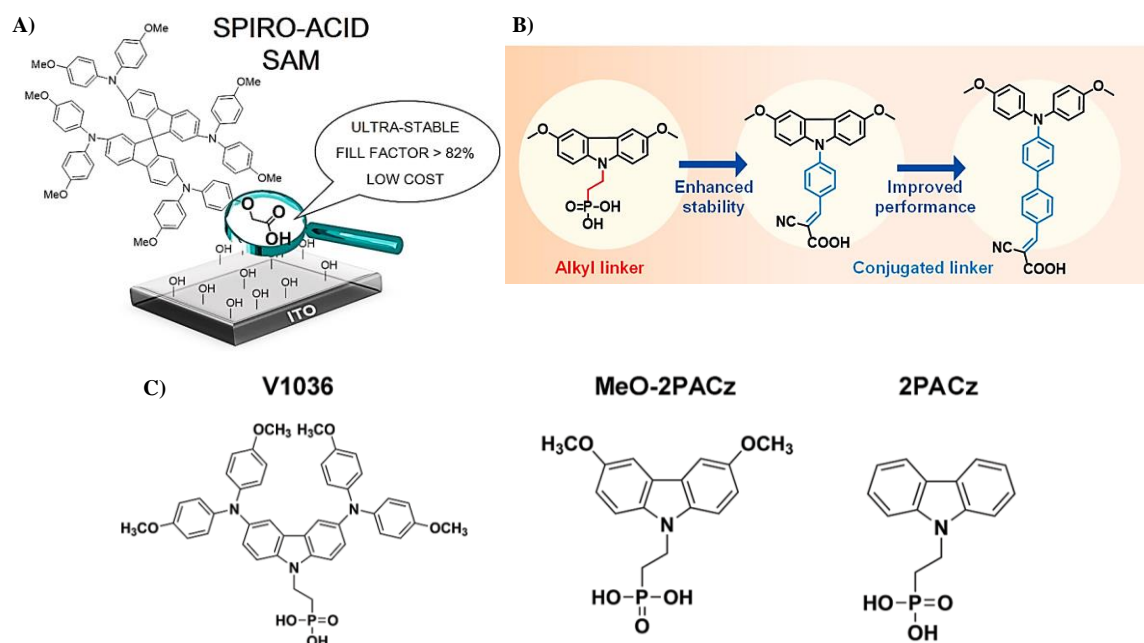


**Figure 1.21.** (A) Structure and schematic representation of the formation of Spiro-Acid-SAM on ITO; (B) Structures of conjugated SAMs and (C) Chemical structures of the SAM molecules V1036, MeO-2PACz and 2PACz. (Adapted from reference 108, 109 and 110)

Shuo Zhang and group developed a conjugated self-assembled monolayers and proved their efficiency as HTM for inverted perovskite solar cells.<sup>109</sup> Unlike the traditional alkyl linker-based SAMs, these conjugated SAMs exhibited enhanced hole-transport capabilities due to their conjugated molecular structure, which facilitates charge transport. Additionally, the conjugated structure stabilizes the electron-rich arylamines through electron/charge delocalization, leading to improved photo- and electrical stabilities. The devices achieved power conversion efficiency of 22.53%

(certified 22.12%) in the inverted PSC (Figure 1.21B). Amran *et al.* reported two novel SAM based HTMs (MeO-2PACz and 2PACz) with carbazole bodies and phosphonic acid anchoring group, and compared the device properties with standard PTAA and a previously reported SAM of V1036.<sup>110</sup> MeO-2PACz-SAM exhibited PCE of 21.1% with a standard triple-cation absorber ( $\text{Cs}_5(\text{MA}_{17}\text{-FA}_{83})_{95}\text{Pb}(\text{I}_{83}\text{Br}_{17})_3$  (CsMAFA)) based PSC and 23.26% in monolithic CIGSe/perovskite tandem solar cell (Figure 1.21C).

### 1.5.2. Organic Light Emitting Diodes and TPA based Hole Transporting/Injecting Materials

OLEDs have garnered significant attention due to their energy efficiency and superior uses in full-color display screens and eco-friendly lighting sources.<sup>111</sup> Tang and Van Slyke's pioneering work in 1987 set the groundwork for OLED technology. Since then, both academic and industrial sectors have worked hard to produce high-performance OLEDs. These efforts have concentrated on increasing luminance efficiency, color gamut, device stability, and manufacturing processes. In recent years, OLEDs have achieved commercial success in indoor lighting as well as other consumer gadgets such as mobile phones, cameras, and televisions. However, further improving OLED performance remains a daunting challenge in order to match competitive lighting requirements and required display quality. Efficient light emission in OLEDs requires the use of multilayer devices consisting of a hole transport layer (HTL), hole injection layer (HIL), electron transport layer (ETL), and emissive layer (EML). These layers are deposited as thin films sequentially between a transparent anode (FTO/ITO) and a reflecting cathode (usually low work function metals such as aluminium, silver, calcium, or magnesium) (Figure 1.22A). In an OLED device, the process involves injecting holes and electrons from the electrode into the device's

respective layers. When a voltage is provided, the anode charges up, causing a potential difference with the cathode. This potential difference allows holes to be injected from the anode into the hole transport layer. Simultaneously, the cathode becomes negatively charged, allowing electrons to be injected into the electron transport layer. The injected electrons and holes combine to generate excitons, which are bonded states of an electron and a hole, inside the emissive layer. The energy level diagram and the electron transfer processes are shown in Figure 1.22B. As the excitons decay from higher to lower energy levels, they emit light known as electroluminescence.

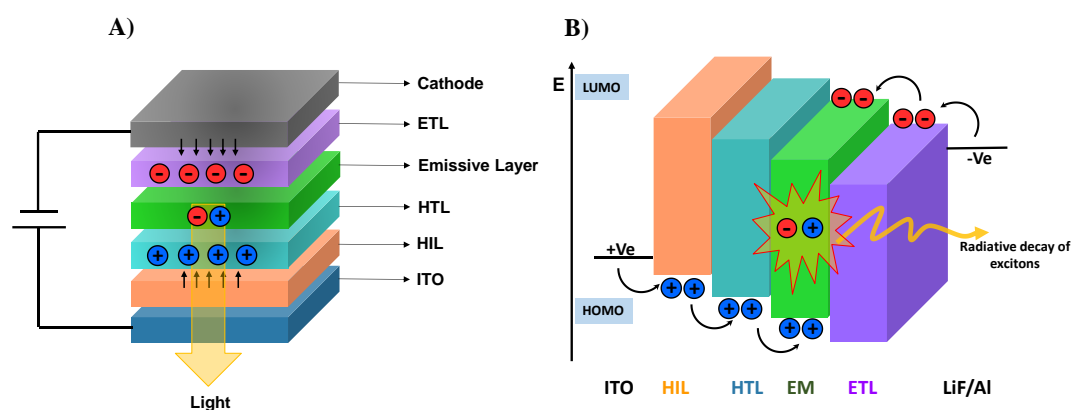


**Figure 1.22.** (A) Multilayer device structure and (B) Energy level diagram of OLEDs.

The statistical spin limit predicts a 1:3 ratio of singlet and triplet excitons from the recombination of electrons and holes in organic semiconductors<sup>112</sup> (Figure 1.23). The emission in fluorescent OLEDs is caused by the radiative decay of singlet excitons. Triplet excitons, on the other hand, have longer lifetimes and tend to undergo non-radiative decay pathways, reducing the device's overall efficiency. Thus, the maximum EQE (ratio of the number of generated photons to the number of injected charges) that could be attained with fluorescent materials is limited to 25%. OLEDs that use phosphorescent materials as the emissive layer are known as phosphorescent organic light-emitting diodes (PHOLEDs). PHOLEDs use the emission

from both singlet and triplet excitons, which leads to better efficiency and brighter light emission than conventional fluorescent OLEDs. Heavy metal atoms can facilitate the rate of spin forbidden process of intersystem crossing (ISC) from  $S_1$  to  $T_1$  due to the enhancement of spin-orbit coupling. As a result, phosphorescent OLEDs achieve an internal quantum efficiency of up to 100%, enabling excitons to be completely used for light emission.<sup>113</sup> Thermally activated delayed fluorescence (TADF) is another phenomenon observed in certain organic materials, that efficiently converts non-radiative triplet excitons back to emissive singlet excitons via thermal energy transfer, resulting in delayed fluorescence emission. In order to activate the RISC process at room temperature,  $\Delta E_{ST}$  (the energy difference between the lowest singlet and triplet state) must be smaller than 0.1 eV. The excitons return to the emissive singlet state after undergoing RISC. After a short delay following the initial excitation, the recombination of these singlet excitons causes delayed fluorescence emission.<sup>111,114</sup> The pictorial representation of the above discussions is depicted in Figure 1.23.

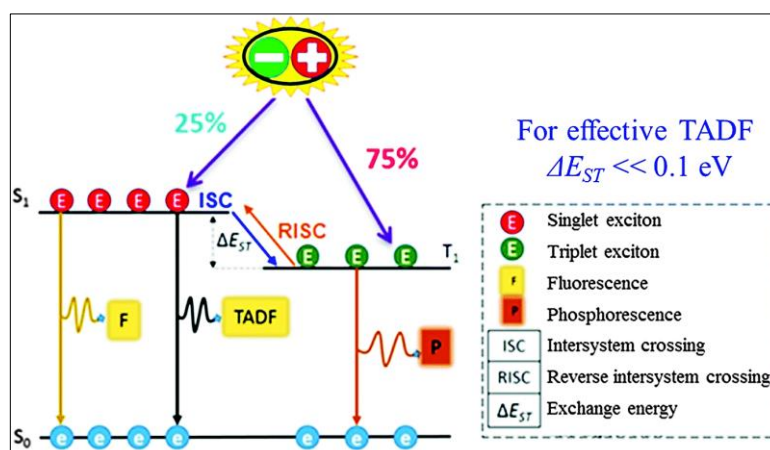


**Figure 1.23.** Singlet and triplet excitons radiation in OLED devices. (Adapted from reference 112)

In OLEDs, TPA-based materials can function as both efficient Hole Transporting Materials (HTMs) and Hole Injecting Layers (HILs). Because of their high hole

mobility, appropriate energy levels, and strong film-forming capabilities, they are attractive alternatives for aiding hole injection and transport, resulting in better device performance. The commonly used hole transport materials in OLEDs are a diphenylamine-naphthalene derivative called NPB and a molecule having biphenyl core structure with two diphenylamine group named as TPD. Both the HTMs exhibit high hole mobility and are highly sublimable. But they exhibit low glass Tg, specifically 65°C for TPD and 96°C for NPB. This low Tg leads to poor morphological stability, resulting in short lifetimes and device degradation in OLEDs. Designing amorphous materials with high glass transition temperatures (Tg) can help to reduce the negative impacts of crystallization and increase film stability. With much better Tg, spiro-linked structures that are comparable to TPD (like spiro-TAD and spiro-MeOTAD) have been developed, resulting in increased morphological stability.<sup>115</sup>

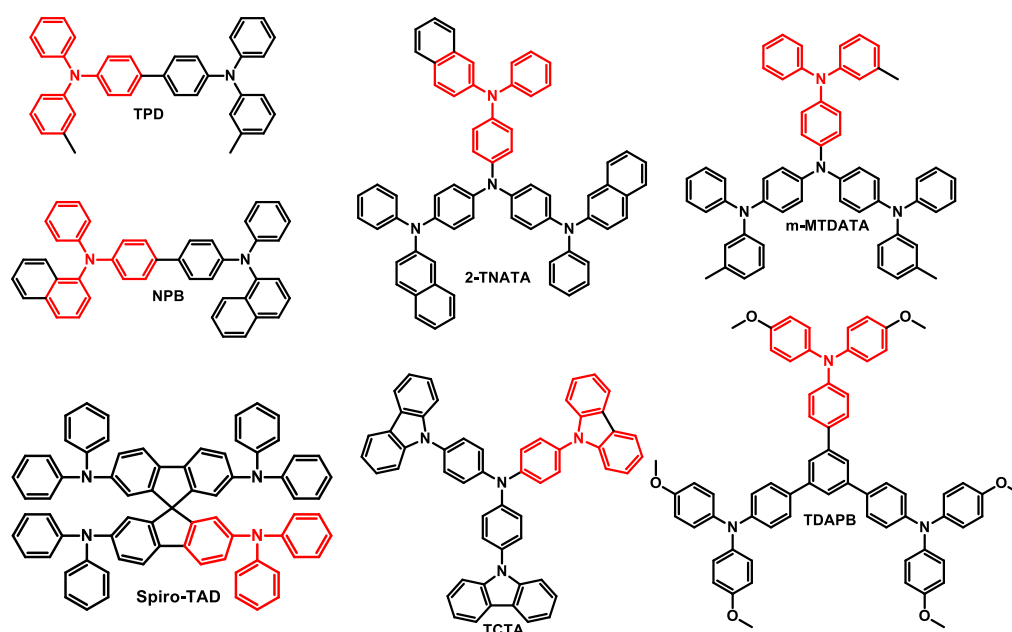


**Figure 1.24.** Chemical structures of TPA based commonly used HTMs and HILs.

Wehrmann *et al.* fabricated the OLED device using derivatives (TDATA and TDAPB) with starburst structure, which have the ability to form thermally stable amorphous films. They utilized a sequential deposition process involving spin-coating

and evaporation techniques for three organic layers. The HTM layer of TDAPB for modulating the injection of holes into the Alq<sub>3</sub> emitting layer was used and resulted in high efficient LEDs.<sup>116</sup> Chae and group developed an OLED device with short driving voltage of 3.0 V and achieved 1000 cd/m<sup>2</sup> luminance. They highlighted the potential of utilizing TCTA as a solution-processed interlayer in phosphorescent OLEDs, offering a promising pathway for efficient and simplified manufacturing of the devices.<sup>117</sup> These substances have improved morphological stability and created thin films of excellent quality. Several small molecules are extensively employed as HILs in OLEDs and commonly used HILs are starburst molecules with a core triphenylamine molecule and three naphthyl-diphenylamine (2-TNATA) and methyl-diphenylamine (m-MTDATA) moiety. The above-mentioned commonly used HTM/HILs and their chemical structures are given in Figure 1.24.

Lee *et al.* reported a novel starburst TPA-tetraphenyl-phenyl derivative known as TTPPPA as HTM, with higher glass-transition temperature and the corresponding OLED device displayed higher EQE compared to the conventional device using NPB.<sup>118</sup> A solution processable triphenylamine-based dendrimer Tr-TPA9 with high T<sub>g</sub> was reported by Tian *et al.* and the OLED device with Alq<sub>3</sub> as the emissive material exhibited a low turn-on voltage of 2.5 V. The devices demonstrated a luminance maximum of approximately 11,058 cd m<sup>-2</sup>, and CE (current efficiency) maximum of 4.01 cd A<sup>-1</sup>.<sup>119</sup> Yang Liu and group combined the hole-transporting feature of TPA with the AIE properties of TPE and the resultant compounds, TPATPE and 2TPATPE exhibited high fluorescence quantum yields up to 100% in thin films. Due to the excellent hole mobility of TPATPE and 2TPATPE together with the appropriate energy level alignment with the anode, the devices without separate hole-transporting layers demonstrated equivalent or even superior performance than those with HTL.<sup>120</sup> A



new type HTM layer was reported by Xingbo Cao and group, named DBTPA. Even at a low current density of 20 mA/cm<sup>2</sup>, the device achieved a brightness value of 1,399 cd/m<sup>2</sup> and a luminous efficiency of 2.85 cd/A.<sup>121</sup> Figure 1.25 shows the chemical structures of the OLED-HTMs discussed above.

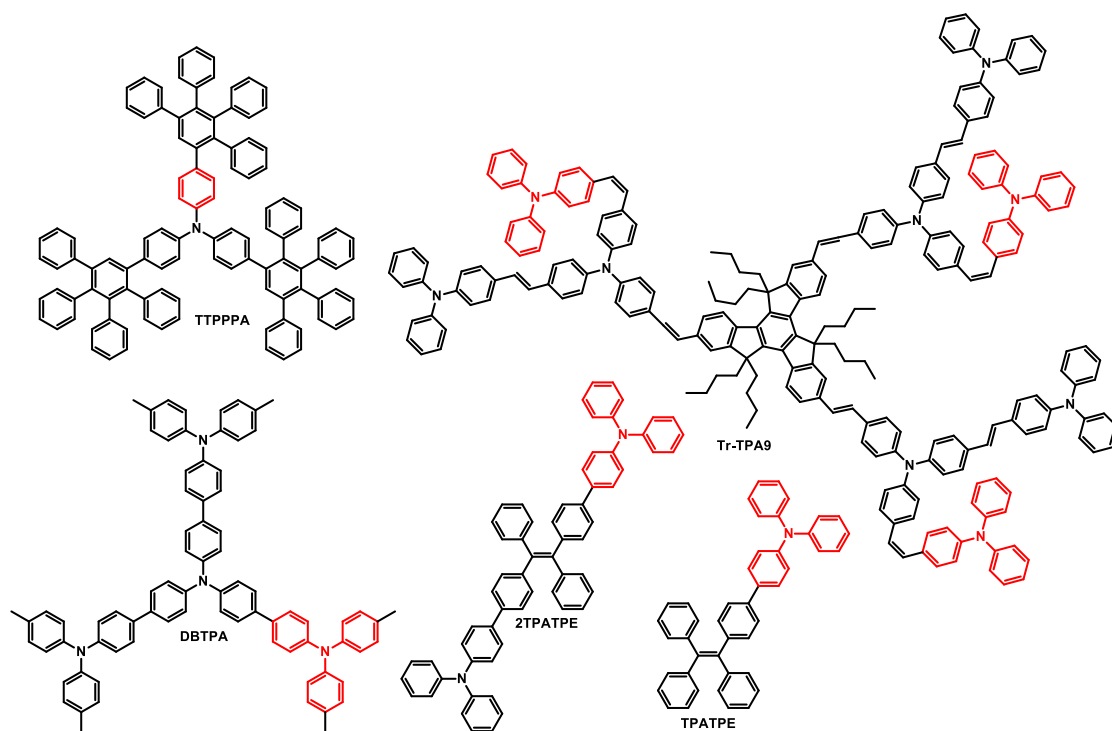


**Figure 1.25.** Chemical structures of TPA based HTMs used in OLEDs.

Park *et al.* reported hole injection layer (HIL) materials which are made up of phenothiazine and phenoxazine derivatives. One of the synthesized materials, 1-PNA-BPBPOX exhibited a high glass transition temperature, low absorption above 450 nm and suitable energy levels compared to 2-TNATA, a commercial HIL material.<sup>122</sup>

Two novel star-shaped oligotriarylamines, FATPA-T and FATPA-Cz for hole injection and transport were successfully synthesized through the Suzuki cross-coupling reaction by Zuoquan Jiang and group. The molecules showed good thermal stability, solution processability and high glass transition temperatures. A double-layer Alq<sub>3</sub>-emitting OLED device were fabricated using FATPA-T and FATPA-Cz, and FATPA-Cz-based device displayed better device characteristics compared to NPB-

based standard device.<sup>123</sup> In 2020, Chang *et al.* developed a series of tetramers derived from triphenylamine and evaluated as hole injecting/transporting layers in organic light-emitting diodes. A tri-layer architecture of the devices was demonstrated with derivative 1 and derivative 2 as HTM and derivative 3 was chosen to be the HIL. Devices with HIL based on derivative 3 achieved higher OLED parameters and indicated the potential of the newly synthesized HTM and HTL.<sup>124</sup> Chai *et al.* developed a novel triphenylamine derivative named TPA-1A which act as both HTM and HIL. The PhOLED from the HTM demonstrated remarkable current (49.13 cd/A) and power (27.56 lm/W) efficiencies and showed improved hole injecting property compared to NPB based devices.<sup>125</sup> The structure of the HILs discussed are given in Figure 1.26.

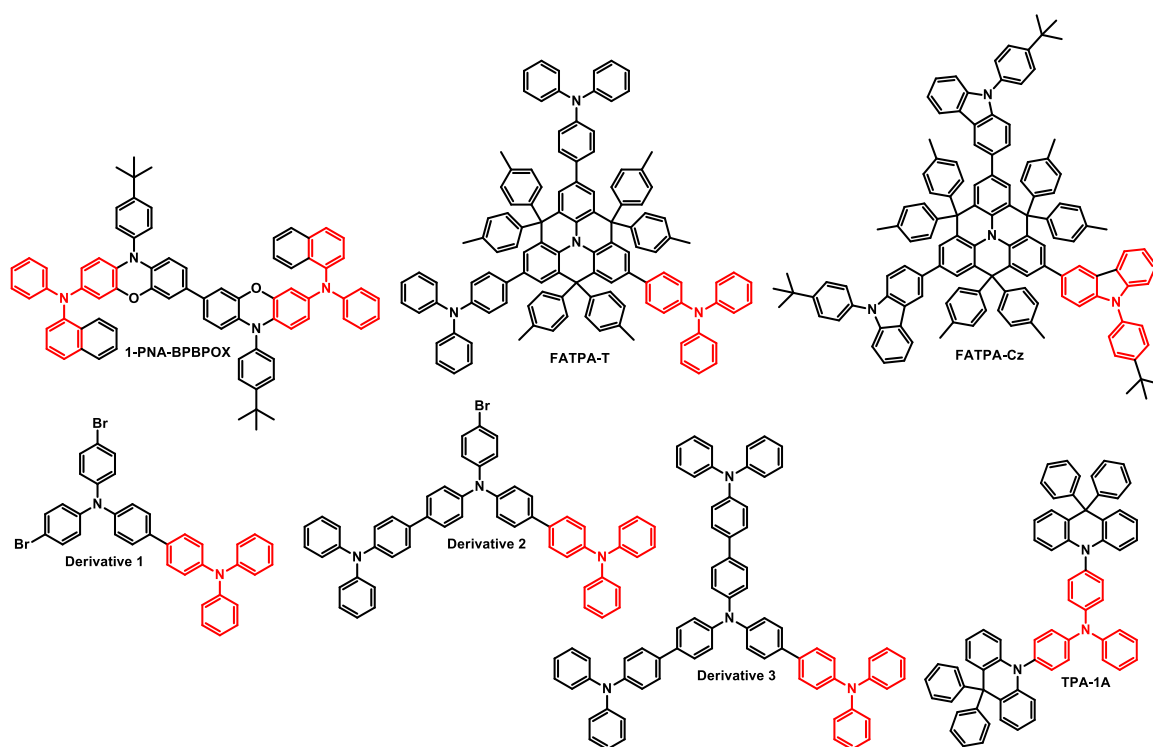


**Figure 1.26.** Chemical structures of TPA based HILs.

## 1.6. Cross-linkable Materials and their Organic Electronics Applications

Cross-linking techniques are commonly employed in organic electronic devices to enhance their performance by improving material properties such as stability, mechanical strength, and charge transport. The solubility of the EC/HTM materials in common organic solvents and film processing via simple coating techniques such as spin coating or spray coating are crucial for ultimate practical device fabrication.<sup>126</sup> While the solubility of electro-active material is important for the large area thin film processing, it will adversely affect the overall device performance due to the delamination of the material from the electrode surface. The material redundantly mixes with the next layer, electrolyte or conducting gel and the consequence will be the localized short-circuiting and device failure. Although polymers can form thin films with better morphological and mechanical stability than small organic molecules and discrete oligomers, the challenges are associated with the synthesis, purification, solubility and the lack of colorless states.<sup>127</sup> Some of the cross-linking techniques used for the film formation in organic electronics are chemical, thermal and photo-cross-linking. Chemical cross-linking is a process that entails the creation of strong covalent bonds between different monomer substances. It can be achieved through various chemical processes such as oxidation and condensation reactions. Chemical cross-linking can enhance the stability of organic materials and reduce the risk of degradation, which is crucial for long-term device performance.<sup>128-131</sup> Photo cross-linking utilizes light to induce cross-linking reactions in materials. Ultraviolet (UV) light is commonly used as a catalyst to initiate the cross-linking process. This technique enables precise spatial control over the cross-linking process, allowing the formation of patterns or selective cross-linking in specific regions of the device.<sup>132-136</sup> In the case of thermal cross-linking, heat is used to induce the cross-linking reaction. Styrene-based materials have been investigated for their potential in thermal cross-

linking processes. Thermal cross-linking involves the formation of covalent bonds between the molecular units of styrene-based materials through the application of temperature. Cross-linking in organic materials can be achieved using a variety of functional groups, each offering unique properties and advantages.<sup>137</sup> Some of the commonly used functional groups for cross-linking organic materials, including small molecules and polymers are Styrenes (-CH=CH<sub>2</sub>), Siloxanes (-Si-O-), Acrylates (-C=C-), Trifluorovinylethers (-CF<sub>2</sub>CF<sub>2</sub>-O-), Oxetanes (cyclic ethers containing a four-membered ring structure) etc.

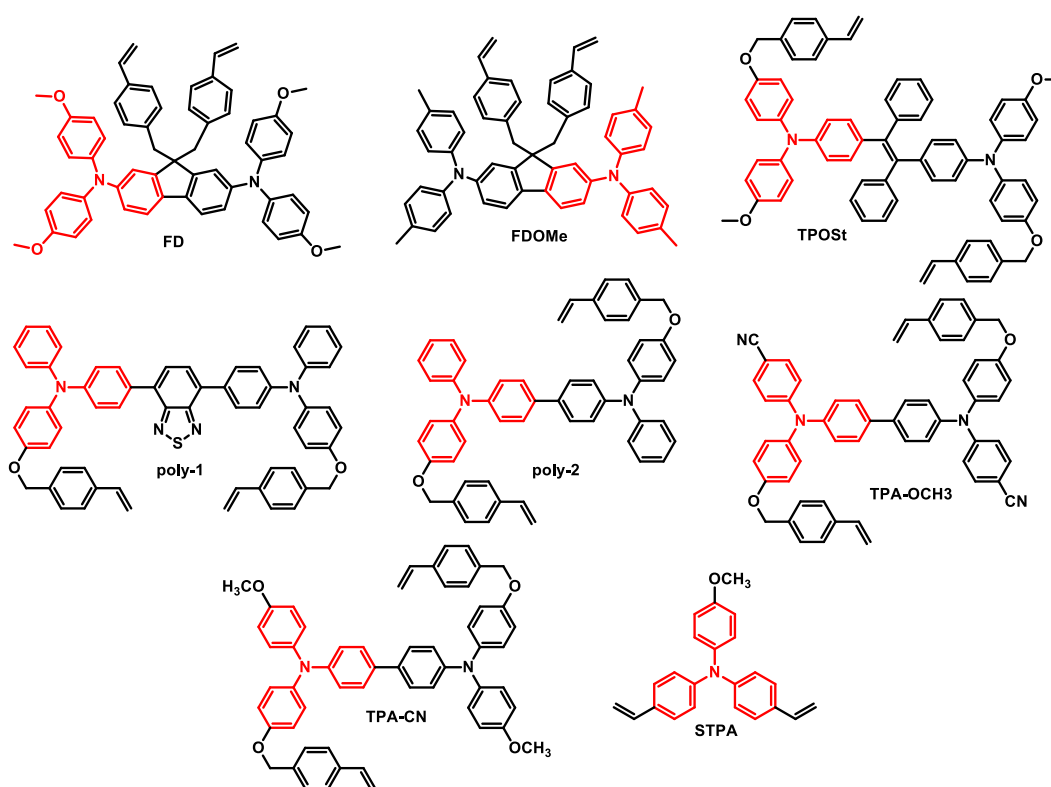


**Figure 1.27.** Chemical structures of the TPA based thermally polymerized molecules used for electrochromic applications.

Organic molecules with unsaturated double bond curing systems are attractive due to their outstanding film properties upon cross-linking.<sup>138,139</sup> Small molecules with a styryl moiety can form morphologically and mechanically stable cross-linked films without any initiator through thermal polymerization, which provides a

covalently connected extended network structure. The main attractions of the styrene polymerization in comparison with other functional groups are: (i) no additional reagent (initiator or cross-linking agent) needed and (ii) no side products are formed during the polymerization, which can interfere with the morphology and optoelectronic properties. This approach has been successfully applied in organic electronic research such as hole transporting materials in OLED, solar cells etc.<sup>138,140,141</sup> Selected examples of TPA based molecules with thermally cross-linkable styryl moieties are given in Figure 1.27.

Our group has developed styrene linked diphenylamine-fluorene derivatives, FD and FDOMe, which formed electroactive films upon thermal cross-linking and exhibited multi-colour electrochromism, with good switching stability and low switching voltage.<sup>142</sup> Similarly, in 2017, we reported diphenylamine-tetraphenylethylene derivatives, TPOSt and TPOMe, with and without cross-linkable styrene moieties, respectively and demonstrated their superior properties such as formation of flawless films on the electrode with excellent stability, transmissive-to-black switching and high optical contrast. In addition, TPOSt exhibited electrofluorochromism, transitioning from a highly fluorescent yellow-green color to a darkened state.<sup>143</sup> In the same year, Skene *et al.* demonstrated a material consisting of benzothiadiazole with two TPA-styrene units that has both electro- and fluorochromic properties (poly-1; Figure 1.27). The films showed reversible switching in the NIR range with the color change from yellow and grey upon applied potential and absorption changed from 460 nm to new broad absorption in the near-infrared region.<sup>144</sup> Triphenylamine and viologen are complimentary electrochromic materials and have been used widely in electrochromic applications. Such dual layer devices are reported to have advantages like enhanced coloration efficiency and open circuit

memory.<sup>145,146</sup> The same group demonstrated an electrochromic device utilizing Bis(triphenylamine) (poly2) as the color-switching layer, exhibiting electrochromic properties and 4-vinylbenzylviologen as the ion storage complimentary layer.<sup>147</sup> Devices showed excellent switching stability with very small color fading after six hours of continuous switching and showed good optical memory after removing the potential, indicating their lower energy consumption. Whereas, electrochromic device fabricated from a single electroactive layer showed a reduction of 50% of the initial color 7 minutes after the potential was removed.

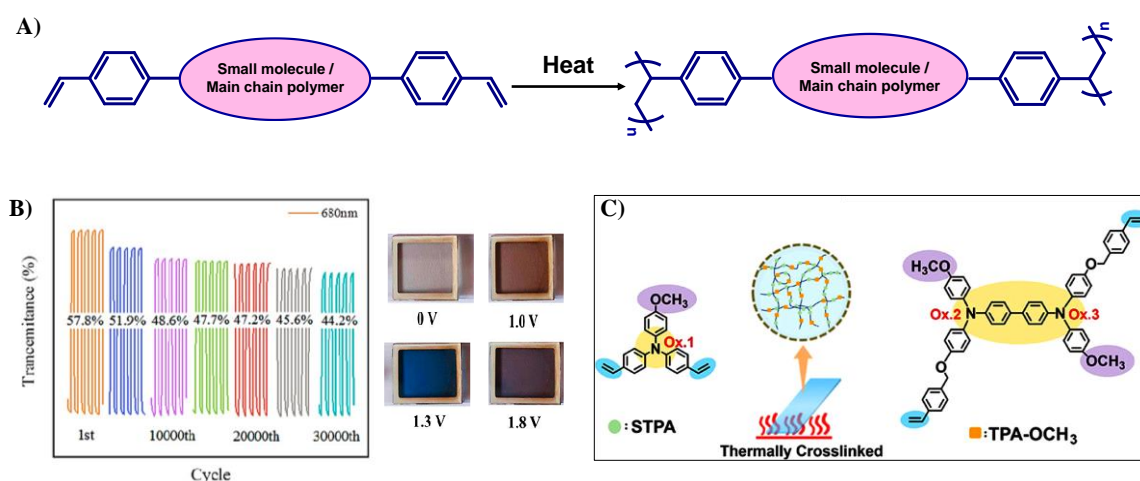


**Figure 1.28.** (A) The process of thermally induced cross-linking in molecules and polymers that contain styrene-functional groups; (B) EC devices of TPA-Styrene derived P(TPA-OCH<sub>3</sub>-co-TPA-CN) polymer with multiple color changes and high cyclic stability and (C) Representation of the structure and thermally cross-linkable EC copolymer of pSTPA-co-TPA-OCH<sub>3</sub>. (Adapted from reference 148 and 149)

A schematic representation of the process of thermally induced cross-linking in molecules and polymers that contain styrene-functional groups is shown in Figure 1.28A. Recently, two TPA derivatives with styryl moieties, TPA-OCH<sub>3</sub> and TPA-CN were reported by Cheng Zhang and group. ECDs of the materials alone and a device with copolymer of TPA-OCH<sub>3</sub> and TPA-CN were fabricated and studied. The device

based on copolymer showed various color changes from colorless-orange-blue-purple and exhibited 57.8% contrast at 680 nm and >30,000 cyclic stability with fast switching time (Figure 1.28B).<sup>148</sup> From the same group, A triphenylamine derivative with a thermally cross-linked vinyl group called STPA was reported and its polymer (pSTPA) was prepared via thermal polymerization. To achieve multicolor display and enhanced cycle stability, a copolymer termed pSTPA-co-TPA-OCH<sub>3</sub> was developed by mixing STPA with TPA-OCH<sub>3</sub> with a molar ratio of 1:1 (Figure 1.28C).<sup>149</sup>

Cross-linkable materials have emerged as a viable candidate in the field of hole-transport layer (HTL) materials. They have the potential to undergo thermal or photochemical cross-linking, resulting in the formation of a durable film with better stability during subsequent solvent treatments of the active layer. This distinguishing feature gives them a significant advantage in the solution-based fabrication process of solar cells. Wong *et al.* developed a thermally curable monomer called VB-DAAF, which is based on a styrene-appended fluorene derivative. The monomer served as a highly efficient p-type organic electrode interlayer and demonstrated resistance against solubility of the precursor solution used. The purpose of this development was to create hybrid solar cells consisting of methylammonium lead iodide Perovskite and fullerene planar heterojunction. The resulting device showcased impressive performance metrics, including an open-circuit voltage of 1.02 V, a short-circuit current of 18.92 mA/cm<sup>2</sup>, and a fill factor (FF) of 0.78. These values corresponded to a notable power conversion efficiency of 15.17% under standard 1 sun AM 1.5G simulated solar irradiation.<sup>150</sup> Ming Shao and colleagues introduced a series of four diphenylamine derivatives containing a fluorene core, known as FDPA molecules as efficient HTMs in inverted p-i-n planar Perovskite solar cells. The molecules are

designed with styryl cross-linking units that enable the formation of insoluble three-dimensional networks under gentle annealing conditions.<sup>142,151</sup>

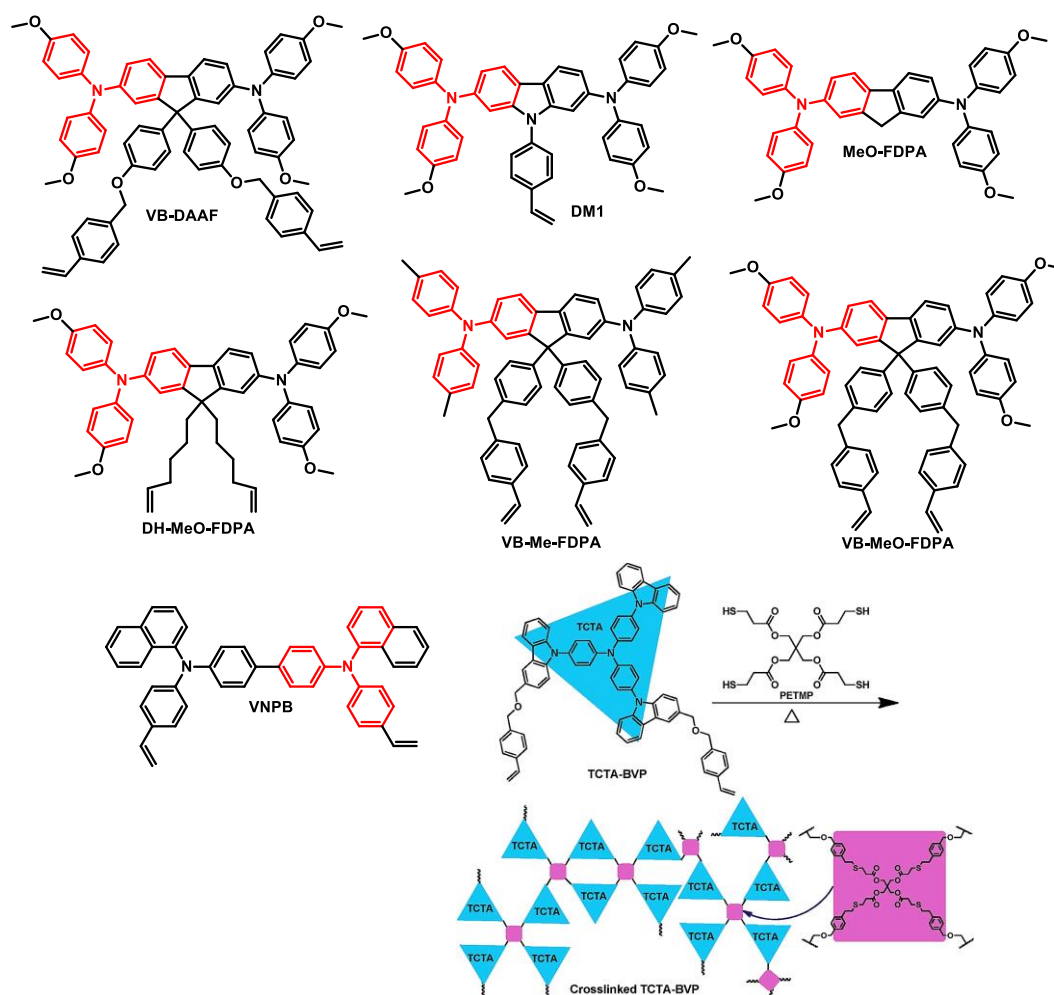


**Figure 1.29.** Chemical structures of the TPA based thermally polymerized molecules, used as hole transporting materials and schematic representation of the cross-linking property of TCTA-BVP and PETMP. (Adapted from reference 153)

Jixian Xu and group have introduced a novel hole-extracting electrical contact known as VNPB, which effectively enhanced the durability and reduced the hysteresis of PSCs. By employing a remote-doping approach, a high-work-function metal oxide layer is utilized to induce the desired free carrier density in the device.<sup>152</sup> Alex K.Y. Jen and his research team have successfully developed a novel cross-linked organic hole-



transporting layer (TCTA-BVP) through a simple thiol-ene thermal reaction.<sup>153</sup> This innovative HTL serves a dual purpose in highly efficient and stable Perovskite solar cell fabrication. Firstly, it aids in the extraction of holes from the Perovskite material, ensuring efficient charge transport. Secondly, it acts as a protective barrier, safeguarding the Perovskite layer. The demonstrated solar cell device achieved a power conversion efficiency of 18.3% without the need for encapsulation, showcasing its exceptional photo and thermal stability. Moreover, the cross-linked HTL exhibited several advantages over the commonly used Spiro-OMeTAD, including higher hole mobility, improved morphological stability and enhanced hydrophobicity. In 2020, Thanh-Tuan Bui and group developed two carbazole-based HTMs (DM1 and DM2) with a polymerizable double bond. The materials exhibited suitable properties as HTMs for the use in Perovskite solar cells. The impact of side chains at the N-position of the carbazole on organic -electrochemical properties was found to be negligible. However, a significant difference in thermal properties was observed between the monomer and its corresponding polymer. Despite having similar photovoltaic performance, the polymeric HTM demonstrated enhanced stability in the solar cell devices.<sup>154</sup> The structures of the above discussed molecules are given in Figure 1.29.

Chain-Shu Hsu and colleagues have successfully showcased a novel approach for developing Perovskite solar cells that eliminate the need for PEDOT:PSS. Their method involves employing a hole-transporting composite material comprising a dual-layered vanadium oxide ( $\text{VO}_x$ ) and a thermally cross-linked triarylamine-based material called X-DVTPD. This innovative strategy enhanced the  $V_{oc}$  and  $J_{sc}$  values of the cells. The hydrophobicity of X-DVTPD facilitated the growth of sizable Perovskite crystals and significantly improved the stability of PSCs. Consequently, their device achieved an efficiency of 18.08%.<sup>155</sup> Sun *et al.* introduced a dopant-free heat cross-

linking HTM derived from spiro-fluorene and xanthene (X65). They utilized this low-cost X65 in the fabrication of an n-i-p perovskite solar cell, and achieved a power conversion efficiency of 17.7%.<sup>156</sup> Baomin Xu *et al.* designed and synthesized a novel side-chain polymer by thermal polymerization of an HTM prepared from methoxytriphenylamine-thiophene units and a styrene side-chain called HTM-M1. The PSC fabricated with the material exhibited highest power conversion efficiency with a value of 17.2%.<sup>157</sup> The above mentioned HTM's chemical structures are shown in Figure 1.30.

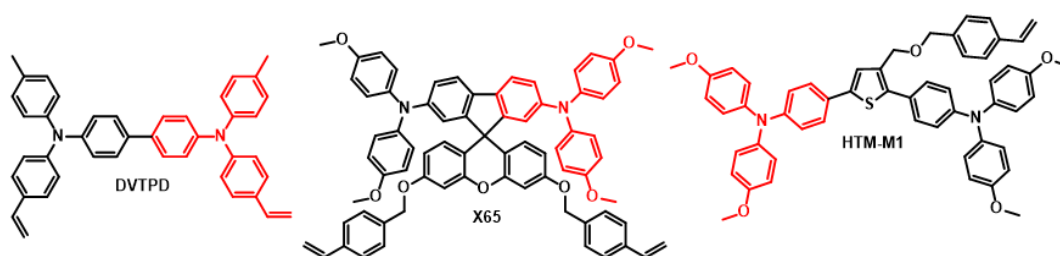


**Figure 1.30.** Chemical structure of the TPA based thermally polymerized molecules as hole transporting materials.

### 1.6.1. Hyper-cross-linking/Hyper-branching of Materials and their Organic Electronics Applications

The network structure of hyper-cross-linked materials is extensively cross-linked in three dimensions with a high density of cross-linking sites, resulting in a large number of linked polymer chains. Due to the presence of interconnected voids within the network structure, hyper-cross-linked materials often exhibit a high level of inherent microporosity. They have a large surface area and a high adsorption capacity for gases and organic molecules. Applications for hyper-cross-linked materials include catalysis, organic and gas adsorbents, supercapacitors, gas separation, electrochromic materials, and ion transporting channels (Figure 1.31A) etc. <sup>158,159</sup> Lin *et al.* developed a novel form of hyper-cross-linked polymer and

employed as an electrode material for electrochromic supercapacitors (Figure 1.31B).<sup>160</sup> The resultant polymer film displayed exceptional stability, reasonable specific capacitance, and energy density. An all-polymer solid-state EC device with PCBDTP-X and PEDOT as the electrodes was developed and the device displayed a high energy density of 18.4 Wh/kg as well as remarkable cyclic stability as an energy storage device.

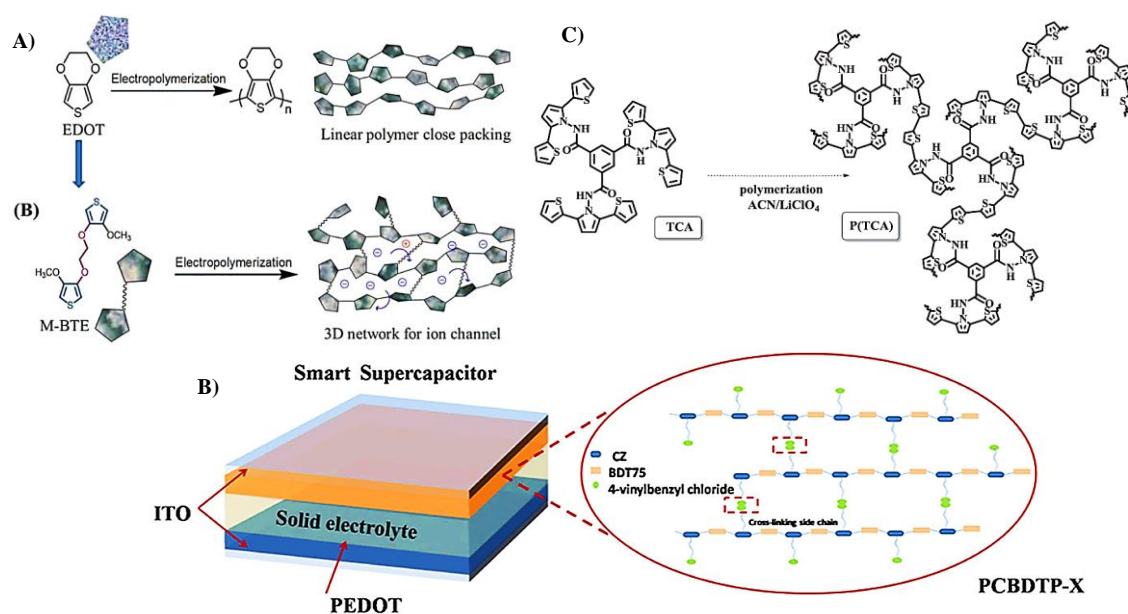


**Figure 1.31.** (A) Illustration of linear polymer of PEDOT and 3D nano-network of PM-BTE; (B) Representation of the all-polymer asymmetric supercapacitor (ASC) EC device structure with PCBDTP-X and PEDOT and (C) Chemical structure of the highly branched star shaped TCA molecule. (Adapted from reference 159, 160 and 162)

Reynolds *et al.* in the year 2000 reported a linear and a star-shaped thiophene-derived polymer (PEBs) with thermochromism and multicolor electrochromic properties. The star polymer is made up of a conjugated hyper-branched poly(triphenylamine) core with PEB arms that showed higher electrochromic properties than the linear one.<sup>161</sup> Metin Ak and his group achieved a high-performance and functional electrochromic device by using a star-shaped dithienylpyrrole derivative (Figure 1.31C).<sup>162</sup> The electrochemical polymerization of

this star-shaped polymer significantly improved its organic electronic and electrochromic characteristics. This enhancement is due to its highly conjugated, three-dimensional form and hyper-branching structure that distinguishing it from linear analogues.

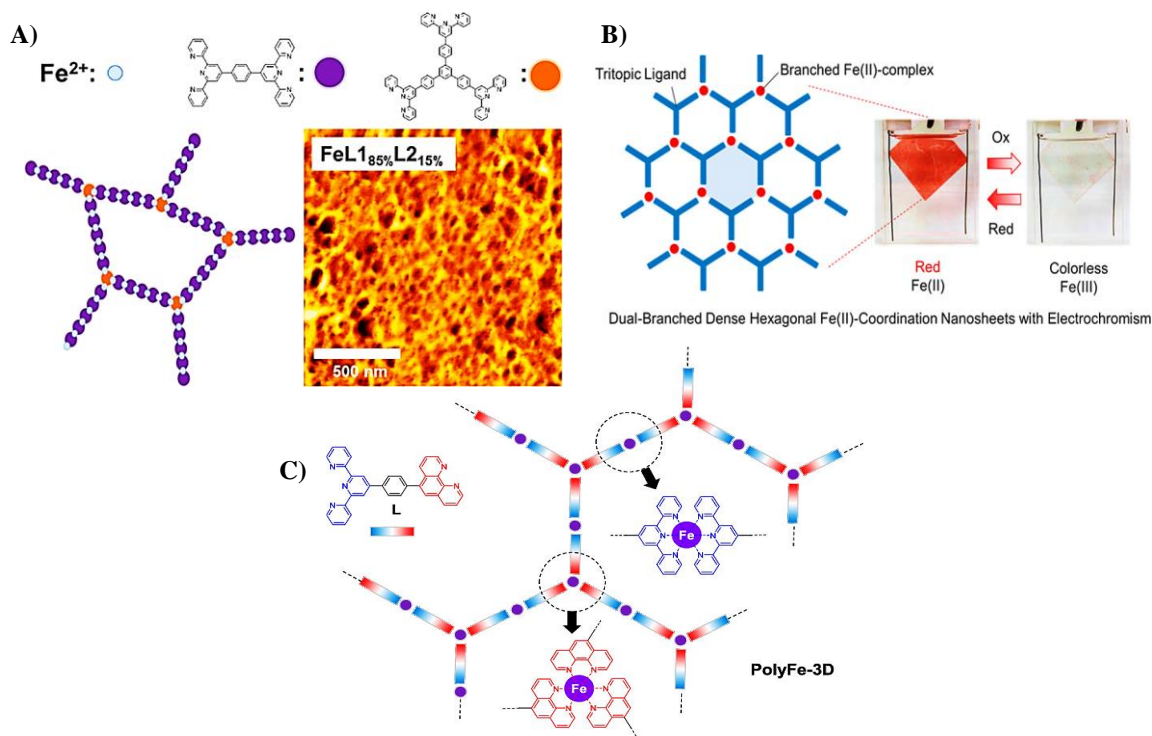


**Figure 1.32.** Hyper- branched polymers in electrochromic applications; (A) Three-dimensional (3-D) Fe(II)-based metallo-supramolecular polymers synthesised from L1 and L2, with porous morphology; (B) Fe(II)-based coordination nanosheets and the red-to-colorless electrochromic behavior and (C) The hyper-branched structure of polyFe-3D. (Adapted from reference 163, 164 and 165)

The combination of hyper-branched structures and metal complexes opens up possibilities for high-performance, multifunctional organic electronic materials. Higuchi *et al.* reported a series of 3-D metallo-supramolecular polymers based on Fe(II), utilising tris(terpyridine) ligand as the cross-linker known as L2 (Figure 1.32A).<sup>163</sup> Significant changes in surface morphology and electrochromic (EC) characteristics were found by varying the ratio of another ligand, L1 in conjunction

with L2. Among the investigated 3-D and 1-D polymers, the film composed of 85% FeL1 and 15% FeL2 displayed the best EC characteristics. This specific film has a porous surface structure with holes varying in diameter from 30 to 50 nm. The same group also developed an electrochromic device using a dual-branched dense hexagonal coordination organic nanosheets (CONASHs) (Figure 1.32B).<sup>164</sup> The CONASHs were synthesised at room temperature (25 °C) using a liquid/liquid interface technique by complexing a new tritopic bidentate ligand (L3phn) with Iron(II) as the branching metal. A mechanically stable film was obtained which was easily transferable to a variety of substrates. The film displayed good stability and optical contrast. PolyFe-3D is another three-dimensionally hyper-branched Fe(II)-based metallo-supramolecular polymer synthesised by Masayoshi Higuchi's group in the year 2021 (Figure 1.32C).<sup>165</sup> It is a single step synthesis for the fabrication of durable EC materials with high coloration efficiency, broad absorption and high contrast. The synthesis of complexes were done using iron salt and terpyridine-phenanthroline ligand. The obtained polyFe-3D film was extremely durable, retaining its electrochromic properties for over 1000 cycles.

## **1.7. Objectives of the Present Investigation**

In recent years, there has been a significant focus on organic electronics in both academic and industrial research. This concerted effort aims to advance the field by exploring new materials and enhancing their properties, including tunability, processability, efficiency, and stability. The development of triphenylamine and its derivatives is important for organic electronic applications due to their electron-donating properties, high thermal stability, tunable energy levels, versatility in molecular design, good film-forming properties, solution processability and cost-effectiveness. Even in the current scenario, these materials continue to demonstrate

superior performance compared to other alternatives, making them highly sought-after in this field. The design and development of triphenylamine-based charge transport materials, as well as the investigation of the underlying principles related to their molecular design, film-forming ability, and application in various organic electronics, are challenging but essential for further improvement in the device's characteristics.

While considering the device fabrication aspects, the solubility of organic EC/HTM materials in common organic solvents and access to film processing via simple and cost-efficient techniques such as spin/spray-coating are advantageous for practical applications of these materials. While polymers form very stable films with better morphology and mechanical stability, the challenges in purification and poor solubility of such materials restrict their wide applications. On the other hand, small molecules and discrete oligomers, which show excellent photophysical and electrochemical features combined with the option of synthetically tuning their structure and properties, are compromised in the quality and morphological as well as the mechanical stability of the films. Crosslinkable small molecules bridge these two classes of molecules where, the synthesis, functionalization, purification and film casting can be done in a similar way as small molecules, cross-linking of which addresses the morphological and mechanical stabilities. The primary focus of this thesis revolves around the molecular design, synthesis, and structural role of triphenylamine-based materials in the development of solution-processable, solvent-resistant, and stable organic thin films for organic electronic devices such as electrochromic devices, PSCs, and OLEDs.

The research presented in this thesis makes a substantial contribution to the field of triphenylamine-based charge transport materials in organic electronic

devices. In this work, we successfully employed two sets of electrochromic derivatives and two sets of hole-transporting materials for electrochromic device, solar cell, and OLED applications. The properties of these synthesized materials were thoroughly characterized employing various analytical and spectroscopic methods. The thermally cross-linkable molecules formed rigid, uniform, and transparent films with high solvent resistance and exhibited excellent thermal and electrochemical stability upon cross-linking. When compared to other derivatives, the hyper-cross-linked films performed better as an electrochromic layer and hole transporting material, demonstrating the importance of a cross-linking techniques in the device performance. The materials also served as hole-injecting/transporting layers in OLEDs and Perovskite solar cells, respectively, ensuring the effective hole transporting ability of the synthesized materials.

## **1.8. References**

- (1) Gayathri, P.; Pannipara, M.; Al-Sehemi, A. G.; Anthony, S. P. Triphenylamine-based stimuli-responsive solid state fluorescent materials. *New J. Chem.* **2020**, *44*, 8680-8696.
- (2) Shirota, Y.; Kageyama, H.: Organic materials for optoelectronic applications: Overview. In *Handbook of Organic Materials for Electronic and Photonic Devices (Second Edition)*; Ostroverkhova, O., Ed.; Woodhead Publishing, **2019**; pp 3-42.
- (3) Rybakiewicz, R.; Zagorska, M.; Pron, A. Triphenylamine-based electroactive compounds: synthesis, properties and application to organic electronics. *Chem. Pap.* **2017**, *71*, 243-268.
- (4) Ostroverkhova, O. Organic Optoelectronic Materials: Mechanisms and Applications. *Chem. Rev.* **2016**, *116*, 13279-13412.
- (5) Mahmood, A. Triphenylamine based dyes for dye sensitized solar cells: A review. *Sol. Energy* **2016**, *123*, 127-144.
- (6) Hao, Q.; Li, Z.-J.; Bai, B.; Zhang, X.; Zhong, Y.-W.; Wan, L.-J.; Wang, D. A Covalent Organic Framework Film for Three-State Near-Infrared Electrochromism and a Molecular Logic Gate. *Angew. Chem. Int. Ed.* **2021**, *60*, 12498-12503.

- (7) Pacansky, J.; Waltman, R. J.; Seki, H. Ab Initio Computational Studies on the Structures and Energetics of Hole Transport Molecules: Triphenylamine. *Bull. Chem. Soc. Jpn.* **1997**, *70*, 55-59.
- (8) Cias, P.; Slugovc, C.; Gescheidt, G. Hole Transport in Triphenylamine Based OLED Devices: From Theoretical Modeling to Properties Prediction. *J. Phys. Chem. A* **2011**, *115*, 14519-14525.
- (9) Wang, B.-C.; Liao, H.-R.; Chang, J.-C.; Chen, L.; Yeh, J.-T. Electronic structure and molecular orbital study of hole-transport material triphenylamine derivatives. *Journal of Luminescence* **2007**, *124*, 333-342.
- (10) Munshi, M. U.; Berden, G.; Martens, J.; Oomens, J. Gas-phase vibrational spectroscopy of triphenylamine: the effect of charge on structure and spectra. *PCCP* **2017**, *19*, 19881-19889.
- (11) Blanchard, P.; Malacrida, C.; Cabanetos, C.; Roncali, J.; Ludwigs, S. Triphenylamine and some of its derivatives as versatile building blocks for organic electronic applications. *Polym. Int.* **2019**, *68*, 589-606.
- (12) Coropceanu, V.; Malagoli, M.; André, J. M.; Brédas, J. L. Charge-Transfer Transitions in Triarylamine Mixed-Valence Systems: A Joint Density Functional Theory and Vibronic Coupling Study. *J. Am. Chem. Soc.* **2002**, *124*, 10519-10530.
- (13) Yen, H.-J.; Liou, G.-S. Solution-Processable Novel Near-Infrared Electrochromic Aromatic Polyamides Based on Electroactive Tetraphenyl-p-Phenylenediamine Moieties. *Chem. Mater.* **2009**, *21*, 4062-4070.
- (14) Yen, H.-J.; Lin, K.-Y.; Liou, G.-S. Transmissive to black electrochromic aramids with high near-infrared and multicolor electrochromism based on electroactive tetraphenylbenzidine units. *J. Mater. Chem.* **2011**, *21*, 6230-6237.
- (15) Svensson, J. S. E. M.; Granqvist, C. G. Electrochromic coatings for "smart windows". *Sol. Energy Mater.* **1985**, *12*, 391-402.
- (16) Chandrasekhar, P.; Zay, B. J.; Birur, G. C.; Rawal, S.; Pierson, E. A.; Kauder, L.; Swanson, T. Large, Switchable Electrochromism in the Visible Through Far-Infrared in Conducting Polymer Devices. *Adv. Funct. Mater.* **2002**, *12*, 95-103.
- (17) Andersson Ersman, P.; Kawahara, J.; Berggren, M. Printed passive matrix addressed electrochromic displays. *Org. Electron.* **2013**, *14*, 3371-3378.



- (18) Österholm, A. M.; Shen, D. E.; Kerszulis, J. A.; Bulloch, R. H.; Kuepfert, M.; Dyer, A. L.; Reynolds, J. R. Four Shades of Brown: Tuning of Electrochromic Polymer Blends Toward High-Contrast Eyewear. *ACS Appl. Mater. Interfaces* **2015**, *7*, 1413-1421.
- (19) Deb, S. K. A Novel Electrophotographic System. *Appl. Opt.* **1969**, *8*, 192-195.
- (20) Deb, S. K. Optical and photoelectric properties and colour centres in thin films of tungsten oxide. *J. Theor. Appl. Phys.* **1973**, *27*, 801-822.
- (21) Platt, J. J. Electrochromism, a Possible Change of Color Producing in Dyes by an Electric Field. *J. Chem. Phys.* **1961**, *34*, 862-863.
- (22) Kortz, C.; Hein, A.; Ciobanu, M.; Walder, L.; Oesterschulze, E. Complementary hybrid electrodes for high contrast electrochromic devices with fast response. *Nat. Commun.* **2019**, *10*, 4874.
- (23) Bi, Z.; Li, X.; Chen, Y.; He, X.; Xu, X.; Gao, X. Large-Scale Multifunctional Electrochromic-Energy Storage Device Based on Tungsten Trioxide Monohydrate Nanosheets and Prussian White. *ACS Appl. Mater. Interfaces* **2017**, *9*, 29872-29880.
- (24) Pan, J.; Zheng, R.; Wang, Y.; Ye, X.; Wan, Z.; Jia, C.; Weng, X.; Xie, J.; Deng, L. A high-performance electrochromic device assembled with hexagonal WO<sub>3</sub> and NiO/PB composite nanosheet electrodes towards energy storage smart window. *Sol. Energy Mater. Sol. Cells* **2020**, *207*, 110337.
- (25) Sheng, K.; Xue, B.; Zheng, J.; Xu, C. A Transparent to Opaque Electrochromic Device Using Reversible Ag Deposition on PProDOT-Me<sub>2</sub> with Robust Stability. *Adv. Opt. Mater.* **2021**, *9*, 2002149.
- (26) Wang, M.; Xing, X.; Perepichka, I. F.; Shi, Y.; Zhou, D.; Wu, P.; Meng, H. Electrochromic Smart Windows Can Achieve an Absolute Private State through Thermochromically Engineered Electrolyte. *Adv. Energy Mater.* **2019**, *9*, 1900433.
- (27) Chen, F.; Ren, Y.; Guo, J.; Yan, F. Thermo- and electro-dual responsive poly(ionic liquid) electrolyte based smart windows. *Chem. Commun.* **2017**, *53*, 1595-1598.
- (28) Daqiqeh Rezaei, S.; Dong, Z.; You En Chan, J.; Trisno, J.; Ng, R. J. H.; Ruan, Q.; Qiu, C.-W.; Mortensen, N. A.; Yang, J. K. W. Nanophotonic Structural Colors. *ACS Photonics* **2021**, *8*, 18-33.
- (29) Neubrech, F.; Duan, X.; Liu, N. Dynamic plasmonic color generation enabled by functional materials. *Sci. Adv.* **2020**, *6*, eabc2709.

- (30) Gugole, M.; Olsson, O.; Rossi, S.; Jonsson, M. P.; Dahlin, A. Electrochromic Inorganic Nanostructures with High Chromaticity and Superior Brightness. *Nano Lett.* **2021**, *21*, 4343-4350.
- (31) Chen, K.; He, J.; Zhang, D.; You, L.; Li, X.; Wang, H.; Mei, J. Bioinspired Dynamic Camouflage from Colloidal Nanocrystals Embedded Electrochromics. *Nano Lett.* **2021**, *21*, 4500-4507.
- (32) Huo, X.; Zhang, H.; Shen, W.; Miao, X.; Zhang, M.; Guo, M. Bifunctional aligned hexagonal/amorphous tungsten oxide core/shell nanorod arrays with enhanced electrochromic and pseudocapacitive performance. *J. Mater. Chem. A* **2019**, *7*, 16867-16875.
- (33) Tong, Z.; Liu, S.; Li, X.; Zhao, J.; Li, Y. Self-supported one-dimensional materials for enhanced electrochromism. *Nanoscale Horiz.* **2018**, *3*, 261-292.
- (34) Dalavi, D. S.; Devan, R. S.; Patil, R. S.; Ma, Y.-R.; Kang, M.-G.; Kim, J.-H.; Patil, P. S. Electrochromic properties of dandelion flower like nickel oxide thin films. *J. Mater. Chem. A* **2013**, *1*, 1035-1039.
- (35) Ma, D.; Shi, G.; Wang, H.; Zhang, Q.; Li, Y. Morphology-tailored synthesis of vertically aligned 1D WO<sub>3</sub> nano-structure films for highly enhanced electrochromic performance. *J. Mater. Chem. A* **2013**, *1*, 684-691.
- (36) Kateb, M.; Safarian, S.; Kolahdouz, M.; Fathipour, M.; Ahamdi, V. ZnO–PEDOT core–shell nanowires: An ultrafast, high contrast and transparent electrochromic display. *Sol. Energy Mater. Sol. Cells* **2016**, *145*, 200-205.
- (37) Cai, G.; Zhu, R.; Liu, S.; Wang, J.; Wei, C.; Griffith, K. J.; Jia, Y.; Lee, P. S. Tunable Intracrystal Cavity in Tungsten Bronze-Like Bimetallic Oxides for Electrochromic Energy Storage. *Adv. Energy Mater.* **2022**, *12*, 2103106.
- (38) Dehmel, R.; Nicolas, A.; Scherer, M. R. J.; Steiner, U. 3D Nanostructured Conjugated Polymers for Optical Applications. *Adv. Funct. Mater.* **2015**, *25*, 6900-6905.
- (39) Zeng, Z.; Peng, X.; Zheng, J.; Xu, C. Heteroatom-Doped Nickel Oxide Hybrids Derived from Metal–Organic Frameworks Based on Novel Schiff Base Ligands toward High-Performance Electrochromism. *ACS Appl. Mater. Interfaces* **2021**, *13*, 4133-4145.
- (40) Hao, Q.; Li, Z.-J.; Bai, B.; Zhang, X.; Zhong, Y.-W.; Wan, L.-J.; Wang, D. A Covalent Organic Framework Film for Three-State Near-Infrared Electrochromism and a Molecular Logic Gate. *Angew. Chem. Int. Ed.* **2021**, *60*, 12498-12503.

- (41) Yu, F.; Liu, W.; Ke, S.-W.; Kurmoo, M.; Zuo, J.-L.; Zhang, Q. Electrochromic two-dimensional covalent organic framework with a reversible dark-to-transparent switch. *Nat. Commun.* **2020**, *11*, 5534.
- (42) Feng, J.-f.; Liu, T.-F.; Cao, R. An Electrochromic Hydrogen-Bonded Organic Framework Film. *Angew. Chem. Int. Ed.* **2020**, *59*, 22392-22396.
- (43) Liang, H.; Li, R.; Li, C.; Hou, C.; Li, Y.; Zhang, Q.; Wang, H. Regulation of carbon content in MOF-derived hierarchical-porous NiO@C films for high-performance electrochromism. *Mater. Horiz.* **2019**, *6*, 571-579.
- (44) Bera, M. K.; Ninomiya, Y.; Higuchi, M. Constructing Alternated Heterobimetallic [Fe(II)/Os(II)] Supramolecular Polymers with Diverse Solubility for Facile Fabrication of Voltage-Tunable Multicolor Electrochromic Devices. *ACS Appl. Mater. Interfaces* **2020**, *12*, 14376-14385.
- (45) Pietsch, M.; Rödlmeier, T.; Schliske, S.; Zimmermann, J.; Romero-Nieto, C.; Hernandez-Sosa, G. Inkjet-printed polymer-based electrochromic and electrofluorochromic dual-mode displays. *J. Mater. Chem. C* **2019**, *7*, 7121-7127.
- (46) Somani, P. R.; Radhakrishnan, S. Electrochromic materials and devices: present and future. *Mater. Chem. Phys.* **2003**, *77*, 117-133.
- (47) Bender, T. P.; Graham, J. F.; Duff, J. M. Effect of Substitution on the Electrochemical and Xerographic Properties of Triarylamine: Correlation to the Hammett Parameter of the Substituent and Calculated HOMO Energy Level. *Chem. Mater.* **2001**, *13*, 4105-4111.
- (48) Onitsuka, K.; Ohara, N.; Takei, F.; Takahashi, S. Synthesis and redox properties of trinuclear ruthenium-acetylide complexes with tri(ethynylphenyl)amine bridge. *Dalton Trans.* **2006**, 3693-3698.
- (49) Ning, Z.; Tian, H. Triarylamine: a promising core unit for efficient photovoltaic materials. *Chem. Commun.* **2009**, 5483-5495.
- (50) Zhang, J.; Liu, G.; Wang, X.-Y.; Yu, G.-A.; Yin, J.; Liu, S.-H. Multistate near-infrared electrochromism and electron transfer in different oligotriphenylamine systems. *Dyes Pigm.* **2017**, *143*, 416-426.
- (51) Zhang, W.-j.; Lin, X.-c.; Li, F.; Huang, Z.-j.; Gong, C.-b.; Tang, Q. Multicolored electrochromic and electrofluorochromic materials containing triphenylamine and benzoates. *New J. Chem.* **2020**, *44*, 16412-16420.

- (52) Motoyama, K.; Koike, T.; Akita, M. Remarkable switching behavior of bimodally stimuli-responsive photochromic dithienylethenes with redox-active organometallic attachments. *Chem. Commun.* **2008**, 5812-5814.
- (53) Jin, H.; Tian, J.; Wang, S.; Tan, T.; Xiao, Y.; Li, X. Novel photochromic and electrochromic diarylethenes bearing triphenylamine units. *RSC Adv.* **2014**, *4*, 16839-16848.
- (54) Zeng, Z.; Wu, J.; Chen, Q.; Shi, Y.; Zheng, J.; Xu, C. A multifunctional triphenylamine schiff-base compound with novel self-assembly morphology transitions. *Dyes Pigm.* **2019**, *170*, 107649.
- (55) Liu, Y.; Wang, C.; Fang, X.; Zhang, J.; Liu, H.; Ma, J.; An, Q.; Hou, C.; Zhao, H.; Sun, Z.; Chu, W. Novel electrofluorochromic materials based on asymmetric D-A-D' type indolocarbazole-imidazole-triarylamine derivatives. *Dyes Pigm.* **2021**, *193*, 109516.
- (56) Lin, H.-T.; Huang, C.-L.; Liou, G.-S. Design, Synthesis, and Electrofluorochromism of New Triphenylamine Derivatives with AIE-Active Pendent Groups. *ACS Appl. Mater. Interfaces* **2019**, *11*, 11684-11690.
- (57) Wu, J.-T.; Lin, H.-T.; Liou, G.-S. Synthesis and Characterization of Novel Triarylamine Derivatives with Dimethylamino Substituents for Application in Optoelectronic Devices. *ACS Appl. Mater. Interfaces* **2019**, *11*, 14902-14908.
- (58) Li, M.; Wei, Y.; Zheng, J.; Zhu, D.; Xu, C. Highly contrasted and stable electrochromic device based on well-matched viologen and triphenylamine. *Org. Electron.* **2014**, *15*, 428-434.
- (59) Fomo, G.; Waryo, T.; Feleni, U.; Baker, P.; Iwuoha, E.: Electrochemical Polymerization. In *Functional Polymers*; Jafar Mazumder, M. A., Sheardown, H., Al-Ahmed, A., Eds.; Springer International Publishing: Cham, **2019**; pp 105-131.
- (60) Fomo, G. Electrochemical Deposition and Properties of Polyaniline Films on Carbon and Precious Metal Surfaces in Perchloric Acid/Acetonitrile. *Int. J. Electrochem. Sci.* **2016**, *11*, 10347-10361.
- (61) Sun, T.-G.; Li, Z.-J.; Shao, J.-Y.; Zhong, Y.-W. Electrochromism in Electropolymerized Films of Pyrene-Triphenylamine Derivatives. *Polymers* **2019**, *11*.
- (62) Zeng, J.; Li, H.; Wan, Z.; Ai, L.; Liu, P.; Deng, W. Colorless-to-black electrochromic materials and solid-state devices with high optical contrast based on cross-linked Poly(4-vinyltriphenylamine). *Sol. Energy Mater. Sol. Cells* **2019**, *195*, 89-98.

- (63) Li, S.; Liu, G.; Ju, X.; Zhang, Y.; Zhao, J. Synthesis, Characterization and Application of Four Novel Electrochromic Materials Employing Nitrotriphenylamine Unit as the Acceptor and Different Thiophene Derivatives as the Donor. *Polymers* **2017**, *9*, 173.
- (64) Cai, S.; Wen, H.; Wang, S.; Niu, H.; Wang, C.; Jiang, X.; Bai, X.; Wang, W. Electrochromic polymers electrochemically polymerized from 2, 5-dithienylpyrrole (DTP) with different triarylamine units: Synthesis, characterization and optoelectrochemical properties. *Electrochim. Acta* **2017**, *228*, 332-342.
- (65) Ouyang, M.; Wang, G.; Zhang, C. A novel electrochromic polymer containing triphenylamine derivative and pyrrole. *Electrochim. Acta* **2011**, *56*, 4645-4649.
- (66) Cheng, S.-H.; Hsiao, S.-H.; Su, T.-H.; Liou, G.-S. Novel Aromatic Poly(Amine-Imide)s Bearing A Pendent Triphenylamine Group: Synthesis, Thermal, Photophysical, Electrochemical, and Electrochromic Characteristics. *Macromolecules* **2005**, *38*, 307-316.
- (67) Liou, G.-S.; Hsiao, S.-H.; Chen, H.-W. Novel high-Tg poly(amine-imide)s bearing pendent N-phenylcarbazole units: synthesis and photophysical, electrochemical and electrochromic properties. *J. Mater. Chem.* **2006**, *16*, 1831-1842.
- (68) Cai, J.; Ma, L.; Niu, H.; Zhao, P.; Lian, Y.; Wang, W. Near infrared electrochromic naphthalene-based polyimides containing triarylamine: Synthesis and electrochemical properties. *Electrochim. Acta* **2013**, *112*, 59-67.
- (69) Kung, Y.-C.; Liou, G.-S.; Hsiao, S.-H. Synthesis and characterization of novel electroactive polyamides and polyimides with bulky 4-(1-adamantoxy)triphenylamine moieties. *J. Polym. Sci., Part A: Polym. Chem.* **2009**, *47*, 1740-1755.
- (70) Yen, H.-J.; Lin, H.-Y.; Liou, G.-S. Novel Starburst Triarylamine-Containing Electroactive Aramids with Highly Stable Electrochromism in Near-Infrared and Visible Light Regions. *Chem. Mater.* **2011**, *23*, 1874-1882.
- (71) Liou, G.-S.; Hsiao, S.-H.; Su, T.-H. Novel thermally stable poly(amine hydrazide)s and poly(amine-1,3,4-oxadiazole)s for luminescent and electrochromic materials. *J. Polym. Sci., Part A: Polym. Chem.* **2005**, *43*, 3245-3256.
- (72) Yen, H.-J.; Liou, G.-S. Synthesis, photoluminescence, and electrochromism of novel aromatic poly(amine-1,3,4-oxadiazole)s bearing anthrylamine chromophores. *J. Polym. Sci., Part A: Polym. Chem.* **2009**, *47*, 1584-1594.
- (73) Hsiao, S.-H.; Wang, H.-M.; Guo, W.; Sun, C.-H. Enhancing Redox Stability and Electrochromic Performance of Polyhydrazides and Poly(1,3,4-oxadiazole)s with 3,6-Di-tert-butylcarbazol-9-yltriphenylamine Units. *Macromol. Chem. Phys.* **2011**, *212*, 821-830.

- (74) Kung, Y.-C.; Hsiao, S.-H. Novel luminescent and electrochromic polyhydrazides and polyoxadiazoles bearing pyrenylamine moieties. *Polym. Chem.* **2011**, *2*, 1720-1727.
- (75) Chuang, Y.-W.; Yen, H.-J.; Wu, J.-H.; Liou, G.-S. Colorless Triphenylamine-Based Aliphatic Thermoset Epoxy for Multicolored and Near-Infrared Electrochromic Applications. *ACS Appl. Mater. Interfaces* **2014**, *6*, 3594-3599.
- (76) Ji, Y.; Zhang, C.; Niu, H.; Zhao, X.; Wang, C.; Qin, C.; Wang, W.; Bai, X. Preparation and electrochromic properties of two series of polyurethanes containing separated triphenylamine moiety with different blocks. *Dyes Pigm.* **2016**, *125*, 106-115.
- (77) Zhang, C.; Hou, Y.; Niu, H.; Lian, Y.; Bai, X.; Wang, C.; Wang, W. The preparation and electrochromic properties of the polyurethanes containing triphenylamine moiety. *J. Electroanal. Chem.* **2014**, *717-718*, 165-171.
- (78) Lin, L.-C.; Yen, H.-J.; Chen, C.-J.; Tsai, C.-L.; Liou, G.-S. Novel triarylamine-based polybenzoxazines with a donor-acceptor system for polymeric memory devices. *Chem. Commun.* **2014**, *50*, 13917-13920.
- (79) Fan, C.; Ye, C.; Wang, X.; Chen, Z.; Zhou, Y.; Liang, Z.; Tao, X. Synthesis and Electrochromic Properties of New Terpyridine-Triphenylamine Hybrid Polymers. *Macromolecules* **2015**, *48*, 6465-6473.
- (80) Kuai, Y.; Li, W.; Dong, Y.; Wong, W.-Y.; Yan, S.; Dai, Y.; Zhang, C. Multi-color electrochromism from coordination nanosheets based on a terpyridine-Fe(ii) complex. *Dalton Trans.* **2019**, *48*, 15121-15126.
- (81) Liu, Y.; Sakamoto, R.; Ho, C.-L.; Nishihara, H.; Wong, W.-Y. Electrochromic triphenylamine-based cobalt(ii) complex nanosheets. *J. Mater. Chem. C* **2019**, *7*, 9159-9166.
- (82) Yao, C.-J.; Zhong, Y.-W.; Yao, J. Five-Stage Near-Infrared Electrochromism in Electropolymerized Films Composed of Alternating Cyclometalated Bisruthenium and Bis-triarylamine Segments. *Inorg. Chem.* **2013**, *52*, 10000-10008.
- (83) Kuai, Y.; Yang, T.; Yuan, F.; Dong, Y.; Song, Q.; Zhang, C.; Wong, W.-Y. Self-assembled flexible metallo-supramolecular film based on Fe(II) ion and triphenylamine-substituted alkyl terpyridine towards electrochromic application. *Dyes Pigm.* **2021**, *194*, 109623.
- (84) Cui, B.-B.; Zhong, Y.-W.; Yao, J. Three-State Near-Infrared Electrochromism at the Molecular Scale. *J. Am. Chem. Soc.* **2015**, *137*, 4058-4061.

- (85) Li, Z.-J.; Shao, J.-Y.; Zhong, Y.-W. Near-Infrared and Two-Wavelength Electrochromism Based on Nanocrystalline TiO<sub>2</sub> Films Functionalized with Ruthenium-Amine Conjugated Complexes. *Inorg. Chem.* **2017**, *56*, 8538-8546.
- (86) Mondal, S.; Chandra Santra, D.; Ninomiya, Y.; Yoshida, T.; Higuchi, M. Dual-Redox System of Metallo-Supramolecular Polymers for Visible-to-Near-IR Modulable Electrochromism and Durable Device Fabrication. *ACS Appl. Mater. Interfaces* **2020**, *12*, 58277-58286.
- (87) Akkerman, Q. A.; Manna, L. What Defines a Halide Perovskite? *ACS Energy Lett.* **2020**, *5*, 604-610.
- (88) Park, N.-G. Perovskite solar cells: an emerging photovoltaic technology. *Mater. Today* **2015**, *18*, 65-72.
- (89) Kojima, A.; Teshima, K.; Shirai, Y.; Miyasaka, T. Organometal Halide Perovskites as Visible-Light Sensitizers for Photovoltaic Cells. *J. Am. Chem. Soc.* **2009**, *131*, 6050-6051.
- (90) Min, H.; Lee, D. Y.; Kim, J.; Kim, G.; Lee, K. S.; Kim, J.; Paik, M. J.; Kim, Y. K.; Kim, K. S.; Kim, M. G.; Shin, T. J.; Il Seok, S. Perovskite solar cells with atomically coherent interlayers on SnO<sub>2</sub> electrodes. *Nature* **2021**, *598*, 444-450.
- (91) Liu, K.; Yao, Y.; Wang, J.; Zhu, L.; Sun, M.; Ren, B.; Xie, L.; Luo, Y.; Meng, Q.; Zhan, X. Spiro[fluorene-9,9'-xanthene]-based hole transporting materials for efficient perovskite solar cells with enhanced stability. *Mater. Chem. Front.* **2017**, *1*, 100-110.
- (92) Chen, Y.-C.; Huang, S.-K.; Li, S.-S.; Tsai, Y.-Y.; Chen, C.-P.; Chen, C.-W.; Chang, Y. J. Facilely Synthesized spiro[fluorene-9,9'-phenanthren-10'-one] in Donor-Acceptor-Donor Hole-Transporting Materials for Perovskite Solar Cells. *ChemSusChem* **2018**, *11*, 3225-3233.
- (93) Lin, P.-H.; Lee, K.-M.; Ting, C.-C.; Liu, C.-Y. Spiro-tBuBED: a new derivative of a spirobifluorene-based hole-transporting material for efficient perovskite solar cells. *J. Mater. Chem. A* **2019**, *7*, 5934-5937.
- (94) Sun, Y.; Wang, C.; Zhao, D.; Yu, J.; Yin, X.; Grice, C. R.; Awni, R. A.; Shrestha, N.; Yu, Y.; Guan, L.; Ellingson, R. J.; Tang, W.; Yan, Y. A New Hole Transport Material for Efficient Perovskite Solar Cells With Reduced Device Cost. *Sol. RRL* **2018**, *2*, 1700175.
- (95) Zhang, F.; Wang, Z.; Zhu, H.; Pellet, N.; Luo, J.; Yi, C.; Liu, X.; Liu, H.; Wang, S.; Li, X.; Xiao, Y.; Zakeeruddin, S. M.; Bi, D.; Grätzel, M. Over 20% PCE perovskite solar cells with superior stability achieved by novel and low-cost hole-transporting materials. *Nano Energy* **2017**, *41*, 469-475.

- (96) Li, M.; Ma, S.; Mateen, M.; Liu, X.; Ding, Y.; Gao, J.; Yang, Y.; Zhang, X.; Wu, Y.; Dai, S. Facile donor (D)- $\pi$ -D triphenylamine-based hole transporting materials with different  $\pi$ -linker for perovskite solar cells. *Sol. Energy* **2020**, *195*, 618-625.
- (97) Fang, L.; Zheng, A.; Ren, M.; Xie, X.; Wang, P. Unraveling the Structure–Property Relationship of Molecular Hole-Transporting Materials for Perovskite Solar Cells. *ACS Appl. Mater. Interfaces* **2019**, *11*, 39001-39009.
- (98) Akin, S.; Bauer, M.; Uchida, R.; Arora, N.; Jacopin, G.; Liu, Y.; Hertel, D.; Meerholz, K.; Mena-Osteritz, E.; Bäuerle, P.; Zakeeruddin, S. M.; Dar, M. I.; Grätzel, M. Cyclopentadithiophene-Based Hole-Transporting Material for Highly Stable Perovskite Solar Cells with Stabilized Efficiencies Approaching 21%. *ACS Appl. Energy Mater.* **2020**, *3*, 7456-7463.
- (99) Elsenety, M. M.; Stergiou, A.; Sygellou, L.; Tagmatarchis, N.; Balis, N.; Falaras, P. Boosting perovskite nanomorphology and charge transport properties via a functional D- $\pi$ -A organic layer at the absorber/hole transporter interface. *Nanoscale* **2020**, *12*, 15137-15149.
- (100) García-Benito, I.; Zimmermann, I.; Urieta-Mora, J.; Aragón, J.; Molina-Ontoria, A.; Ortí, E.; Martín, N.; Nazeeruddin, M. K. Isomerism effect on the photovoltaic properties of benzotrithiophene-based hole-transporting materials. *J. Mater. Chem. A* **2017**, *5*, 8317-8324.
- (101) Rodríguez-Seco, C.; Méndez, M.; Roldán-Carmona, C.; Pudi, R.; Nazeeruddin, M. K.; Palomares, E. J. Minimization of Carrier Losses for Efficient Perovskite Solar Cells through Structural Modification of Triphenylamine Derivatives. *Angew. Chem. Int. Ed.* **2020**, *59*, 5303-5307.
- (102) Chen, C.; Ding, X.; Li, H.; Cheng, M.; Li, H.; Xu, L.; Qiao, F.; Li, H. Highly Efficient Phenoxazine Core Unit Based Hole Transport Materials for Hysteresis-Free Perovskite Solar Cells. *ACS Appl. Mater. Interfaces* **2018**, *10*, 36608-36614.
- (103) Xue, R.; Zhang, M.; Xu, G.; Zhang, J.; Chen, W.; Chen, H.; Yang, M.; Cui, C.; Li, Y.; Li, Y. Molecular design with silicon core: toward commercially available hole transport materials for high-performance planar p-i-n perovskite solar cells. *J. Mater. Chem. A* **2018**, *6*, 404-413.
- (104) Chen, J.; Xia, J.; Gao, W.-J.; Yu, H.-J.; Zhong, J.-X.; Jia, C.; Qin, Y.-S.; She, Z.; Kuang, D.-B.; Shao, G. Tetraphenylbutadiene-Based Symmetric 3D Hole-Transporting Materials for Perovskite Solar Cells: A Trial Trade-off between Charge Mobility and Film Morphology. *ACS Appl. Mater. Interfaces* **2020**, *12*, 21088-21099.



- (105) Wu, G.; Zhang, Y.; Kaneko, R.; Kojima, Y.; Islam, A.; Sugawa, K.; Otsuki, J.; Liu, S. Anthradithiophene based hole-transport material for efficient and stable perovskite solar cells. *J. Energy Chem.* **2020**, *48*, 293-298.
- (106) Zhao, L.; Qiu, L.; Xia, D.; Liu, S.; Yi, X.; Fan, J.; Lin, K.; Fan, R.; Guo, Y.; Yang, Y. Cyclooctatetrathiophene-Cored Three-Dimensional Hole Transport Material Enabling Over 19% Efficiency of Perovskite Solar Cells. *ACS Appl. Energy Mater.* **2019**, *2*, 8173-8180.
- (107) Roy, P.; Kumar Sinha, N.; Tiwari, S.; Khare, A. A review on perovskite solar cells: Evolution of architecture, fabrication techniques, commercialization issues and status. *Sol. Energy* **2020**, *198*, 665-688.
- (108) Li, W.; Cariello, M.; Méndez, M.; Cooke, G.; Palomares, E. Self-Assembled Molecules for Hole-Selective Electrodes in Highly Stable and Efficient Inverted Perovskite Solar Cells with Ultralow Energy Loss. *ACS Appl. Energy Mater.* **2023**, *6*, 1239-1247.
- (109) Zhang, S.; Wu, R.; Mu, C.; Wang, Y.; Han, L.; Wu, Y.; Zhu, W.-H. Conjugated Self-Assembled Monolayer as Stable Hole-Selective Contact for Inverted Perovskite Solar Cells. *ACS Mater. Lett.* **2022**, *4*, 1976-1983.
- (110) Al-Ashouri, A.; Magomedov, A.; Roß, M.; Jošt, M.; Talaikis, M.; Chistiakova, G.; Bertram, T.; Márquez, J. A.; Köhnen, E.; Kasparavičius, E.; Levenco, S.; Gil-Escrig, L.; Hages, C. J.; Schlattmann, R.; Rech, B.; Malinauskas, T.; Unold, T.; Kaufmann, C. A.; Korte, L.; Niaura, G.; Getautis, V.; Albrecht, S. Conformal monolayer contacts with lossless interfaces for perovskite single junction and monolithic tandem solar cells. *Energy Environ. Sci.* **2019**, *12*, 3356-3369.
- (111) Zou, S.-J.; Shen, Y.; Xie, F.-M.; Chen, J.-D.; Li, Y.-Q.; Tang, J.-X. Recent advances in organic light-emitting diodes: toward smart lighting and displays. *Mater. Chem. Front.* **2020**, *4*, 788-820.
- (112) Wang, J.; Chepelianskii, A.; Gao, F.; Greenham, N. C. Control of exciton spin statistics through spin polarization in organic optoelectronic devices. *Nat. Commun.* **2012**, *3*, 1191.
- (113) Jou, J.-H.; Kumar, S.; Agrawal, A.; Li, T.-H.; Sahoo, S. Approaches for fabricating high efficiency organic light emitting diodes. *J. Mater. Chem. C* **2015**, *3*, 2974-3002.
- (114) Jhulki, S.; Moorthy, J. N. Small molecular hole-transporting materials (HTMs) in organic light-emitting diodes (OLEDs): structural diversity and classification. *J. Mater. Chem. C* **2018**, *6*, 8280-8325.
- (115) Salbeck, J.; Yu, N.; Bauer, J.; Weissörtel, F.; Bestgen, H. Low molecular organic glasses for blue electroluminescence. *Synth. Met.* **1997**, *91*, 209-215.

- (116) Elschner, A.; Bruder, F.; Heuer, H. W.; Jonas, F.; Karbach, A.; Kirchmeyer, S.; Thurm, S.; Wehrmann, R. PEDT/PSS for efficient hole-injection in hybrid organic light-emitting diodes. *Synth. Met.* **2000**, *111-112*, 139-143.
- (117) Park, J. J.; Park, T. J.; Jeon, W. S.; Pode, R.; Jang, J.; Kwon, J. H.; Yu, E.-S.; Chae, M.-Y. Small molecule interlayer for solution processed phosphorescent organic light emitting device. *Org. Electron.* **2009**, *10*, 189-193.
- (118) Tong, Q.-X.; Lai, S.-L.; Chan, M.-Y.; Lai, K.-H.; Tang, J.-X.; Kwong, H.-L.; Lee, C.-S.; Lee, S.-T. High Tg Triphenylamine-Based Starburst Hole-Transporting Material for Organic Light-Emitting Devices. *Chem. Mater.* **2007**, *19*, 5851-5855.
- (119) Yang, Z.; Xu, B.; He, J.; Xue, L.; Guo, Q.; Xia, H.; Tian, W. Solution-processable and thermal-stable triphenylamine-based dendrimers with truxene cores as hole-transporting materials for organic light-emitting devices. *Org. Electron.* **2009**, *10*, 954-959.
- (120) Liu, Y.; Chen, S.; Lam, J. W. Y.; Lu, P.; Kwok, R. T. K.; Mahtab, F.; Kwok, H. S.; Tang, B. Z. Tuning the Electronic Nature of Aggregation-Induced Emission Luminogens with Enhanced Hole-Transporting Property. *Chem. Mater.* **2011**, *23*, 2536-2544.
- (121) Cao, X.; Wen, Y.; Guo, Y.; Yu, G.; Liu, Y.; Yang, L.-M. Undoped, red organic light-emitting diodes based on a N,N,N',N'-tetraphenylbenzidine (TPD) derivative as red emitter with a triphenylamine derivative as hole-transporting layer. *Dyes Pigm.* **2010**, *84*, 203-207.
- (122) Park, Y.; Kim, B.; Lee, C.; Lee, J.; Lee, J. H.; Park, J. High efficiency new hole injection materials for organic light emitting diodes based on dimeric phenothiazine and phenoxazine moiety derivatives. *J. Nanosci. Nanotechnol.* **2012**, *12*, 4356-4360.
- (123) Jiang, Z.; Ye, T.; Yang, C.; Yang, D.; Zhu, M.; Zhong, C.; Qin, J.; Ma, D. Star-Shaped Oligotriarylamines with Planarized Triphenylamine Core: Solution-Processable, High-Tg Hole-Injecting and Hole-Transporting Materials for Organic Light-Emitting Devices. *Chem. Mater.* **2011**, *23*, 771-777.
- (124) Krucaite, G.; Blazelevicius, D.; Tavgeniene, D.; Grigalevicius, S.; Lin, C.-H.; Shao, C.-M.; Chang, C.-H. Tetramer of triphenylamine and similar derivatives with bromine atoms as hole injecting/transporting materials for efficient red phosphorescent OLEDs. *Opt. Mater.* **2020**, *108*, 110225.
- (125) Braveenth, R.; Bae, I.-J.; Wang, Y.; Kim, S. H.; Kim, M.; Chai, K. Y. Acridine-Triphenylamine Based Hole-Transporting and Hole-Injecting Material for Highly Efficient Phosphorescent-Based Organic Light Emitting Diodes. *Appl. Sci.* **2018**, *8*, 1168.

- (126) Butt, M. A. Thin-Film Coating Methods: A Successful Marriage of High-Quality and Cost-Effectiveness—A Brief Exploration. *Coatings* **2022**, *12*, 1115.
- (127) Agarwala, P.; Kabra, D. A review on triphenylamine (TPA) based organic hole transport materials (HTMs) for dye sensitized solar cells (DSSCs) and perovskite solar cells (PSCs): evolution and molecular engineering. *J. Mater. Chem. A* **2017**, *5*, 1348-1373.
- (128) Sun, S.; Jia, P.; Lu, M.; Lu, P.; Gao, Y.; Zhong, Y.; Tang, C.; Zhang, Y.; Wu, Z.; Zhu, J.; Zhang, Y.; Yu, W. W.; Bai, X. Enhanced Flexibility and Stability of Emissive Layer Enable High-Performance Flexible Light-Emitting Diodes by Cross-Linking of Biomass Material. *Adv. Funct. Mater.* **2022**, *32*, 2204286.
- (129) Wang, Y.; Yin, Z.; Xie, Z.; Zhao, X.; Zhou, C.; Zhou, S.; Chen, P. Polysiloxane Functionalized Carbon Dots and Their Cross-Linked Flexible Silicone Rubbers for Color Conversion and Encapsulation of White LEDs. *ACS Appl. Mater. Interfaces* **2016**, *8*, 9961-9968.
- (130) Liu, L.; Li, S.; Wu, L.; Chen, D.; Cao, K.; Duan, Y.; Chen, S. Enhanced flexibility and stability of PEDOT:PSS electrodes through interfacial crosslinking for flexible organic light-emitting diodes. *Org. Electron.* **2021**, *89*, 106047.
- (131) Cao, Q.; Yang, J.; Wang, T.; Li, Y.; Pu, X.; Zhao, J.; Zhang, Y.; Zhou, H.; Li, X.; Li, X. Star-polymer multidentate-cross-linking strategy for superior operational stability of inverted perovskite solar cells at high efficiency. *Energy Environ. Sci.* **2021**, *14*, 5406-5415.
- (132) Kim, B. J.; Miyamoto, Y.; Ma, B.; Fréchet, J. M. J. Photocrosslinkable Polythiophenes for Efficient, Thermally Stable, Organic Photovoltaics. *Adv. Funct. Mater.* **2009**, *19*, 2273-2281.
- (133) Lanzi, M.; Salatelli, E.; Di-Nicola, F. P.; Zuppiroli, L.; Pierini, F. A new photocrosslinkable oligothiophene for organic solar cells with enhanced stability. *Mater. Chem. Phys.* **2017**, *186*, 98-107.
- (134) Rumer, J. W.; Ashraf, R. S.; Eisenmenger, N. D.; Huang, Z.; Meager, I.; Nielsen, C. B.; Schroeder, B. C.; Chabynyc, M. L.; McCulloch, I. Dual Function Additives: A Small Molecule Crosslinker for Enhanced Efficiency and Stability in Organic Solar Cells. *Adv. Energy Mater.* **2015**, *5*, 1401426.
- (135) Griffini, G.; Douglas, J. D.; Piliago, C.; Holcombe, T. W.; Turri, S.; Fréchet, J. M. J.; Mynar, J. L. Long-Term Thermal Stability of High-Efficiency Polymer Solar Cells Based on Photocrosslinkable Donor-Acceptor Conjugated Polymers. *Adv. Mater.* **2011**, *23*, 1660-1664.
- (136) Wu, S.-C.; Strover, L. T.; Yao, X.; Chen, X.-Q.; Xiao, W.-J.; Liu, L.-N.; Wang, J.; Visoly-Fisher, I.; Katz, E. A.; Li, W.-S. UV-Cross-linkable Donor-Acceptor Polymers Bearing a

---

Photostable Conjugated Backbone for Efficient and Stable Organic Photovoltaics. *ACS Appl. Mater. Interfaces* **2018**, *10*, 35430-35440.

(137) Hempe, M.; Paschek, J.; Schelter, J.; Umbach, A.; Meerholz, K.; Reggelin, M. Crosslinkable Bis(diphenylamine)-Substituted Mixed Dihydroindeno[1,2-b]fluorenes for Solution-Processed Multilayer Organic Light-Emitting Diodes. *ChemPlusChem* **2020**, *85*, 151-158.

(138) Hung, W.-Y.; Lin, C.-Y.; Cheng, T.-L.; Yang, S.-W.; Chaskar, A.; Fan, G.-L.; Wong, K.-T.; Chao, T.-C.; Tseng, M.-R. A new thermally crosslinkable hole injection material for OLEDs. *Org. Electron.* **2012**, *13*, 2508-2515.

(139) Chen, C.-P.; Huang, C.-Y.; Chuang, S.-C. Highly Thermal Stable and Efficient Organic Photovoltaic Cells with Crosslinked Networks Appending Open-Cage Fullerenes as Additives. *Adv. Funct. Mater.* **2015**, *25*, 207-213.

(140) Patel, D. G.; Graham, K. R.; Reynolds, J. R. A Diels–Alder crosslinkable host polymer for improved PLED performance: the impact on solution processed doped device and multilayer device performance. *J. Mater. Chem.* **2012**, *22*, 3004-3014.

(141) Huang, F.; Cheng, Y.-J.; Zhang, Y.; Liu, M. S.; Jen, A. K. Y. Crosslinkable hole-transporting materials for solution processed polymer light-emitting diodes. *J. Mater. Chem.* **2008**, *18*, 4495-4509.

(142) Abraham, S.; Ganesh, G. P. T.; Varughese, S.; Deb, B.; Joseph, J. Cross-Linkable Fluorene-Diphenylamine Derivatives for Electrochromic Applications. *ACS Appl. Mater. Interfaces* **2015**, *7*, 25424-25433.

(143) Abraham, S.; Mangalath, S.; Sasikumar, D.; Joseph, J. Transmissive-to-Black Electrochromic Devices Based on Cross-Linkable Tetraphenylethene-Diphenylamine Derivatives. *Chem. Mater.* **2017**, *29*, 9877-9881.

(144) Wałęsa-Chorab, M.; Skene, W. G. Visible-to-NIR Electrochromic Device Prepared from a Thermally Polymerizable Electroactive Organic Monomer. *ACS Appl. Mater. Interfaces* **2017**, *9*, 21524-21531.

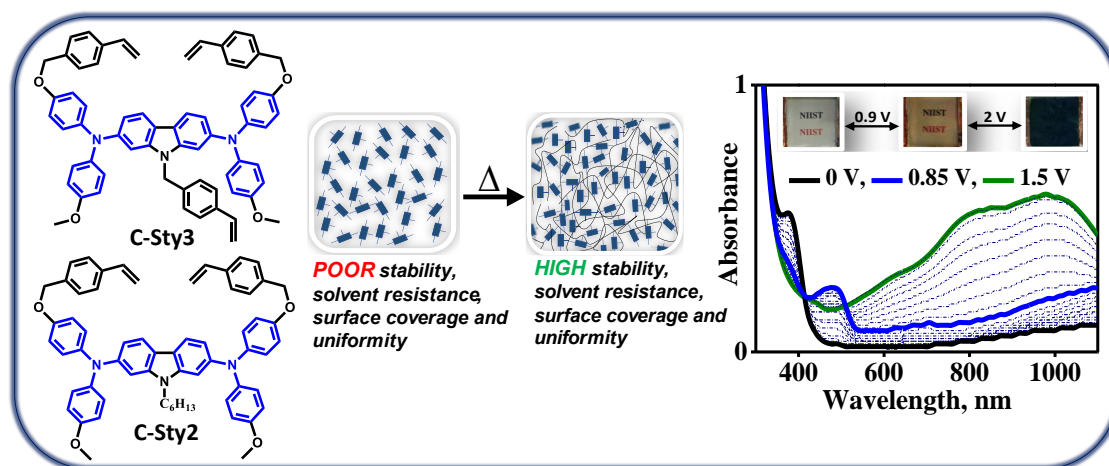
(145) Liu, H.-S.; Pan, B.-C.; Huang, D.-C.; Kung, Y.-R.; Leu, C.-M.; Liou, G.-S. Highly transparent to truly black electrochromic devices based on an ambipolar system of polyamides and viologen. *NPG Asia Mater.* **2017**, *9*, e388-e388.

- (146) Zhuang, Y.; Zhao, W.; Wang, L.; Li, F.; Wang, W.; Liu, S.; Huang, W.; Zhao, Q. Soluble triarylamine functionalized symmetric viologen for all-solid-state electrochromic supercapacitors. *Sci. China Chem.* **2020**, *63*, 1632-1644.
- (147) Wałęsa-Chorab, M.; Skene, W. G. Extending the Color Retention of an Electrochromic Device by Immobilizing Color Switching and Ion-Storage Complementary Layers. *Electronic Materials* **2020**.
- (148) Lv, X.; Li, J.; Xu, L.; Zhu, X.; Tameev, A.; Nekrasov, A.; Kim, G.; Xu, H.; Zhang, C. Colorless to Multicolored, Fast Switching, and Highly Stable Electrochromic Devices Based on Thermally Cross-Linking Copolymer. *ACS Appl. Mater. Interfaces* **2021**, *13*, 41826-41835.
- (149) Lv, X.; Shao, M.; Zhu, X.; Xu, L.; Ouyang, M.; Zhou, C.; Dong, J.; Zhang, C. Thermally Cross-Linked Copolymer for Highly Transparent to Multicolor-Showing Electrochromic Materials. *ACS Appl. Polym. Mater.* **2023**, *5*, 3595-3603.
- (150) Chiang, T.-Y.; Fan, G.-L.; Jeng, J.-Y.; Chen, K.-C.; Chen, P.; Wen, T.-C.; Guo, T.-F.; Wong, K.-T. Functional p-Type, Polymerized Organic Electrode Interlayer in CH<sub>3</sub>NH<sub>3</sub>PbI<sub>3</sub> Perovskite/Fullerene Planar Heterojunction Hybrid Solar Cells. *ACS Appl. Mater. Interfaces* **2015**, *7*, 24973-24981.
- (151) Zhang, Y.; Kou, C.; Zhang, J.; Liu, Y.; Li, W.; Bo, Z.; Shao, M. Crosslinked and dopant free hole transport materials for efficient and stable planar perovskite solar cells. *J. Mater. Chem. A* **2019**, *7*, 5522-5529.
- (152) Xu, J.; Voznyy, O.; Comin, R.; Gong, X.; Walters, G.; Liu, M.; Kanjanaboos, P.; Lan, X.; Sargent, E. H. Crosslinked Remote-Doped Hole-Extracting Contacts Enhance Stability under Accelerated Lifetime Testing in Perovskite Solar Cells. *Adv. Mater.* **2016**, *28*, 2807-2815.
- (153) Li, Z. a.; Zhu, Z.; Chueh, C.-C.; Luo, J.; Jen, A. K. Y. Facile Thiol-Ene Thermal Crosslinking Reaction Facilitated Hole-Transporting Layer for Highly Efficient and Stable Perovskite Solar Cells. *Adv. Energy Mater.* **2016**, *6*, 1601165.
- (154) Magaldi, D.; Ulfa, M.; Nghiễm, M.-P.; Sini, G.; Goubard, F.; Pauporté, T.; Bui, T.-T. Hole transporting materials for perovskite solar cells: molecular versus polymeric carbazole-based derivatives. *J. Mater. Sci.* **2020**, *55*, 4820-4829.
- (155) Chang, C.-C.; Tao, J.-H.; Tsai, C.-E.; Cheng, Y.-J.; Hsu, C.-S. Cross-linked Triarylamine-Based Hole-Transporting Layer for Solution-Processed PEDOT:PSS-Free Inverted Perovskite Solar Cells. *ACS Appl. Mater. Interfaces* **2018**, *10*, 21466-21471.

- (156) Wang, L.; Zhang, F.; Liu, T.; Zhang, W.; Li, Y.; Cai, B.; He, L.; Guo, Y.; Yang, X.; Xu, B.; Gardner, J. M.; Kloo, L.; Sun, L. A crosslinked polymer as dopant-free hole-transport material for efficient n-i-p type perovskite solar cells. *J. Energy Chem.* **2021**, *55*, 211-218.
- (157) Wu, J.; Liu, C.; Hu, M.; Deng, X.; Tan, W.; Tian, Y.; Xu, B. Polystyrene with a methoxytriphenylamine-conjugated-thiophene moiety side-chain as a dopant-free hole-transporting material for perovskite solar cells. *J. Mater. Chem. A* **2018**, *6*, 13123-13132.
- (158) Liu, H.; Li, Q.; Li, Q.; Jin, W.; Li, X.; Hameed, A.; Qiao, S. Rational skeletal rigidity of conjugated microporous polythiophenes for gas uptake. *Polym. Chem.* **2017**, *8*, 6733-6740.
- (159) Qin, L.; Ding, Z.; Hanif, M.; Jiang, J.; Liu, L.; Mo, Y.; Xie, Z.; Ma, Y. Poly(3,4-dioxythiophene) soft nano-network with a compatible ion transporting channel for improved electrochromic performance. *Polym. Chem.* **2016**, *7*, 6954-6963.
- (160) Sun, Y.; Zhu, G.; Zhao, X.; Kang, W.; Li, M.; Zhang, X.; Yang, H.; Guo, L.; Lin, B. Solution-processable, hypercrosslinked polymer via post-crosslinking for electrochromic supercapacitor with outstanding electrochemical stability. *Sol. Energy Mater. Sol. Cells* **2020**, *215*, 110661.
- (161) Wang, F.; Wilson, M. S.; Rauh, R. D.; Schottland, P.; Thompson, B. C.; Reynolds, J. R. Electrochromic Linear and Star Branched Poly(3,4-ethylenedioxythiophene-didodecyloxybenzene) Polymers. *Macromolecules* **2000**, *33*, 2083-2091.
- (162) Soganci, T.; Gumusay, O.; Soyleyici, H. C.; Ak, M. Synthesis of highly branched conducting polymer architecture for electrochromic applications. *Polymer* **2018**, *134*, 187-195.
- (163) Hu, C.-W.; Sato, T.; Zhang, J.; Moriyama, S.; Higuchi, M. Three-Dimensional Fe(II)-based Metallo-Supramolecular Polymers with Electrochromic Properties of Quick Switching, Large Contrast, and High Coloration Efficiency. *ACS Appl. Mater. Interfaces* **2014**, *6*, 9118-9125.
- (164) Mondal, S.; Ninomiya, Y.; Yoshida, T.; Mori, T.; Bera, M. K.; Ariga, K.; Higuchi, M. Dual-Branched Dense Hexagonal Fe(II)-Based Coordination Nanosheets with Red-to-Colorless Electrochromism and Durable Device Fabrication. *ACS Appl. Mater. Interfaces* **2020**, *12*, 31896-31903.
- (165) Narayana, Y. S. L. V.; Mondal, S.; Rana, U.; Ninomiya, Y.; Santra, D. C.; Yoshida, T.; Higuchi, M. One-Step Synthesis of a Three-Dimensionally Hyperbranched Fe(II)-Based Metallo-Supramolecular Polymer Using an Asymmetrical Ditopic Ligand for Durable

Electrochromic Films with Wide Absorption, Large Optical Contrast, and High Coloration Efficiency. *ACS Appl. Electron. Mater.* **2021**, *3*, 2044-2055.

## Effect of Hyper-crosslinking on the Electrochromic Device Properties of Carbazole-Diphenylamine Derivatives



### 2.1. Abstract

Triphenylamine derivatives are promising organic electrochromic (EC) materials due to their easy synthesis, low oxidation potentials, high charge carrier mobilities, electrochemical stability, coloration efficiency and tunability of electrochromic properties via substitution. Further, the cross-linking strategy provides added advantage to the small molecule-based EC devices in terms of better-quality EC films with enhanced electrochromic properties. Herein, we discuss the electrochromic properties of two carbazole-diphenylamine derivatives, **C-Sty2**, and **C-Sty3** with two and three thermally cross-linkable styryl units, respectively, following a donor- $\pi$ -donor (D- $\pi$ -D) design, where both carbazole moiety and cross-linking styrene groups modulate the photophysical and electrochromic properties. Both the styryl derivatives formed rigid, uniform and transparent films with high



solvent resistance and exhibited excellent thermal and electrochemical stability upon cross-linking. **C-Sty3**, with three cross-linkable styryl units could form more extended cross-links leading to hyper-crosslinked films with distinct, regular and porous morphology compared to **C-Sty2**. Spectroelectrochemical studies of the films showed a color change from a transparent colorless state to an initial light-yellow color and then a final dark blue color with color contrast of 65% at 890 nm for **C-Sty2** and 78% at 850 nm for **C-Sty3**. The hyper-crosslinked films of **C-Sty3** demonstrated enhanced coloration efficiency ( $248 \text{ cm}^2/\text{C}$ ), optical contrast and open circuit memory compared to **C-Sty2**. Electrochemical Impedance Spectroscopy (EIS) analysis showed lower solution and charge transfer resistances ( $R_s$  &  $R_{ct}$ , respectively) for hyper-crosslinked films of **C-Sty3** indicating higher conductivity and ion diffusion compared to **C-Sty2**. Thus, a comparison of the electrochromic properties of two polymers with the same electroactive groups reveal the significance of hyper-crosslinking in the electrochromic properties of these cross-linked polymers. Furthermore, the EC properties of the hyper-crosslinked donor- $\pi$ -donor derivative, **C-Sty3** was compared to previously reported molecules, demonstrating the importance of highly branched conducting polymers for electrochromic applications.

## 2.2. Introduction

Electrochromic (EC) devices respond to applied voltage through changes in their optical properties such as transmittance, reflectance and absorbance. Novel materials are being developed for electrochromic devices due to their applications in smart windows, anti-glazing mirrors, e-papers, display devices etc.<sup>1-3</sup> Among various classes of materials exhibiting electrochromic properties, organic small molecules possess beneficial features like ease of structural tuning, solution processability, intense coloration and fast switching.<sup>4,5</sup> Despite these advantages, EC device fabrication with small organic molecules suffer from poor film and device quality, which detrimentally affect their overall EC performance.

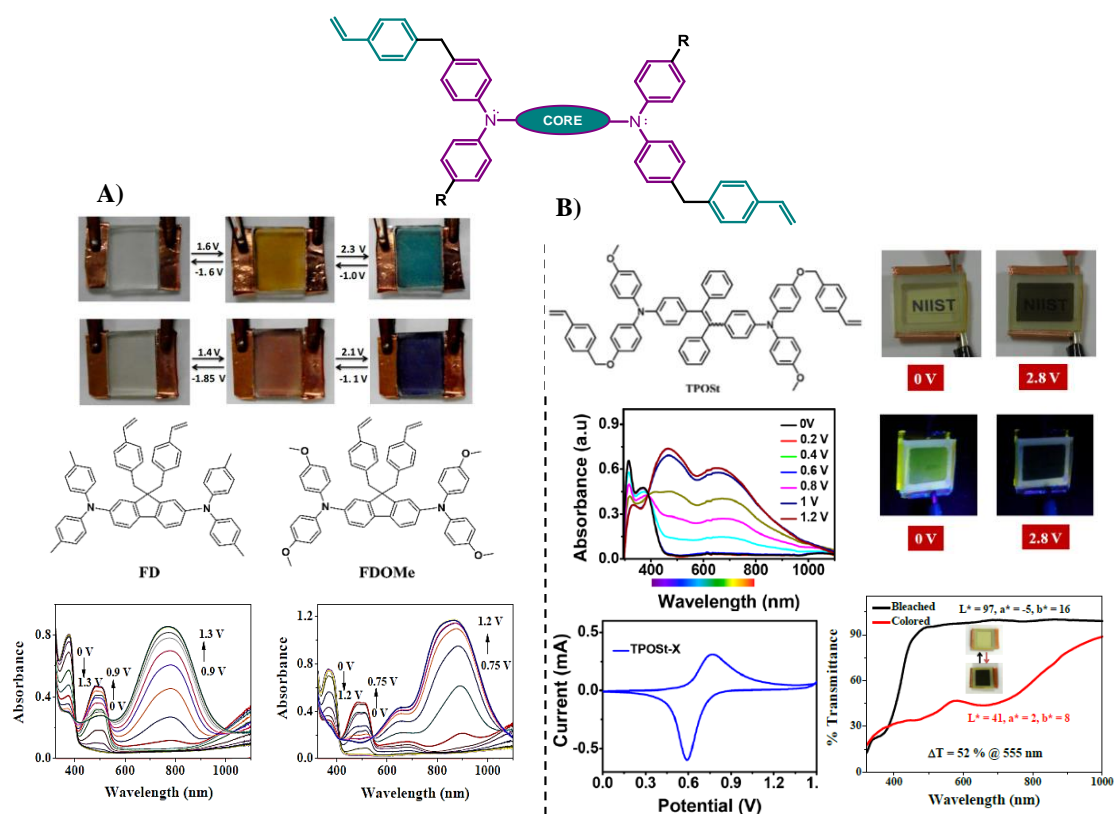


**Figure 2.1.** (A) Donor- $\pi$ -Donor design of organic small molecules and Electrochromic devices of cross-linkable Donor- $\pi$ -Donor type small organic molecules (B and C) reported from our group, utilizing cross-linking strategy for overcoming film and device stability issues. (Adapted from reference 6 and 7)

In the recent past, we and several other groups have utilized the cross-linking strategy with small organic molecules for overcoming film and device stability issues of Electrochromic devices (Figure 2.1A).<sup>6-10</sup> The attachment of cross-linking groups like siloxane, oxetane, benzocyclobutene, benzoxazine, and styrene endows the films of these molecules with excellent solvent resistance. Previously, we demonstrated the multicolour electrochromism of fluorene-diphenylamine derivatives (Figure 2.1B)<sup>6</sup> and transmissive-to-black electrochromic and fluorescent to-dark electrofluorochromic dual behaviours of a tetraphenylethene-diphenylamine derivative (Figure 2.1).<sup>7</sup> All these derivatives were incorporated with two thermally cross-linkable styryl moieties that ensured flawless film formation with excellent color contrast and electrochromic switching stabilities.

Introducing more than two cross-linkable groups in the monomer molecules can result in extensively cross-linked polymers with improved charge transfer and conductivity properties resulting in subsequent enhancement in electrochromic properties such as coloration efficiency, contrast ratios, lifetime and response times. Hyper-crosslinked polymers are reported to have greater ionic and electron conductivity due to their highly branched and microporous structure.<sup>11-13</sup> For example, Fei Wang and group compared the electrochromic properties of linear and star structured poly(3,4-ethylenedioxythiophene-didodecyloxybenzenes) (PEBs) and demonstrated that the star polymer has superior thermal stability, processability, and durability in addition to the electrochromic qualities of its linear parent.<sup>14</sup> Metin Ak and group discovered the superior optoelectronic and electrochromic properties of a star shaped polymer (TCA) due to its more conjugated three-dimensional shape and extremely branched structure in comparison with linear analogues.<sup>15</sup>

Another challenge in EC technology for applications like smart windows, eyewear, display devices, etc. is the development of darker shades from a thin film with a transparent initial state. Several attempts of fine-tuning of the optoelectronic properties of electroactive materials and devices have been reported in the past decade by leading research groups around the globe.<sup>16-18</sup> Reynolds' group have uncovered many elements affecting the electrochromic properties like coloration, switching kinetics and optical contrast in organic electrochromic polymers.<sup>2,19-23</sup> Yanjun Hou *et al.* reported an organic-inorganic hybrid EC material (PDPAP-TEOSPU) which switched from initial colorless state to dark blue, with an optical transmittance change up to 84% and coloration efficiency of  $188 \text{ cm}^2 \text{ C}^{-1}$ .<sup>24</sup> Similarly, conjugated polymer based on cross-linked poly(4-vinyltriphenylamine) and tungsten trioxide, widely used electrochromic polymers like, PANI, PolyProDOT-Me<sub>2</sub>, and polyimides are reported to exhibit transparent to dark switching with high contrast ratio.<sup>25-27</sup> Corrente *et al.* reported new organic mixed valence compounds (MVs), featuring two or three amino redox centres bridged by a dibenzofulvene (DBF) unit.<sup>28</sup> The electro-optical properties of these MVs were fine-tuned through functionalization on the exocyclic fulvene bond of the DBF moiety, allowing all three redox centres to participate in electron transfer processes based on the applied voltage. These MVs were used to fabricate transmissive-to-black switching electrochromic devices with intermediate color switching characteristics. Notably, these devices exhibited absorption across the entire NIR range (800 - 2200 nm) through the excitation of highly charged triphenylamine radical species, leading to intense intervalence charge transfer transitions. The devices demonstrated high optical contrast, fast response times, and excellent switching stability over 10,000 cycles (Figure 2.2A).

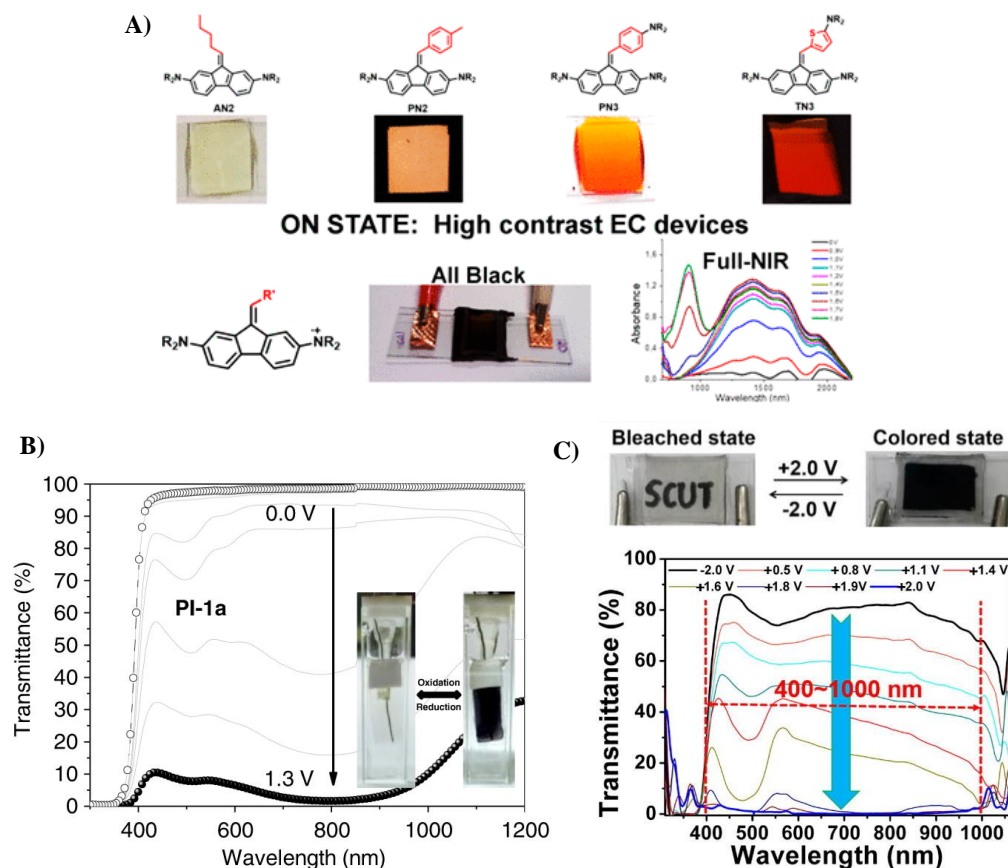


**Figure 2.2.** Examples for electrochromic devices exhibiting transparent to dark switching with high contrast ratio. (A) The electro-optical properties of dibenzofulvene based MV systems with high optical contrast; (B) Colorless-to-colored switching of electrochromic polymer film PI-1a and (C) PVT-PA-Cl and WO<sub>3</sub> color-complementary electrochromic devices. (Adapted from reference 28, 29 and 30)

A facile strategy has been developed by Qiang Zhang *et al.* to create colorless-to-colored switching electrochromic polyimides by incorporating alicyclic non-linear-twisted structures for minimizing the charge transfer complex formation.<sup>29</sup> The resulting electrochromic polymer film (PI-1a) exhibited a high contrast ratio of up to 91.4% from 380 to 780 nm and up to 96.8% at 798 nm. The asymmetric structure of PI-1a film enabled fast electrochemical and electrochromic behaviors, with a switching and bleaching time of 1.3 s and 1.1 s, respectively, attributed to loose chain stacking and enhanced counterion penetration. The colorless-to-black electrochromic

device based on PI-1a demonstrated an overall integrated contrast ratio of up to 80% (Figure 2.2B).

Jinming Zeng and group developed a polymer called Poly(4-vinyltriphenylamine) (PVTPA) and used them to fabricate color-complementary electrochromic devices (ECDs) with ethyl viologen (EV) or tungsten trioxide ( $\text{WO}_3$ ).<sup>30</sup> The ECDs showed reversible color changes between colorless and black, high optical contrast in the visible and near-infrared region, and fast switching times. Among the ECDs, ECD 5, based on PVTPA-Cl and  $\text{WO}_3$  films, exhibited the highest optical contrast in the near-infrared region and shorter switching time (Figure 2.2C).

Wide band-gap, triphenylamine derivatives are a well-studied class of organic EC materials due to their high charge carrier mobilities, low oxidation potentials, reversible redox properties, transparent to visible color-switching with high optical contrast, thermal and electrochemical stability, and tunability of electrochromic properties via easy substitution.<sup>31-33</sup> In our earlier work, we have adopted a donor- $\pi$ -donor design strategy for the design of cross-linkable electrochromic molecules, with two diphenylamine donor groups bridged by a  $\pi$ -core, such as fluorene, and tetraphenylethylene and two styrene moieties that can be cross-linked are attached to the diphenylamine groups.<sup>6,7</sup> The  $\pi$ -core in these derivatives influence the electrochromic properties via differential electronic coupling of the donor units in the neutral and oxidized states. In the current design, we have introduced N-substituted carbazole as the  $\pi$ -core and two and three styrene groups are attached to the diphenylamine and carbazole part, which is shown to have significant role in controlling the EC parameters, both in film and device conditions (Chart 2.1).

Carbazole provides through-bond conjugation enabling efficient coupling of the two donor-units and an easy derivatization route to attach alkyl or other cross-

linkable moieties as pendent groups. Carbazole derivatives are widely used as hole-transporting materials in organic photovoltaics<sup>34-38</sup> and as host and active materials

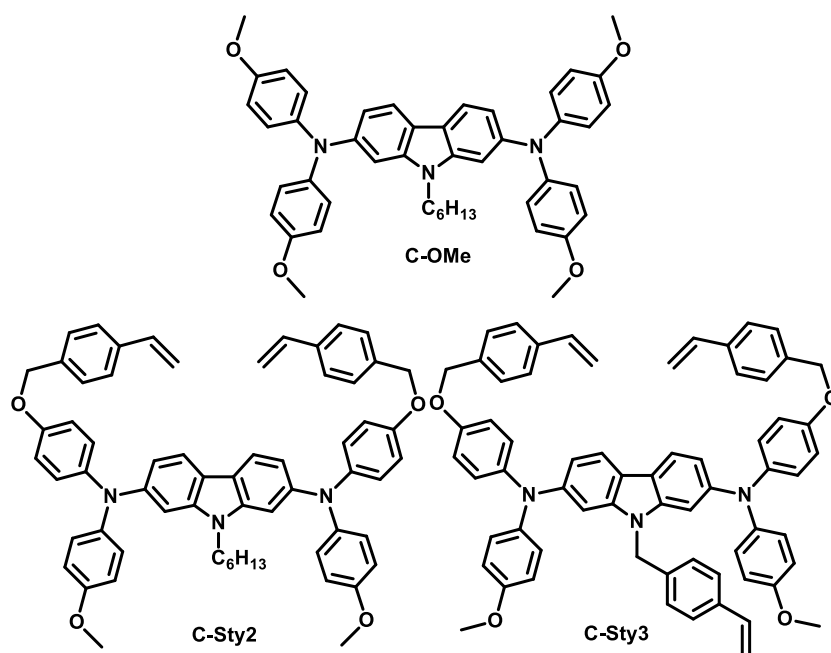
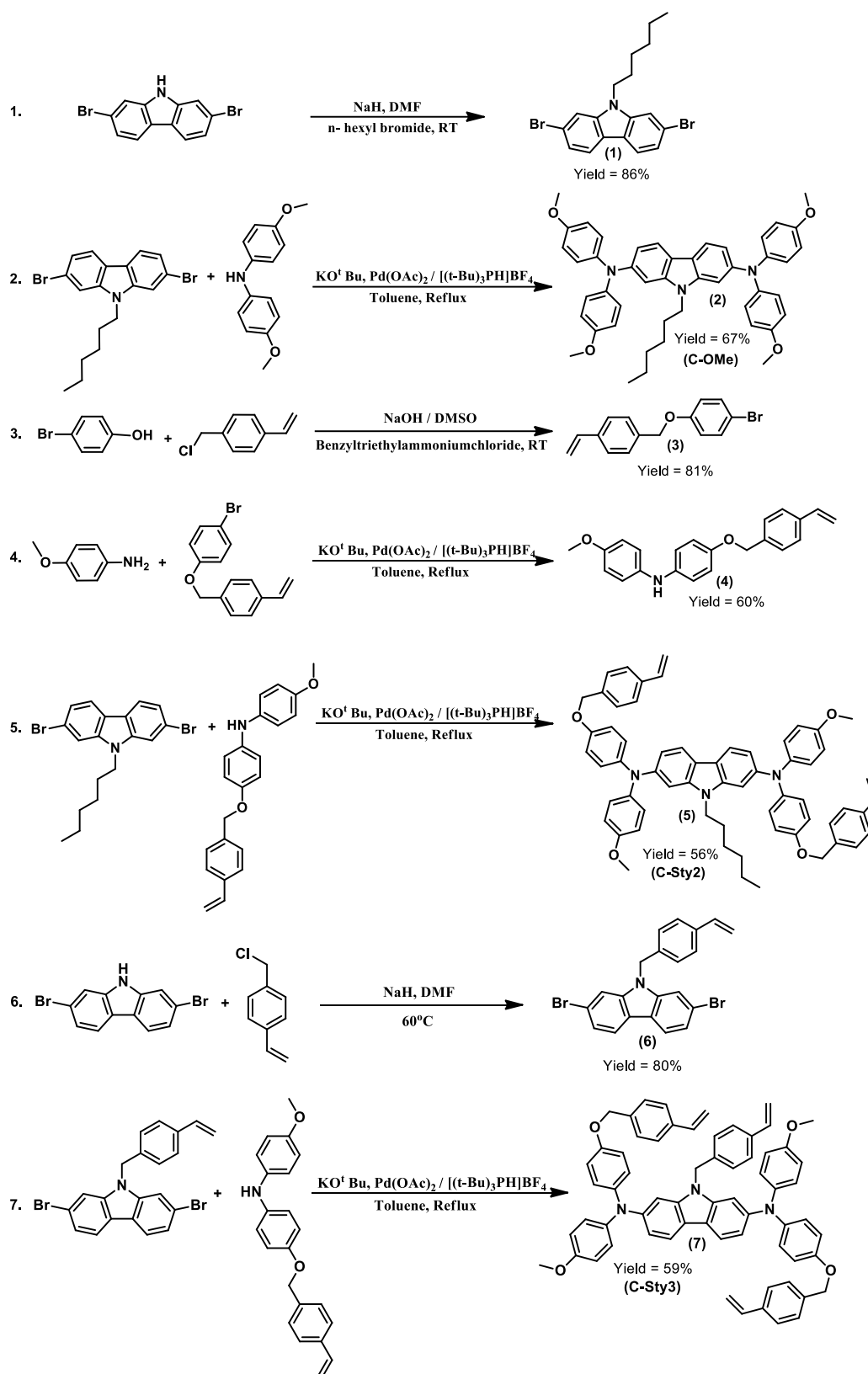


**Chart 2.1.** Molecular structures of **C-OMe**, **C-Sty2**, **C-Sty3**.

in light emitting diode applications.<sup>39-42</sup> Electrochromic polymer materials based on carbazole have been explored in many ways as electroactive films. For example, electrochemically polymerized long poly-carbazole chains,<sup>43-45</sup> copolymers from carbazole and different monomers like thiophene, bithiophene, and 3,4-ethylenedioxythiophene (EDOT),<sup>46,47</sup> small molecules and polymers of carbazole as centre core and side chain have been studied for their electrochromic properties.<sup>48-52</sup> Although, cross-linkable, carbazole-triarylamine derivatives are used as hole transporting materials for Perovskite solar cells,<sup>53</sup> electrochromic applications of these derivatives are not reported. In the present work, we report three carbazole-diphenylamine derivatives (Chart 2.1; **C-OMe**, **C-Sty2**, **C-Sty3**) which were synthesized via palladium-catalysed Buchwald–Hartwig cross-coupling amination reactions (Scheme 2.1) and characterized through <sup>1</sup>H and <sup>13</sup>C NMR, HRMS, FT-IR and CHN elemental analysis (detailed synthesis and characterisation are discussed in

Experimental Section). The optical, electrochemical, and electrochromic properties of these derivatives were thoroughly investigated in solution, film, and device states.



Scheme 2.1. Synthesis of C-OMe, C-Sty2 and C-Sty3.



Among the three derivatives, **C-OMe** has no styrene group attached to it and acts as a model compound for comparing the properties with **C-Sty2** and **C-Sty3**. A comparative analysis of the electrochromic properties of cross-linked **C-Sty2** and hyper-crosslinked **C-Sty3** polymers with the same electroactive groups highlight the significance of hyper-crosslinking in the EC films. **C-Sty3**, with three styryl sub-units, forms rigid and smoother films with reduced roughness, compact surface, better coloration efficiency, optical contrast and, open circuit memory compared to **C-Sty2**.

### **2.3. Results and Discussion**

The carbazole-diphenylamine derivatives were synthesized in good yields by a modified Buchwald-Hartwig coupling reaction as per Scheme 2.1. 9-hexyl-*N*<sup>2</sup>,*N*<sup>2</sup>,*N*<sup>7</sup>,*N*<sup>7</sup>-tetrakis(4-methoxyphenyl)-9*H*-carbazole-2,7-diamine (**C-OMe**) and 9-hexyl-*N*<sup>2</sup>,*N*<sup>7</sup>-bis(4-methoxyphenyl)-*N*<sup>2</sup>,*N*<sup>7</sup>-bis(4-((4-vinylbenzyl)oxy)phenyl)-9*H*-carbazole-2,7-diamine (**C-Sty2**) were synthesised from the reaction between 2,7-Dibromo-9-hexyl-9*H*-carbazole and the corresponding diphenylamine derivatives. *N*<sup>2</sup>,*N*<sup>7</sup>-bis(4-methoxyphenyl)-9-(4-vinylbenzyl)-*N*<sup>2</sup>,*N*<sup>7</sup>-bis(4-((4-vinylbenzyl)oxy)phenyl)-9*H*-carbazole-2,7-diamine (**C-Sty3**) was synthesized from the coupling reaction between 2,7-dibromo-9-(4-vinylbenzyl)-9*H*-carbazole and 4-methoxy-*N*-(4-(4-vinylbenzyloxy)phenyl)aniline. The structures of **C-OMe**, **C-Sty2** and **C-Sty3** were characterized by <sup>1</sup>H and <sup>13</sup>C NMR, HRMS, FT-IR, and CHN-elemental analysis techniques.

The solution state absorption properties of **C-OMe**, **C-Sty2**, and **C-Sty3** were studied in different solvents like DMF, THF, chlorobenzene, and toluene. Absorption spectra of these D-π-D derivatives showed slight negative solvatochromism indicating minor perturbations in the dipole moments during excitation process. For example,

**C-Sty3** showed an absorption maximum of 394 nm in toluene, with a blue shift of 8 nm in more polar DMF. The observed negative solvatochromism could be due to a larger dipole moment and better stabilization of the ground state in polar solvents, which is observed prior in 2,7-donor substituted carbazole derivatives.<sup>54,55</sup> These derivatives showed negligible absorption beyond 450 nm, ensuring complete transparency in the visible range. Further, these derivatives were moderately fluorescent both in solid state and solution with emission maxima in the 410 nm - 425 nm range and 1% - 10% solid state fluorescence quantum yields (Table 2.1 & Figure 2.3).

**Table 2.1.** Absorption and emission properties in different solvents and solid-state quantum yield. \*

Compounds	$\lambda_{\text{abs}}$ , nm ( $\epsilon$ , M <sup>-1</sup> cm <sup>-1</sup> )				$\lambda_{\text{em}}$ , nm				$\Phi_{\text{F}}$ , %
	DMF	THF	CB	Tol	DMF	THF	CB	Tol	
C-OMe	387 (3.2 x 10 <sup>4</sup> )	388 (3.9 x 10 <sup>4</sup> )	390 (3.2 x 10 <sup>4</sup> )	392 (4.3 x 10 <sup>4</sup> )	423	418	416	414	10 ± 0.02
C-Sty2	386 (2.5 x 10 <sup>4</sup> )	388 (3.5 x 10 <sup>4</sup> )	390 (2.6 x 10 <sup>4</sup> )	392 (3.9 x 10 <sup>4</sup> )	424	419	415	413	2.5 ± 0.02
C-Sty3	386 (2.1 x 10 <sup>4</sup> )	390 (3.3 x 10 <sup>4</sup> )	392 (2.4 x 10 <sup>4</sup> )	394 (3.5 x 10 <sup>4</sup> )	425	420	417	415	0.98 ± 0.02

\* CB: Chlorobenzene,  $\Phi_{\text{F}}$ : Fluorescence quantum yield in solid state.

However, their fluorescence was significantly quenched in annealed, amorphous films and devices, due to self-quenching. Solution state cyclic voltammetry and square wave analysis of all the carbazole-diphenylamine derivatives showed two reversible anodic peaks at 0.55 V and 0.8 V corresponding to the formation of polarons and bipolarons, respectively (Figures 2.4A and 2.4B). In general, organic small molecules form poor quality films on glass, ITO and FTO

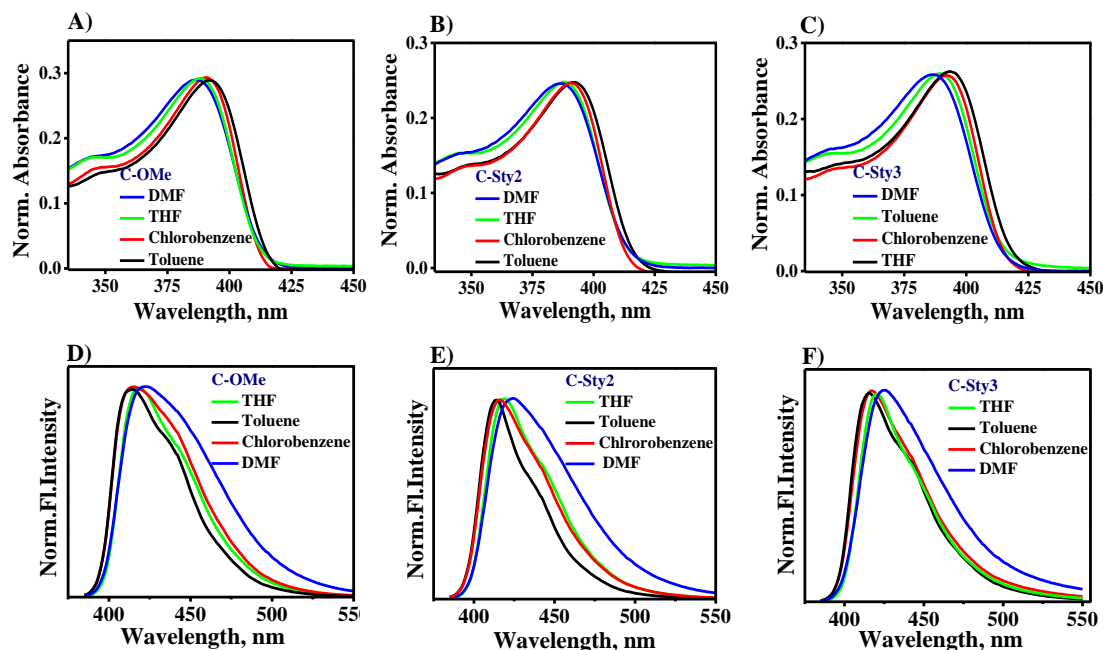


**Figure 2.3.** Normalized absorption spectra of (A) **C-OMe**, (B) **C-Sty2** and (C) **C-Sty3** in DMF, THF, Chlorobenzene and Toluene and Emission spectra of (D) **C-OMe**, (E) **C-Sty2** and (F) **C-Sty3** in DMF, THF, Chlorobenzene and Toluene.

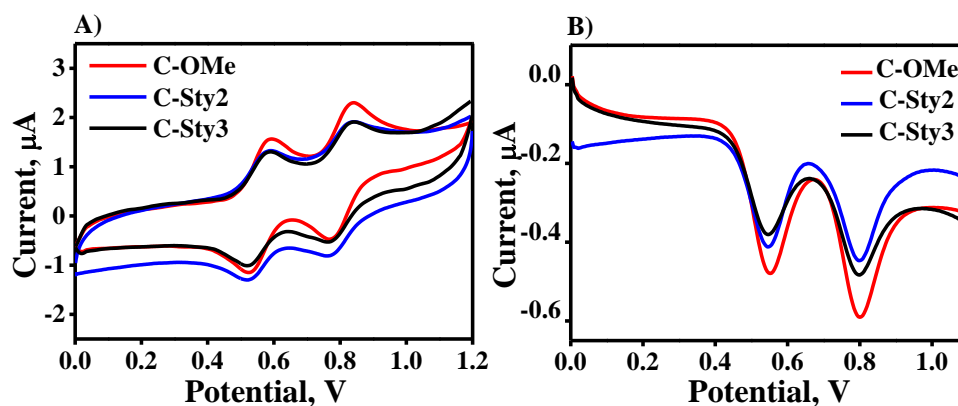


**Figure 2.4.** (A) Cyclic voltammograms of **C-OMe**, **C-Sty2** and **C-Sty3** in Chlorobenzene, supporting electrolyte 0.1 M TBAPF<sub>6</sub>, scan rate 50 mV s<sup>-1</sup> and (B) square wave voltammograms of **C-OMe**, **C-Sty2**, and **C-Sty3** in chlorobenzene, supporting electrolyte 0.1 M TBAPF<sub>6</sub>.

substrates, which are unfavourable for fabrication of efficient electrochromic devices. Thermal cross-linking of small molecules is shown to be an effective strategy to improve film, thermal, electrochemical and long-term operational stabilities of

electrochromic devices. Two/three styrene moieties were introduced in **C-Sty2/C-Sty3** structural design to understand the effect of cross-linkable functionalities in the film formation and electrochromic device properties. The formation of stable, thermally cross-linked films were confirmed via DSC, FT-IR, WAXD, UV-VIS and AFM analyses. Here onwards, the films formed via thermal cross-linking of **C-Sty2** and **C-Sty3** are represented as **C-Sty2x** and **C-Sty3x**, respectively. DSC analysis showed an endothermic melting curve at 141 °C for **C-OMe**, whereas the melting temperature shifted to lower temperatures for the other two derivatives (**C-Sty2**, 94 °C and **C-Sty3**, 109 °C). The cross-linking temperatures were observed after melting transition at 166 °C for **C-Sty2** and 153 °C and 170 °C for **C-Sty3** and was absent for **C-OMe** (Figure 2.5).

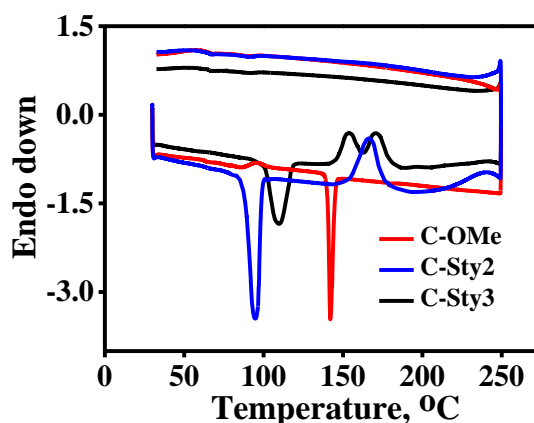


**Figure 2.5.** DSC heating curves of **C-OMe**, **C-Sty2** and **C-Sty3** with a heating rate of 10 °C min<sup>-1</sup> under N<sub>2</sub> atmosphere.

FT-IR spectrum of the compounds before and after thermal cross-linking displayed the absence of peaks attributed to the out-of-plane deformation vibration of the vinyl group present in the monomer. The peaks at 991 cm<sup>-1</sup> and 909 cm<sup>-1</sup> of **C-Sty2** and 989 cm<sup>-1</sup> and 911 cm<sup>-1</sup> of **C-Sty3** were significantly attenuated after polymerisation indicating efficient cross-linking of the films (Figures 2.6A & 2.6B).

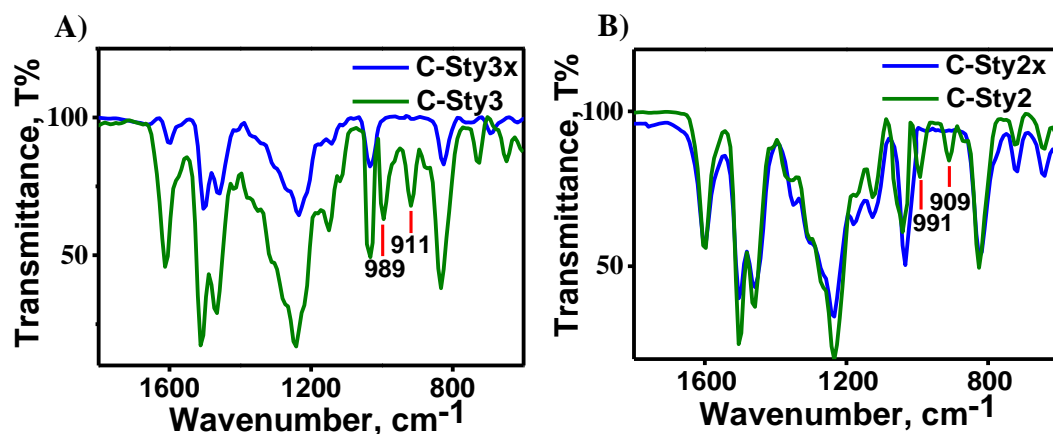


**Figure 2.6.** Normalized FT-IR spectra of (A) C-Sty3 and (B) C-Sty2 before and after cross-linking.

Wide-angle X-ray diffraction (WAXD) studies of C-Sty2 and C-Sty3, before and after thermal cross-linking showed the change from a more crystalline phase to an amorphous phase after thermal annealing (Figures 2.7A & 2.7B).

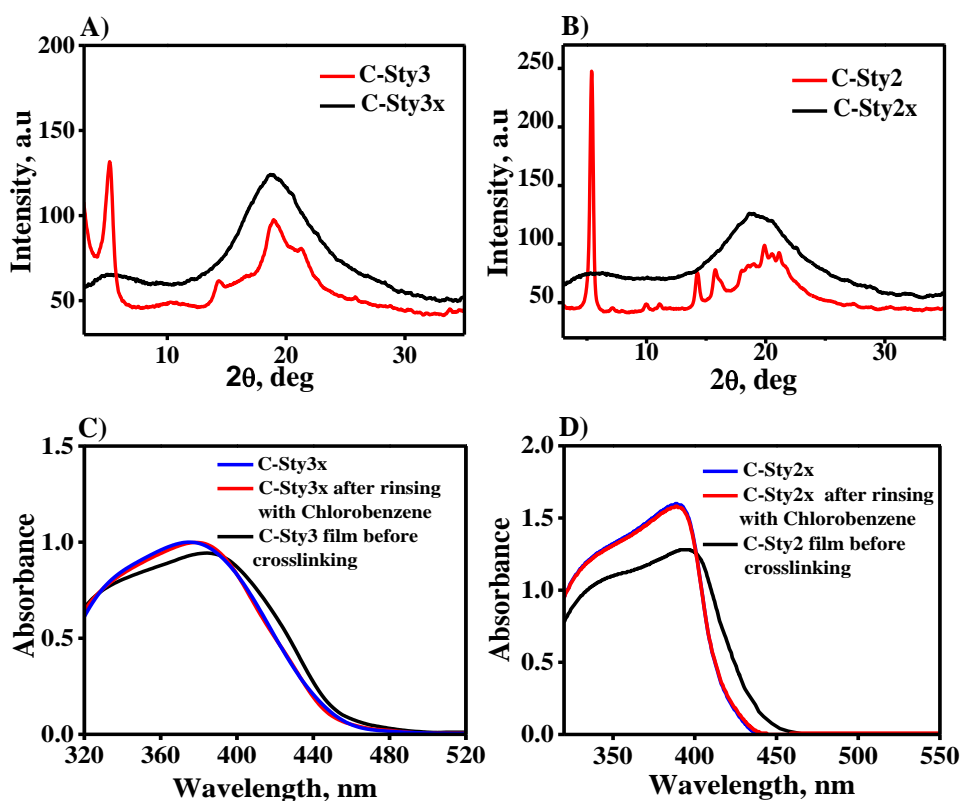


**Figure 2.7.** Wide-angle x-ray diffraction (WAXD) pattern of (A) C-Sty3 and (B) C-Sty2 before and after cross-linking and UV-VIS absorption spectra of (C) C-Sty3 and (D) C-Sty2 before and after cross-linking and after rinsing with chlorobenzene.

The UV-VIS absorption spectra of thin films of **C-Sty2** and **C-Sty3** on quartz substrates with and without thermal annealing above 150 °C showed slight changes in absorbance with apparent hypsochromic shift after cross-linking. These changes indicate the reorganization of the chromophores in the amorphous state, leading to better surface coverage after cross-linking.<sup>7</sup> The absorption spectra of cross-linked films before and after washing with chlorobenzene showed negligible changes in absorbance indicating high solvent resistance of the cross-linked films (Figures 2.7C & 2.7D). On the other hand, non-crosslinked films of all derivatives are readily dissolved in most organic solvents.

CV and square wave analysis of cross-linked films on FTO displayed two reversible peaks with half-wave potentials at 0.5 V and 0.76 V for **C-Sty2x** and 0.56 V and 0.8 V for **C-Sty3x**, which are attributed to successive one electron oxidations of the two diphenylamine units leading to mono- and di-cationic, oxidized states. The cyclic voltammograms and square wave voltammograms of the films are shown in Figure 2.8.

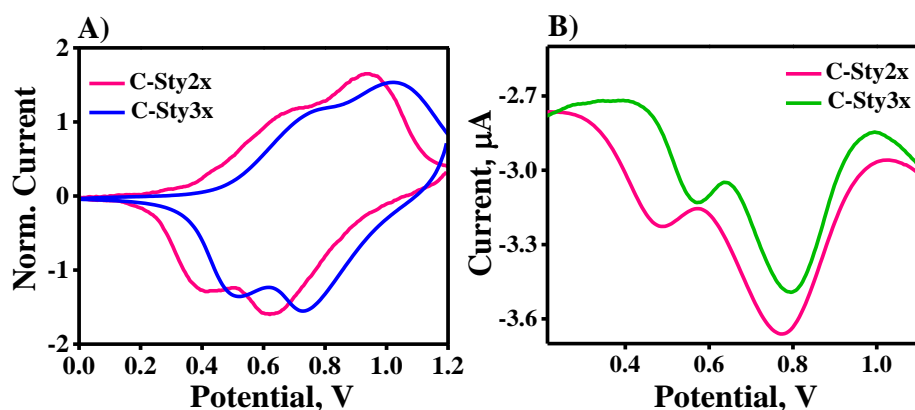


**Figure 2.8.** (A) Cyclic voltammograms of **C-Sty2x** and **C-Sty3x** films on FTO in 0.1 M TBAPF<sub>6</sub>/acetonitrile, scan rate 50 mV s<sup>-1</sup> and (B) Square wave voltammograms of **C-Sty2x** and **C-Sty3x** films on FTO substrate.

Electrochemical stability of the cross-linked films were determined by performing continuous 500 switching cycles in 0.1 M TBAPF<sub>6</sub>/acetonitrile and both

the films demonstrated very good switching stability with negligible changes at 20 s pulse width with a transmittance loss of 3% for **C-Sty2x** and 1% for **C-Sty3x** at 890 nm and 850 nm, respectively, indicating the material's stability towards voltage switching (Figure 2.9). Both materials showed switching stability comparable with the reported triphenylamine-based electrochromic materials prepared by electropolymerization and thermal annealing methods.<sup>56,57</sup>

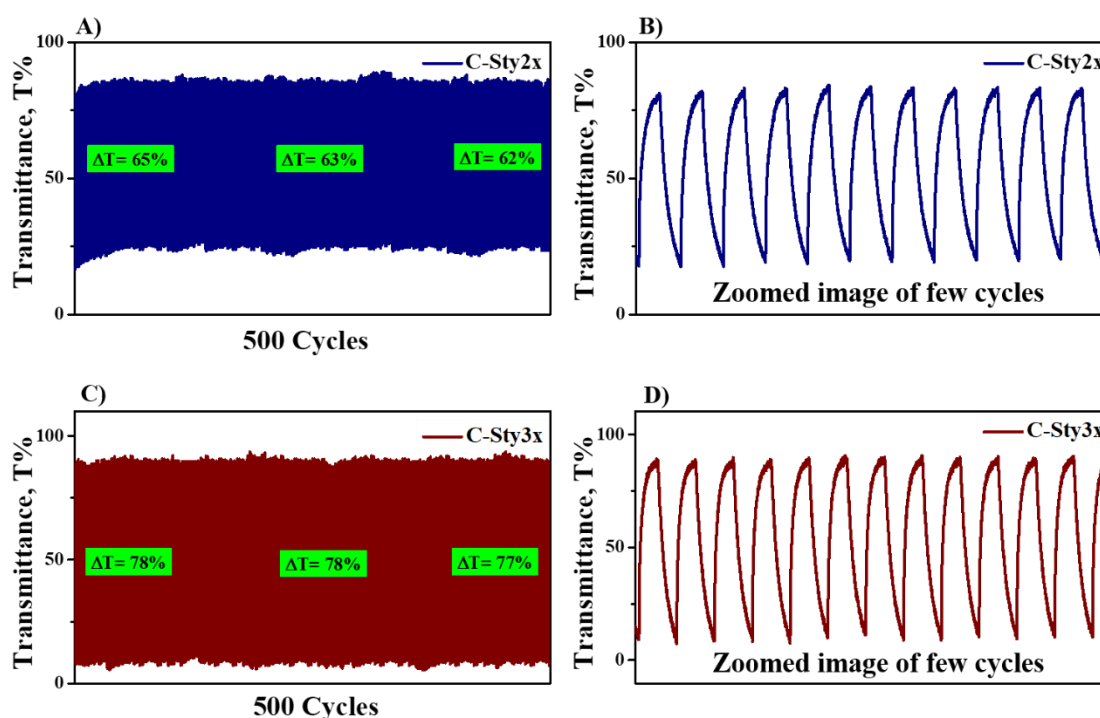


**Figure 2.9.** Switching analyses of (A) **C-Sty2x** and (D) **C-Sty3x** at 890 nm and 850 nm, respectively, at 20 s pulse width for 500 cycles and zoomed images of few cycles of (B) **C-Sty2x** and (C) **C-Sty3x** switching analyses.

Film morphology plays an important role in modifying the electrochromic properties of the polymer. The surface morphology changes upon thermal cross-linking were further probed by AFM analysis (Figure 2.10), which showed better surface alignment upon cross-linking with an apparent reduction in surface roughness values. For example, for **C-Sty2/C-Sty2x**, arithmetic roughness average of the surface, Ra changed from 2.76 nm to 1.97 nm and root mean square surface

roughness,  $R_q$  changed from 3.4 nm to 2.51 nm while for **C-Sty3/C-Sty3x**,  $R_a$  changed from 0.357 nm to 0.141 nm and  $R_q$  changed from 0.449 nm to 0.172 nm. **C-Sty3** after polymerisation formed cross-linked films with lower roughness and thickness than **C-Sty2**. Both the films exhibited rigid and regular morphology with **C-Sty3x** having clear grains and a compact surface when compared to **C-Sty2x** (Figures 2.10C and 2.10F).

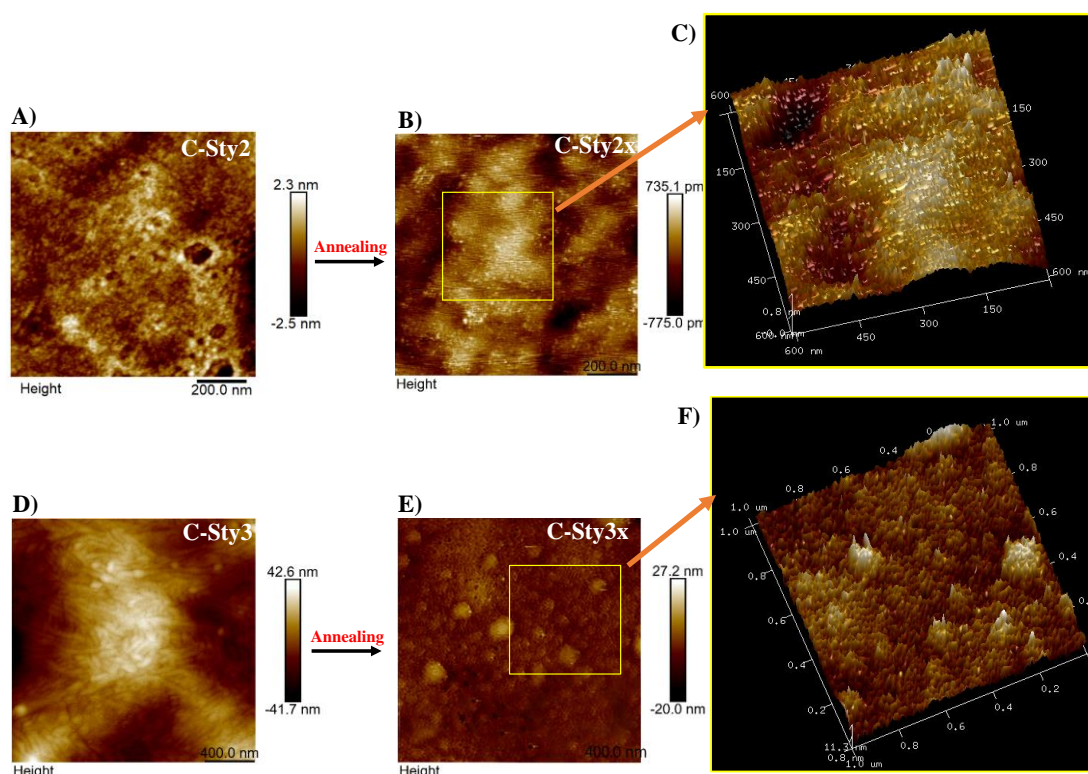


**Figure 2.10.** AFM images of (A) **C-Sty2** and (D) **C-Sty3** before cross-linking; (B) **C-Sty2x** and (E) **C-Sty3x** after cross-linking and zoomed and 3D images of (C) **C-Sty2x** and (F) **C-Sty3x**.

Thermal stability of these derivatives were probed via thermogravimetric analysis (TGA) and the decomposition temperature ( $T_d$ ) at 5% weight loss under nitrogen were found to be 380 °C, 410 °C and 427 °C for **C-OMe**, **C-Sty2** and **C-Sty3**, respectively (Figure 2.11). Both the cross-linkable derivatives, **C-Sty2** and **C-Sty3** displayed good thermal stability without much weight loss up to 400 °C. The film state



photoluminescence (PL) spectra of **C-Sty2** and **C-Sty3**, before and after thermal cross-linking, exhibited complete quenching of the fluorescence after cross-linking, due to enhanced aggregation induced quenching in the amorphous, cross-linked polymer (Figure 2.12).

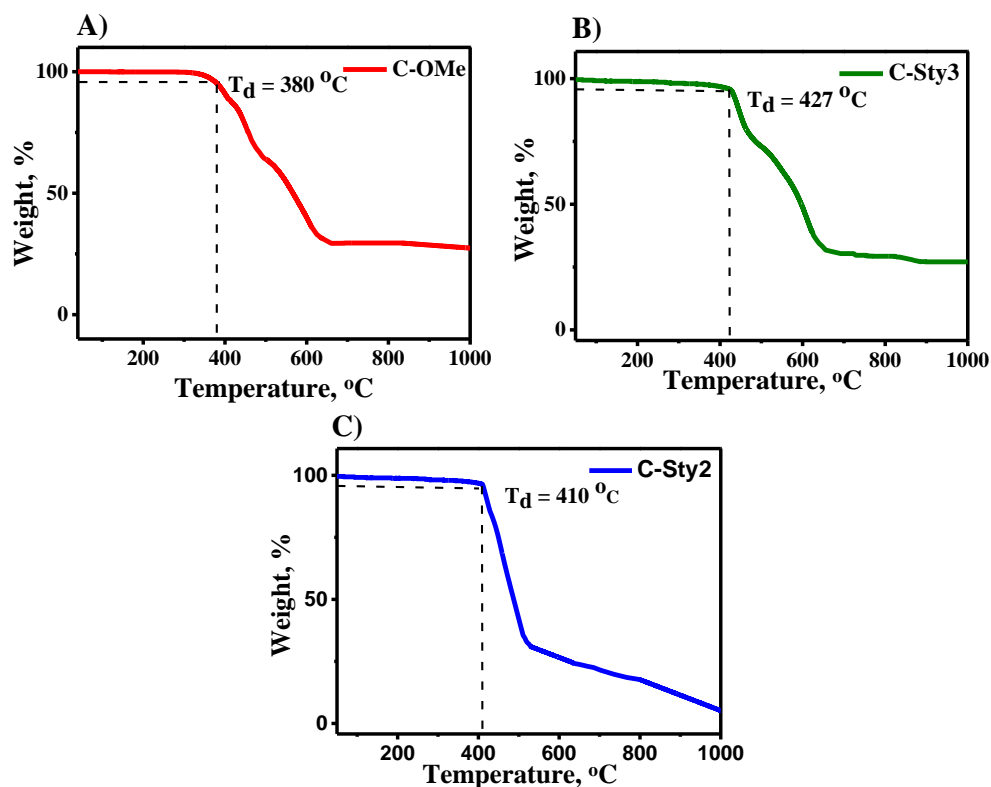


**Figure 2.11.** TGA heating curves of (A) **C-OMe**, (B) **C-Sty3** and (C) **C-Sty2**.

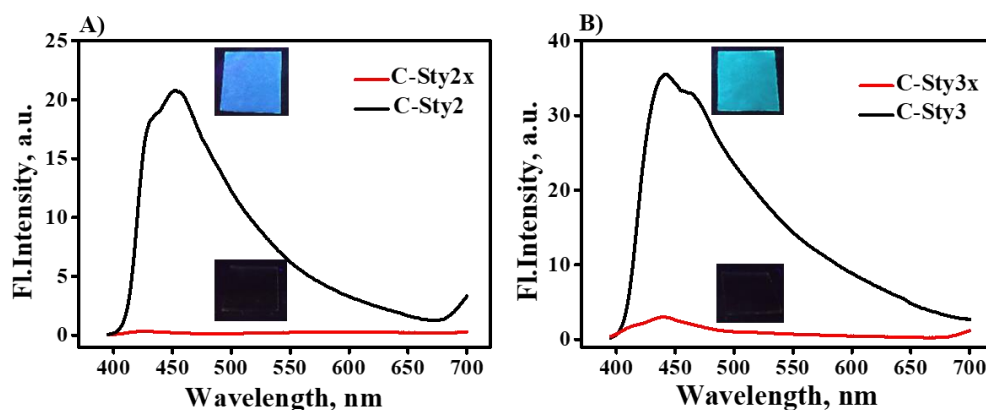


**Figure 2.12.** Fluorescence spectra of (A) **C-Sty2** and (B) **C-Sty3** before and after cross-linking.

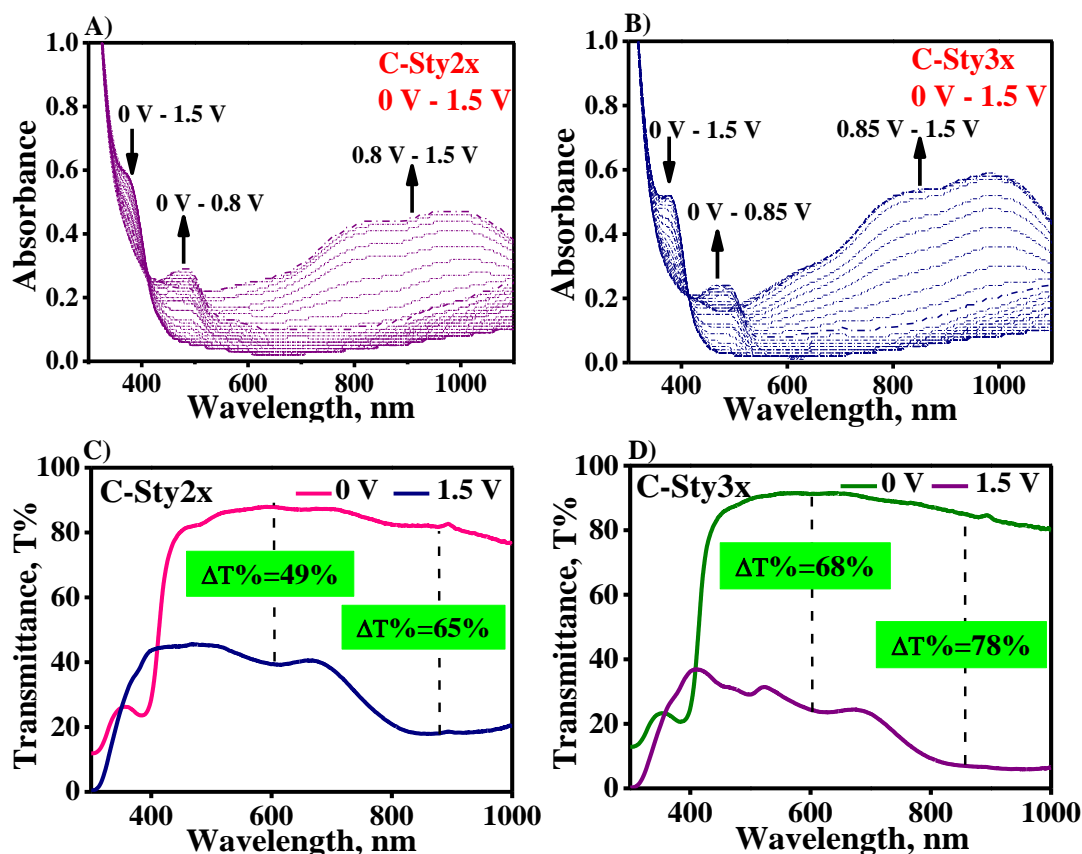


**Figure 2.13.** Spectroelectrochemical responses of (A) **C-Sty2x** and (B) **C-Sty3x** films on FTO (thickness of the films used are  $150 \pm 10$  nm and  $130 \pm 10$  nm for **C-Sty2x** and **C-Sty3x**, respectively); Transmittance spectra of (C) **C-Sty2x** and (D) **C-Sty3x** films at colored (1.5 V) and bleached state (0 V) (the thickness of the **C-Sty2x** and **C-Sty3x** films used for transmittance study are  $245 \pm 10$  nm and  $230 \pm 10$  nm, respectively).

The spectroelectrochemical responses of the films on FTO substrates were studied by applying different potentials from 0 V to 1.5 V (Figures 2.13A & 2.13B). **C-Sty2x** and **C-Sty3x** showed similar absorption changes against the applied potentials. For **C-Sty2x**, the initial neutral state has an absorption maximum of around 372 nm, the absorbance of which gradually decreases with an increase in the applied potential from 0 V to 1.5 V. During 0 V - 0.8 V, absorption around 483 nm and a long wavelength absorption band above 1000 nm developed, which correspond to the mono-cation formation and the film color changed from a transmissive colorless to a transparent

light-yellow state. From 0.8 V to 1.5 V, broad absorption covering from 600 nm to 1100 nm with two peaks around 830 nm and 987 nm were formed, and the color of the film changed from yellow to dark blue (Figure 2.13A). Similarly, the neutral state of **C-Sty3x** displayed an absorbance maximum around 375 nm, which gradually decreased upon applying voltage from 0 V to 0.85 V, with concomitant formation of new absorptions around 477 nm and above 1000 nm. Further increase in voltage from 0.85 V to 1.5 V, resulting in a broad absorption peak in the visible-NIR range with absorbance maxima around 830 nm and 987 nm. The color of the **C-Sty3x** film has varied due to differences in absorbance in a similar manner as **C-Sty2x**, with a significantly deeper blue during the second oxidation (Figure 2.13B). The transmittance changes of the films in coloured (1.5 V) and bleached state (0 V) showed a contrast difference ( $\Delta T\%$ ) of 65% at 890 nm for **C-Sty2x** and 78% at 850 nm for **C-Sty3x** films on FTO substrates (Figures 2.13C & 2.13D).

The coloration efficiency of the films were calculated using the equation 2.1 for coloration efficiency ( $\eta$ ),

$$\eta = \frac{\Delta OD}{Qd} = \log [Tb/Tc]/Qd \quad \text{Equation 2.1}$$

where Tb and Tc are the transmittance of the films in the bleached and coloured states at a particular wavelength, respectively and Qd is the amount of charge transferred per unit area. Coloration efficiency was determined to be 162 cm<sup>2</sup>/C for **C-Sty2x** at 890 nm, and 248 cm<sup>2</sup>/C for **C-Sty3x** at 850 nm. The double-potential-step chronoamperometry of the films were conducted in order to find out the charge (area under the curve) and are shown in Figure 2.14.

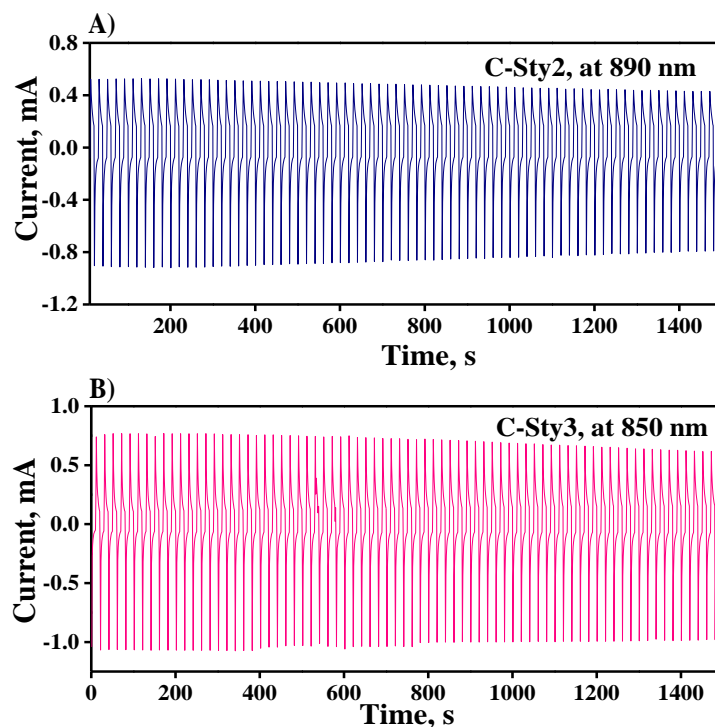


**Figure 2.14.** Chronoamperometry plot of (A) **C-Sty2x** ( $Q_d = 4.36 \times 10^{-3} \text{ C.cm}^{-2}$ ) and (B) **C-Sty3x** ( $Q_d = 4.04 \times 10^{-3} \text{ C.cm}^{-2}$ ) films.

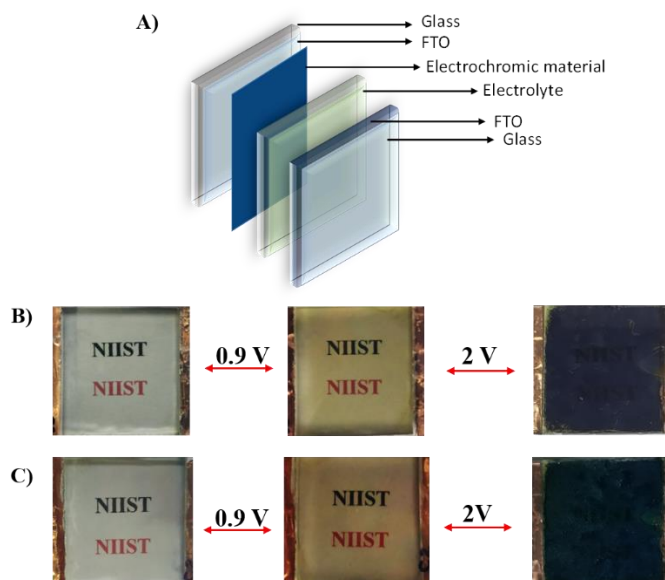


**Figure 2.15.** (A) Device architecture and Images of the devices (B) **C-Sty2** and (C) **C-Sty3** at applied potentials of 0, 0.9, and 2 V.

Despite of having a thinner film than **C-Sty2x** (film thickness =  $245 \pm 10 \text{ nm}$ ), **C-Sty3x** (film thickness =  $230 \pm 10 \text{ nm}$ ) produced high contrast of transmittance changes

with the highest degree of coloration efficiency at 850 nm, demonstrating the impact of charge transfer in different kind of cross-linked films. Electrochromic devices were fabricated by following the architecture, FTO/Electrolyte/EC layer/FTO as shown in Figure 2.15A. Materials were spin-coated on electrodes, thermally cross-linked and then used as the electrochromic layer. The thickness of the **C-Sty2x** and **C-Sty3x** films used for the device fabrication were  $245 \pm 10$  nm and  $230 \pm 10$  nm, respectively. Figures 2.15B & 2.15C show the photographs of the devices at 0 V, 0.9 V, and 2 V and the corresponding transmittance spectra demonstrated a change in transmittance of 61% for **C-Sty2x** device and 70% for **C-Sty3x** device at 890 nm and 850 nm, respectively (Figures 2.16A & 2.16B).

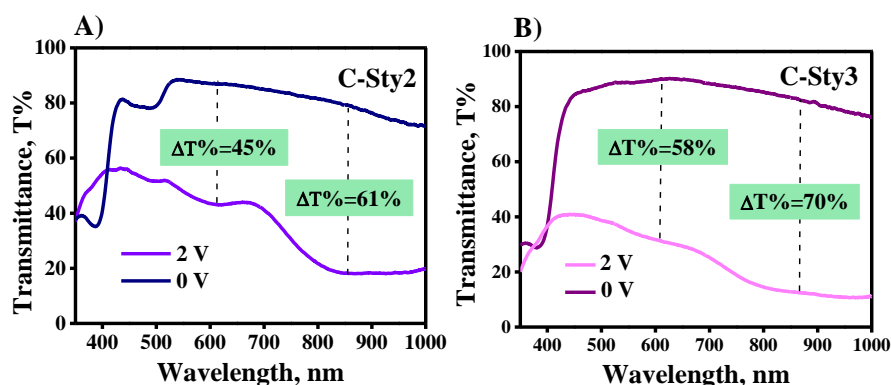


**Figure 2.16.** Transmittance spectra of (A) **C-Sty2x** and (B) **C-Sty3x** devices in coloured and bleached state.

The color of the devices changed from transparent (0 V) to transmissive yellow (0.9 V) to dark blue (2 V) in both cases with  $L^*a^*b^*$  values for the colors under different applied voltages as follows. **C-Sty2x** device showed  $L^*$ : 86.74,  $a^*$ : -1.46,  $b^*$ : 9.07 at 0 V;  $L^*$ : 86.95,  $a^*$ : -6.14,  $b^*$ : 20.6 at 0.9 V and  $L^*$ : 42.73,  $a^*$ : -7.6,  $b^*$ : -11.97 at 2 V whereas, **C-Sty3x** device showed  $L^*$ : 86.36,  $a^*$ : -1.23,  $b^*$ : 9.1,  $L^*$ : 86.68,  $a^*$ : -6.02,  $b^*$ : 20.78 and  $L^*$ : 38.03,  $a^*$ : -8.9,  $b^*$ : -15.20 at 0 V, 0.9 V and 2 V, respectively. The spectroelectrochemical response of the **C-Sty2x** and **C-Sty3x** devices to various

applied potentials showed similar changes as that of the corresponding FTO films (Figures 2.17A & 2.17B).

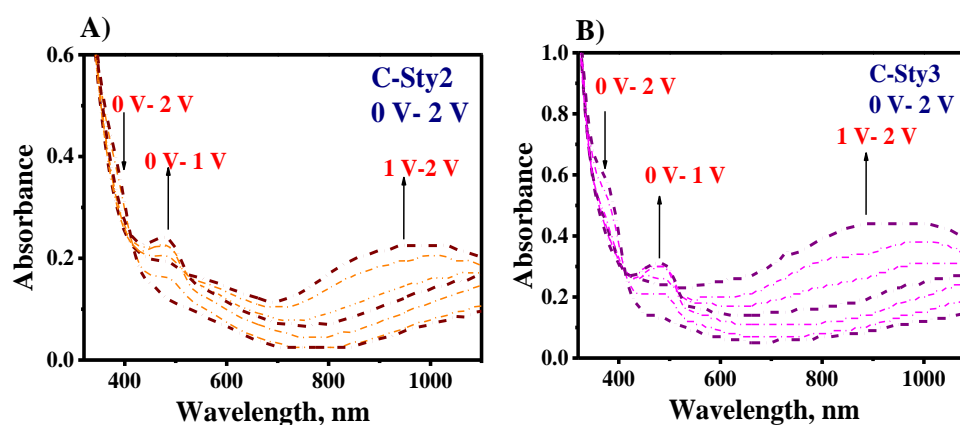


**Figure 2.17.** Spectroelectrochemical response of (A) C-Sty2x and (B) C-Sty3x devices.

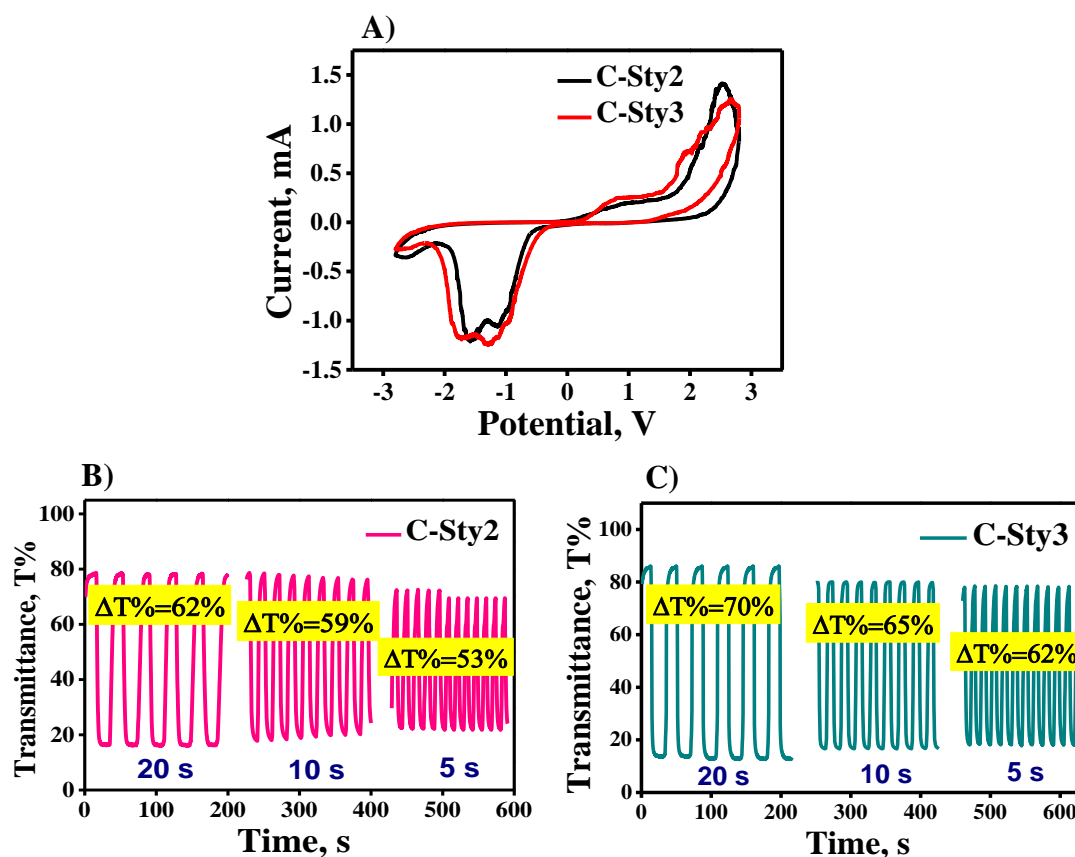


**Figure 2.18.** (A) CV analyses of C-Sty2x and C-Sty3x devices at a scan rate of  $50 \text{ mVs}^{-1}$  and Transmittance spectra of (B) C-Sty2 and (C) C-Sty3 devices at 890 nm and 850 nm, respectively with the pulse widths of 20, 10, 5 s.

The cyclic voltammetry analysis of the devices exhibited two peaks around 0.9 V and 2 V corresponding to the mono-cation and di-cation formation (Figure 2.18A). The multiple cyclic switching of the devices revealed the stability and switching time through the transmittance measurements with respect to time at different pulse widths. The transmittance changes ( $\% \Delta T$ ) at 20 s, 10 s, and 5 s pulse width at 890 nm (**C-Sty2x** device) and 850 nm (**C-Sty3x** device) showed minor loss in transmittance. For example, the **C-Sty2x** device exhibited a transmittance loss of 3% from 20 s to 10 s and 6% from 10 s to 5 s pulse width change (Figure 2.18B) and for **C-Sty3x** device, 5% and 3% reductions were observed for 20 s to 10 s and 10 s to 5 s change in pulse width, respectively (Figure 2.18C).

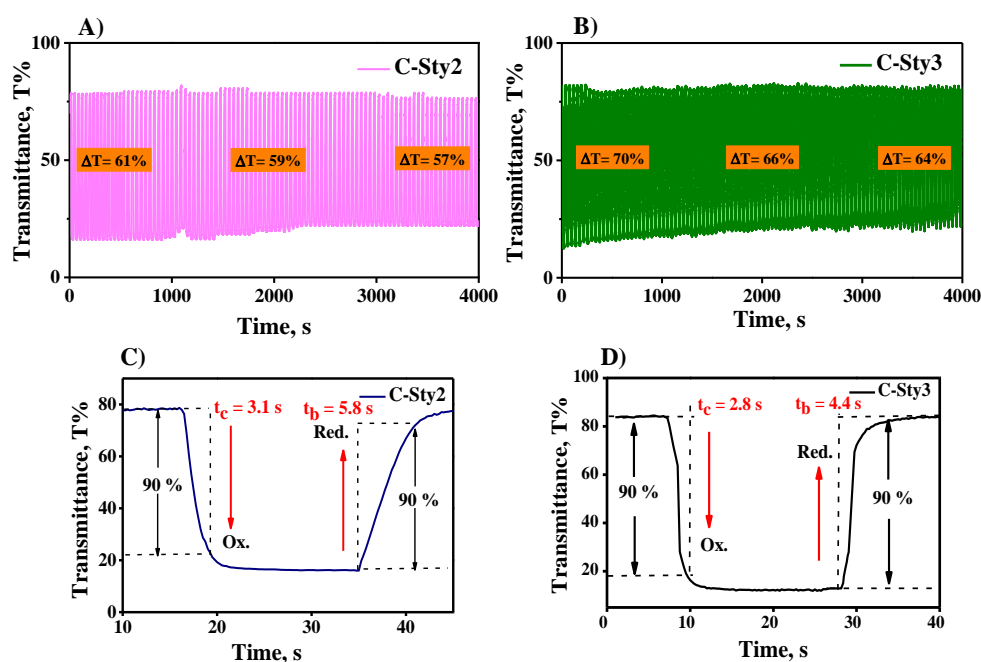


**Figure 2.19.** Switching analyses of (A) **C-Sty2x** at 890 nm and (B) **C-Sty3x** at 850 nm devices at 20 s pulse width for 100 cycles and electrochromic switching time of (C) **C-Sty2** and (D) **C-Sty3** devices at 890 nm and 850 nm, respectively.

**C-Sty2x** and **C-Sty3x** devices showed reasonably good stability and reversibility over 100 cycles at a switching pulse width of 20 s (Figures 2.19A & 2.19B). Both **C-Sty2x** and **C-Sty3x** devices demonstrated a transmittance loss of 6% and 4% after 100

cycles at 890 nm and 850 nm, respectively. The coloration and bleaching time required for the **C-Sty2x** device at 890 nm were found to be 3.1 s and 5.8 s (Figure 2.19C), and that of **C-Sty3x** device at 850 nm were 2.8 s and 4.4 s, respectively (Figure 2.19D). Further, the open-circuit memory of the devices were studied by monitoring the transmittance change of the oxidized state of both **C-Sty2x** and **C-Sty3x** devices at 890 nm and 850 nm, respectively for over 2 hours and 20 minutes. The **C-Sty2x** and **C-Sty3x** devices retained 75% and 90% of the initial color even after many hours under open-circuit conditions, respectively (Figures 2.20A & 2.20B).

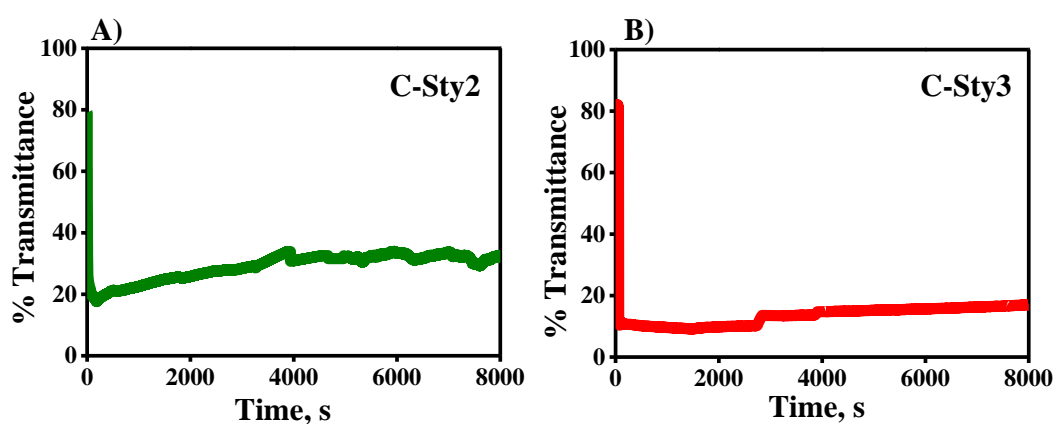


**Figure 2.20.** Open circuit memory of devices: (A) **C-Sty2** at 890 nm and (B) **C-Sty3** at 850 nm.

A comparison of the spectroelectrochemical and device properties of **C-Sty2x** and **C-Sty3x** showed that **C-Sty3x**, with three cross-linkable styrene units form smoother films with rigid and compact surface and exhibited better thermal stability, darker color in the oxidized state, higher coloration efficiency and open circuit memory. Electrochemical impedance spectroscopy (EIS) can be employed to evaluate the electrical conductivity and ion transport of the crosslinked films. The Nyquist plots obtained via EIS analysis show the impedance spectra for **C-Sty2x** and **C-Sty3x** measured in conventional three electrode configuration in the frequency range of 100



kHz to 10 MHz. The experimental and model-based Nyquist plots and equivalent circuit fitted are shown in Figure 2.21.

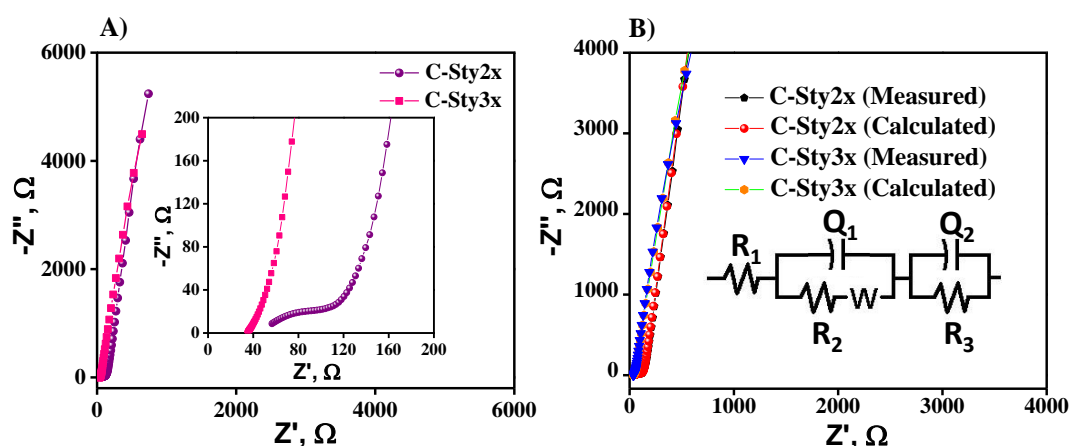


**Figure 2.21.** (A) Nyquist plots of **C-Sty2x** and **C-Sty3x** films on FTO in 0.1 M TBAPF<sub>6</sub>/acetonitrile measured in a frequency range of 100 kHz to 10 MHz and (B) The experimental and model-based Nyquist plots and the equivalent circuit obtained from EC-Lab Software (active surface area of the film is 5 cm<sup>2</sup>).

The impedance spectra can be divided into two regions: a semicircle arc in the high-frequency zone and a straight line in the low-frequency region. The equivalent series resistance (ESR), or  $R_s$ , is given by the intercept on the real axis in the high frequency range and consists of the inherent resistances of the electroactive material, the bulk resistance of the electrolyte, and the contact resistance at the electrode/electrolyte interface. Second, the diameter of a semicircle in the high-frequency range can be used to determine the charge transfer resistance ( $R_{ct}$ ), which results from electron diffusion. Third, the slope of the EIS curve in the low-frequency region can be used to represent Warburg resistance ( $W$ ), which represents the diffusion of redox species in the electrolyte.<sup>58,59</sup> The **C-Sty2x** and **C-Sty3x** circuit model obtained after the fitting of Nyquist plots using the EC-Lab Software is  $R_1 + Q_1 / (R_2 + W) + Q_2 / R_3$ , where  $Q_1$  and  $Q_2$  are the constant phase element (CPE) representing capacitance of the electrochemical double layer,  $R_1$  is the solution

resistance and  $R_2$  is the charge transfer resistance.<sup>60-62</sup> The high frequency part gives the  $R_s$  values of 44.02  $\Omega$  and 34.55  $\Omega$  by **C-Sty2x** and **C-Sty3x**, respectively and the fitted  $R_{ct}$  values for **C-Sty2x** and **C-Sty3x** are 101.7  $\Omega$  and 62.99  $\Omega$ , respectively. The absence of a prominent semi-circle arc in the high frequency area and low charge transfer resistance indicate fast charge transfer at the film-electrolyte interface, implying improved conductivity of **C-Sty3x**.<sup>63</sup>

Further comparison of device properties of the carbazole-diphenylamine derivatives with previously reported D- $\pi$ -D derivatives with fluorene<sup>6</sup> and tetraphenylethylene<sup>7</sup>  $\pi$ -cores revealed that the  $\pi$ -core and nature of crosslinking has significant influence on the EC device properties. For example, derivatives with cross-linkable fluorene core (**FDOMe-X**)<sup>6</sup> showed transparent to dark blue coloration upon oxidation, while **TPOSt-X** with tetraphenylethylene core<sup>7</sup> exhibited a transparent to dark grey electrochromism along with significant electrofluorochromism from a highly fluorescent neutral state to dark oxidized state. Compared to these derivatives, **C-Sty2x** and **C-Sty3x** showed significantly different coloration properties with a transparent to dark blue electrochromic change upon oxidation with significant absorption spanning the visible range (Figure 2.22). Compared to all other derivatives, hyper-crosslinked **C-Sty3x** showed better coloration efficiency and optical contrast with a significantly lower switching response time for coloration and bleaching. Thus, the D- $\pi$ -D design strategy with multiple cross-linking units and different  $\pi$ -cores provide a series of organic EC materials with tuneable properties (Table 2.2).

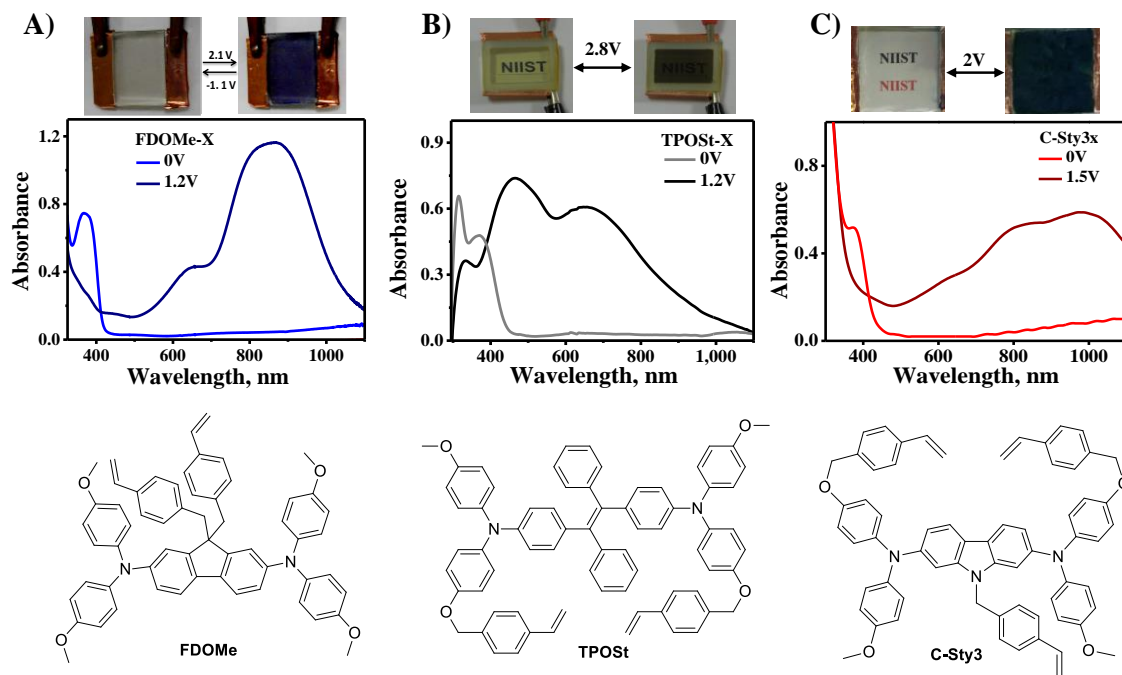


**Figure 2.22.** Device photographs, spectroelectrochemical response and molecular structure of (A) FDOMe, (B) TPOSt and (C) C-Sty3.

**Table 2.2.** Comparison of electrochromic properties

Compounds	Coloration efficiency (Film), cm <sup>2</sup> /C	$\Delta T\%$ (device), Film thickness	Color coordinates (device)	Response times (device), Seconds	
				C	B
FD	117 (at 760nm)	61% at 760nm, 60 -70 nm		5.8	2.3
FDOMe	179 (at 760nm)	58% at 910 nm, 60 -70 nm		10.4	3.2
TPOSt		52 % at 555 nm 155±5 nm	L* = 97, a* = -5, b* = 16 (neutral) L* = 41, a* = 2, b* = 8 (coloured)	4.2	8.1
C-Sty2	162 (at 890nm)	61% at 890nm, 245±10 nm	L*: 86.74, a*: -1.46, b*: 9.07 (neutral) L*: 42.73, a*: -7.6, b*: -11.97 (coloured)	3.1	5.8
C-Sty3	<b>248 (at 850nm)</b>	<b>70%</b> at 850nm, 230±10 nm	L*: 86.36, a*: -1.23, b*: 9.1 (neutral) L*: 38.03, a*: -8.9, b*: -15.20 (coloured)	<b>2.8</b>	<b>4.4</b>

## 2.4. Conclusions

In conclusion, we have developed and discussed the electrochromic properties of two donor- $\pi$ -donor type carbazole-diphenylamine derivatives, **C-Sty2**, and **C-Sty3** incorporated with two and three styryl units, respectively, and compared the cross-linking effect on electrochromic properties. The cross-linking properties were examined thoroughly with different techniques like FT-IR, DSC, AFM, WAXD, etc. The CV and spectroelectrochemical studies of **C-Sty2x** and **C-Sty3x** film and device revealed mono- and di-cation formation with color change from a colorless, transparent initial state to a transmissive yellow and then to dark blue. The maximum color contrast obtained from the transmittance plot is 62% at 890 nm for the **C-Sty2x** device and 70% at 850 nm for the **C-Sty3x** device. The devices exhibited good switching stability with low switching voltages, relatively low switching time and excellent open circuit memory. In contrast to **C-Sty2**, **C-Sty3** with three styryl subunits forms films that are rigid, smooth and compact surface with reduced thickness, regular morphology and clear grains. The **C-Sty3x** performed better in terms of coloration efficiency, optical contrast, and open circuit memory. The EIS studies showed fast charge transfer at the **C-Sty3** film-electrolyte interface than **C-Sty2** films with  $R_{ct}$  values of 62.99  $\Omega$  and 101.7  $\Omega$ , respectively, corroborating the enhanced EC properties of **C-Sty3** film-based devices. The electrochromic performances of **C-Sty3** polymer were compared to previously reported D- $\pi$ -D systems with fluorene and tetraphenylethylene as  $\pi$ -cores and two cross-linkable styrene moieties, demonstrating the strategy to aid a new material design for obtaining electrochromic materials with higher coloration efficiency, contrast and optical memory. Thus, the derivatives with their easy synthesis, solution processability, extensive cross-linked and stable film formation having increased solvent resistance, good coloration efficiency, and optical contrast and open circuit memory give the potential for these materials to turn out to be suitable for electrochromic applications.

## **2.5. Experimental Section**

### **2.5.1. Materials and Methods**

All chemicals and solvents were purchased from Sigma-Aldrich, TCI-India Pvt. Ltd., Merck, Spectrochem Pvt. Ltd. and used as received. FTO substrate with surface resistivity of  $8\Omega/\text{sq}$  was purchased from Sigma-Aldrich and cleaned by ultrasonication with water, acetone, and isopropyl alcohol for 15 minutes each. Moisture and oxygen-sensitive reactions were carried out under an argon atmosphere in dry solvents.  $^1\text{H}$  and  $^{13}\text{C}$  nuclear magnetic resonance (NMR) spectra were recorded at 300K on a DPX 500 MHz spectrometer with tetramethylsilane as the internal standard. ESI-HRMS spectra were recorded from a JEOL JSM 600. Infrared spectra were recorded in the solid-state (KBr) using Shimadzu IR Prestige- 21 Fourier Transform Infrared Spectrophotometer. The solution state absorbance measurements were done on a Shimadzu UV-Vis spectrophotometer (UV-2600) and the film state absorbance and transmittance measurements were done using an Ocean Optics UV-VIS modular spectrometer (DH-2000-BAL). The fluorescence quantum yield of the powder samples was calculated using a calibrated integrating sphere in the SPEX Fluorolog spectrofluorometer. The absolute quantum yield was determined on the basis of de Mello method. DSC analyses were done using TA instruments DSC Q2000 model with intra cooler facility. Thermogravimetric analyses (TGA) were performed on a Shimadzu, DTG-60 instrument under a nitrogen atmosphere at a heating rate of  $10\text{ }^\circ\text{C}/\text{minute}$ . WAXD analysis was done using XEUSS SAXS/WAXS system by Xenocs, using Ni-filtered Cu  $K\alpha$  radiation ( $\lambda=0.15405\text{ nm}$ ) and 1D pattern was generated from the 2D images using Fit2D software. The thickness of the samples was measured using the Dektak XT profilometer. AFM images of the films before and after annealing were recorded using an AFM-Bruker Multitop Nanoscope V

instrument operating under tapping mode and the roughness of the films were found out using Nanoscope Analysis 1.5 software. Cyclic Voltammetry (CV, BASI CV-50W) for liquid state samples were performed under argon atmosphere using 0.1 M tetrabutylammonium hexafluorophosphate (TBAPF<sub>6</sub>) in acetonitrile as supporting electrolyte, glassy carbon as working electrode, Ag/AgCl electrode as reference electrode and platinum wire as counter electrode with a scan rate of 50 mV/s. Cyclic voltammetry of the films and devices were performed on PARSTAT 4000A Potentiostat. Spectroelectrochemistry of electrochromic devices and films were recorded on Ocean Optics Spectrometer DH-2000-BAL using a PARSTAT 4000A Potentiostat for the electrochemical redox process. Spectroelectrochemical responses of the films were done by dipping the cross-linked films in 0.1 M TBAPF<sub>6</sub> in dry acetonitrile solution using Ag/AgCl electrode and Pt wire as reference electrode and counter electrode, respectively. The blank was done using bare FTO in 0.1 M TBAPF<sub>6</sub> in dry acetonitrile solution in a cuvette having 1 cm path length. The  $L^*a^*b^*$  values for the colours under different applied voltages were found out using a HunterLab - UltraScan VIS Spectrophotometer, 110 V/220 V w/SAV & UV control, and EasyMatch QC version 4.0 software. The EIS was measured in the frequency range of 100 kHz to 10 MHz. An electrochemical cell of three-electrode system using Ag/AgCl as reference electrode, Pt wire as counter electrode and films coated on FTO substrates as working electrode in a 0.1 M TBAPF<sub>6</sub>/Acetonitrile electrolyte were used. The measurements were conducted in a CHI660E series electrochemical workstation.

### 2.5.2. Electrolyte Preparation

The electrolyte used for the electrochromic devices were prepared by adding 20 wt% LiClO<sub>4</sub> and 30 wt% of propylene carbonate to the measured amount of PMMA

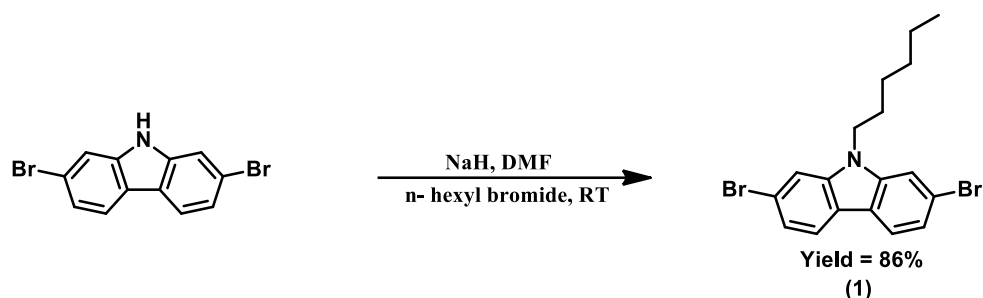
( $M_w = 120000$ ) in THF (2 g PMMA + 0.2 g  $\text{LiClO}_4$  + 300  $\mu\text{L}$  propylene carbonate in 20 mL THF) and the was stirred at 80 °C till complete dissolution, followed by stirring at room temperature overnight. PMMA and  $\text{LiClO}_4$  were dried under vacuum for 12 h at 90 °C and 110 °C, respectively before use. The mixture was poured into a clean petri dish and the solvent was allowed to evaporate at room temperature. The required amount of electrolyte film was peeled off from the petri dish and used.

### **2.5.3. Electrochromic Device Fabrication**

The electrochromic devices were fabricated using FTO-coated glass substrates as the working electrodes and followed the architecture Glass/FTO/electrolyte/EC layer/FTO/Glass. After cleaning the electrodes (2.5 cm  $\times$  2.5 cm FTO-coated glass slide) by sonicating with water, acetone, and isopropyl alcohol for 15 minutes each, the electrodes were annealed at 500 °C followed by UV-ozone treatment. Solutions of **C-Sty2** or **C-Sty3** (150 mg/ml) in chlorobenzene were spin-coated at 1500 rpm for 30 seconds. The spin-coated transparent thin films were then kept for polymerization in a glovebox by annealing at respective temperatures for 30 minutes. The prepared solid electrolyte was sandwiched between the cross-linked film and counter FTO electrode. To prevent the diffusion of oxygen and moisture into the fabricated device, commercial epoxy is used for sealing the edges of the devices. Copper tape was applied to both sides of the bare FTO for efficient and uniform electrical contact while connecting to the potentiostat.

## 2.5.4. Synthesis and Characterization of the Molecules

### 2.5.4a. Synthesis of 2, 7-Dibromo-9-hexyl-carbazole (1)



**Scheme 2.2.**

2, 7 - Dibromo-9*H*-carbazole (1 g, 3.07 mmol) and NaH (1.02 g, 4.23 mmol) were transferred to a 100 ml two neck flask and subjected to three vacuum/nitrogen refill cycles in order to remove water and oxygen. Anhydrous DMF was added (50 mL) followed by 1-bromohexane (0.67 g, 3.9 mmol) and the mixture was stirred for 4 h at 130 °C. The reaction mixture was diluted with water and extracted with ethyl acetate. Then the combined organic layer was dried over sodium sulphate and the solvent was evaporated and dried under reduced pressure. Column chromatography on Si-gel (SiO<sub>2</sub>, Hexane/ EtOAc, 8:2) gave Compound **1** as white solid (Yield = 86%).

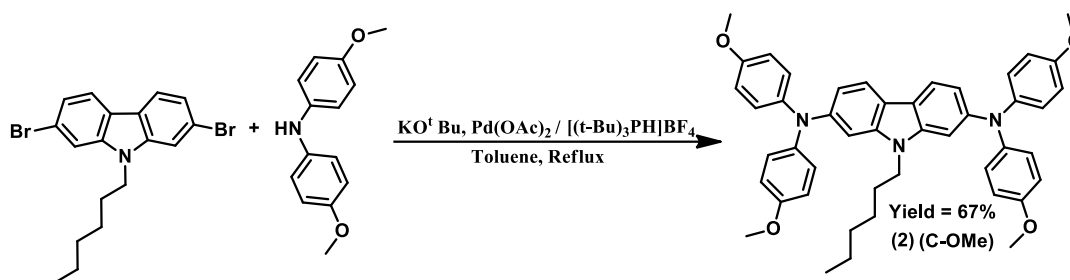
**<sup>1</sup>H NMR** (CD<sub>3</sub>CN, 500 MHz):  $\delta$  = 8.01 (d, 2H, *J* = 8.5 Hz), 7.74 (s, 2H), 7.36 (d, 2H, *J* = 8.5 Hz), 4.28 (t, 2H, *J* = 7.5 Hz), 1.79 (t, 2H, *J* = 7 Hz), 1.29 (m, 6H), 0.85 (t, 3H, *J* = 7.5 Hz).

**<sup>13</sup>C NMR** (125 MHz, Acetone-d<sub>6</sub>):  $\delta$  = 141.57, 122.34, 121.80, 121.28, 119.35, 112.37, 42.81, 31.37, 26.42, 22.35, 13.35.

**ESI-HRMS:** *m/z* calculated for (C<sub>18</sub>H<sub>19</sub>Br<sub>2</sub>N): 409.1582, *m/z* found: 409.3215.

### 2.5.4b. Synthesis of 9-hexyl-*N*<sup>2</sup>, *N*<sup>2</sup>,*N*<sup>7</sup>,*N*<sup>7</sup>-tetrakis(4-methoxyphenyl)-9*H*-carbazole-2,7-diamine (2) (C-OMe)





Scheme 2.3.

*N*-Hexyl-2,7-dibromocarbazole (**1**) (1.5 g, 3.66 mmol), bis (4-methoxy phenyl) amine (2.5 g, 10.98 mmol), potassium tert-butoxide (1.23 g, 10.98 mmol), Pd(OAc)<sub>2</sub> (0.16 g, 0.732 mmol), and ((*t*-Bu)<sub>3</sub>PH)BF<sub>4</sub> (0.42 g, 1.464 mmol) were transferred to a 250 ml three neck flask and was subjected to three vacuum/Argon refill cycles in order to remove water and oxygen. Anhydrous toluene was added (60 mL), and the mixture was stirred for 12 h at 110 °C or until the reaction was complete by TLC analysis. The product was collected by extraction with addition of ethylacetate and DI-water, followed by a brine solution. The toluene/ethylacetate layer was dried with anhydrous sodium sulphate, filtered, concentrated and dried under reduced pressure. The collected crude solids were purified by column chromatography. (hexane/EtOAc, 9:1) to give a pale-yellow solid (Yield = 67%).

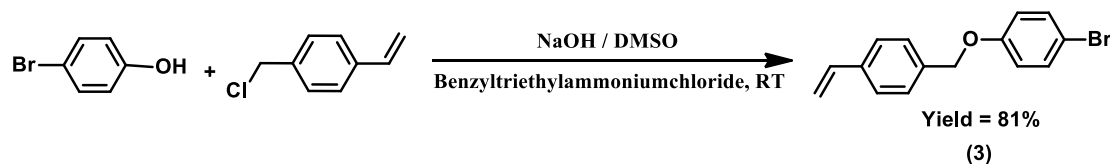
<sup>1</sup>H NMR (500 MHz, Acetone-d<sub>6</sub>): δ = 7.784 (d, 2H, *J* = 8.5 Hz), 6.98 (d, 9H, *J* = 8.5 Hz), 6.88 (d, 8H, *J* = 9 Hz), 6.7-6.65 (m, 3H), 3.97 (t, 2H, *J* = 7 Hz), 3.78 (s, 12H), 1.6 (t, 2H, *J* = 6.58 Hz), 1.15 (m, 6H), 0.81 (t, 3H, *J* = 7 Hz).

<sup>13</sup>C NMR (125 MHz, Acetone-d<sub>6</sub>): δ = 155.67, 146.63, 141.93, 141.84, 125.71, 119.75, 117.74, 114.77, 117.57, 102.28, 54.81, 42.05, 31.26, 26.45, 22.23, 13.35.

**ESI-HRMS:** *m/z* calculated for C<sub>46</sub>H<sub>47</sub>N<sub>3</sub>O<sub>4</sub>: 705.3567, *m/z* found: 705.3458.

**CHN Analysis:** Calculated CHN (%) for C<sub>46</sub>H<sub>47</sub>N<sub>3</sub>O<sub>4</sub>: C, 78.27; H, 6.71; N, 5.93, Found: C, 78.14; H, 6.54; N, 5.74.

## 2.5.4c. Synthesis of 1-bromo-4-(4-vinylbenzyloxy)benzene (3)



Scheme 2.4.

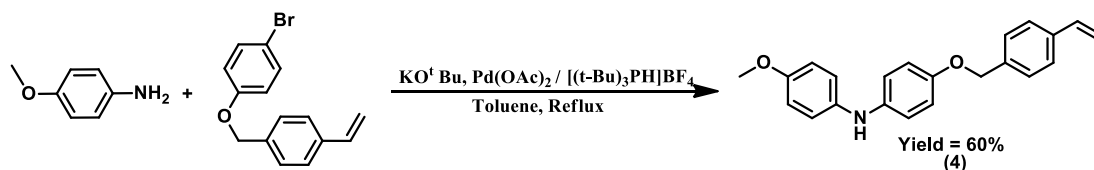
4-bromophenol (3 g, 17.3 mmol) in dimethyl sulfoxide (DMSO, 50 ml) was degassed with nitrogen for 30 min, and then benzyltriethylammoniumchloride (0.39 g, 1.73 mmol) and aqueous NaOH (50 wt%, 34.6 mmol) were added. After the reaction mixture turned red, 4-vinylbenzyl chloride (3.96 g, 25.95 mmol, 3.65 ml) was added. The mixture was stirred for 12 h at room temperature. The product was collected by extraction with addition of DCM and DI-water, followed by a brine solution. The combined organic layers were dried over anhydrous sodium sulphate, filtered, and dried under vacuum. Further purification of the residue by column chromatography over silica gel (8% ethylacetate-hexane) yielded compound 2 as white solid (Yield = 81%).

<sup>1</sup>H NMR (500 MHz, Acetone-d<sub>6</sub>):  $\delta$  = 7.46 (dd,  $J$  = 8 Hz, 2H), 7.42 (m, 4H), 6.84 (m, 2H), 6.71 (m, 1H), 5.7 (d,  $J$  = 17.5 Hz, 1H), 5.23 (d,  $J$  = 11 Hz, 1H), 5.13 (s, 2H).

<sup>13</sup>C NMR (125 MHz, Acetone-d<sub>6</sub>)  $\delta$  = 158.17, 136.55, 136.70, 132.20, 127.84, 126.26, 116.98, 113.52, 112.39, 69.57.

ESI-HRMS:  $m/z$  calculated: 288.0150,  $m/z$  Found: 288.2905.

## 2.5.4d. Synthesis of 4-methoxy-N-(4-(4-vinylbenzyloxy)phenyl)aniline (4)



Scheme 2.5.

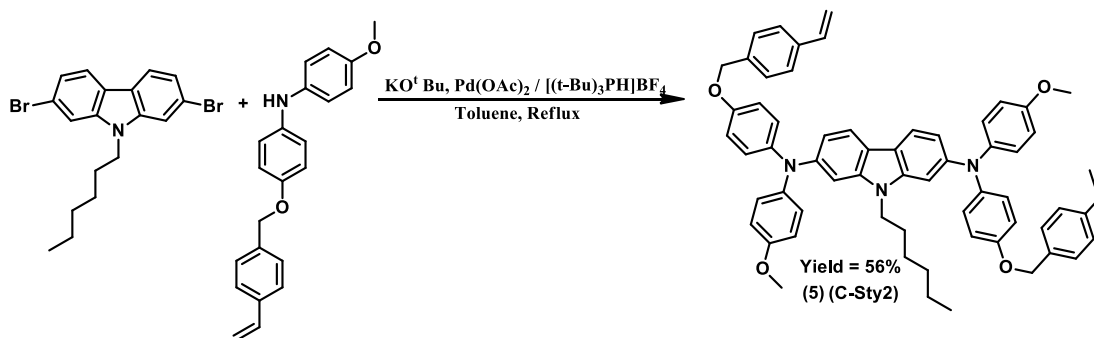
In a 100 ml three neck flask, 1-bromo-4-(4-vinylbenzyloxy)benzene (3 g, 10.41 mmol), p-anisidine (1.92 g, 15.62 mmol), KO<sup>t</sup>Bu (2.4 g, 20.83 mmol), Pd(OAc)<sub>2</sub> (0.24 g, 1.04 mmol) and ((*t*-Bu)<sub>3</sub>PH)BF<sub>4</sub> (0.9 g, 3.12 mmol) were added and was subjected to three vacuum/Argon refill cycles in order to remove water and oxygen. Anhydrous toluene was added (60 mL), and the mixture was stirred for 24 h at 110 °C or until the reaction was complete by TLC. After cooling to room temperature, the solution was poured into water and extracted with dichloromethane. The combined organic layers were dried over anhydrous sodium sulphate, filtered, and dried under vacuum. The residue was purified by column chromatography on neutral alumina (15% Ethyl acetate - hexane) to yield white solid (yield = 60%).

<sup>1</sup>H NMR (500 MHz, Acetone-d<sub>6</sub>): δ = 7.46 (dd, *J* = 16.5 Hz, 4H), 6.99 (m, 4H), 6.91 (m, 2H), 6.83 (m, 2H), 6.81 (s, 1H), 5.8 (d, *J* = 17.5 Hz, 1H), 5.27 (d, *J* = 11 Hz, 1H), 5.06 (s, 2H), 3.75 (s, 3H).

<sup>13</sup>C NMR (125 MHz, Acetone-d<sub>6</sub>) δ = 153.94, 152.77, 138.9, 138.84, 138.17, 137.66, 137.06, 136.64, 127.72, 126.18, 118.93, 118.88, 118.35, 118.31, 115.69, 114.47, 113.29, 69.76, 54.83.

ESI-HRMS: *m/z* calculated for C<sub>22</sub>H<sub>21</sub>NO<sub>2</sub>: 331.1572, *m/z* Found: 332.1656.

#### 2.5.4e. Synthesis of 9-hexyl-N<sup>2</sup>,N<sup>7</sup>-bis(4-methoxyphenyl)-N<sup>2</sup>,N<sup>7</sup>-bis(4-(4vinylbenzyl)oxy)phenyl)-9H-carbazole-2,7diamine (5) (C-Sty2)



Scheme 2.6.

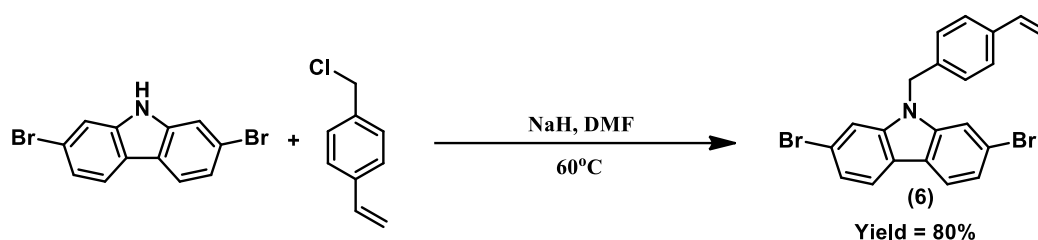
N-Hexyl-2,7-dibromocarbazole (0.4 g, 0.9776 mmol), 4-methoxy-N-(4-((4-vinylbenzyl)oxy)phenyl)aniline (0.8 g, 2.44 mmol), potassium tert-butoxide (0.27 g, 2.44 mmol), Pd(OAc)<sub>2</sub> (0.04 g, 0.1955 mmol), and (t-Bu)<sub>3</sub>PHBF<sub>4</sub> (0.12 g, 0.391 mmol) were transferred to a 100 mL three neck round bottom flask. The flask was subjected to three vacuum/Argon refill cycles in order to remove water and oxygen. Anhydrous toluene was added (30 mL), and the mixture was stirred for 12 h at 110 °C or until the reaction was complete by TLC analysis. The product was collected by extraction with addition of ethylacetate and DI-water, followed by a brine solution. The toluene-ethylacetate layer was dried with anhydrous sodium sulphate, filtered, and concentrated. The collected crude solids were purified by column chromatography (hexane: ethylacetate, 9:1) to give a pale-yellow solid (Yield: 56%).

**<sup>1</sup>H NMR** (500 MHz, Acetone-d<sub>6</sub>): δ = 7.82 (d, 2H, *J* = 8.5 Hz), 7.5 (m, 8H), 7.05 (m, 8H), 6.97 (d, *J* = 9 Hz, 6H), 6.88 (d, *J* = 9 Hz, 4H), 6.8 (m, 4H), 5.84 (d, *J* = 18 Hz, 2H), 5.15 (d, *J* = 11 Hz, 2H), 5.1 (s, 4H), 3.99 (m, 2H), 3.79 (s, 6H), 1.62 (t, *J* = 6.58 Hz, 2H), 1.192 (m, 6H), 0.795 (3H, t, *J* = 7 Hz).

**<sup>13</sup>C NMR** (125 MHz, Acetone-d<sub>6</sub>): δ = 155.73, 154.66, 146.56, 142.14, 141.94, 141.75, 137.30, 137.18, 136.62, 127.79, 126.22, 125.85, 125.51, 119.81, 117.79, 115.58, 114.86, 114.59, 113.40, 102.38.

**ESI-HRMS:** *m/z* calculated for C<sub>62</sub>H<sub>59</sub>N<sub>3</sub>O<sub>4</sub>: 909.4506, *m/z* found: 909.4384.

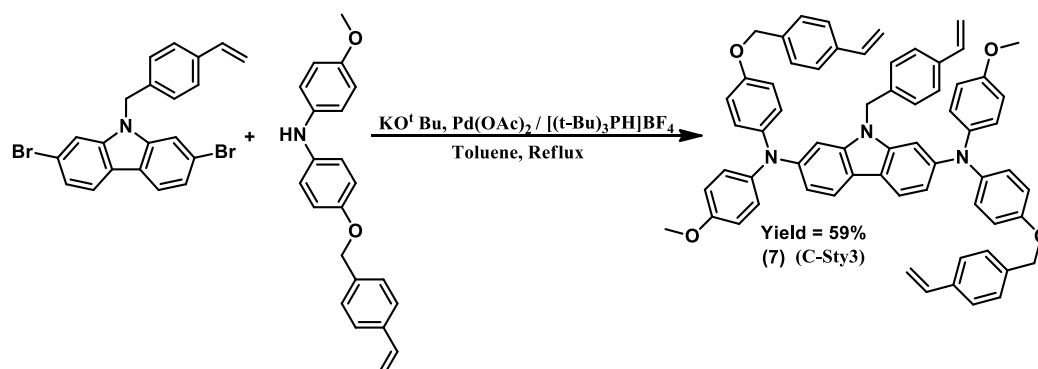
**CHN Analysis:** Calculated CHN (%) for C<sub>62</sub>H<sub>59</sub>N<sub>3</sub>O<sub>4</sub>: C, 82.82; H, 6.53; N, 4.62, Found: C, 81.46; H, 6.36; N, 4.55.

**2.5.4f. Synthesis of 2,7-dibromo-9-(4-vinylbenzyl)-9H-carbazole (6)****Scheme 2.7.**

In a 100 ml two neck flask, 2, 7-dibromocarbazole (1 g, 3.07 mmol) was dissolved in DMF (25 ml) at RT and NaH (0.09 g, 3.68 mmol) was slowly added to the solution. After addition of NaH, 4-chloromethyl styrene (0.56 g, 3.68mmol) was added to the reaction mixture. The reaction was stirred at 60 °C for 10 hours. It is then poured into aqueous NH<sub>4</sub>Cl solution and extracted with chloroform. The collected crude solids were dried with Na<sub>2</sub>SO<sub>4</sub>, and concentrated. Column was carried out in ethylacetate:hexane (1:9) to give a white solid (Yield: 80%).

<sup>1</sup>H NMR (CDCl<sub>3</sub>, 500 MHz):  $\delta$  = 7.95 (d, 2H, *J* = 8.5 Hz), 7.49 (s, 2H), 7.36 (m, 4H), 7.05 (d, 2H, *J* = 8 Hz), 6.67 (m, 1H), 5.7 (d, 1H, *J* = 17.5 Hz), 5.41 (s, 2H), 5.23 (d, 1H, *J* = 10.5 Hz).

**ESI-HRMS:** *m/z* calculated for (C<sub>21</sub>H<sub>15</sub>Br<sub>2</sub>N): 443.1585, *m/z* found: 443.3346.

**2.5.4g. Synthesis of N<sup>2</sup>,N<sup>7</sup>-bis(4-methoxyphenyl)-9-(4-vinylbenzyl)-N<sup>2</sup>,N<sup>7</sup>-bis(4-((4-vinylbenzyl)oxy)phenyl)-9H-carbazole-2,7-diamine (7) (C-Sty3)****Scheme 2.8.**

2,7-dibromo-9-(4-vinylbenzyl)-9*H*-carbazole (0.1 g, 0.2 mmol), 4-methoxy-N-(4-(4-vinylbenzyloxy)phenyl)aniline (0.19 g, 0.5 mmol), potassium tert butoxide (0.07 g, 0.5 mmol), Pd (OAc)<sub>2</sub> (0.005 g, 0.2 mmol) and (*t*-Bu<sub>3</sub>)PHBF<sub>4</sub> (0.02 g, 0.06 mmol) were transferred to a 100 mL three neck round bottom flask. The flask was subjected to three vacuum/Argon refill cycles in order to remove water and oxygen. Anhydrous toluene was added and the mixture was stirred for 12 h at 110 °C or until the reaction was complete by TLC analysis. The product was collected by extraction with addition of ethylacetate and DI-water, followed by a brine solution. The toluene-ethylacetate layer was dried with anhydrous sodium sulphate, filtered, and concentrated. The collected crude solids were purified by column chromatography (hexane: ethylacetate, 7:3) to give a pale yellow solid (Yield = 59%).

**<sup>1</sup>H NMR** (500 MHz, Acetone-*d*<sub>6</sub>): δ = 7.82 (d, 2H, *J* = 8.5 Hz), 7.5 (m, 8H), 7.3 (d, 2H, *J* = 8.5 Hz), 7.02 (m, 10H), 7.00 (m, 6H), 6.88 (d, 4H, *J* = 9 Hz), 6.75 (m, 5H), 5.85 (s, 2H), 5.8 (m, 1H), 5.23 (m, 5H), 5.08 (s, 4H), 3.77 (s, 6H).

**<sup>13</sup>C NMR** (125 MHz, Acetone-*d*<sub>6</sub>): δ = 155.80, 154.73, 146.65, 142.14, 141.99, 141.57, 137.32, 137.19, 136.62, 136.55, 127.79, 126.22, 125.95, 125.6, 119.81, 117.85, 115.60, 114.86, 114.60, 113.38, 102.44, 69.64, 54.83, 45.52.

**ESI-HRMS:** *m/z* calculated for C<sub>65</sub>H<sub>55</sub>N<sub>3</sub>O<sub>4</sub>: 941.4193, *m/z* found: 941.4212.

**CHN Analysis:** Calculated CHN (%) for C<sub>65</sub>H<sub>55</sub>N<sub>3</sub>O<sub>4</sub>: C, 82.86; H, 5.88; N, 4.46, Found: C, 82.07; H, 5.83; N, 4.44.

### 2.5.5. NMR and ESI-HRMS Spectra of C-OMe, C-Sty2 and C-Sty3

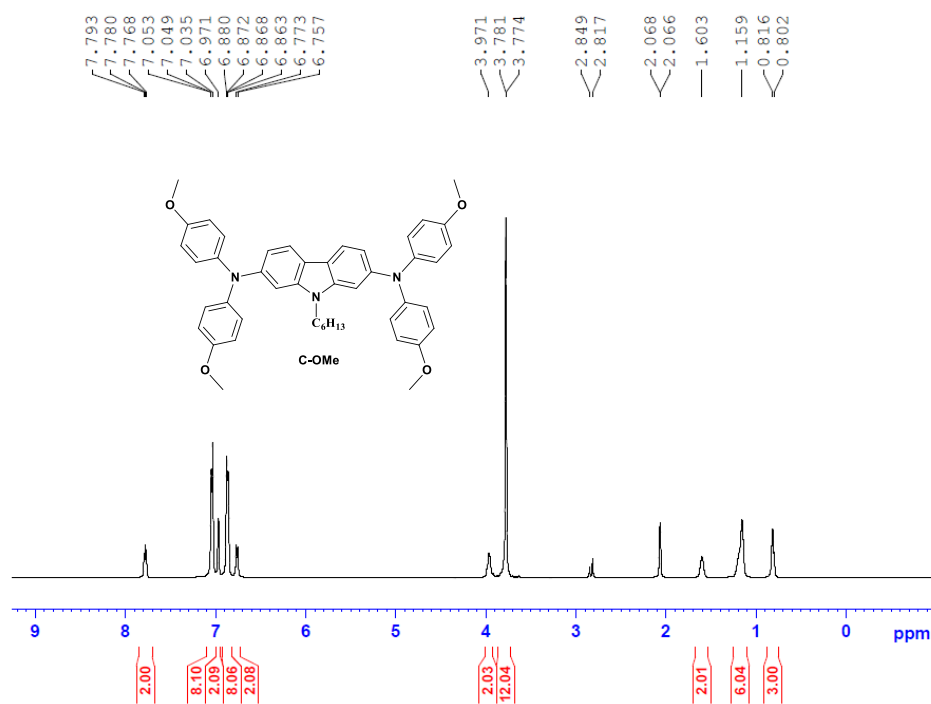


Figure 2.23.  $^1\text{H}$  NMR of C-OMe in acetone- $d_6$ .

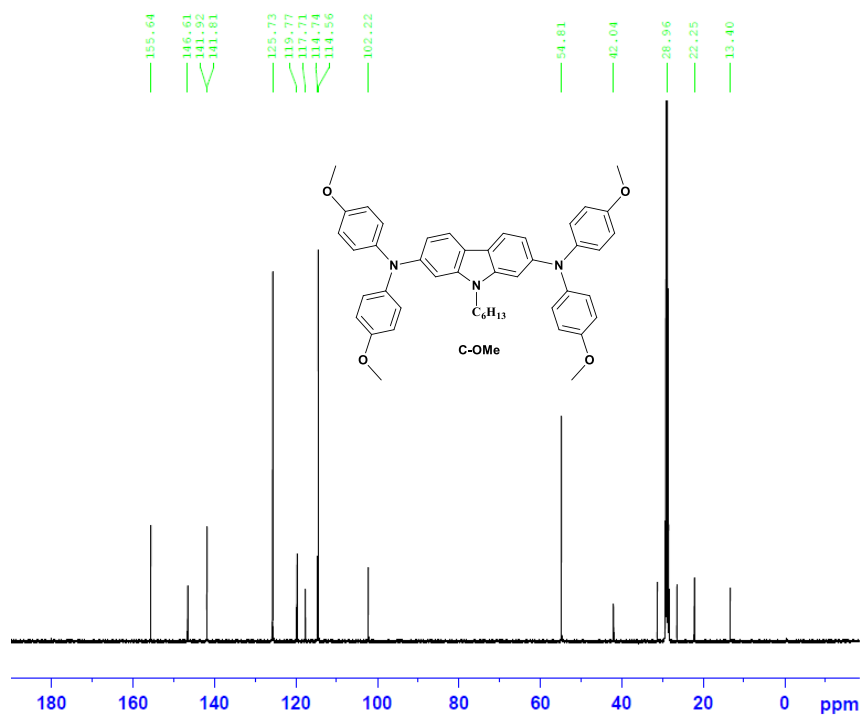
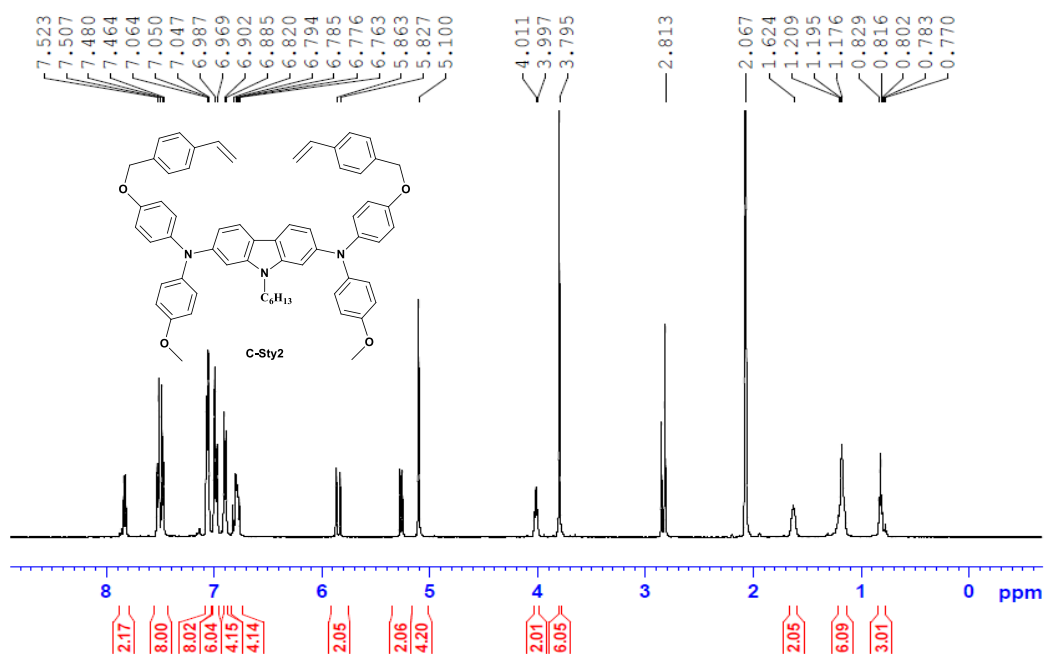
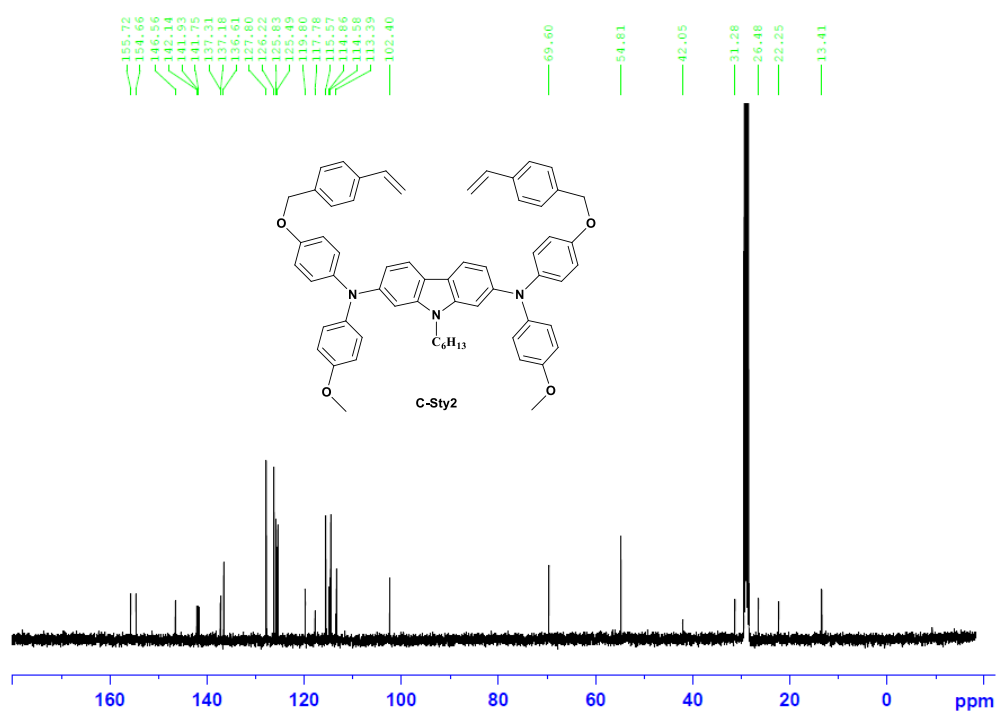


Figure 2.24.  $^{13}\text{C}$  NMR of C-OMe in acetone- $d_6$ .

Figure 2.25. <sup>1</sup>H NMR of C-Sty2 in acetone-d<sub>6</sub>.Figure 2.26. <sup>13</sup>C NMR of C-Sty2 in acetone-d<sub>6</sub>.



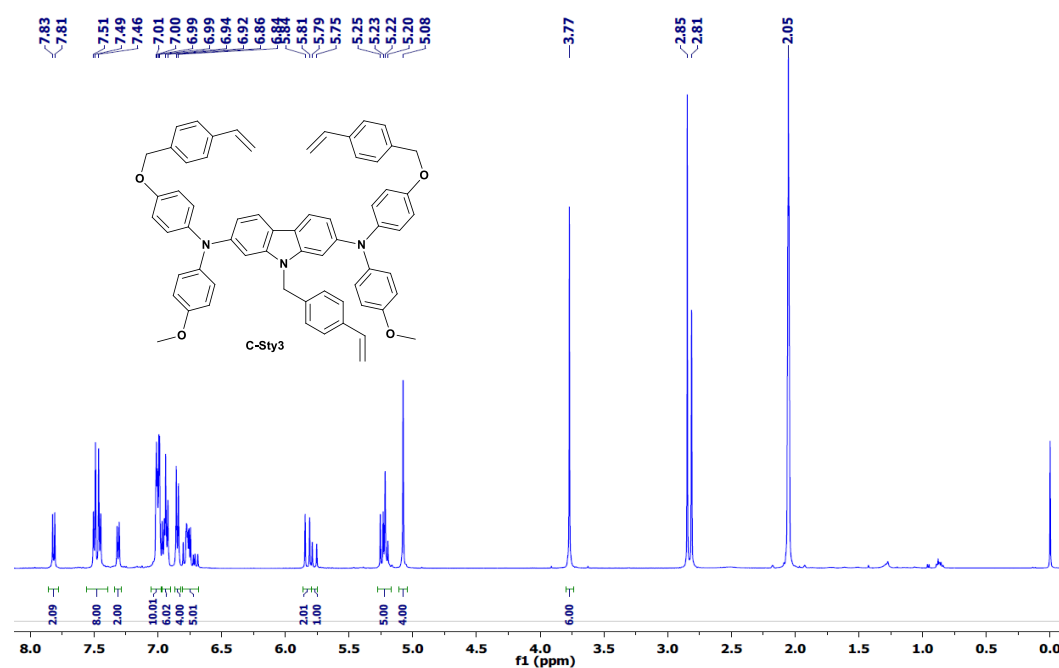


Figure 2.27. <sup>1</sup>H NMR of C-Sty3 in acetone-d<sub>6</sub>.

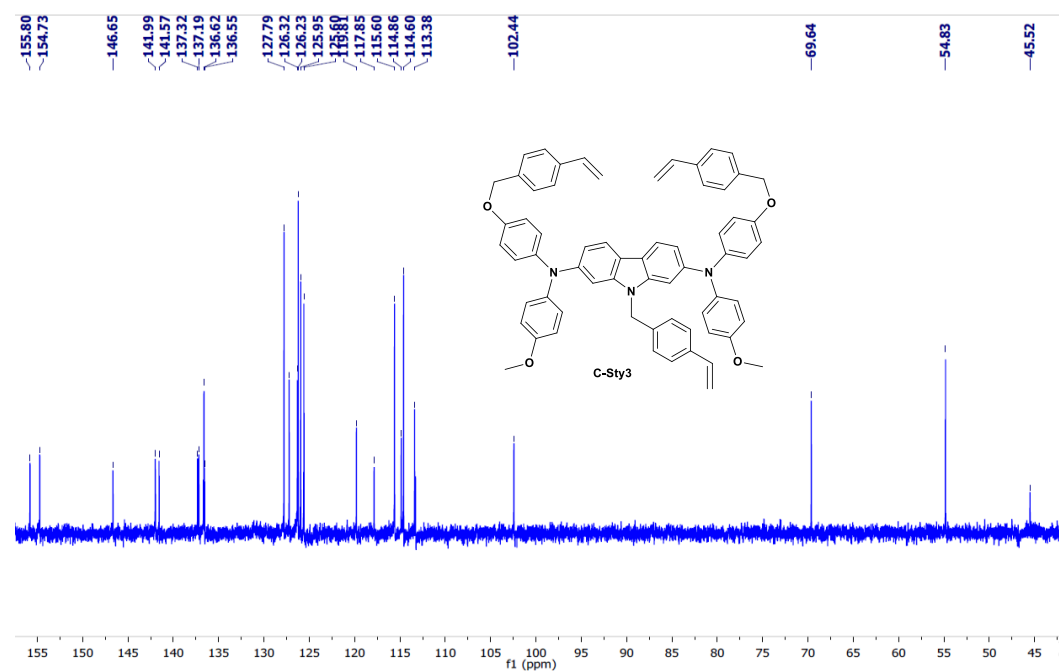


Figure 2.28. <sup>13</sup>C NMR of C-Sty3 in acetone-d<sub>6</sub>.

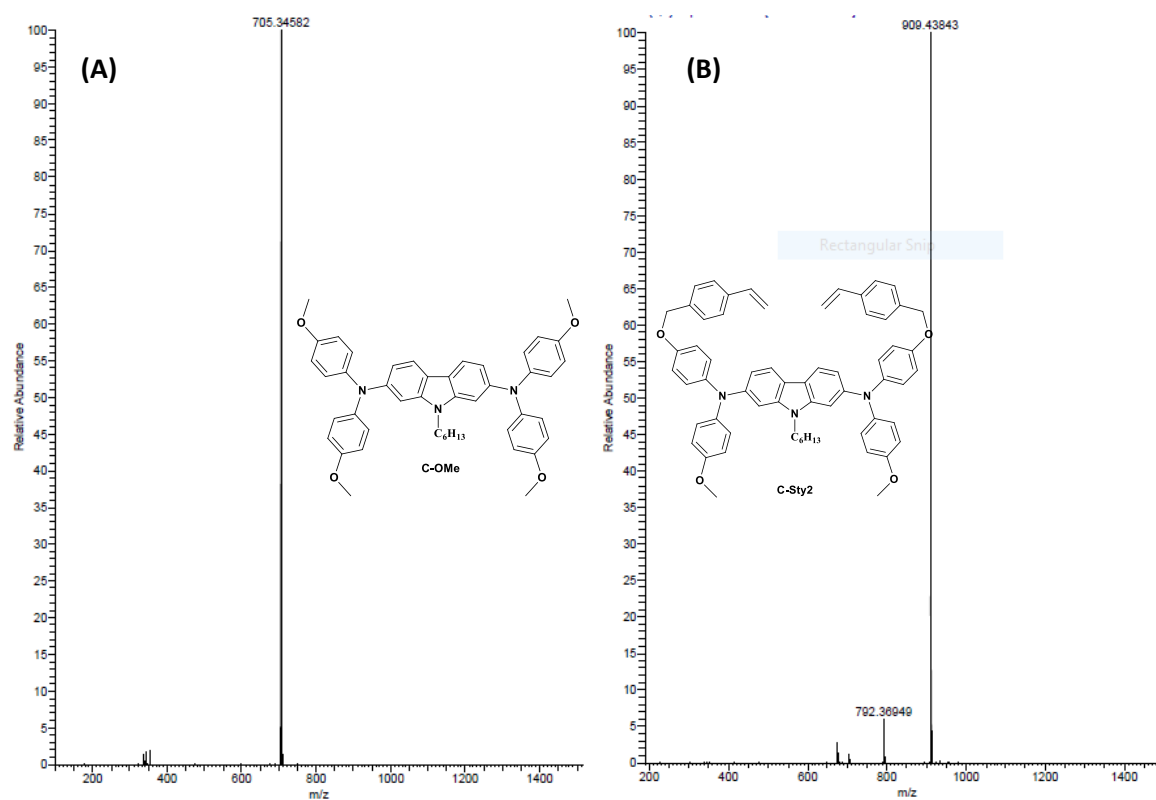


Figure 2.29. ESI-HRMS spectra of (A) C-OMe and (B) C-Sty2.

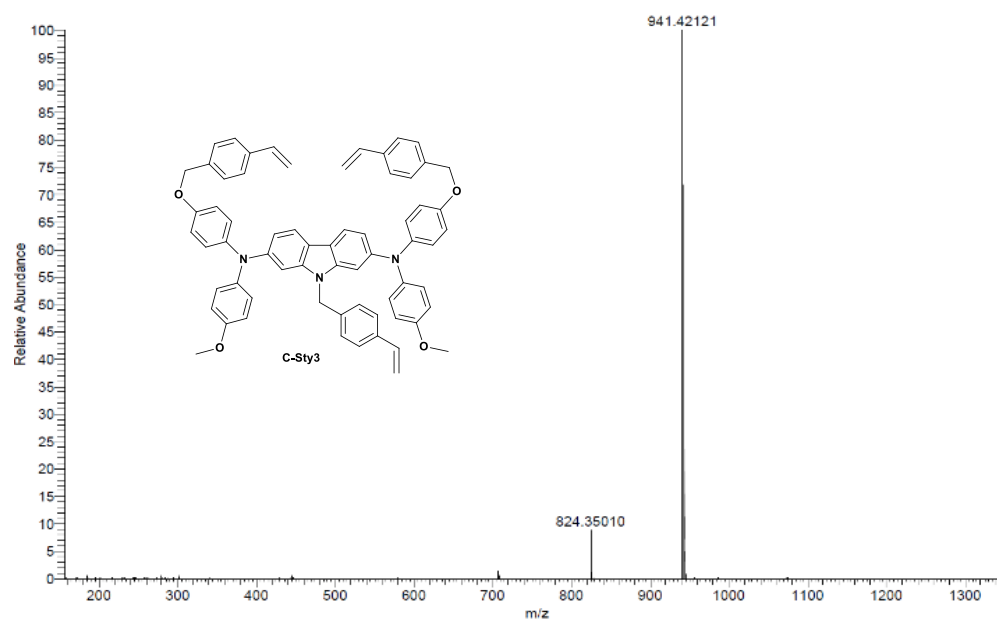


Figure 2.30. ESI-HRMS of C-Sty3.

## 2.6. References

- (1) Argun, A. A.; Aubert, P.-H.; Thompson, B. C.; Schwendeman, I.; Gaupp, C. L.; Hwang, J.; Pinto, N. J.; Tanner, D. B.; MacDiarmid, A. G.; Reynolds, J. R. Multicolored Electrochromism in Polymers: Structures and Devices. *Chem. Mater.* **2004**, *16*, 4401-4412.
- (2) Beaujuge, P. M.; Reynolds, J. R. Color Control in  $\pi$ -Conjugated Organic Polymers for Use in Electrochromic Devices. *Chem. Rev.* **2010**, *110*, 268-320.
- (3) Fang, H.; Zheng, P.; Ma, R.; Xu, C.; Yang, G.; Wang, Q.; Wang, H. Multifunctional hydrogel enables extremely simplified electrochromic devices for smart windows and ionic writing boards. *Mater. Horiz* **2018**, *5*, 1000-1007.
- (4) Mortimer, R. J. Organic electrochromic materials. *Electrochim. Acta* **1999**, *44*, 2971-2981.
- (5) Yen, H.-J.; Liou, G.-S. Recent advances in triphenylamine-based electrochromic derivatives and polymers. *Polym. Chem.* **2018**, *9*, 3001-3018.
- (6) Abraham, S.; Ganesh, G. P. T.; Varughese, S.; Deb, B.; Joseph, J. Cross-Linkable Fluorene-Diphenylamine Derivatives for Electrochromic Applications. *ACS Appl. Mater. Interfaces* **2015**, *7*, 25424-25433.
- (7) Abraham, S.; Mangalath, S.; Sasikumar, D.; Joseph, J. Transmissive-to-Black Electrochromic Devices Based on Cross-Linkable Tetraphenylethene-Diphenylamine Derivatives. *Chem. Mater.* **2017**, *29*, 9877-9881.
- (8) Wałęsa-Chorab, M.; Skene, W. G. Visible-to-NIR Electrochromic Device Prepared from a Thermally Polymerizable Electroactive Organic Monomer. *ACS Appl. Mater. Interfaces* **2017**, *9*, 21524-21531.
- (9) Lv, X.; Li, J.; Xu, L.; Zhu, X.; Tameev, A.; Nekrasov, A.; Kim, G.; Xu, H.; Zhang, C. Colorless to Multicolored, Fast Switching, and Highly Stable Electrochromic Devices Based on Thermally Cross-Linking Copolymer. *ACS Appl. Mater. Interfaces* **2021**, *13*, 41826-41835.
- (10) Lv, X.; Shao, M.; Zhu, X.; Xu, L.; Ouyang, M.; Zhou, C.; Dong, J.; Zhang, C. Thermally Cross-Linked Copolymer for Highly Transparent to Multicolor-Showing Electrochromic Materials. *ACS Appl. Polym. Mater.* **2023**, *5*, 3595-3603.
- (11) Su, K.; Sun, N.; Yan, Z.; Jin, S.; Li, X.; Wang, D.; Zhou, H.; Yao, J.; Chen, C. Dual-Switching Electrochromism and Electrofluorochromism Derived from Diphenylamine-Based Polyamides with Spirobifluorene/Pyrene as Bridged Fluorescence Units. *ACS Appl. Mater. Interfaces* **2020**, *12*, 22099-22107.

- (12) Frolov, D. G.; Makhaeva, E. E.; Keshtov, M. L. Electrochromic behavior of films and «smart windows» prototypes based on  $\pi$ -conjugated and non-conjugated poly(pyridinium triflate)s. *Synth. Met.* **2019**, *248*, 14-19.
- (13) Kamata, K.; Suzuki, T.; Kawai, T.; Iyoda, T. Voltammetric anion recognition by a highly cross-linked polyviologen film. *J. Electroanal. Chem.* **1999**, *473*, 145-155.
- (14) Wang, F.; Wilson, M. S.; Rauh, R. D.; Schottland, P.; Thompson, B. C.; Reynolds, J. R. Electrochromic Linear and Star Branched Poly(3,4-ethylenedioxythiophene-didodecyloxybenzene) Polymers. *Macromolecules* **2000**, *33*, 2083-2091.
- (15) Soganci, T.; Gumusay, O.; Soyleyici, H. C.; Ak, M. Synthesis of highly branched conducting polymer architecture for electrochromic applications. *Polymer* **2018**, *134*, 187-195.
- (16) Bhandari, S.; Deepa, M.; Srivastava, A. K.; Joshi, A. G.; Kant, R. Poly(3,4-ethylenedioxythiophene)-Multiwalled Carbon Nanotube Composite Films: Structure-Directed Amplified Electrochromic Response and Improved Redox Activity. *J. Phys. Chem. B* **2009**, *113*, 9416-9428.
- (17) Hsiao, S.-H.; Liou, G.-S.; Kung, Y.-C.; Yen, H.-J. High Contrast Ratio and Rapid Switching Electrochromic Polymeric Films Based on 4-(Dimethylamino)triphenylamine-Functionalized Aromatic Polyamides. *Macromolecules* **2008**, *41*, 2800-2808.
- (18) Navarathne, D.; Skene, W. G. Dynachromes – dynamic electrochromic polymers capable of property tuning and patterning via multiple constitutional component exchange. *J. Mater. Chem. C* **2013**, *1*, 6743-6747.
- (19) Gaupp, C. L.; Reynolds, J. R. Multichromic Copolymers Based on 3,6-Bis(2-(3,4-ethylenedioxythiophene))-N-alkylcarbazole Derivatives. *Macromolecules* **2003**, *36*, 6305-6315.
- (20) Sankaran, B.; Reynolds, J. R. High-Contrast Electrochromic Polymers from Alkyl-Derivatized Poly(3,4-ethylenedioxythiophenes). *Macromolecules* **1997**, *30*, 2582-2588.
- (21) Sapp, S. A.; Sotzing, G. A.; Reynolds, J. R. High Contrast Ratio and Fast-Switching Dual Polymer Electrochromic Devices. *Chem. Mater.* **1998**, *10*, 2101-2108.
- (22) Schwendeman, I.; Hickman, R.; Sönmez, G.; Schottland, P.; Zong, K.; Welsh, D. M.; Reynolds, J. R. Enhanced Contrast Dual Polymer Electrochromic Devices. *Chem. Mater.* **2002**, *14*, 3118-3122.

- (23) Österholm, A. M.; Shen, D. E.; Kerszulis, J. A.; Bulloch, R. H.; Kuepfert, M.; Dyer, A. L.; Reynolds, J. R. Four Shades of Brown: Tuning of Electrochromic Polymer Blends Toward High-Contrast Eyewear. *ACS Appl. Mater. Interfaces* **2015**, *7*, 1413-1421.
- (24) Wang, S.; Cai, S.; Cai, W.; Niu, H.; Wang, C.; Bai, X.; Wang, W.; Hou, Y. Organic-inorganic hybrid electrochromic materials, polysilsesquioxanes containing triarylamine, changing color from colorless to blue. *Sci. Rep.* **2017**, *7*, 14627.
- (25) Zhang, J.; Tu, J.-p.; Zhang, D.; Qiao, Y.-q.; Xia, X.-h.; Wang, X.-l.; Gu, C.-d. Multicolor electrochromic polyaniline-WO<sub>3</sub> hybrid thin films: One-pot molecular assembling synthesis. *J. Mater. Chem.* **2011**, *21*, 17316-17324.
- (26) Jamdegni, M.; Kaur, A. Highly efficient dark to transparent electrochromic electrode with charge storing ability based on polyaniline and functionalized nickel oxide composite linked through a binding agent. *Electrochim. Acta* **2019**, *331*, 135359.
- (27) Su, K.; Sun, N.; Tian, X.; Guo, S.; Yan, Z.; Wang, D.; Zhou, H.; Zhao, X.; Chen, C. Highly soluble polyimide bearing bulky pendant diphenylamine-pyrene for fast-response electrochromic and electrofluorochromic applications. *Dyes Pigm.* **2019**, *171*, 107668.
- (28) Corrente, G. A.; Fabiano, E.; Manni, F.; Chidichimo, G.; Gigli, G.; Beneduci, A.; Capodilupo, A.-L. Colorless to All-Black Full-NIR High-Contrast Switching in Solid Electrochromic Films Prepared with Organic Mixed Valence Systems Based on Dibenzofulvene Derivatives. *Chem. Mater.* **2018**, *30*, 5610-5620.
- (29) Zhang, Q.; Tsai, C.-Y.; Li, L.-J.; Liaw, D.-J. Colorless-to-colorful switching electrochromic polyimides with very high contrast ratio. *Nat. Commun.* **2019**, *10*, 1239.
- (30) Zeng, J.; Yang, H.; Zhong, C.; Rajan, K.; Sagar, R. U. R.; Qi, X.; Deng, Y.; Jiang, H.; Liu, P.; Liang, T. Colorless-to-black electrochromic devices based on ambipolar electrochromic system consisting of cross-linked poly(4-vinyltriphenylamine) and tungsten trioxide with high optical contrast in visible and near-infrared regions. *Chem. Eng. J.* **2021**, *404*, 126402.
- (31) Topal, S.; Savlug Ipek, O.; Sezer, E.; Ozturk, T. Electrochromic-Hybrid energy storage material consisting of triphenylamine and dithienothiophene. *Chem. Eng. J.* **2022**, *434*, 133868.
- (32) Wałęsa-Chorab, M.; Muras, K.; Filiatrault, H. L.; Skene, W. G. Suitability of alkyne donor- $\pi$ -donor- $\pi$ -donor scaffolds for electrofluorochromic and electrochromic use. *J. Mater. Chem. C* **2022**, *10*, 3691-3703.
- (33) Yu, T.; Theato, P.; Yao, H.; Liu, H.; Di, Y.; Sun, Z.; Guan, S. Colorless Electrochromic/Electrofluorochromic Dual-Functional Triphenylamine-Based Polyimides:

Effect of a Tetraphenylethylene-Based  $\pi$ -Bridge on optoelectronic properties. *Chem. Eng. J.* **2023**, *451*, 138441.

(34) Gao, L.; Schloemer, T. H.; Zhang, F.; Chen, X.; Xiao, C.; Zhu, K.; Sellinger, A. Carbazole-Based Hole-Transport Materials for High-Efficiency and Stable Perovskite Solar Cells. *ACS Appl. Energy Mater.* **2020**, *3*, 4492-4498.

(35) Leijtens, T.; Ding, I. K.; Giovenzana, T.; Bloking, J. T.; McGehee, M. D.; Sellinger, A. Hole Transport Materials with Low Glass Transition Temperatures and High Solubility for Application in Solid-State Dye-Sensitized Solar Cells. *ACS Nano* **2012**, *6*, 1455-1462.

(36) Liu, H.; He, B.; Lu, H.; Tang, R.; Wu, F.; Zhong, C.; Li, S.; Wang, J.; Zhu, L. Carbazole-based D-A type hole transport materials to enhance the performance of perovskite solar cells. *Sustain. Energy Fuels* **2022**, *6*, 371-376.

(37) Teh, C. H.; Daik, R.; Lim, E. L.; Yap, C. C.; Ibrahim, M. A.; Ludin, N. A.; Sopian, K.; Mat Teridi, M. A. A review of organic small molecule-based hole-transporting materials for meso-structured organic-inorganic perovskite solar cells. *J. Mater. Chem. A* **2016**, *4*, 15788-15822.

(38) Xu, B.; Sheibani, E.; Liu, P.; Zhang, J.; Tian, H.; Vlachopoulos, N.; Boschloo, G.; Kloo, L.; Hagfeldt, A.; Sun, L. Carbazole-Based Hole-Transport Materials for Efficient Solid-State Dye-Sensitized Solar Cells and Perovskite Solar Cells. *Adv. Mater.* **2014**, *26*, 6629-6634.

(39) Ledwon, P. Recent advances of donor-acceptor type carbazole-based molecules for light emitting applications. *Org. Electron.* **2019**, *75*, 105422.

(40) Li, M. C3-C3' and C6-C6' Oxidative Couplings of Carbazoles. *Chem. Eur. J.* **2019**, *25*, 1142-1151.

(41) Tao, Y.; Yang, C.; Qin, J. Organic host materials for phosphorescent organic light-emitting diodes. *Chem. Soc. Rev.* **2011**, *40*, 2943-2970.

(42) Wex, B.; Kaafarani, B. R. Perspective on carbazole-based organic compounds as emitters and hosts in TADF applications. *J. Mater. Chem. C* **2017**, *5*, 8622-8653.

(43) Ates, M.; Uludag, N. Carbazole derivative synthesis and their electropolymerization. *J. Solid State Electrochem.* **2016**, *20*, 2599-2612.

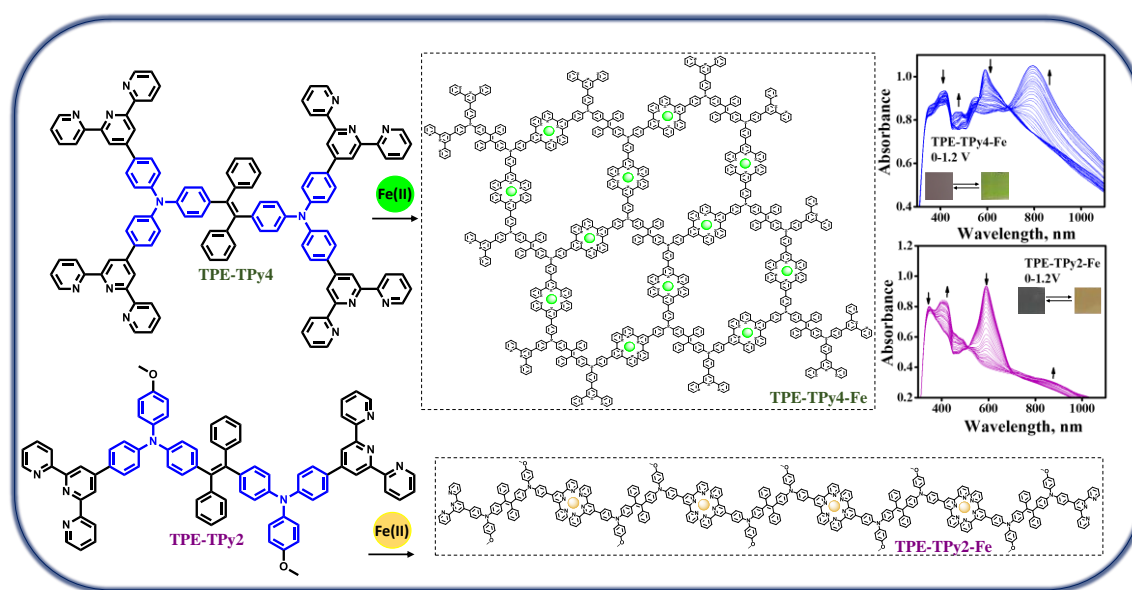
(44) Zhou, P.; Wan, Z.; Liu, Y.; Jia, C.; Weng, X.; Xie, J.; Deng, L. Synthesis and electrochromic properties of a novel conducting polymer film based on dithiafulvenyl-triphenylamine-di(N-carbazole). *Electrochim. Acta* **2016**, *190*, 1015-1024.

- (45) Zhang, Y.; Liu, F.; Hou, Y.; Niu, H. Soluble high coloration efficiency electrochromic polymers based on (N-phenyl)carbazole, triphenylamine and 9,9-dioctyl-9H-fluorene. *Synth. Met.* **2019**, *247*, 81-89.
- (46) Cansu-Ergun, E. G. Covering the More Visible Region by Electrochemical Copolymerization of Carbazole and Benzothiadiazole Based Donor-Acceptor Type Monomers. *Chin. J. Polym. Sci.* **2019**, *37*, 28-35.
- (47) Akbayrak, M.; Cansu-Ergun, E. G.; Önal, A. M. Synthesis and electro-optical properties of a new copolymer based on EDOT and carbazole. *Des. Monomers Polym.* **2016**, *19*, 679-687.
- (48) Liu, Y.; Chao, D.; Yao, H. New triphenylamine-based poly(amine-imide)s with carbazole-substituents for electrochromic applications. *Org. Electron.* **2014**, *15*, 1422-1431.
- (49) Liu, F.-h.; Bai, J.; Yu, G.; Ma, F.-h.; Hou, Y.-j.; Niu, H.-j. Synthesis, electrochromic properties and flash memory behaviors of novel D-A-D polyazomethines containing EDOT and thiophene units. *Org. Electron.* **2020**, *77*, 105538.
- (50) Karon, K.; Lapkowski, M.; Dabuliene, A.; Tomkeviciene, A.; Kostiv, N.; Grazulevicius, J. V. Spectroelectrochemical characterization of conducting polymers from star-shaped carbazole-triphenylamine compounds. *Electrochim. Acta* **2015**, *154*, 119-127.
- (51) Data, P.; Zassowski, P.; Lapkowski, M.; Domagala, W.; Krompiec, S.; Flak, T.; Penkala, M.; Swist, A.; Soloduchko, J.; Danikiewicz, W. Electrochemical and spectroelectrochemical comparison of alternated monomers and their copolymers based on carbazole and thiophene derivatives. *Electrochim. Acta* **2014**, *122*, 118-129.
- (52) Cansu-Ergun, E. G.; Önal, A. M. Carbazole based electrochromic polymers bearing ethylenedioxy and propylenedioxy scaffolds. *J. Electroanal. Chem.* **2018**, *815*, 158-165.
- (53) Daskeviciute-Geguziene, S.; Magomedov, A.; Daskeviciene, M.; Genevičius, K.; Nekrašas, N.; Jankauskas, V.; Kantminiene, K.; McGehee, M. D.; Getautis, V. Cross-linkable carbazole-based hole transporting materials for perovskite solar cells. *Chem. Commun.* **2022**, *58*, 7495-7498.
- (54) Joseph, V.; Justin Thomas, K. R.; Yang, W. Y.; Kumar Yadav, R. A.; Kumar Dubey, D.; Jou, J.-H. Tetra-substituted Dipolar Carbazoles: Tuning Optical and Electroluminescence Properties by Linkage Variation. *Asian J. Org. Chem.* **2018**, *7*, 1654-1666.
- (55) Palayangoda, S. S.; Cai, X.; Adhikari, R. M.; Neckers, D. C. Carbazole-Based Donor-Acceptor Compounds: Highly Fluorescent Organic Nanoparticles. *Org. Lett.* **2008**, *10*, 281-284.

- (56) Zhang, L.; Zhan, W.; Dong, Y.; Yang, T.; Zhang, C.; Ouyang, M.; Li, W. Liquid/Liquid Interfacial Suzuki Polymerization Prepared Novel Triphenylamine-Based Conjugated Polymer Films with Excellent Electrochromic Properties. *ACS Appl. Mater. Interfaces* **2021**, *13*, 20810-20820.
- (57) Fu, W.; Chen, H.; Han, Y.; Wang, W.; Zhang, R.; Liu, J. Electropolymerization of D-A-D type monomers consisting of triphenylamine and substituted quinoxaline moieties for electrochromic devices. *New J. Chem.* **2021**, *45*, 19082-19087.
- (58) Rakhi, R. B.; Chen, W.; Cha, D.; Alshareef, H. N. Substrate Dependent Self-Organization of Mesoporous Cobalt Oxide Nanowires with Remarkable Pseudocapacitance. *Nano Lett.* **2012**, *12*, 2559-2567.
- (59) Rakhi, R. B.; Ahmed, B.; Anjum, D.; Alshareef, H. N. Direct Chemical Synthesis of MnO<sub>2</sub> Nanowhiskers on Transition-Metal Carbide Surfaces for Supercapacitor Applications. *ACS Appl. Mater. Interfaces* **2016**, *8*, 18806-18814.
- (60) Wang, W.; Guo, S.; Lee, I.; Ahmed, K.; Zhong, J.; Favors, Z.; Zaera, F.; Ozkan, M.; Ozkan, C. S. Hydrous Ruthenium Oxide Nanoparticles Anchored to Graphene and Carbon Nanotube Hybrid Foam for Supercapacitors. *Sci. Rep.* **2014**, *4*, 4452.
- (61) Liu, C.; Luo, H.; Xu, Y.; Wang, W.; Liang, Q.; Mitsuzaki, N.; Chen, Z. Cobalt-phosphate-modified Mo:BiVO<sub>4</sub> mesoporous photoelectrodes for enhanced photoelectrochemical water splitting. *J. Mater. Sci.* **2019**, *54*, 10670-10683.
- (62) Jayabalan, A. D.; Din, M. M. U.; Indu, M. S.; Karthik, K.; Ragupathi, V.; Nagarajan, G. S.; Panigrahi, P.; Murugan, R. Electrospun 3D CNF-SiO<sub>2</sub> fabricated using non-biodegradable silica gel as prospective anode for lithium-ion batteries. *Ionics* **2019**, *25*, 5305-5313.
- (63) Gupta, B.; Singh, A. K.; Prakash, R. Electrolyte effects on various properties of polycarbazole. *Thin Solid Films* **2010**, *519*, 1016-1019.



## Terpyridine Appended Tetraphenylethylene-Diphenylamine Derivatives and their Iron Metallopolymers: Photophysical and Electrochromic Properties



### 3.1. Abstract

Designing ligands with varying numbers of coordination sites can result in metallo-polymers (MPs) with linear and branched structures and these structural differences can have a significant impact on their thermal, morphological, and electrochromic characteristics. In this regard, two tetraphenylethylene-diphenylamine-terpyridine based ligands, **TPE-TPy2** and **TPE-TPy4**, having two and four terpyridine units attached to the diarylamine moiety, were synthesised, and their photophysical, thermal, electrochemical, and metal interaction studies were investigated in this chapter. The linear and hyperbranched Fe(II)-based metallo-

polymers were prepared by complexing Fe(II) salt with a 1:1 ratio of **TPE-TPy2** and a 2:1 ratio of **TPE-TPy4**, respectively. The obtained metallo-polymers were fully characterized using techniques like UV-Vis absorption, Fourier-Transform infrared spectroscopy (FT-IR), <sup>1</sup>H NMR and X-ray photoelectron spectroscopy (XPS). The cyclic voltammetry of the metallo-polymer films prepared by spray coating on FTO substrates revealed a single reversible redox peak with half-wave potentials of 0.72 V and 0.70 V for **TPE-TPy2-Fe** and **TPE-TPy4-Fe**, respectively. Peaks corresponding to triphenylamine oxidations and metal ion oxidation overlap in the same region, at all scan rates for the polymer films. Both the metallo-polymer films on FTO showed surface-confined electrochemical processes as the rate determining step with a reversible color change from dark greyish blue to yellow for **TPE-TPy2-Fe** and purple to green for **TPE-TPy4-Fe**. The spectroelectrochemistry of the films revealed concomitant changes corresponding to the Fe(II) to Fe(III) oxidation and oxidation of triphenylamine groups. Both the polymers demonstrated remarkable stability without significant transmittance loss for more than 300 switching cycles. Hyperbranched polymers of **TPE-TPy4-Fe** have electrochromic features predominantly due to triphenylamine oxidation including open circuit memory and near-infrared absorption. These hyperbranched polymers also exhibited better coloration efficiency (243 cm<sup>2</sup>C<sup>-1</sup> at 585 nm) and shorter electrochromic switching times (2.8 s for oxidation and 0.9 s for reduction) compared to linear metallo-polymers of **TPE-TPy2-Fe**.

## 3.2. Introduction

The development of materials with advanced properties is becoming increasingly appealing as a result of their technological applications. Scientists are fascinated by the fast-growing field of synthetic organic polymers and the intriguing potential for creating novel, easily processed materials by introducing metal ions to synthetic polymer strands. They are commonly employed as photo- and electroluminescent materials, photovoltaic materials, high refractive index and non-linear optical materials, liquid crystalline materials, precursors to functional ceramic materials, and stimuli-responsive materials.<sup>1</sup> Stimuli-responsive materials are becoming more important for a variety of applications due to their capacity to change functionalities when subjected to external stimuli. Metallo-polymers (MPs) have several unique benefits in this field due to the combinations of advantageous properties of both metal complexes and polymers. These materials have several applications in memory devices technology,<sup>2,3</sup> biological sensors,<sup>4,5</sup> electrochromic,<sup>6-8</sup> photochromic<sup>9,10</sup> and thermochromic<sup>11-14</sup> devices, etc. Electrochromic materials, which change color in response to electric stimuli, are widely used in smart windows, display devices, electrochromic sensors, energy storage devices etc.<sup>15</sup> Among the other electrochromic materials such as metal oxides ( $\text{WO}_3$ ,  $\text{NiO}$ ,  $\text{MoO}_3$ , and  $\text{V}_2\text{O}_5$ ), organic molecules (triphenylamine and viologen derivatives), and conducting polymers (PEDOT, PANI, PPy, PTh etc),<sup>16</sup> metallo-polymers have well defined redox properties and intense coloration. Metallo-polymers can undergo a variety of electronic transitions, including MLCT in which an electron is transferred from the metal centre's partially filled d-orbital to the organic ligand's vacant  $\pi^*$  orbital. This transition involves an alteration in the metal's oxidation state, which may result in a

shift in the absorption spectrum towards higher energy. LMCT is another transition that occurs when an electron is transferred from the filled  $\pi$  to the empty  $d^*$  orbital of the organic ligand and metal center, respectively. Metallo-polymers containing conjugated organic ligands exhibit  $\pi$ - $\pi^*$  transitions in the organic ligand molecules, and metal with partially filled  $d$  orbital undergoes  $d$ - $d^*$  transitions. Figure 3.1 illustrates the probable electronic transitions that most MPs exhibit during EC process.<sup>17</sup>

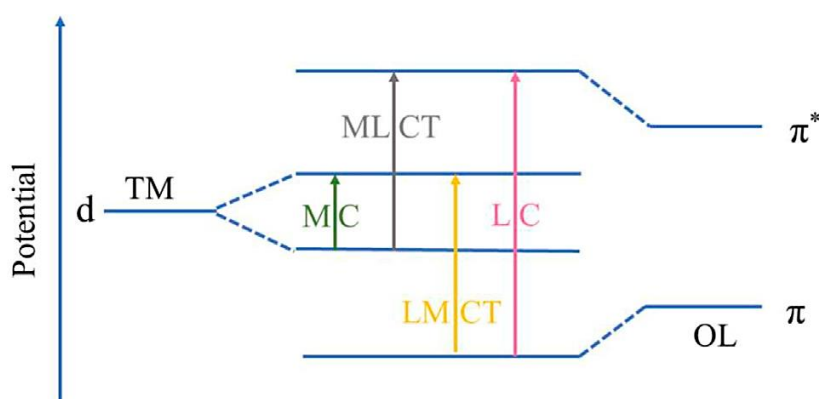


**Figure 3.1.** The electronic transitions during the EC process in Metallo-polymers. (Adapted from reference 17)

MLCT transitions in metallo-polymers are more intense because they are both spin- and Laporte-allowed transitions. The spin selection rule states that transitions between two energy states with the same spin multiplicity are allowed ( $\Delta S=0$ ) and MLCT transitions obey this rule. Laporte's selection rule states that transitions occur between states with different symmetry or parity, where changes in dipole and transition momentum integral are non-zero. That is, a transition happens when two states have different parity or symmetry (p-d, s-p, d-f, etc.). Since the d-d/s-s transition involved similar parity changes, it is Laporte forbidden.

Electrochromic devices made of metallo-polymers provide versatile and promising solutions for a variety of applications. Ying-Chih Liao and his group

demonstrated the possibility to create displays using an all-solution technique by utilising metallo-polymers as EC materials.<sup>18</sup> They used inkjet printing techniques to create multicolour EC devices out of two primary colours derived from Fe and Ru-based terpyridine metallo-polymers (Figure 3.2A). Masayoshi Higuchi and group demonstrated EC properties of a hybrid terpyridine ligand based polymer consisting of Fe(II) or Ru(II) ions.<sup>19</sup> The device exhibited five color display in a potential range of -2.5 to 2.5V. Using these EC polymers, they produced various kinds of display sizes, including a 10-inch panel (Figure 3.2B).

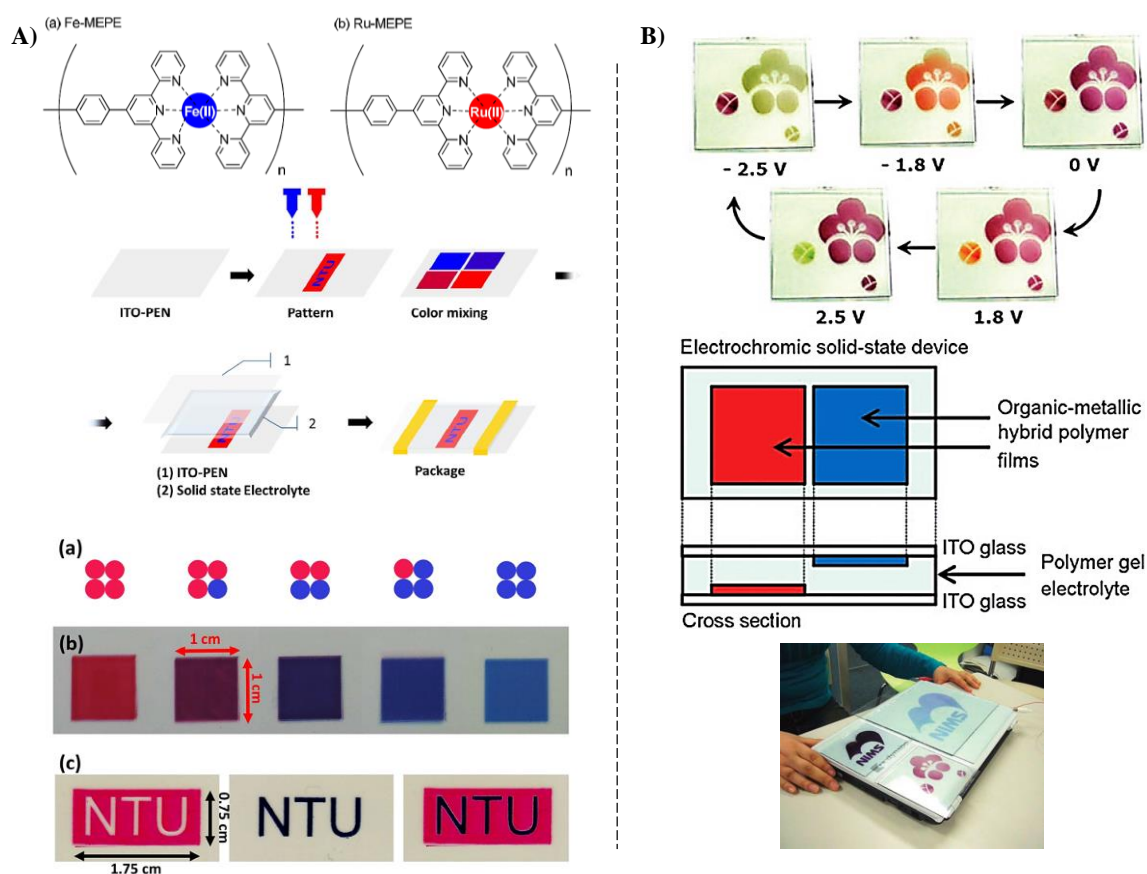


**Figure 3.2.** (A) Multicolour EC films with EC subpixels: structure of the metallo-polymers, fabrication techniques and photographs of the devices and (B) Ru-Fe multicolour EC device structure, color change and photograph of the large area device. (Adapted from reference 18 and 19)

The properties of MPs depend on the ligand design and the transition metal used. To obtain desirable structural arrangements, organic ligands in metallopolymers are frequently designed to have specific symmetries and bonding directions. For example, ligands having two, three, four, or six-fold symmetry and bonding orientations can be developed. This symmetry and bonding arrangement allow the ligands to establish specific connections with the metal centres (Figure 3.3).<sup>20</sup>

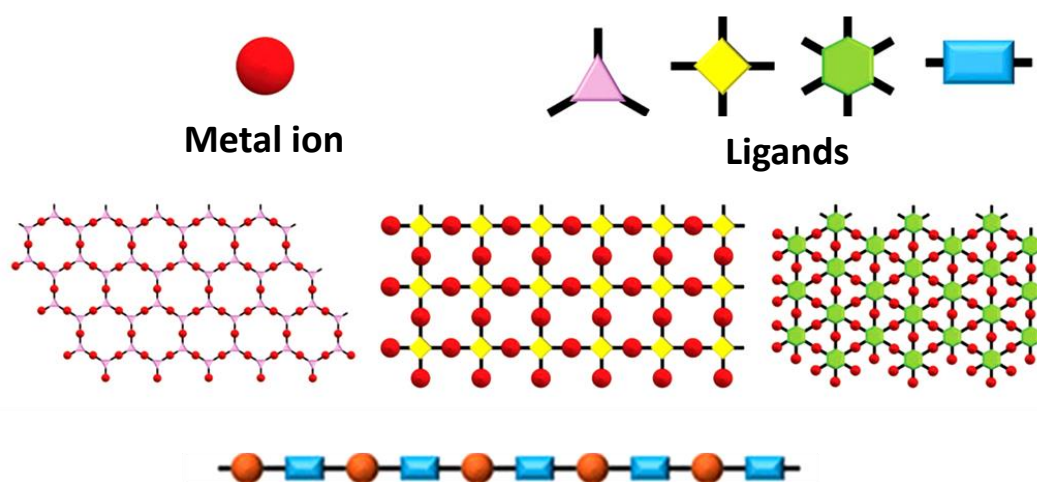


**Figure 3.3.** Schematic illustration of different metallo-polymers formed from ligands with different number of coordination sites. (Adapted from reference 20 and modified)

Research efforts over the last decade have revealed that the ligand structure has a considerable impact on the EC characteristics of metallo-polymers. 2,2':6',2''-Terpyridine based N-hetero aromatics have been extensively used as a tridentate ligand for d-block metal ions and play a key role in tuning the electronic and steric properties of metallo-polymers. Masayoshi Higuchi and his group have reported various iron-terpyridine metallo-polymers having distinct structures and electrochromic properties. For example, they synthesised metallo-supramolecular polymers with three-dimensional structures ( $\text{FeL}_{185\%}\text{L}_{215\%}$ ) that exhibited a highly

porous structure and facilitated smooth ionic transport during the redox process. These characteristics resulted in better electrochromic properties compared to a 1-D linear polymer (Figure 3.4A).<sup>21</sup> Similarly, zigzag-structured, triphenylamine-terpyridine ligand-based Fe-polymers (polyFe-N and polyRu-N) with NIR absorption<sup>22</sup> (Figure 3.4B), a single step synthesised 3D-iron polymer using an asymmetrical ditopic ligand containing terpyridine and phenanthroline (Figure 3.4C),<sup>23</sup> nanocomposites made up from a linear, iron(II)-polymer, named as polyFe and imidazoline derived material (Figure 3.4D)<sup>23</sup> and a highly dense, hexagonal tritopic ligand with branched Fe(II) coordination (Figure 3.4E)<sup>22</sup> are some reported examples of metallo-polymers with unique structures and electrochromic properties.

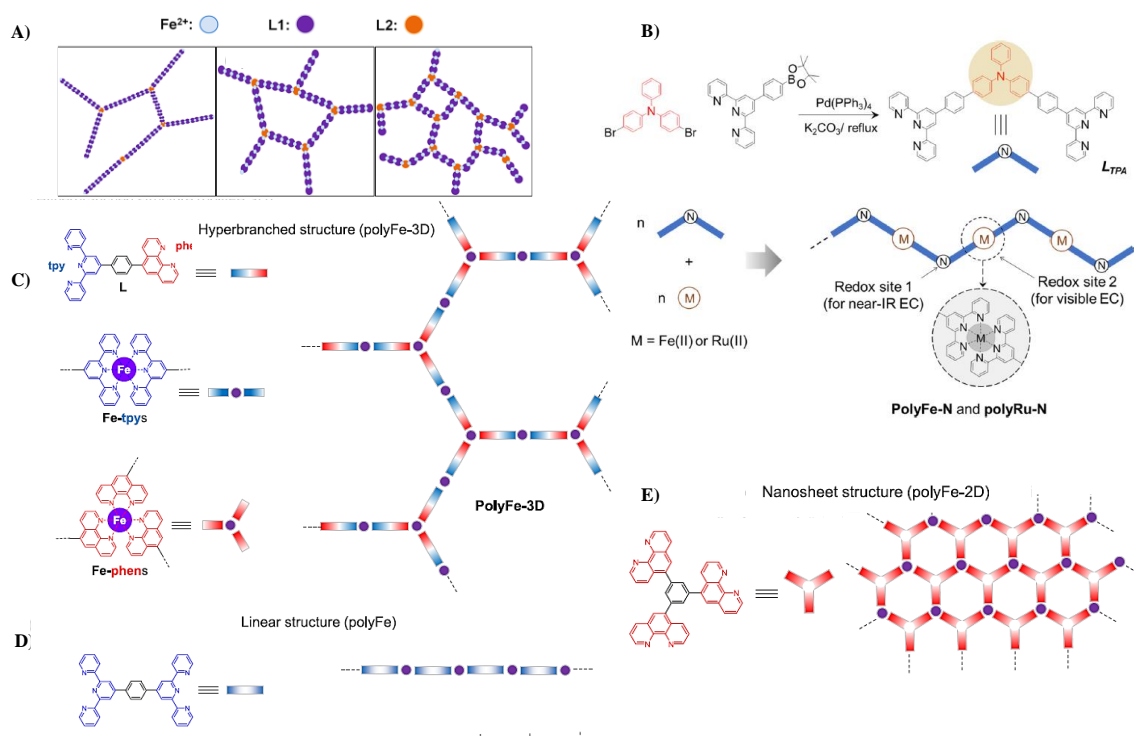


**Figure 3.4.** Structures of different electrochromic iron-terpyridine metallo-polymers. (A) 3D-MPs formed from different ligand-metal ratios; (B) zigzag-structured MP; (C) PolyFe-3D; (D) Linear polyFe and (E) Fe(II) coordination nanosheet, reported by Masayoshi Higuchi and group. (Adapted from references 21-24)

Design of metallo-polymers using triphenylamine moiety with 2,2':6,2''-terpyridine as the peripheral arms gained attention of the researchers since the corresponding metallo-polymers can achieve combined properties like multiple color change, NIR absorption, good contrast ratio, optical memory and stability. The relationship between structure and performance in terpyridine-triphenylamine complexes in electrochromic behaviour have been studied by leading groups.<sup>8,24-26</sup> Tao *et al.* reported a series of “D- $\pi$ -A- $\pi$ -D” complexes formed from terpyridine and triphenylamine (D) moieties and proved that ligands containing triphenylamine with rigid structure showed enhanced memory ability and long-term stability (p-FeL1) (Figure 3.5A). The spectroelectrochemistry of the polymers showed a drop in MLCT absorption and a new broad IVCT absorption band formation due to TPA oxidation at potentials ranging from 0 to 2 V. The strength of the IVCT band changed with ligand modification, as shown in Figure 3.5B.<sup>27</sup>

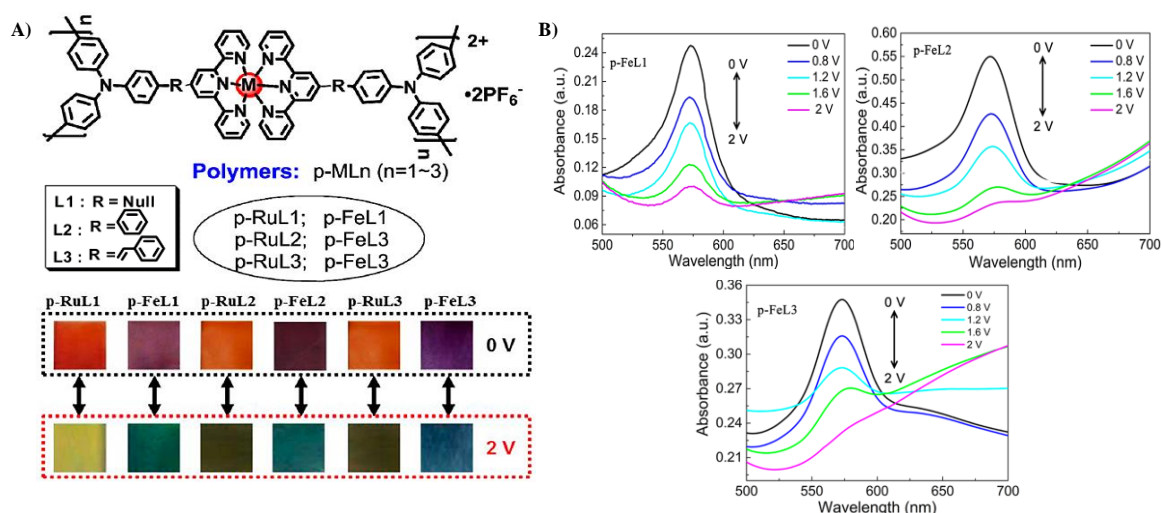


**Figure 3.5.** (A) Structural design and photographs of electrochromic hybrid-polymer films and (B) Spectroelectrochemistry of Fe-polymer films at voltages ranging from 0 to 2 V. (Adapted from reference 28)



Shankar and group demonstrated distinct electrical conductivities and excellent operational stability under continuous cycling by varying the ligand structures in metallo-polymers.<sup>28,29</sup> Three tetraterpyridine ligands, each with variations in their core architecture (phenyl, tetraphenylethynyl, and bithiophene) were developed. The electrochromic metallo-polymers containing  $\text{Fe}^{2+}$  as the coordinating metal ion, exhibited good molecular permeability and spectroelectrochemical properties, which were directly influenced by the specific ligand structure used. The electrochromic films of phenyl-based ligand exhibited remarkably high coloration efficiency (up to  $1050 \text{ cm}^2/\text{C}$ ) and superior optical contrast (up to 76%), accompanied by a color-to-color redox transition. The Metallo-polymer produced from TPE-based ligand achieved the highest volumetric capacitance up to  $544.6 \text{ F cm}^{-3}$  at a current density of  $1 \text{ A g}^{-1}$  and energy density up to  $75.5 \text{ mWh cm}^{-3}$ .

### 3.2.1. The Randles-Sevcik Equation and Electrochemical Processes

In cyclic voltammetry, electrochemical processes can be classified into two main categories: diffusion and surface-controlled process. Diffusional processes involve the transport of electroactive species to and from the electrode surface, i.e., mass transport is responsible for controlling this process. The rate of the electrochemical reaction is limited by the diffusion of particles in the electrolyte solution. Surface-controlled processes take place when the electrochemical reaction happens right at the electrode surface without significant involvement of mass transport. The kinetics of the surface reactions (oxidation/reduction) in these processes regulate the current response and act as the rate determining step. Both processes are scan-rate dependent. The Randles-Sevcik equation (Equation 3.1) is used in electrochemistry to analyze and interpret the current response to scan rate.<sup>30,31</sup>

$$i_p = 0.4463 nFA C \sqrt{\frac{nFvD}{RT}} \quad \text{Equation (3.1)}$$

$i_p$  = Peak current (Amperes)

$n$  = Number of electrons transferred in a redox cycle

$F$  = Faraday's constant (96485.339 C/mol)

$R$  = Universal gas constant (8.31447 J K<sup>-1</sup> mol<sup>-1</sup>)

$T$  = Absolute temperature

$A$  = The electrode surface area in working (cm<sup>2</sup>)

$C$  = Molar concentration of redox-active species (mol/cm<sup>3</sup>)

$D$  = The diffusion coefficient (cm<sup>2</sup>/s)

$v$  = Scan rate (V/s)

The plot of peak current vs square root of scan-rate for a diffusion-controlled redox system exhibits a linear trend. If the peak current is linearly proportional to the scan rate, the rate is determined by the kinetically controlled surface reaction.

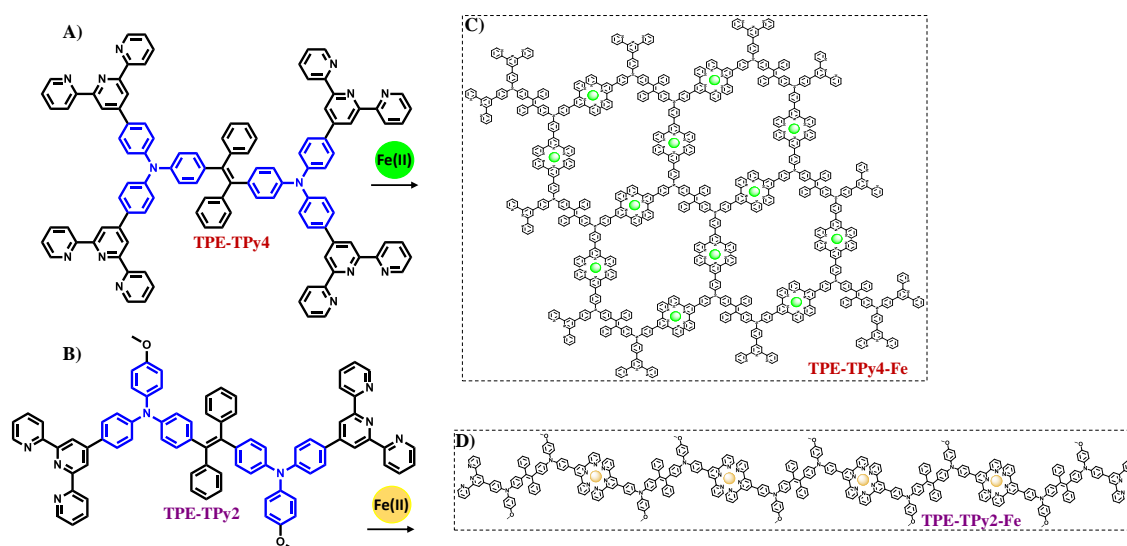


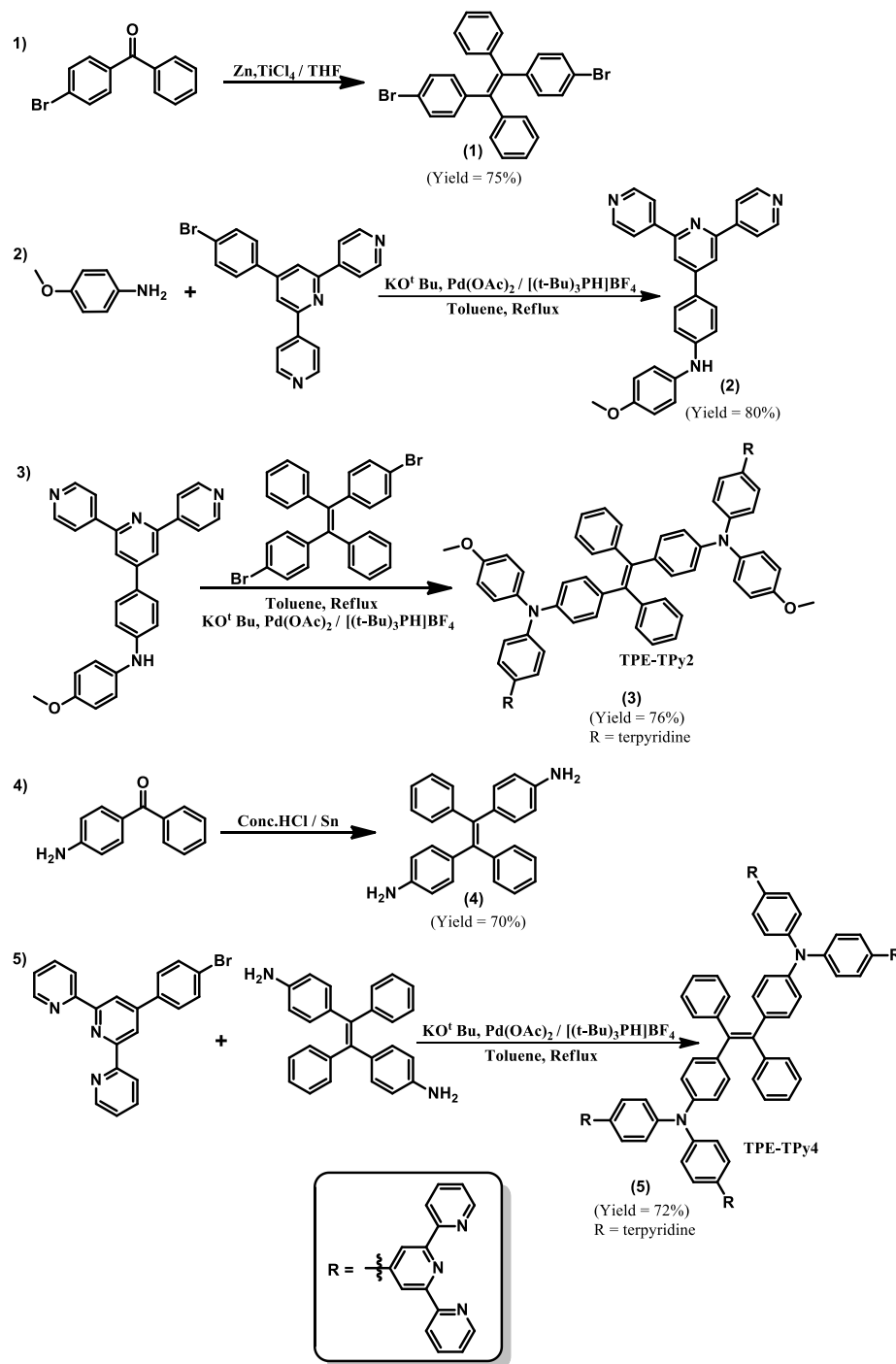
**Figure 3.6.** Molecular structures of (A) TPE-TPy2 and (B) TPE-TPy4 ligands; Schematic representation of (C) TPE-TPy2-Fe and (D) TPE-TPy4-Fe metallopolymers formed from the complexation.

Incorporating multiple terpyridine units into a ligand can significantly influence the molecular structure, electronic and electrochromic properties of the resulting complex. Herein, we present the synthesis and characterization of two Terpyridine appended Tetraphenylethylene-Diphenylamine derivatives as ligands and their Fe(II) ion based metallo-polymers. The tetraphenylethene core group is chosen for the current EC design based on its favourable spectroelectrochemistry. Figure 3.6 shows the structures of the ligands **TPE-TPy2** and **TPE-TPy4** and a schematic illustration of their metallo-polymer structures. First one is a linear polymer prepared by 1:1 complexation of Fe<sup>2+</sup> and **TPE-TPy2** ligand and the other is a hyperbranched metallo-polymer formed from the 1:2 complexation of ligand **TPE-TPy4** and Fe<sup>2+</sup>. Prepared metallo-polymers were thoroughly characterised using different techniques such as, UV-Vis absorption, FT-IR, <sup>1</sup>H NMR and XPS. The spectroelectrochemistry of the films revealed concomitant changes corresponding to the Fe(II) to Fe(III) and triphenylamine oxidation. Remarkably, hyperbranched metallo-polymer showed electrochromic features predominantly due to triphenylamine oxidation like high open circuit memory and NIR absorption. The hyperbranched **TPE-TPy4-Fe** metallo-polymer outperformed the linear **TPE-TPy2-Fe** metallo-polymer in terms of open circuit memory, coloration efficiency and switching time.

### 3.3. Results and Discussion

The ligands, **TPE-TPy2** and **TPE-TPy4**, were synthesized by Pd catalyzed, Buchwald-Hartwig cross-coupling reactions as shown in Scheme 3.1. For example 4,4'-(1,2-diphenylethylene-1,2-diyl)bis(*N*-(4-([2,2':6',2''-terpyridin]4'-yl)phenyl)-*N*-(4-methoxyphenyl)aniline; **TPE-TPy2**) was synthesized by the coupling between 1,2-bis(4-bromophenyl)-1,2-diphenylethylene and 4-([2,2':6',2''-terpyridin]-4'-yl)-*N*-(4-

methoxyphenyl)aniline while 4,4'-(1,2-diphenylethene-1,2-diyl)bis(*N,N*-bis(4-([2,2':6',2''-terpyridin]-4'-yl)phenyl)aniline; **TPE-TPy4**) was synthesized by the coupling between 4,4'-(1,2-diphenylethene-1,2-diyl)dianiline and 4'-(4-bromophenyl)-2,2':6',2''-terpyridine.



**Scheme 3.1.** Synthesis of TPE-TPy2 and TPE-TPy4 molecules.

The characteristic UV-Vis absorption spectra for ligand molecules in solution and in solid state are given in Figure 3.7A and 3.7B.

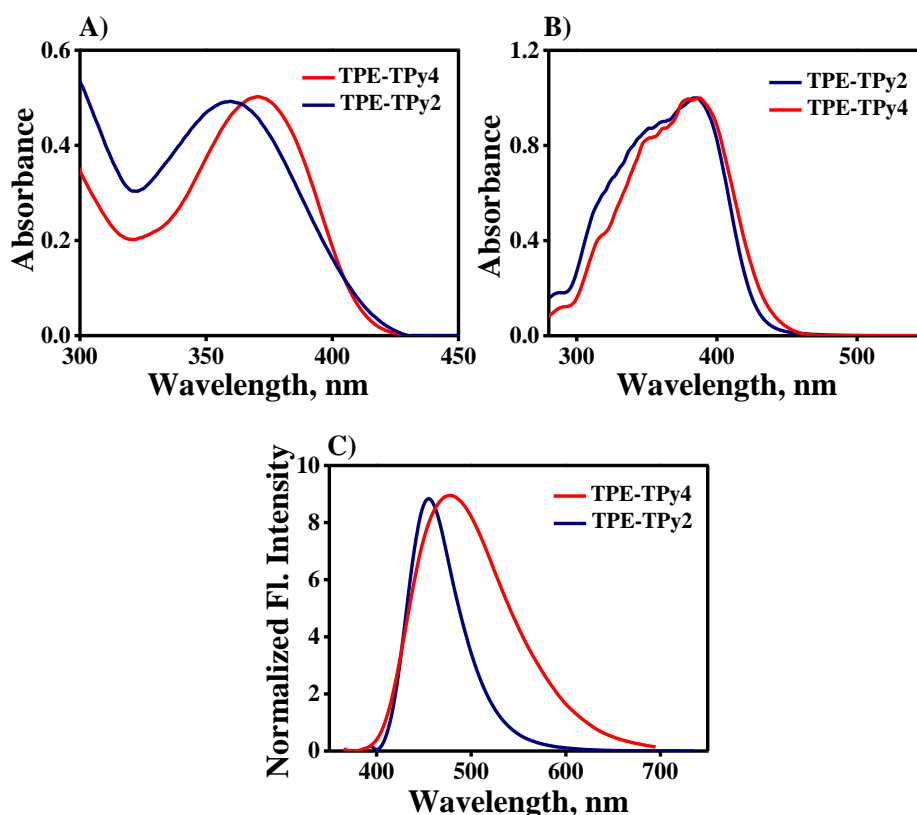


**Figure 3.7.** (A) Absorption spectra of **TPE-TPy2** and **TPE-TPy4** in THF; (B) Solid state absorption spectra of **TPE-TPy2** and **TPE-TPy4** and (C) Normalized fluorescence spectra of **TPE-TPy2** and **TPE-TPy4** in THF (excitation at 360 nm 370 nm for **TPE-TPy2** and **TPE-TPy4**, respectively).

**TPE-TPy2** THF solutions showed an absorption maximum of 360 nm with negligible absorption above 420 nm ensuring transparency in the visible region. Absorption spectrum of **TPE-TPy4** in THF showed a 10 nm red shift with a maximum around 370 nm. The peaks at 360 nm for **TPE-TPy2** and 370 nm for **TPE-TPy4** were assigned to the  $\pi$ - $\pi^*$  transition and the red shift in the  $\pi$ - $\pi^*$  absorption for the **TPE-TPy4** ligand is due to the increased molecular conjugation. The solid-state absorption spectra of the ligands were broad compared to the solution state with absorption maxima for both ligands centered at 383 nm. The emission spectra of the ligands were

obtained in THF, as shown in Figure 3.7C, and both **TPE-TPy2** and **TPE-TPy4** showed blue fluorescent emission bands at 455 nm and 476 nm, respectively. Notably, **TPE-TPy2** showed a narrow emission (FWHM = 62 nm) compared to **TPE-TPy4** (FWHM = 110 nm), probably due to the extended conjugation and differential degree of excited state planarization for these two ligands.

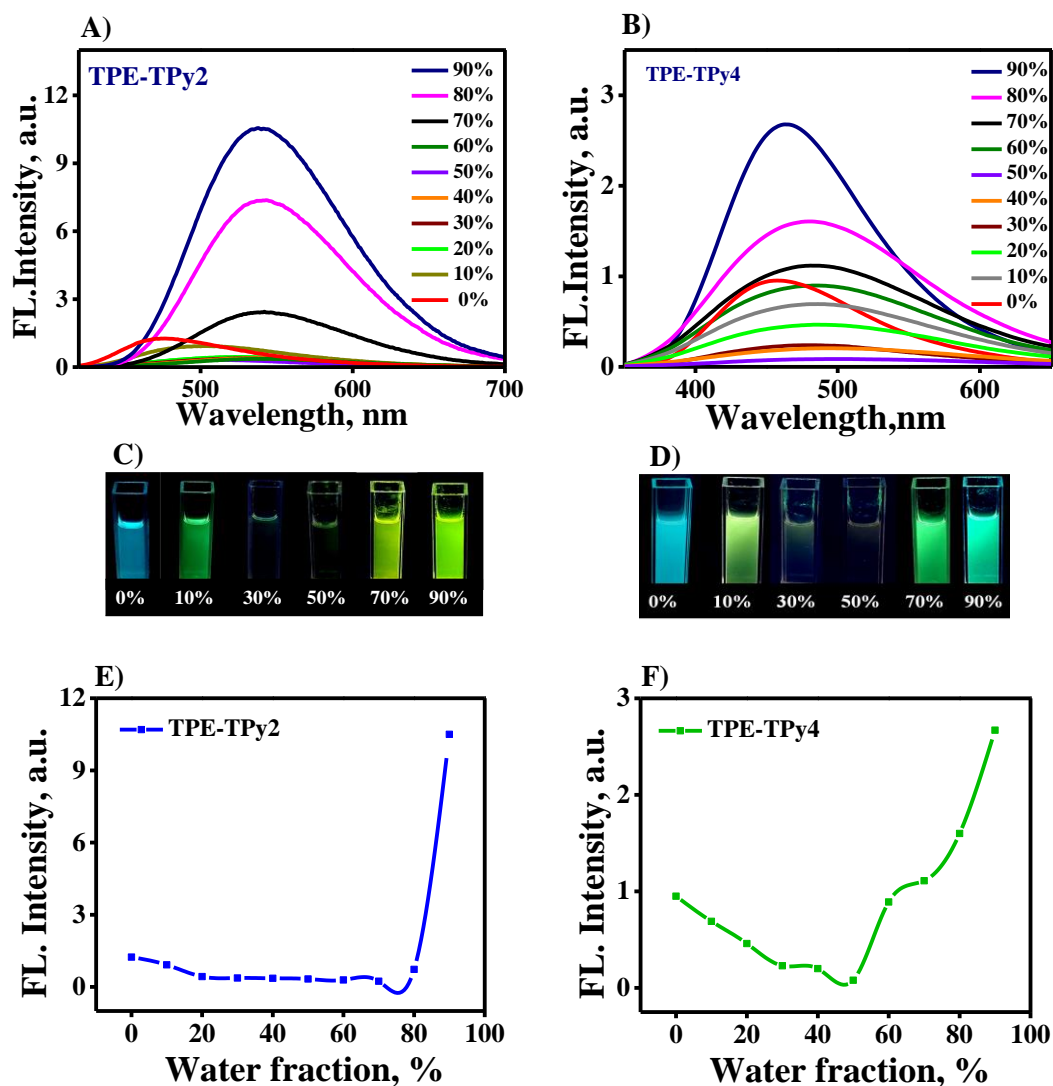


**Figure 3.8.** Emission spectra of (A) **TPE-TPy2** and (B) **TPE-TPy4** in THF and different THF/water mixtures; Photographs of the (C) **TPE-TPy2** and (D) **TPE-TPy4** in 0, 10, 30, 50, 70 and 90 percentage THF/water mixtures taken under UV illumination; Dependence of fluorescence intensity on solvent compositions of the THF/water mixtures for (E) **TPE-TPy2** and (F) **TPE-TPy4** at their emission maximum,  $\lambda_{em}$ .

Tetraphenylethene (TPE), the core we have selected for the ligands is a typical AIE-active unit that has been extensively studied and applied in various fields such as sensors and electroluminescent devices. We have probed the basic AIE-behavior of these ligands in various THF-water mixtures (Figure 3.8). Both the ligands are soluble in organic solvents like THF, toluene, DCM, DMSO, and acetone, whereas they are partially soluble in methanol and insoluble in water. The benzene rings of the tetraphenylethylene moiety can rotate around the central olefin in a good solvent, which non-radiatively deactivates the excited state of TPE molecules and renders them weakly emissive or non-emissive. For example, in THF both **TPE-TPy2** and **TPE-TPy4** showed weak fluorescence with maxima at 455 nm and 476 nm, respectively. In THF-water mixtures, significant changes in fluorescence maxima and intensity of **TPE-TPy2** and **TPE-TPy4** were observed with increasing the water fraction. As shown in Figure 3.8A and Figure 3.8B, the fluorescence intensity of both ligands showed an initial decrease with an increase in the fraction of water up to 60%, followed by a significant enhancement of fluorescence at higher water fractions. At a water fraction of 90%, the emission intensities of both **TPE-TPy2** and **TPE-TPy4**, respectively were 8 and 3-folds higher, than in pure THF. **TPE-TPy4** has four bulky terpyridine units connected to the TPE core, whereas **TPE-TPy2** has two and the bulkiness imposes a barrier for intramolecular rotations of the phenyl ring in TPE. As expected, **TPE-TPy2** demonstrated lower fluorescence maximum in THF and greater enhancement in fluorescence intensity in higher water fractions accompanied with a larger red shift in its fluorescence maximum compared to **TPE-TPy4**. The photographs of ligands in different THF/water mixtures under UV light are shown in Figures 3.8C and 3.8D. Figures 3.8E and 3.8F show the plots of ligand fluorescence

intensity dependency at their emission maximum ( $\lambda_{em}$ ) on different THF/water mixtures.

A closer look at the changes in fluorescence maximum of **TPE-TPy2** and **TPE-TPy4** reveals an interesting trend. For example, the fluorescence maximum of **TPE-TPy2** in pure THF (470 nm) changes to 515 nm in 10% water-fraction, followed by an aggregation caused quenching up to 60% water-fraction. At 90% water fraction **TPE-TPy2** showed a fluorescence maximum of 540 nm with an enhanced fluorescence (AIE) compared to that of THF solutions. Similar trend was observed for **TPE-TPy4** with an initial change of fluorescence maximum from 450 nm in THF to 490 nm in 10% water-fraction and a final change to 465 nm in 90% water fraction, with an initial quenching (ACQ) followed by an enhancement (AIE). The initial changes in fluorescence could be attributed to the changes in ground and excited state molecular structure due to solvent polarity changes, while the latter changes correspond to the hydrophobic aggregation leading to AIE.<sup>32,33</sup>

Figure 3.9A depicts the thermal properties of the ligands determined by TGA under nitrogen at a heating rate of 10 °C min<sup>-1</sup>. The TGA thermograms revealed that the decomposition temperatures ( $T_{d5\%}$ ) of the ligands **TPE-TPy2** and **TPE-TPy4** are 435 °C and 455 °C, respectively, indicating the high temperature stability of the ligands. Their respective melting points measured using a calibrated digital melting point apparatus were found to be 260 °C and 310 °C. **TPE-TPy4** exhibited higher temperature resistance than **TPE-TPy2**. The cyclic voltammograms of the ligands in chlorobenzene with 0.1 M TBAPF<sub>6</sub> showed two well-resolved reversible peaks with half-wave potentials around 0.47 V and 0.78 V for **TPE-TPy2** and 0.43 V and 0.72 V for **TPE-TPy4**, indicating the radical cation and dication formation in the triphenylamine units (Figure 3.9B).



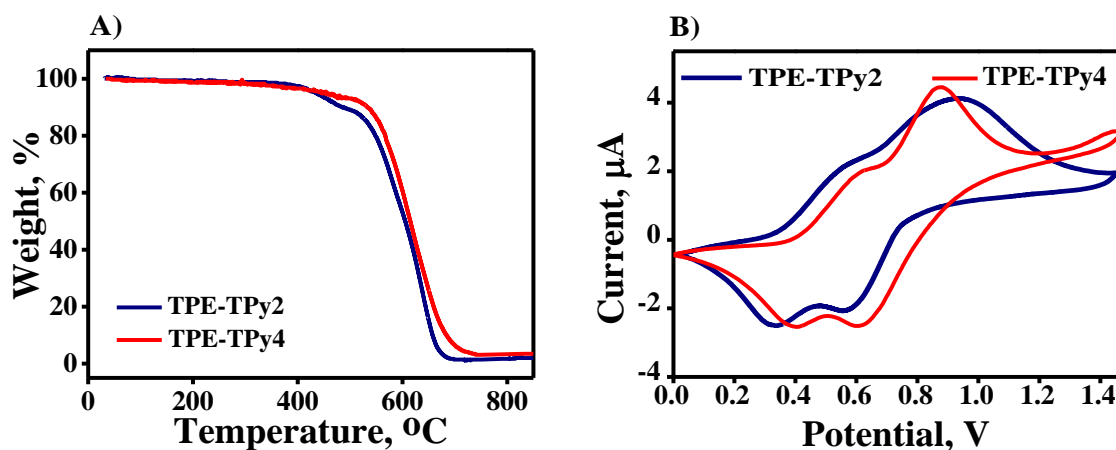


**Figure 3.9.** (A) TGA thermograms of the ligands **TPE-TPy2** and **TPE-TPy4** and (B) Cyclic voltammograms of the ligands **TPE-TPy2** and **TPE-TPy4** in 0.1 M TBAPF<sub>6</sub> in chlorobenzene at 50 mV/s scan rate.

The changes in UV-Vis spectra of ligands upon titration with Fe<sup>2+</sup> ions are shown in Figure 3.10. The concentrations of both ligands were kept constant at 5 μM and the titration was performed by gradually adding Fe(II) salt solution. **TPE-TPy2** and **TPE-TPy4** exhibited absorption spectra with maxima at 360 nm and 370 nm, respectively. Titration of Fe<sup>2+</sup> with **TPE-TPy2** molecule revealed the enhancement of characteristic iron metallo-polymer bands at 585 nm (MLCT) and 430 nm,<sup>27,34</sup> with a gradual decrease in absorbance at 360 nm (Figure 3.10A). These bands ultimately achieved their maximum with the addition of up to 1 equivalent of iron (II) salt. Figure 3.10B depicts the variation in absorption maximum at 585 nm with regard to the concentration of Fe<sup>2+</sup>. The maximum absorption value was attained at an equivalent molar concentration, and further addition had no effect on absorption. The binding stoichiometry of **TPE-TPy2** to Fe<sup>2+</sup> is therefore determined to be 1:1. Further, **TPE-TPy4** also demonstrated the formation of new bands at 580 nm and 420 nm, upon addition of Fe<sup>2+</sup> ions (Figure 3.10C), with concomitant decrease of absorbance at 370 nm. The characteristic MLCT for **TPE-TPy4** - Fe(II) complex at 580 nm gets saturated

when the concentration of iron (II) solution is more than 9  $\mu\text{M}$  (approximately twice the concentration of the ligand), indicating a 1:2 stoichiometry for the interaction between **TPE-TPy4** and  $\text{Fe}^{2+}$  ions. The plot of the variation in the absorption maximum at 580 nm with the addition of  $\text{Fe}^{2+}$  is shown in Figure 3.10D.

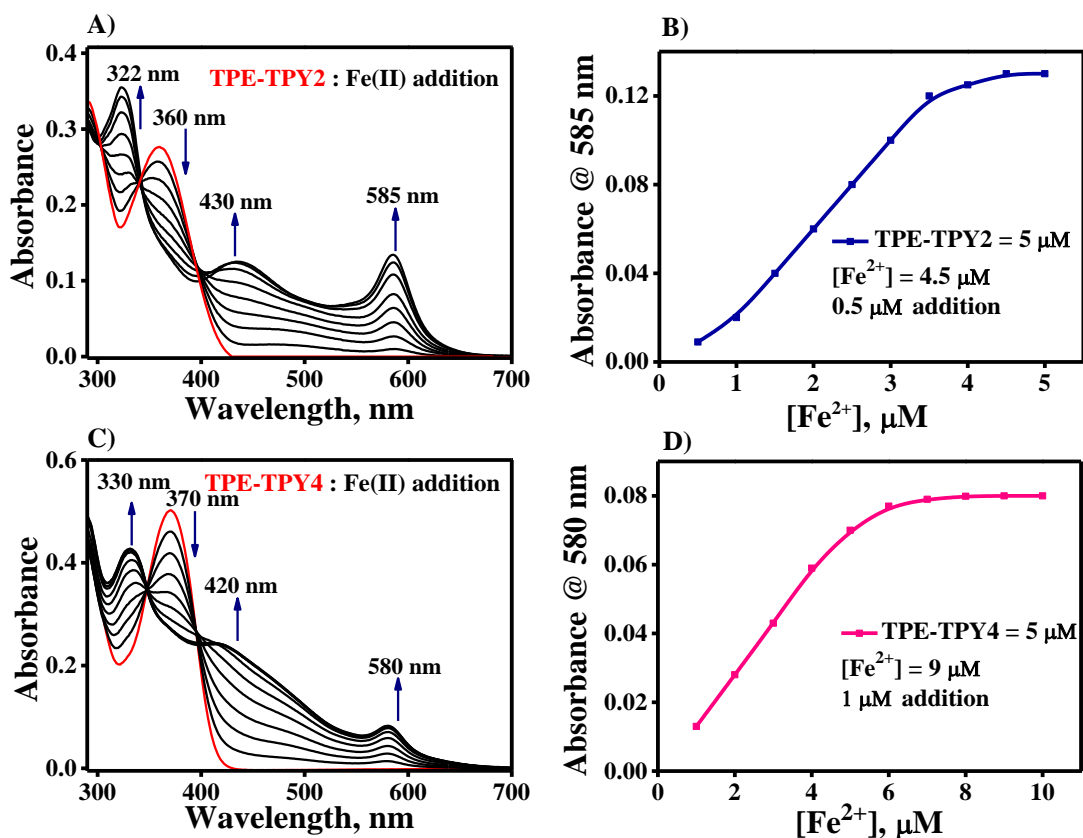


**Figure 3.10.** UV-Vis absorption spectra of (A) **TPE-TPy2** and (B) **TPE-TPy4** in presence of different concentrations of  $\text{Fe}(\text{II})$  in THF. [**TPE-TPy2**] and [**TPE-TPy4**] = 5  $\mu\text{M}$ ; The variation in absorption maximum vs  $[\text{Fe}^{2+}]$  recorded at (C) 585 nm for **TPE-TPy2**, and (D) 580 nm for **TPE-TPy4**.

As terpyridine is a renowned metal chelating ligand, we have explored the interactions of  $\text{Fe}^{2+}$  with **TPE-TPy2** and **TPE-TPy4** and found out the binding stoichiometry for the ligands and  $\text{Fe}^{2+}$  using the Job's plot method.<sup>35,36</sup> In order to determine the stoichiometry, the mole fraction of  $\text{Fe}^{2+}$  is varied from 0 to 1, while the sum of the concentrations of  $\text{Fe}^{2+}$  and ligand is kept constant (5  $\mu\text{M}$ ). The Job's plot of

the ligand **TPE-TPy2** and metal ion showed a maximum absorbance when the mole fraction of the  $\text{Fe}^{2+}$  reached 0.5 at 585 nm, indicating a 1:1 binding stoichiometry between the  $\text{Fe}^{2+}$  ion and **TPE-TPy2** (Figure 3.11A). While in the case of **TPE-TPy4**, the mole fraction of  $\text{Fe}^{2+}$  at the maximum absorbance measured at 580 nm was 0.66, reflecting a 2:1 stoichiometry between the  $\text{Fe}^{2+}$  and ligand (Figure 3.11B).

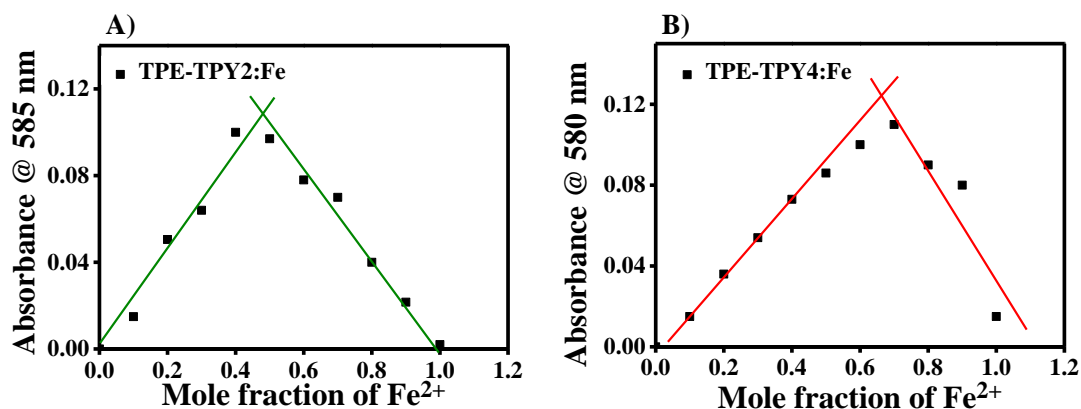


**Figure 3.11.** Dependence of the absorbance at 585 nm and 580 nm for (A) **TPE-TPy2** and (B) **TPE-TPy4**, respectively, vs the  $\text{Fe}^{2+}$  mole fraction (ratio of concentration of  $\text{Fe}^{2+}$  ion to that of the total ligand and  $\text{Fe}^{2+}$  ( $5 \mu\text{M}$ )).

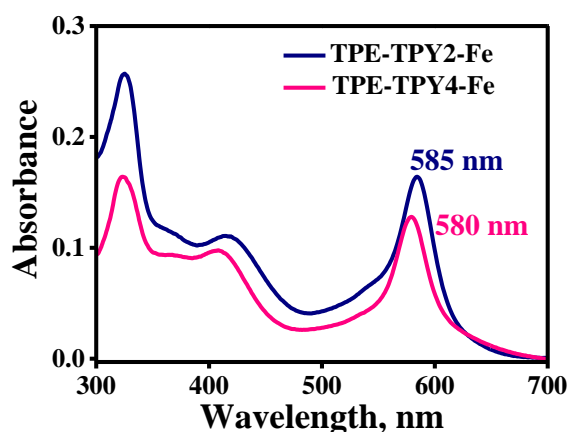


**Figure 3.12.** UV-Vis absorption spectra of **TPE-TPy2-Fe** and **TPE-TPy4-Fe** polymers in acetonitrile.

The metallo-polymers **TPE-TPy2** and **TPE-TPy4** were synthesized by refluxing the ligands with iron(II) perchlorate hydrate in 1:1 and 1:2 molar ratios of **TPE-TPy2** and **TPE-TPy4**, respectively. Then a saturated solution of ammonium

hexafluorophosphate in water was added and the iron-hexafluorophosphate salt of the respective polymers were precipitated out. Synthetic details are discussed in detail in the experimental section. The characteristic UV-Vis spectra of the metallopolymers in acetonitrile are shown in Figure 3.12.

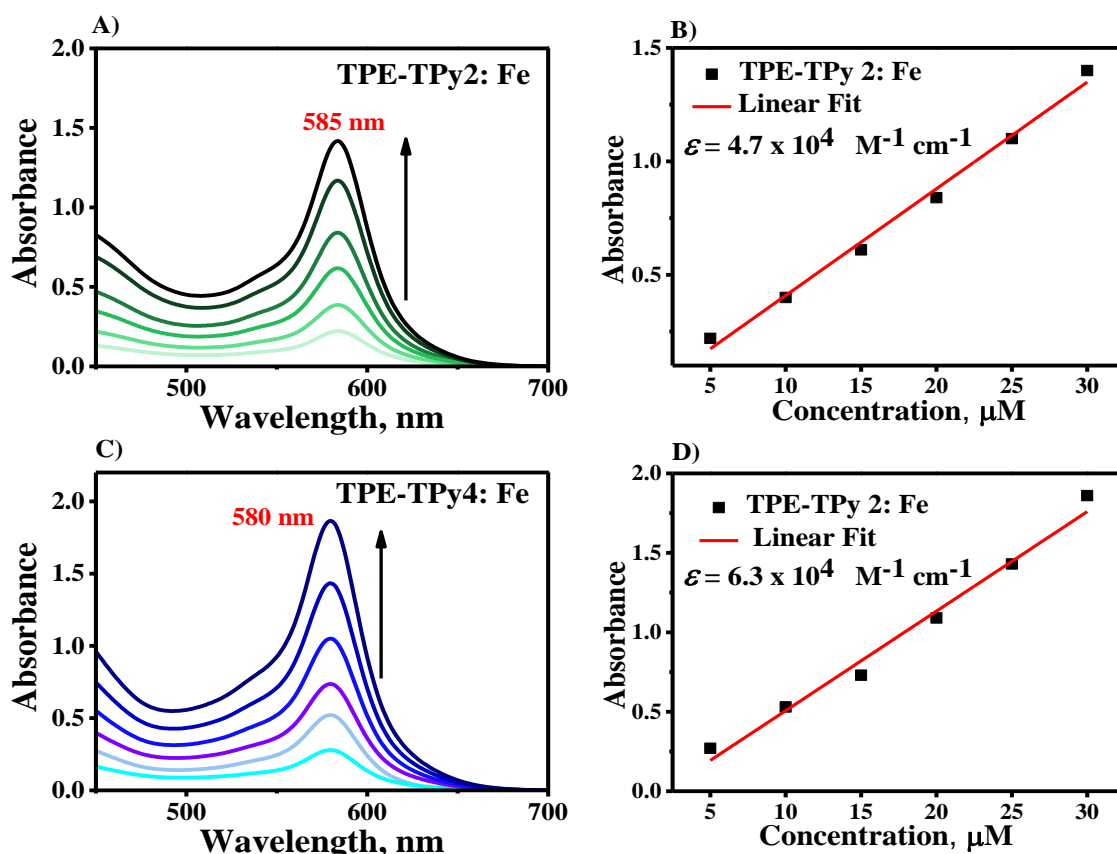


**Figure 3.13.** Concentration dependent UV spectra of (A) TPE-TPy2-Fe and (C) TPE-TPy4-Fe [5 -30 μM] and the linear correlation between the MLCT band intensity and concentration of (B) TPE-TPy2-Fe and (D) TPE-TPy4-Fe.

The strong peaks in the range of 580/585 nm by both the MPs were caused by MLCT - transition from the metal centers to the unfilled  $\pi^*$ - based LUMO of the ligand, with high extinction coefficients of  $4.7 \times 10^4 \text{ M}^{-1} \text{ cm}^{-1}$  for TPE-TPy2-Fe and  $6.3 \times 10^4 \text{ M}^{-1} \text{ cm}^{-1}$  for TPE-TPy4-Fe. These characteristics align with typical MLCT band formations, characterized by intense and strong absorption bands in the visible region, accompanied by high molar extinction coefficients ( $\epsilon \sim 10^4 \text{ M}^{-1} \text{ cm}^{-1}$ ), (Figure

3.13).<sup>37</sup> The spectra of the synthesized MPs match those of the ligand - iron salt titration, confirming the metal - ligand interactions.

Furthermore, the iron-terpyridine polymers were studied using  $^1\text{H}$  NMR spectroscopy and the downfield shifting and broadened spectrum revealed the ligand - metal coordinative interaction. **TPE-TPy4-Fe** polymers displayed more broad signals than **TPE-TPy2-Fe** polymers because of a reduction in tumbling speed on the NMR time scale, confirming extensive polymerization (Figure 3.14).<sup>38,39</sup>

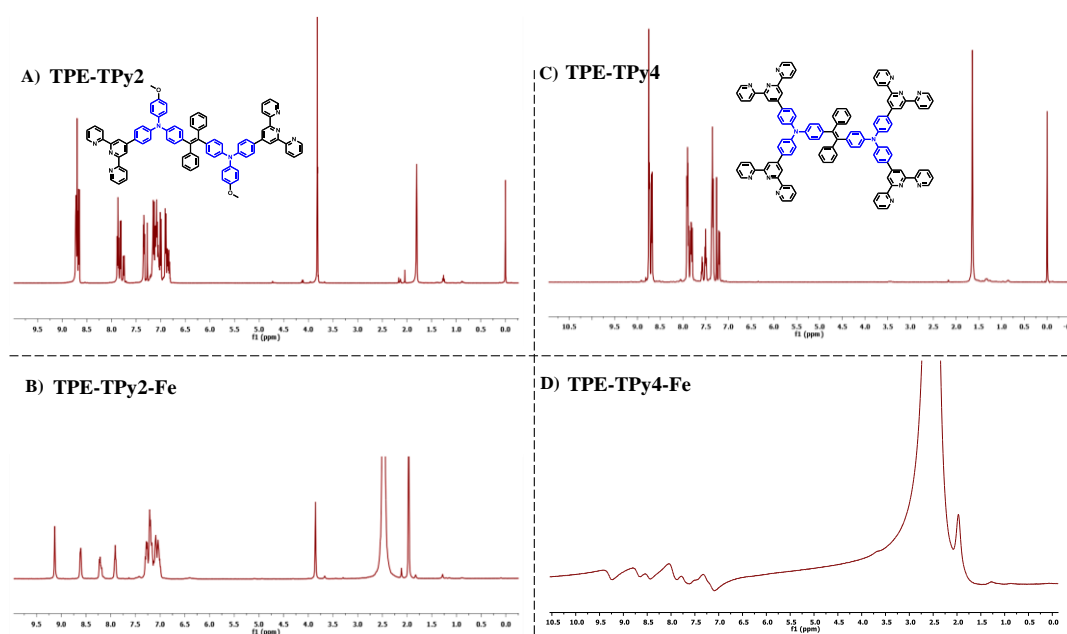


**Figure 3.14.**  $^1\text{H}$  NMR spectrum of (A) **TPE-TPy2** in  $\text{CDCl}_3$  and (B) **TPE-TPy2-Fe** in acetonitrile- $d_3$ ;  $^1\text{H}$  NMR spectrum of (C) **TPE-TPy4** in  $\text{CDCl}_3$  and (D) **TPE-TPy4-Fe** in acetonitrile- $d_3$ .

FT-IR analyses of monomers and polymers were used to acquire further confirmation regarding polymer formation and are shown in Figures 3.15A and 3.15B. The C=C stretching frequencies of **TPE-TPy2** and **TPE-TPy4** are slightly shifted to  $1589\text{ cm}^{-1}$  and  $1590\text{ cm}^{-1}$ , respectively, after polymerization.<sup>25,40</sup> TGA analyses of metallo-polymers were performed in a  $\text{N}_2$  atmosphere (Figure 3.15C). Both polymers lost nearly 20% of their weight when the temperature was elevated to  $500\text{ }^\circ\text{C}$ . When

the temperature was raised to 1000 °C, additional 35% loss in **TPE-TPy2-Fe** and 25% loss in **TPE-TPy4-Fe** was observed due to the breakdown of the polymers' main aromatic moieties.<sup>40,41</sup> Compared to linear **TPE-TPy2-Fe**, the hyperbranched **TPE-TPy4-Fe** polymer showed greater thermal stability similar to its parent ligand.

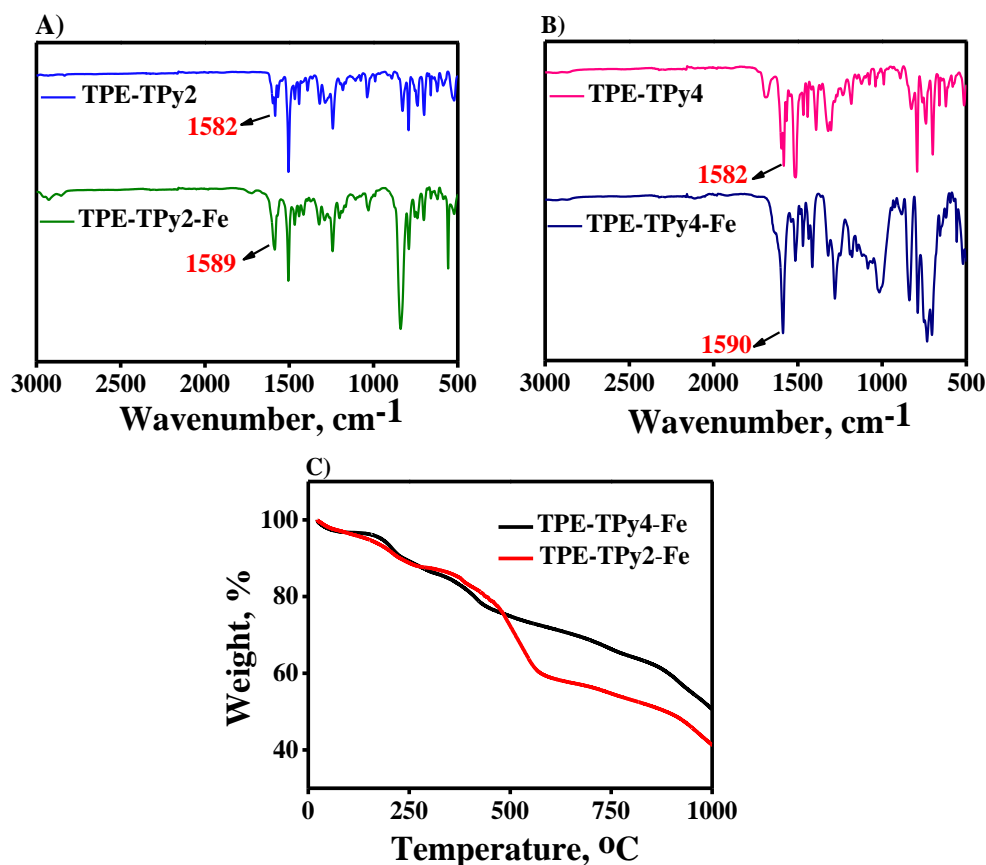


**Figure 3.15.** FT-IR spectra of (A) **TPE-TPy2-Fe** and (B) **TPE-TPy4-Fe**; (C) TGA analysis of the metallo-polymers.

The qualitative and quantitative analyses of the elements of both ligands and MPs were examined by means of XPS. XPS data of both the ligands and metallo-polymers showed the characteristic peaks corresponding to nitrogen. N 1s XPS spectra of both the ligands showed two nitrogen species correspond to terpyridine - nitrogen and triphenylamine - nitrogen at 398 eV and 400 eV, respectively. The ratio of the two N 1s (N<sub>TPA 1s</sub>:N<sub>Terpyridine 1s</sub>) peaks of **TPE-TPy2-Fe** and **TPE-TPy4-Fe** were 1:3.19 and 1:6.3, which is very close to the ideal values (1:3 for **TPE-TPy2-Fe** and 1:6

for **TPE-TPy4-Fe**) as in Figures 3.16A and 3.16C. However, the N 1s peaks of metallo-polymer showed one extra peak at 399 eV, which represents the Fe(II)-coordinated nitrogen (Figures 3.16B and 3.16D).

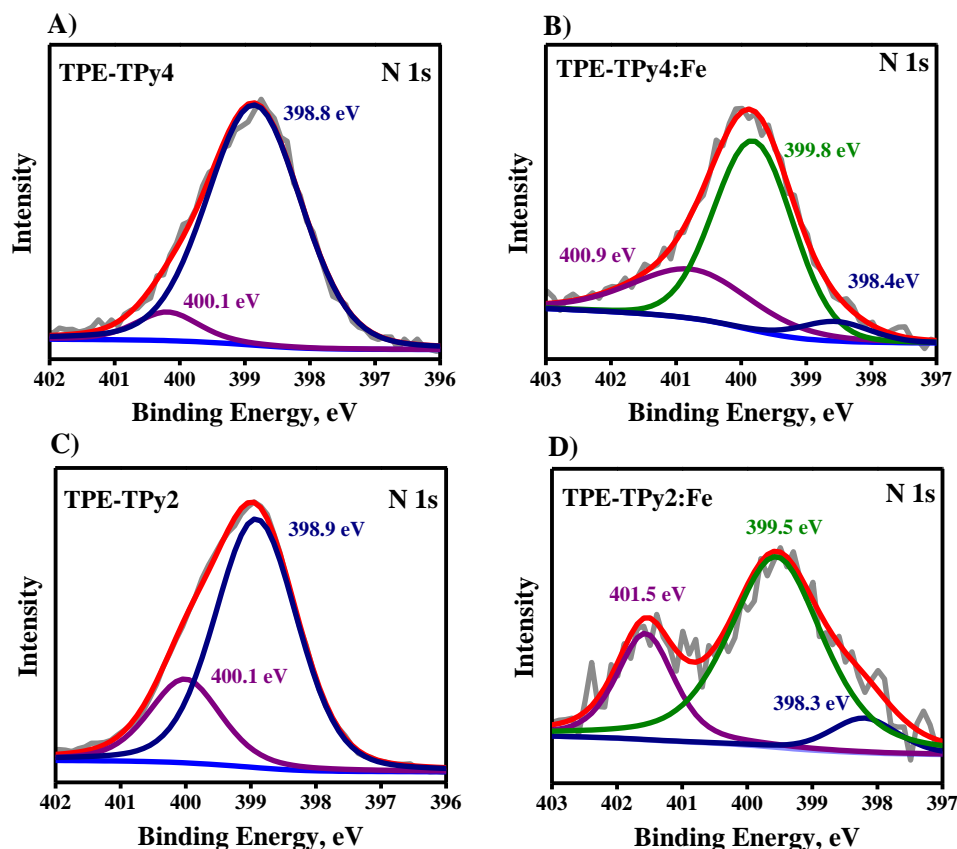


**Figure 3.16.** HR-XPS spectra of N 1s of (A) **TPE-TPy4**; (B) **TPE-TPy4-Fe**; (C) **TPE-TPy2** and (D) **TPE-TPy2-Fe**.

The peaks at 398 eV correspond to the free terpyridine-nitrogen due to the incomplete coordination. The ratio of the coordinated and uncoordinated terpyridine N 1s peaks of metallo-polymers reflects the level of degree of coordination in these assemblies. **TPE-TPy2-Fe** exhibited a ratio of  $\sim 1:5.9$  free terpyridine and coordinated nitrogen, while **TPE-TPy4-Fe** showed a ratio of  $\sim 1:8.5$ . The lower ratio of free terpyridine nitrogen for **TPE-TPy4-Fe** indicates that **TPE-TPy4-Fe** has been polymerized more extensively than **TPE-TPy2-Fe**.

The surface morphology of the spray coated films were analyzed using AFM. Figure 3.17 shows the AFM images and the inset images are the photographs of the spray coated films on FTO. The AFM images of hyperbranched **TPE-TPy4-Fe** polymer showed uniformly distributed grain like structures with root mean square average (Rq) and arithmetic average (Ra) values of 30.2 nm and 23.9 nm, respectively. **TPE-TPy2-Fe** showed comparatively higher roughness values with more clustered grains. The Rq and Ra values of **TPE TPy2-Fe** were 33.7 nm and 25.3 nm, respectively.

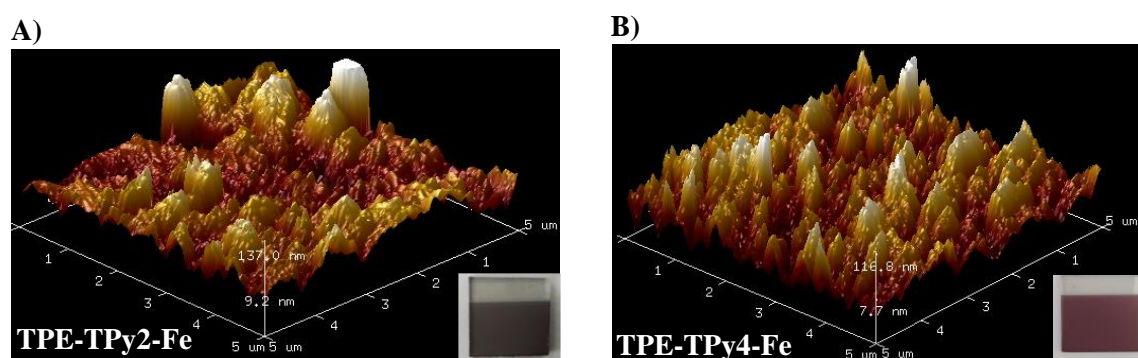


**Figure 3.17.** Atomic force microscopy (AFM) images showing the surface morphology of spray coated (A) **TPE-TPy2-Fe** and (B) **TPE-TPy4-Fe** films on FTO; Inset images are the photographs of spray coated polymer films.

The CV of the films were performed using a three-electrode setup using Ag/AgCl and Pt wire as reference and counter electrode, respectively, in an aqueous solution of 0.1 M LiClO<sub>4</sub> electrolyte. At 50 mV/s scan rate, both polymers exhibited reversible redox peaks with halfwave potentials of 0.72 V and 0.7 V for **TPE-TPy2-Fe** and **TPE-TPy4-Fe**, respectively. Peaks corresponding to triphenylamine oxidations and metal ion oxidation overlap in the same region at all scan rates for the polymer films and are shown in Figures 3.18A and 3.18B. To further understand the process, we examined the relationship between the anodic (ipa) and cathodic (ipc) peak currents with scan rate. The rate-determining step can be the diffusion of ionic species from the bulk



solution to the electrode surface when the peak currents are linearly proportional to the square root of the scan rate, whereas when the peak currents are linearly

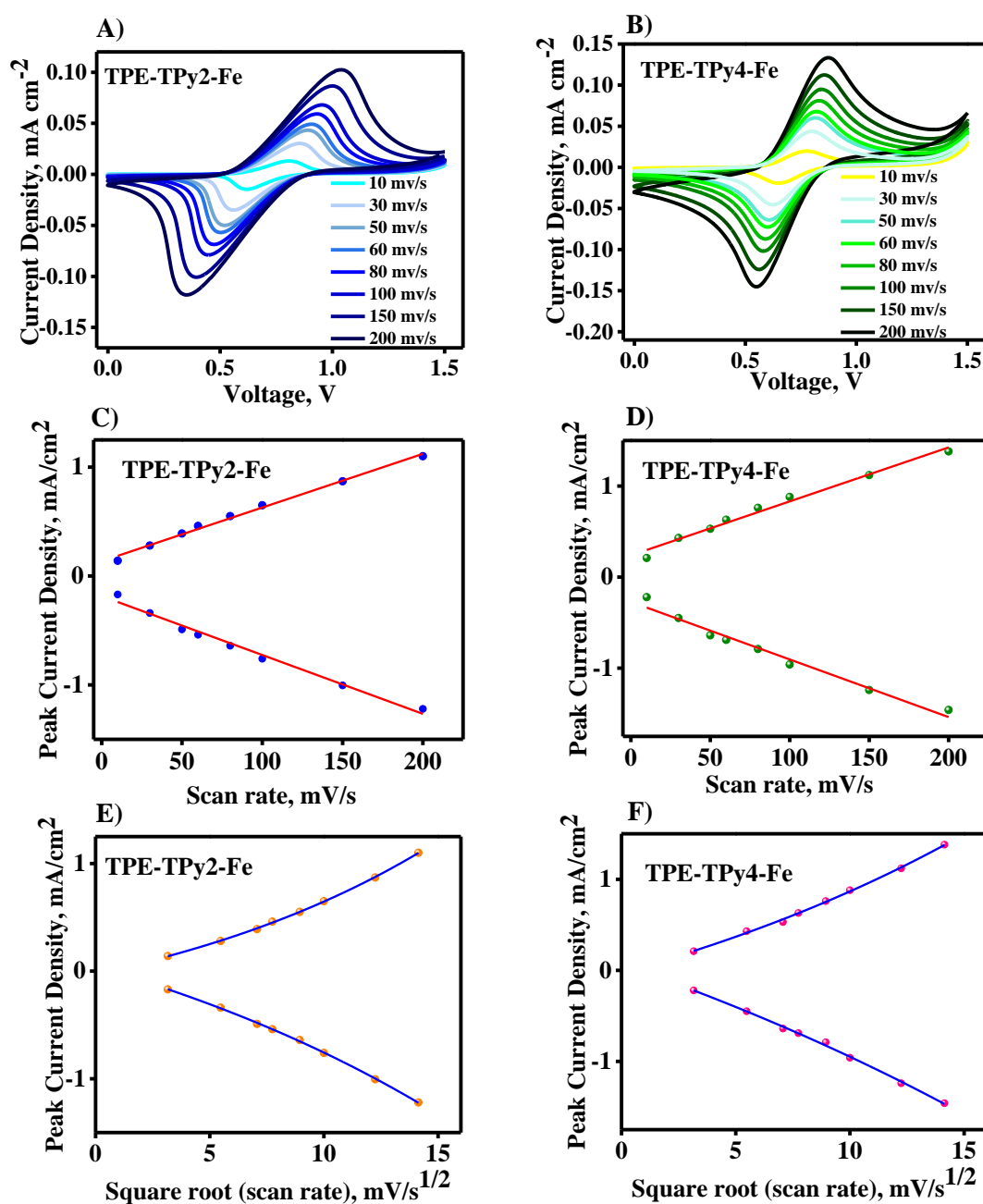


**Figure 3.18.** Cyclic voltammograms of metallo-polymers constructed from (A) **TPE-TPy2-Fe** and (B) **TPE-TPy4-Fe** at different scan rates; Linear correlation between the current densities and scan rate (C and D) and exponential correlation between the current densities and square root of scan rate (E and F) for **TPE-TPy2-Fe** and **TPE-TPy4-Fe**, respectively. All experiments were carried out using Ag/AgCl and Pt wire as reference and counter electrode, respectively. 0.1 M LiClO<sub>4</sub> in water was used as the supporting electrolyte.

proportional to the scan rate, the rate-determining step becomes the surface - controlled or kinetically controlled electrochemical process.<sup>29,41</sup> The Figures 3.18C - 3.18F indicate that peak currents increase linearly with scan rate and nonlinearly with the square root of scan rate. These studies proved that the redox process in both films are based on surface-confined electrochemical processes that are not constrained by the diffusion of ions in bulk solution.

During the cyclic voltammetry experiments, the redox process was followed by a reversible color change from a dark greyish blue to yellow in the case of **TPE-TPy2-Fe** polymer and purple to green in the case of **TPE-TPy4-Fe** polymer. The photographs of the film at 0 V and 1.2 V in 0.1 M LiClO<sub>4</sub>-water electrolyte and the associated CIE coordinates are shown in Figures 3.19A - 3.19D. The cyclic voltammogram of metallo-polymer films at a 50 mV/s scan rate demonstrated good electrochemical stability in an aqueous solution of 0.1 M LiClO<sub>4</sub> electrolyte even after 50 CV cycles (Figures 3.19E and 3.19F). EC characteristics of the metallo-polymers were further investigated using a spectro-electrochemical experiment in an aqueous solution of 0.1 M LiClO<sub>4</sub> electrolyte with a Pt (counter electrode) and Ag/AgCl (reference electrode). The spectral variations were examined using potentials ranging from 0 V to 1.2 V. Both polymers showed an MLCT charge transition band in their neutral states at 0 V. As the potential increased, the **TPE-TPy2-Fe** polymer changed color from a dark greyish blue to yellow, along with a reduction in the MLCT band and emergence of two additional bands. The typical TPA oxidation band developed as a small, but wide band from 800 nm to 1000 nm, with a maximum at 880 nm (Figure 3.20A). **TPE-TPy4-Fe** polymers demonstrated a broad absorption band ranging from 690 nm to 1000 nm with higher absorption intensity and a maximum at 790 nm, compared to **TPE-TPy2-Fe** polymers. At the same time, a small absorption peak at

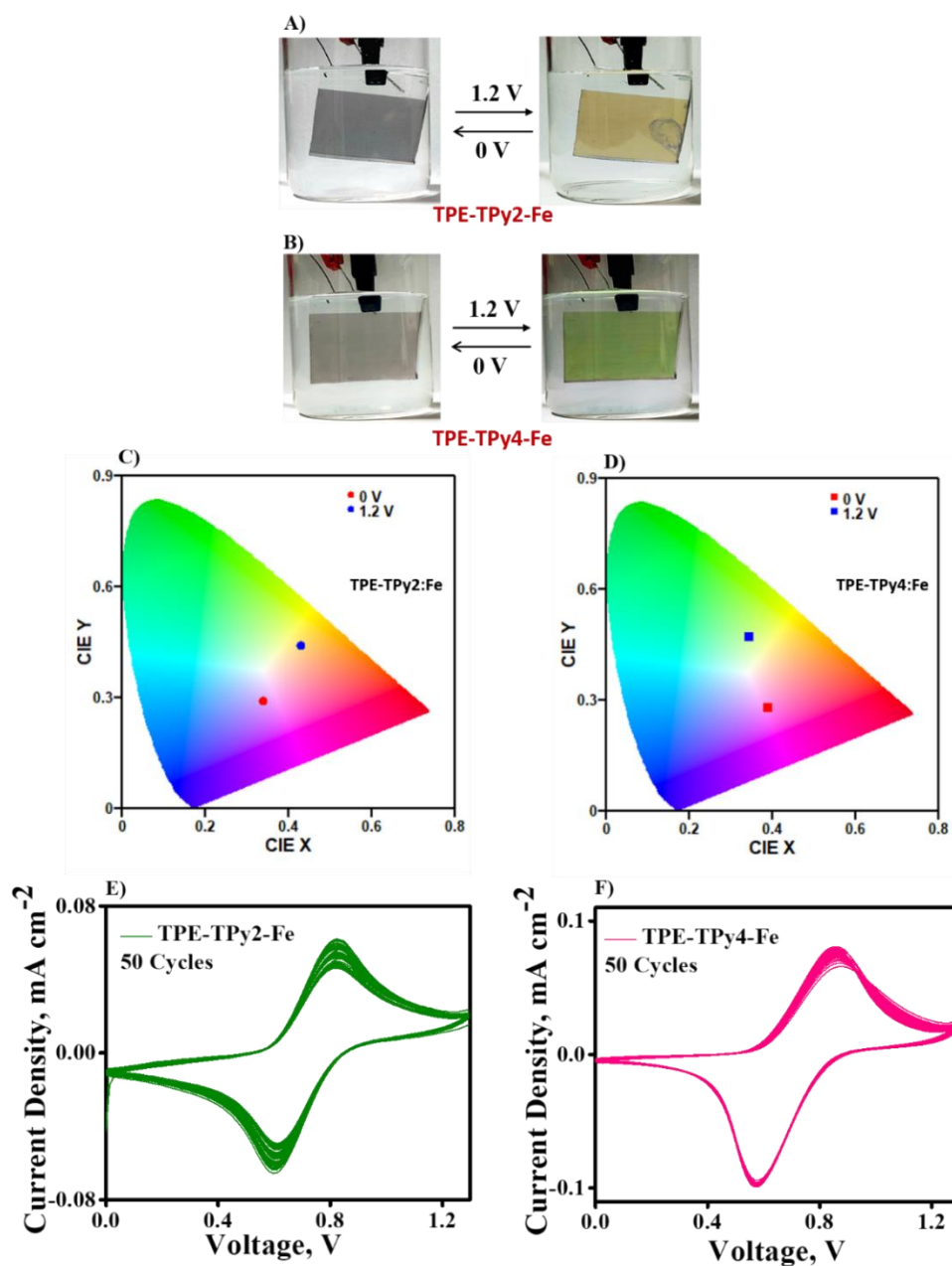


**Figure 3.19.** The photographs of the (A) TPE-TPy2-Fe and (B) TPE-TPy4-Fe polymers spray coated on FTO substrates at 0 V and 1.2 V in an aqueous solution of 0.1 M LiClO<sub>4</sub> electrolyte; CIE color coordinates of the (C) TPE-TPy2-Fe and (D) TPE-TPy4-Fe films at 0 V and 1.2 V; 50 CV cycles of (E) TPE-TPy2-Fe and (F) TPE-TPy4-Fe films at a scan rate of 50 mV/s.

480 nm appeared, which was connected with the oxidation of Fe(II) ions (Figure 3.20B). A color change from purple to green was observed during the redox processes.

The films' spectroelectrochemistry indicated simultaneous changes associated with the oxidation of triphenylamine groups and the Fe(II).

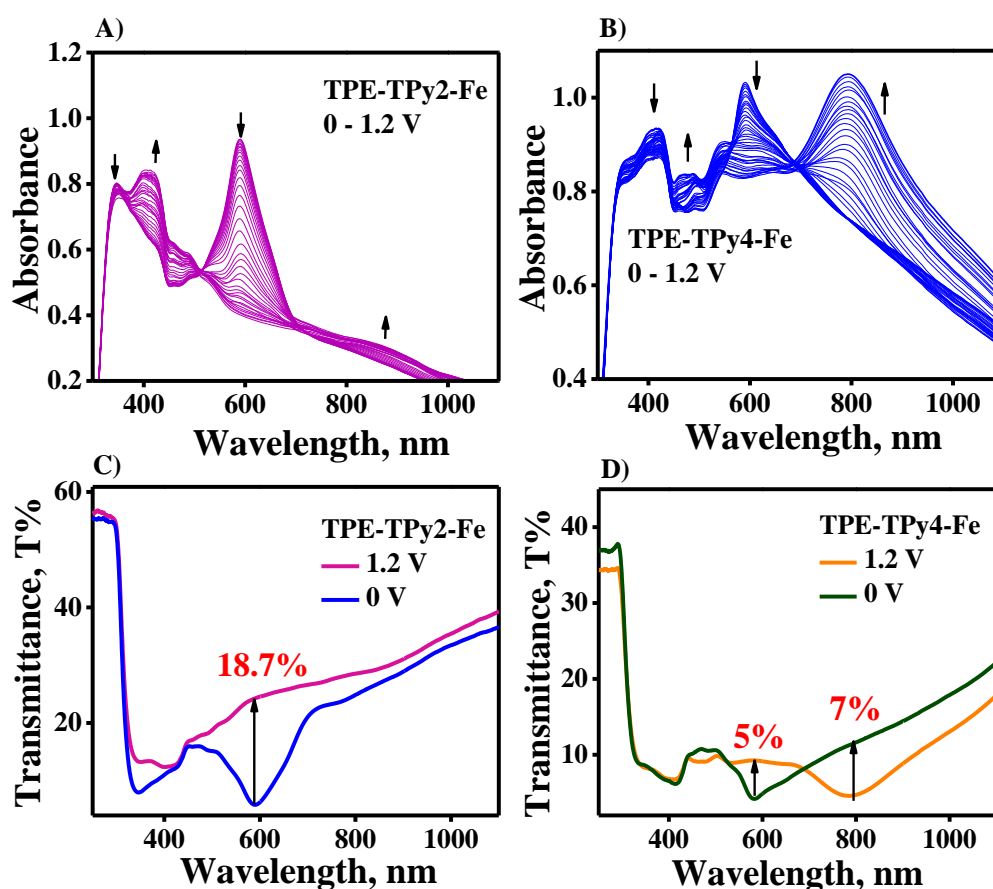


**Figure 3.20.** UV-Vis absorption spectral changes of (A) **TPE-TPy2-Fe** and (B) **TPE-TPy4-Fe** films spray coated on FTO substrate at various applied potentials from 0 V to 1.2 V; Transmittance spectra of (C) **TPE-TPy2-Fe** and (D) **TPE-TPy4-Fe** polymers on FTO substrates in their oxidised (1.2 V) and reduced (0 V) state.

The transmittance study was carried out to understand the optical contrast of polymers in their oxidized and reduced states. **TPE-TPy2-Fe** and **TPE-TPy4-Fe** polymers demonstrated about 18.7% and 5% change in transmittance at 585 nm and 580 nm, respectively, while **TPE-TPy4-Fe** polymer demonstrated 7% transmittance change at 790 nm, as shown in the Figures 3.20C and 3.20D.

To investigate the cyclic stability, we measured the change in transmittance of the MLCT peak at their respective wavelengths while the potential was cycled

between 0 V and 1.2 V at a 10 s pulse width. Even after 300 cycles, both **TPE-TPy4-Fe** and **TPE-TPy2-Fe** films displayed stable color change with no substantial decrease in transmittance, as illustrated in Figures 3.21A – 3.21C.

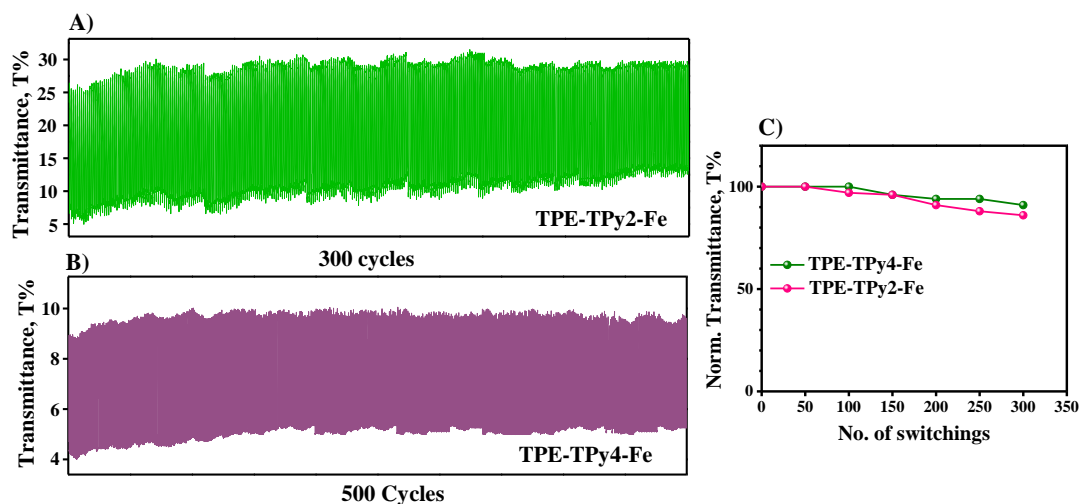


**Figure 3.21.** Electrochromic switching experiments for (A) **TPE-TPy2-Fe** (at 585 nm) and (B) **TPE-TPy4-Fe** (at 580 nm) films on FTO for 300 and 500 switching cycles, respectively with 10 s pulse width; (C) A secondary plot showing the variation in stability with the number of switching cycles.

The time required for the coloration/bleach to reach more than 90% of its maximum color for **TPE-TPy2-Fe** and **TPE-TPy4-Fe**, respectively, were 3.4 s and 2.8 s for oxidation and 1 s and 0.9 s for reduction. The single coloration and bleaching cycles are shown in Figures 3.22A and 3.22B. The memory ability of electrochromic **TPE-TPy2-Fe** and **TPE-TPy4-Fe** polymer films were examined, which may be described as the films' capability to maintain the transmittance after the potential was switched off. The **TPE-TPy2-Fe** film had a shorter memory than the **TPE-TPy4-Fe** film, which took less than 30 seconds to regain the initial transmittance. In the case of **TPE-TPy4-Fe**, 75% of the oxidation state transmittance remained unchanged more than half an hour after the applied voltage was removed (Figure 3.22C). This implies that the ligand alters a material's optical memory regardless of the binding metal ion.

As the ligand's rigidity rises, so does the stability of the oxidation state of the metal ion ( $\text{Fe}^{3+}$ ), which improves the electrochromic film's memory.

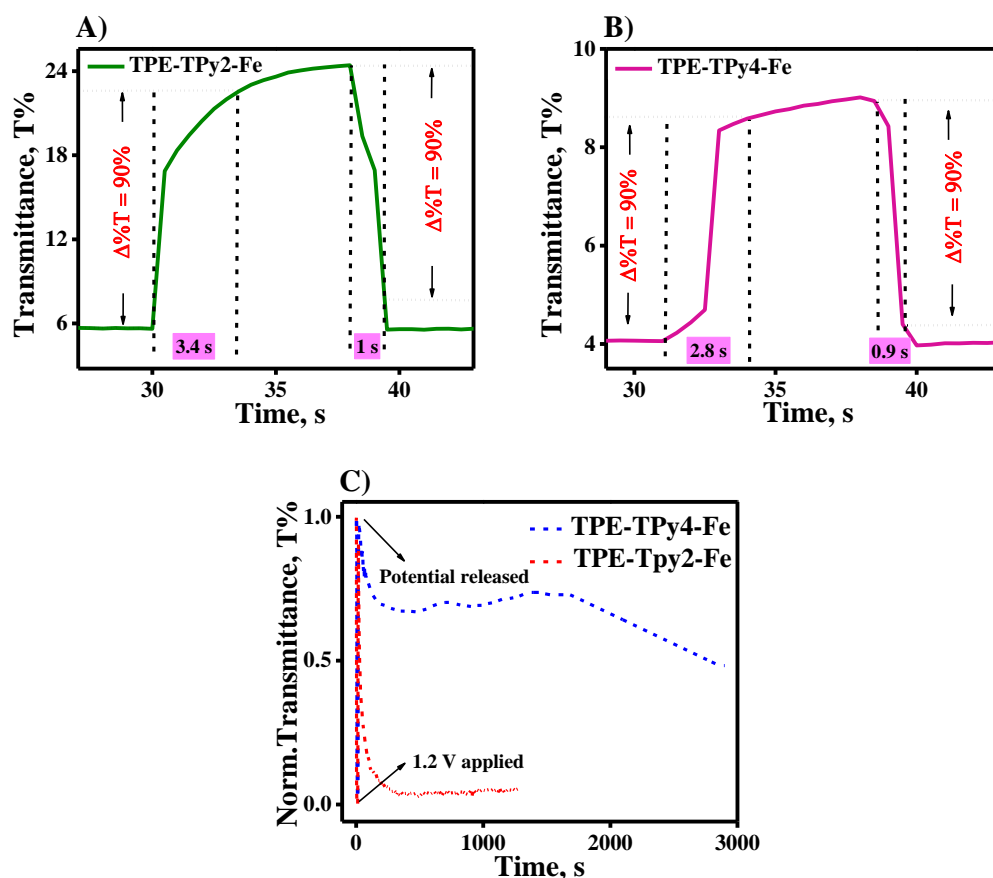


**Figure 3.22.** The response times for the (A) **TPE-TPy2-Fe** (at 585 nm) and (B) **TPE-TPy4-Fe** (at 580 nm) polymers on FTO substrates at 10 s pulse width and (C) Optical memory effect of the metallo-polymers on FTO after the potential at 1.2 V vs Ag/AgCl was released (measured at their MLCT wavelength).

From the film studies, we observed that **TPE-TPy4-Fe** polymer possesses dominant triphenylamine characteristic features such as NIR absorption in spectroelectrochemistry experiments and better optical memory than **TPE-TPy2-Fe** polymer.<sup>27</sup> The coloration efficiency ( $\eta$ ) is defined as the degree of optical density change ( $\Delta OD$ ) caused by the electronic charge that is injected or ejected ( $Q_d$ ). The coloration efficiency ( $\eta$ ) values of the spray coated metallo-polymer films on FTO in an aqueous solution of 0.1 M  $\text{LiClO}_4$  electrolyte were calculated. The charge density

for **TPE-TPy2-Fe** and **TPE-TPy4-Fe**, obtained from the chronoamperometric studies (Figure 3.23) were  $3.067 \times 10^{-3} \text{ C/cm}^2$  and  $1.45 \times 10^{-3} \text{ C/cm}^2$ , respectively. The hyperbranched metallo-polymer **TPE-TPy4-Fe** showed higher coloration efficiency with a value of  $243 \text{ cm}^2 \text{ C}^{-1}$  at 580 nm than linear **TPE-TPy2-Fe** which has a coloration efficiency of  $205 \text{ cm}^2 \text{ C}^{-1}$  measure at 585 nm.

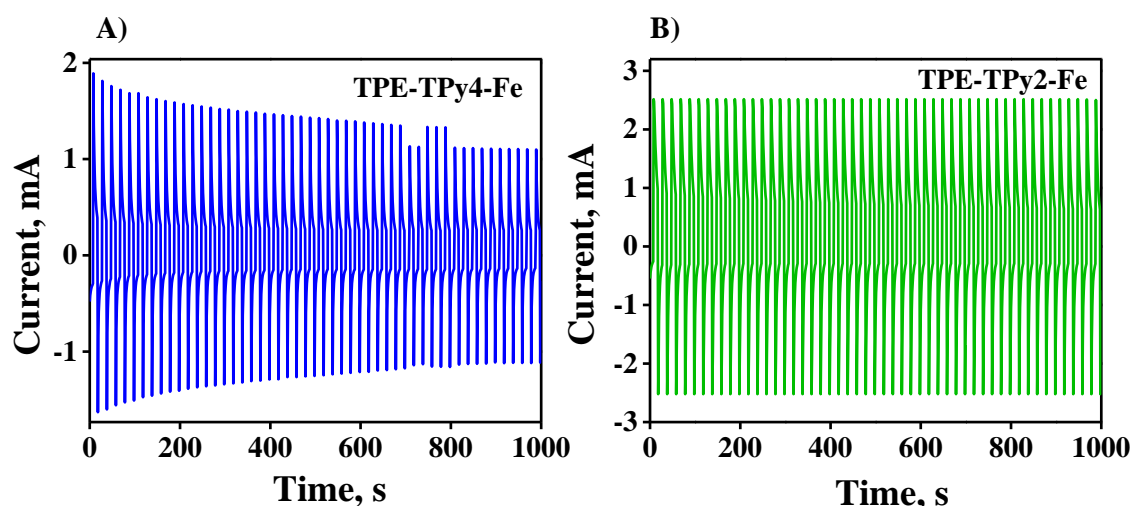


**Figure 3.23.** The chronoamperometric studies of (A) **TPE-TPy4-Fe** and (B) **TPE-TPy2-Fe** polymers on FTO substrates at 10 s pulse width; (Electrode area used was  $5 \text{ cm}^2$ ).

### 3.4. Conclusions

Two Fe(II)-based metallo-polymers with TPE-Diphenylamine-Terpyridine ligands (**TPE-TPy2-Fe** and **TPE-TPy4-Fe**) were synthesized and the structures were confirmed by UV-Vis absorption, FT-IR,  $^1\text{H}$  NMR and XPS studies. The surface-confined electrochemical processes were detected via the non-linear connection between the peak current and the root of the scan rate during the redox processes. The CV analyses showed a reversible redox peak and color change with  $\Delta T\%$  of 18.7% and 5% at 585 nm and 580 nm, respectively, for **TPE-TPy2-Fe** and **TPE-TPy4-Fe** polymers. The hyperbranched **TPE-TPy4-Fe** metallo-polymer displayed better open circuit memory (75% of the oxidation state transmittance remained unchanged for

more than 30 minutes), a lower switching time (2.8 s for oxidation and 0.9 s for reduction) and higher coloration efficiency ( $243 \text{ cm}^2 \text{ C}^{-1}$  at 585 nm) than that of the **TPE-TPy2-Fe** linear polymer. These results reveal the effect of ligand structures on the characteristics of metallo-polymers via changing the structure, as well as a molecular design for an electrochromic material with high open circuit memory and shorter switching kinetics.

### **3.5. Experimental Section**

#### **3.5.1. Materials and Methods**

The chemicals and solvents used in the study were purchased from Sigma-Aldrich, Merck, Spectrochem, and Alfa Aesar. Unless specifically mentioned, all reagents were used as received without further purification. Dry solvents and an argon environment were used to perform moisture- and oxygen-sensitive reactions. Organic extracts were dried using anhydrous sodium or magnesium sulfate powder, while solvents were removed under reduced pressure using a rotary evaporator. The FTO substrate, with a surface resistivity of  $10 \text{ } \Omega/\text{sq}$ , was purchased from Sigma-Aldrich. Prior to use, the FTO substrate underwent a cleaning process involving sonication in water, acetone, and isopropyl alcohol for 15 minutes each. The proton ( $^1\text{H}$ ) and carbon-13 ( $^{13}\text{C}$ ) nuclear magnetic resonance (NMR) spectra were acquired at 300K on a DPX 500 MHz spectrometer using tetramethylsilane as the internal standard. ESI-HRMS spectra were obtained using a JEOL JSM 600. Shimadzu IR Prestige- 21 Fourier Transform Infrared Spectrophotometer was used to record infrared spectra in solid-state (KBr). The solution state absorbance was measured with a Shimadzu UV-Vis spectrophotometer (UV-2600), and the film state absorbance and transmittance were measured with an Ocean Optics UV-VIS modular



spectrophotometer (DH-2000-BAL). TGA studies were carried out using a Shimadzu DTG-60 instrument in a nitrogen atmosphere at a heating rate of 10 °C/minute. The thickness of the samples were measured using Dektak XT profilometer. AFM images of the films were captured using an AFM-Bruker Multitop Nanoscope V instrument in tapping mode, and the roughness of the films was determined using Nanoscope Analysis 1.5 software. Spray coating was carried out using the Nordson EFD EV Series automated dispensing system and the programs were created using the Dispense Motion software. The electrolyte for the electrochemical experiments was made by dissolving the calculated amount of anhydrous lithium perchlorate ( $\text{LiClO}_4$ ) of analytical reagent grade in Millipore Milli-Q water. Under Argon atmosphere, cyclic voltammetry was performed on liquid and film samples using 0.1 M TBAPF<sub>6</sub> in chlorobenzene and an aqueous solution of 0.1 M  $\text{LiClO}_4$  as supporting electrolyte, respectively, glassy carbon as working electrode, Ag/AgCl electrode as reference electrode and platinum wire as counter electrode on PARSTAT 4000A Potentiostat. The Ocean Optics Spectrometer DH-2000-BAL was used to record the spectroelectrochemistry of electrochromic polymer films and for the electrochemical redox process, a PARSTAT 4000A Potentiostat was used. The film's spectroelectrochemical responses were measured by immersing them in 0.1 M  $\text{LiClO}_4$  aqueous solution and using an Ag/AgCl electrode and a Pt wire as the reference and counter electrodes, respectively. The blank measurement was performed in a cuvette with a 1 cm path length using bare FTO in an aqueous solution of 0.1 M  $\text{LiClO}_4$ . The CIE coordinate values for the colors were determined using a HunterLab - UltraScan VIS Spectrophotometer, 110 V/220 V w/SAV & UV control, and EasyMatch QC version 4.0 software. X-ray photoelectron spectroscopy, PHI 5000 VersaProbe II, ULVAC-PHI Inc., USA was used for recording the high-resolution spectra of the major elements

which is equipped with a microfocussed (200  $\mu\text{M}$ , 15 KV) monochromatic Al-K $\alpha$  X-ray source ( $h\nu = 1486.6 \text{ eV}$ ) and the data was processed using PHI's Multipak software.

### **3.5.2. Synthesis of Metallo-polymers**

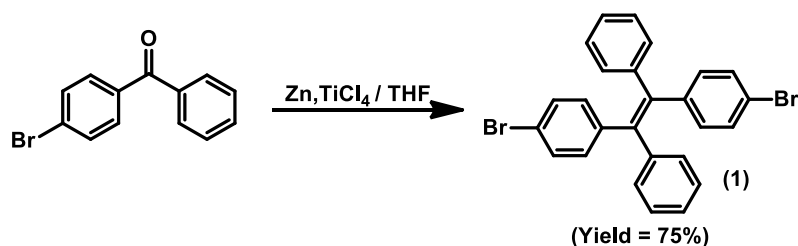
In a two-necked round-bottom flask, an equimolar amount of the ligand, **TPE-TPy2** (200 mg, 0.17 mmol) or **TPE-TPy4** (200 mg, 0.125 mmol) in THF and Iron (II) perchlorate hydrate ( $\text{Fe}(\text{ClO}_4)_2 \cdot 6\text{H}_2\text{O}$ ) in methanol (42.7 mg, 0.17 mmol for **TPE-TPy2-Fe** preparation and 63.7 mg, 0.25 mmol for **TPE-TPy4-Fe** preparation) were heated to reflux overnight at 67  $^\circ\text{C}$ . The reaction solution was cooled to room temperature and a saturated aqueous solution of ammonium hexafluorophosphate was added and stirred for one hour. The solution was filtered and the precipitate was washed with water and ether. Finally, the solid was dried under vacuum for overnight.

### **3.5.3. Polymer Film Preparation**

By using the spray coating technique, the polymer films were prepared on cleaned FTO (resistivity  $\sim 10 \Omega/\text{cm}^2$ ). The bare FTO substrates were exposed to a UV/ozone chamber for 2 minutes before being sprayed, and then an acetonitrile solution of the metallo-polymers (1 mg/ml) was sprayed over the substrates. A 100 ml solution of the metallo-polymers was prepared and filtered to remove small, insoluble particles using a micro syringe filter. The thickness of the films measured using profilometer and **TPE-TPy2-Fe** and **TPE-TPy4-Fe** were found to be  $145 \pm 6 \text{ nm}$  and  $157 \pm 5 \text{ nm}$ , respectively.

### 3.5.4. Synthesis and Characterization of the Molecules

#### 3.5.4.a. Synthesis of 1,2-bis(4-bromophenyl)-1,2-diphenylethylene (1)



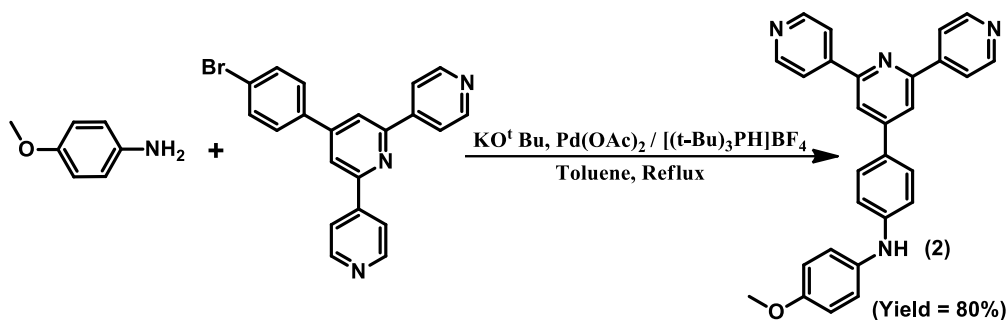
Scheme 3.2.

In a three-neck RB flask with an argon atmosphere, a suspension of Zinc powder (6.3 g, 95.74 mmol) in THF (240 ml) was prepared. TiCl<sub>4</sub> (10.5 ml, 95.74 mmol) was then added dropwise to the suspension. The resultant mixture was refluxed for 4 hours, cooled to room temperature, and then slowly added to a solution of 4-bromobenzophenone (5.00 g, 19.15 mmol) in THF (50 ml). Following a 14-hour period of refluxing, the mixture was cooled to room temperature, diluted with chloroform and saturated sodium bicarbonate solution (until no bubbles emerged), and stirred for 5 hours. The resultant mixture was then extracted with chloroform and water after being filtered through a celite pad. The mixed organic layer was then dried over the solvent and Na<sub>2</sub>SO<sub>4</sub>. The white crude product was then purified by column chromatography using hexane as eluting solvent. The compound was obtained as a white powder (yield = 75%).

<sup>1</sup>H NMR (500 MHz, acetone-d<sub>6</sub>): δ = 7.33 (4H, m), δ = 7.13 (6H, m), δ = 7.03 (4H, m), δ = 6.97 (4H, m).

ESI-HRMS: m/z calculated for (C<sub>26</sub>H<sub>18</sub>Br<sub>2</sub>): 489.9775, Found: 489.9710.

### 3.5.4.b. Synthesis of 4- ([2, 2':6', 2''-terpyridin]-4'-yl)-N-(4-methoxyphenyl)-aniline (2)



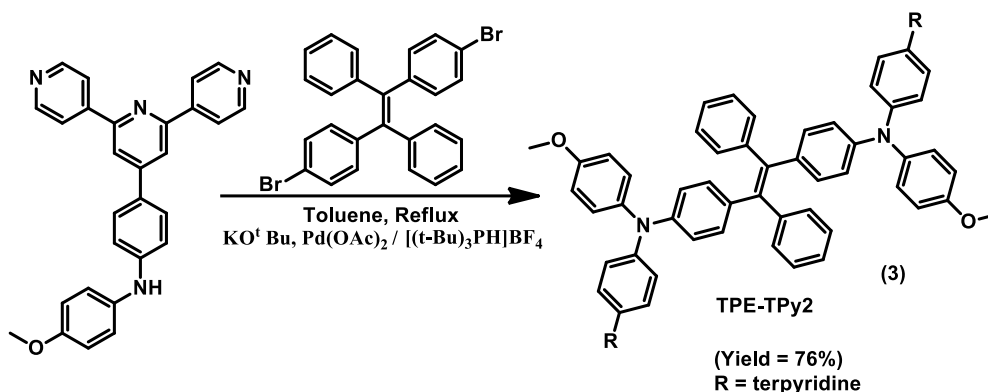
**Scheme 3.3.**

4'-(4-bromophenyl) 2,2': 6',2'' terpyridine (1.5 g, 3.86 mmol), p-anisidine (0.72 g, 5.80 mmol), KO<sup>t</sup>Bu (0.87 g, 7.8 mmol) and Pd(OAc)<sub>2</sub> (0.09 g, 0.38 mmol) were taken in a 100 ml two neck flask fitted with a septum. Toluene (10 ml) and tritert-butylphosphine tetrafluoroborate (0.34 g, 1.1 mmol) were added and the reaction was refluxed for 24 h under nitrogen atmosphere. After cooling to room temperature, the solution was poured into water and extracted with dichloromethane. The combined organic layers were dried over anhydrous sodium sulphate, filtered and dried under vacuum. The residue was purified by column chromatography over silica gel (50% ethyl acetate-hexane) to yield a brown powder (yield = 80%).

**<sup>1</sup>H NMR** (500 MHz, CDCl<sub>3</sub>): δ = 8.74 (2H, m), δ = 8.73 (2H, s), δ = 8.68 (2H, m), δ = 7.89 (2H, m), δ = 7.83 (2H, m), δ = 7.36 (d, *J* = 6 Hz, 2H), δ = 7.14 (d, *J* = 8 Hz, 2 Hz), δ = 7.00 (d, *J* = 9 Hz, 2H), δ = 6.91 (d, *J* = 9 Hz, 2H), δ = 3.83 (3H, s).

**ESI-HRMS:** *m/z* calculated for (C<sub>28</sub>H<sub>22</sub>N<sub>4</sub>O): 430.1794, Found: 431.1817.

### 3.5.4.c. Synthesis of 4,4'-(1,2-diphenylethylene-1,2-diyl)bis(*N*-(4-([2,2':6',2''-terpyridin]-4'-yl) phenyl)-*N*-(4-methoxyphenyl)aniline) (TPE-TPy2)



**Scheme 3.4.**

1,2-bis (4-bromophenyl)-1,2-diphenylethylene (0.5 g, 1.01 mmol), 4-([2,2':6',2''-terpyridin]-4'-yl)-*N*-(4-methoxyphenyl)aniline (1.1g, 2.54 mmol), KO<sup>t</sup>Bu (0.3 g, 2.54 mmol) and Pd(OAc)<sub>2</sub> (0.02 g, 0.1 mmol) were taken in a 100 ml two neck flask fitted with a septum. Toluene (10 ml) and tritert-butylphosphine tetrafluoroborate (0.1 g, 0.3 mmol) were added and the reaction was refluxed for 24 h under nitrogen atmosphere. After cooling to room temperature, the solution was poured into water and extracted with dichloromethane. The combined organic layers were dried over anhydrous sodium sulphate filtered and dried under vacuum. The residue was purified by column chromatography over silica gel (50% ethyl acetate-hexane) to yield yellow powder (yield = 76%).

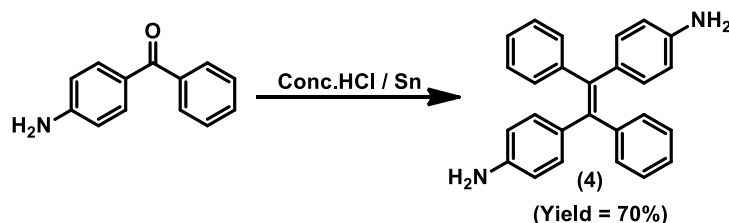
<sup>1</sup>H NMR (500 MHz, CDCl<sub>3</sub>): δ = 8.72 (4H, m), δ = 8.6 (4H, m), δ = 8.57 (4H, s), δ = 7.81 (4H, m), δ = 7.8 (4H, m), δ = 7.7 (4H, m), δ = 7.68 (4H, m), δ = 7.4 (d, *J* = 7 Hz, 4H), δ = 7.3 (d, *J* = 7.8 Hz, 4H) (d, *J* = 7.8 Hz, 4H), δ = 6.94 (d, *J* = 8 Hz, 4H), δ = 6.92 (d, *J* = 8.1 Hz, 4H), δ = 6.85 (4H, m), δ = 6.83 (d, *J* = 7 Hz, 4H), δ = 3.74 (6H, s).

<sup>13</sup>C NMR (125 MHz, CDCl<sub>3</sub>): δ = 149.22, 149.13, 148.99, 145.79, 143.8, 140.09, 138.71, 136.85, 136.70, 132.35, 131.44, 130.59, 127.91, 127.66, 127.52, 127.36, 126.41,

123.74, 123.62, 122.93, 121.93, 121.36, 121.26, 118.35, 117.96, 114.86, 114.80, 55.44.

**MALDI-TOF:**  $m/z$  calculated for ( $C_{82}H_{60}N_8O_2$ ): 1189.4839, Found: 1189.4922.

#### 3.5.4.d. Synthesis of 4,4'-(1,2-diphenylethene-1,2-diyl)dianiline (**4**)



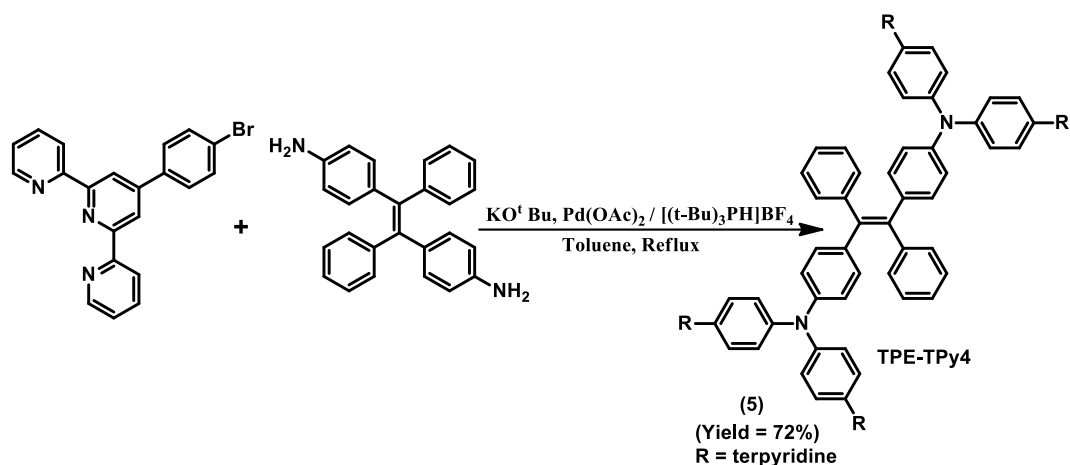
**Scheme 3.5.**

4-aminobenzophenone (1 g, 5.1 mmol) was dissolved in concentrated hydrochloric acid (30 mL) at 60 °C under stirring, followed by the addition of tin powder (2.4 g, 20 mmol), and the reaction mixture was stirred at 75 °C for 5 h. After cooling, the mixture was vacuum filtrated and washed by NaOH (1 M) and H<sub>2</sub>O. After drying overnight at room temperature, compound was obtained as a greenish yellow powder in 65% yield.

**<sup>1</sup>H NMR** (500 MHz, CD<sub>3</sub>OD):  $\delta$  = 6.57 (d,  $J$  = 8.5 Hz, 4H), 7.05 (s, 4H), 7.38 (m, 4H), 7.5 (m, 2H), 7.53 (m, 4H), 7.58 (d,  $J$  = 8 Hz, 4H).

**ESI-HRMS:**  $m/z$  calculated for ( $C_{26}H_{22}N_2$ ): 362.1817, Found: 363.1861.

### 3.5.4.e Synthesis of 4,4'-(1,2-diphenylethene-1,2-diyl)bis(*N,N*-bis(4-([2,2':6',2''-terpyridin]-4'-yl)phenyl)aniline) (TPE-TPy4)



**Scheme 3.6.**

TPE-2NH<sub>2</sub> (0.36 g, 0.98 mmol), 4'-(4-bromophenyl)2,2':6',2''terpyridine (1.7 g, 1.441 mmol), KO<sup>t</sup>Bu (0.33 g, 2.94 mmol) and Pd(OAc)<sub>2</sub> (0.067 g, 0.294 mmol) were taken in 100 ml two neck flask fitted with a septum. Toluene (10 ml) and tri-tert-butylphosphine (0.09 g, 0.294 mmol) were added and the reaction mixture was refluxed for 24 h under nitrogen atmosphere. After cooling to room temperature, the solution was poured into water and extracted with dichloromethane. The combined organic layers were dried over anhydrous sodium sulphate. **TPE-TPy4** was obtained as a yellowish powder with 72% yield.

**<sup>1</sup>H NMR** (500 MHz, Toluene, d<sub>8</sub>): δ = 8.92 (m, 8H), 8.90 (s, 8H), 8.56 (m, 8H), 8.52 (d, *J*=9Hz, 4H), 8.50 (m, 8H), 8.47 (d, *J* = 8.5 Hz, 8H), 8.40 (m, 8H), 7.44 (d, *J* = 8Hz, 8H), 7.39 (m, 8H), 7.17(m, 2H), 7.38 (d, 8 Hz, 4H).

**<sup>13</sup>C NMR** (125 MHz, CDCl<sub>3</sub>): δ = 207.32, 156.24, 156.00, 149.15, 136.89, 134.51, 132.07, 131.93, 129.78, 128.68, 128.22, 125.61, 123.86, 121.36, 118.56, 77.29, 77.03, 76.78, 30.31, 30.15, 30.00.

**MALDI-TOF**: *m/z* calculated for (C<sub>110</sub>H<sub>74</sub>N<sub>14</sub>): 1591.6254, Found: 1591.596.

### 3.5.5. NMR and Mass Spectra of TPE-TPy4 and TPE-TPy2

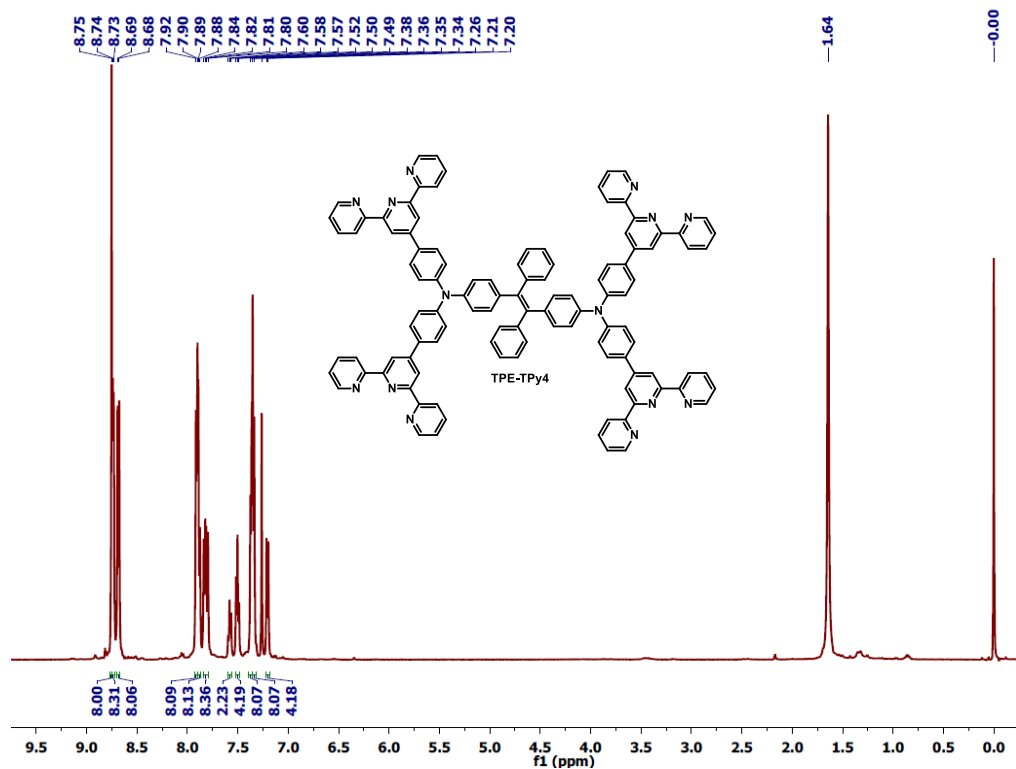


Figure 3.24. <sup>1</sup>H NMR of TPE-TPy4 in toluene d<sub>8</sub>.

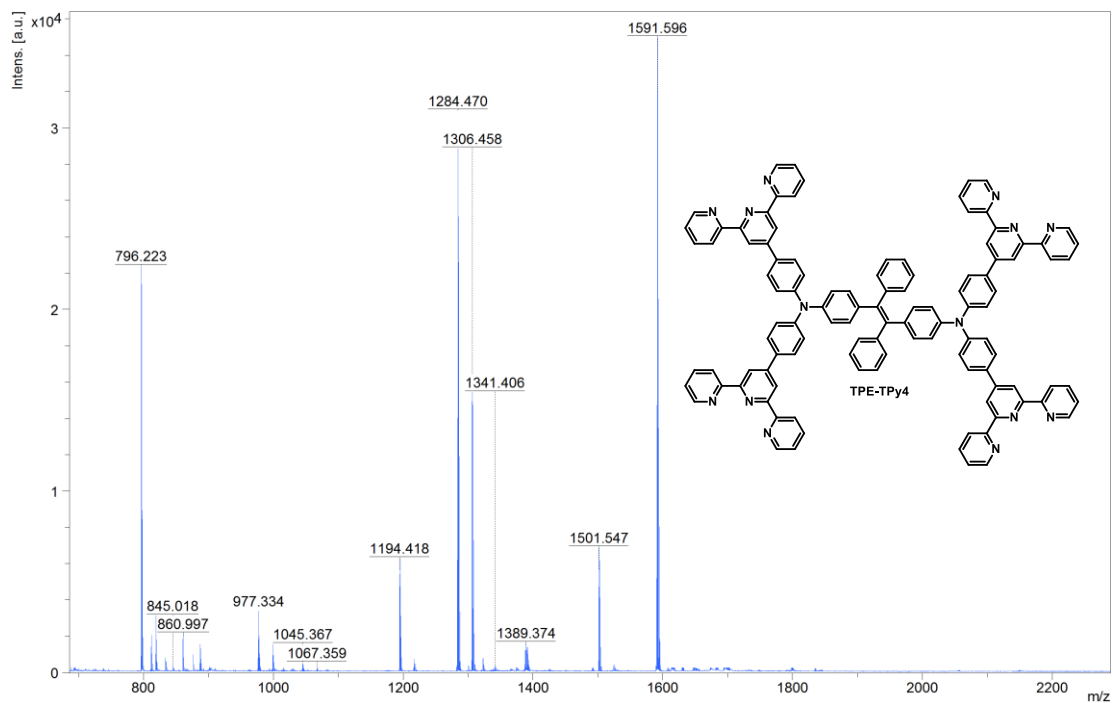
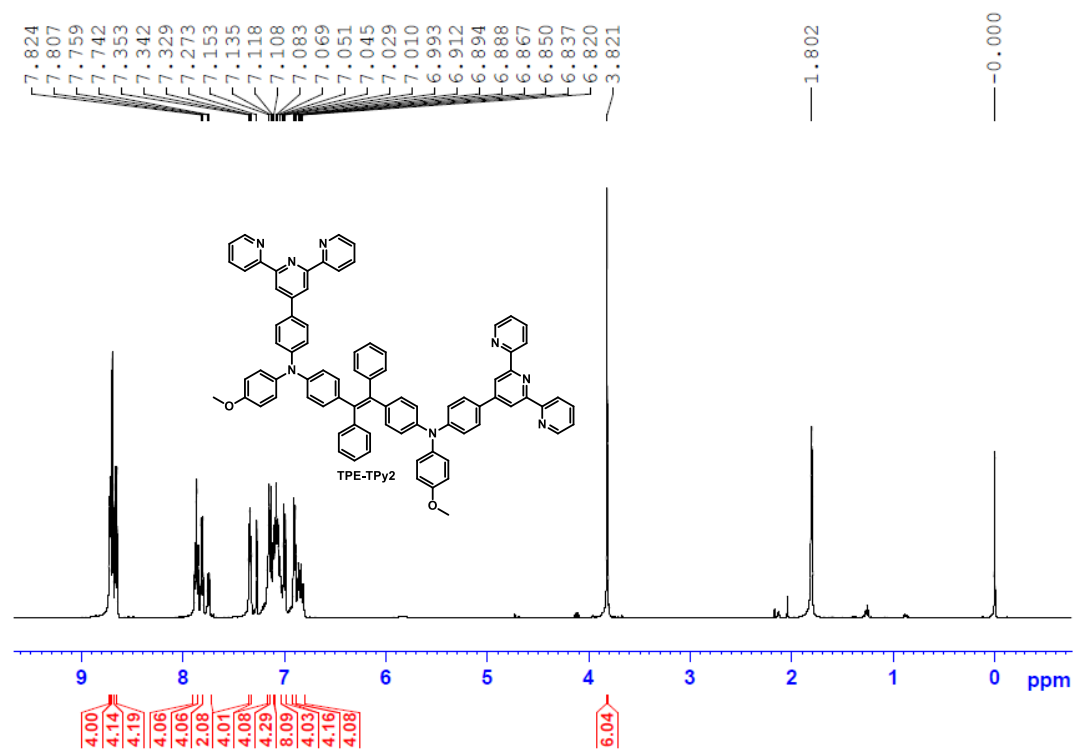
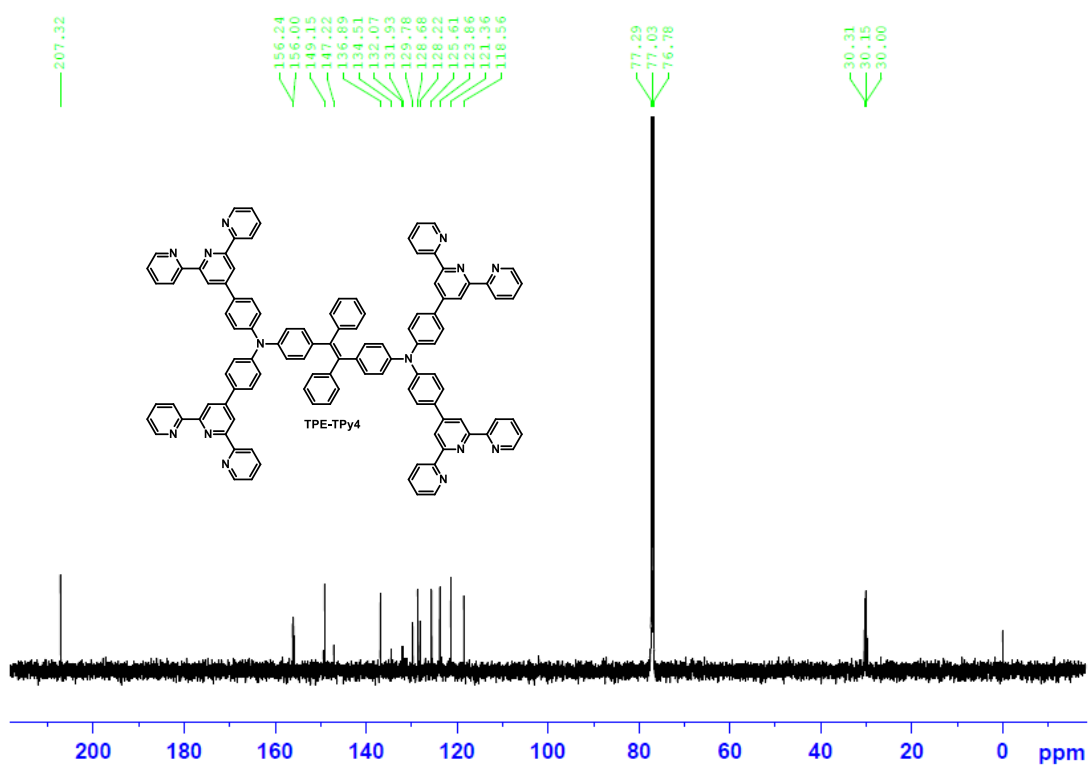


Figure 3.25. MALDI-TOF of TPE-TPy4.





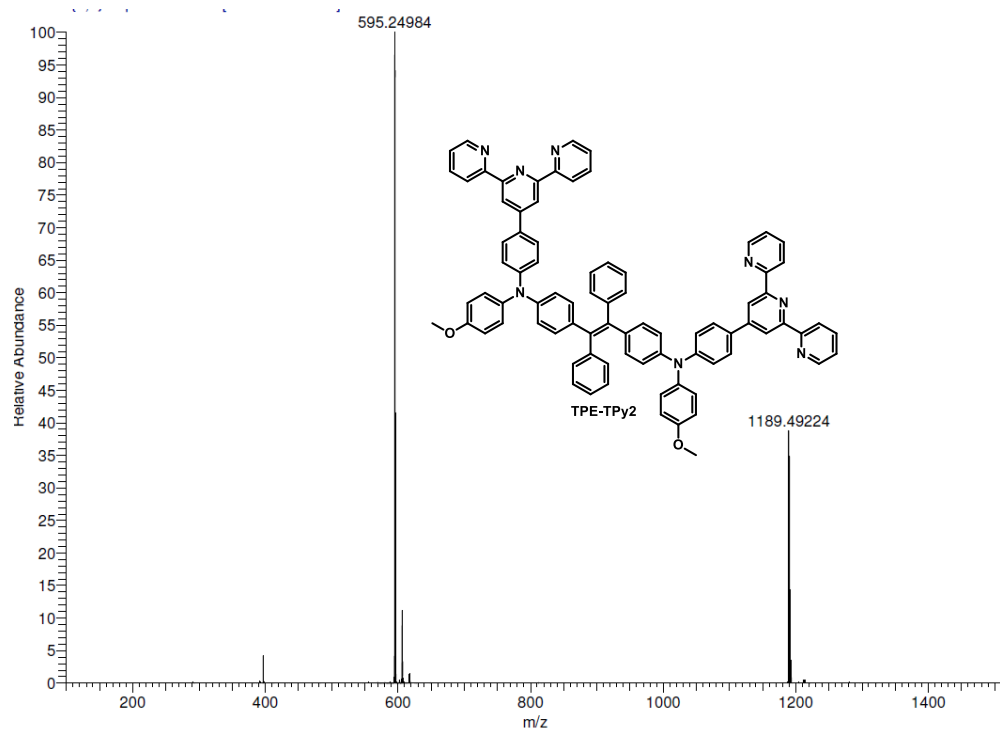


Figure 3.28. MALDI-TOF of TPE-TPy2.

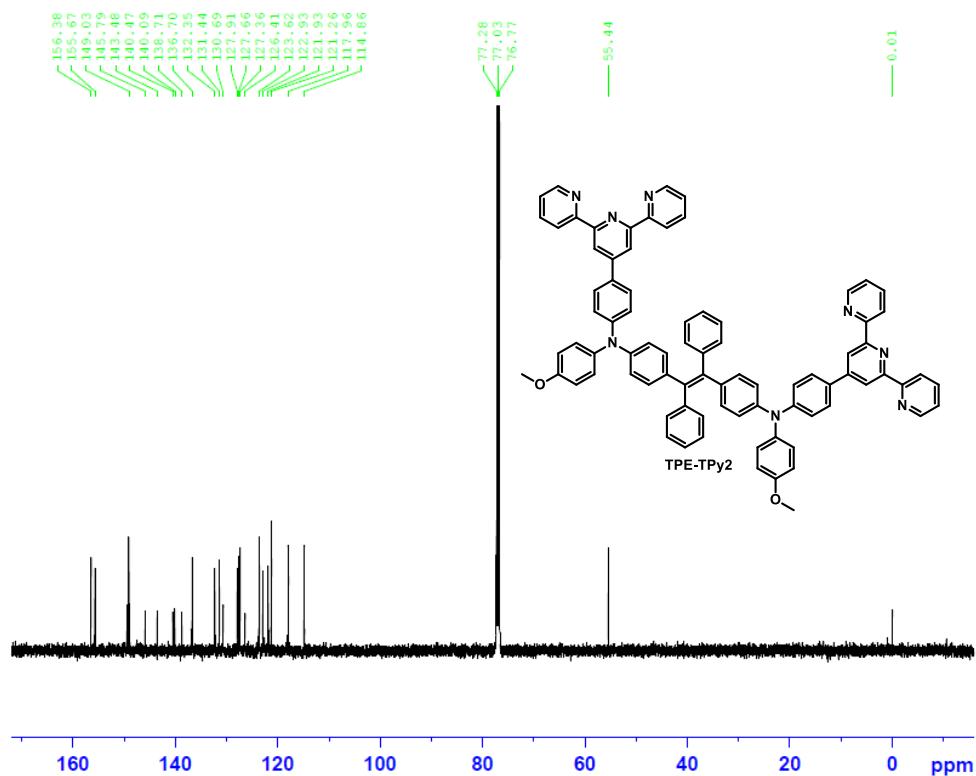


Figure 3.29. <sup>13</sup>C NMR of TPE-TPy2 in CDCl<sub>3</sub>.

### 3.6. References

- (1) Whittell, G. R.; Manners, I. Metallopolymers: New Multifunctional Materials. *Adv. Mater.* **2007**, *19*, 3439-3468.
- (2) Cui, B.-B.; Yao, C.-J.; Yao, J.; Zhong, Y.-W. Electropolymerized films as a molecular platform for volatile memory devices with two near-infrared outputs and long retention time. *Chem. Sci* **2014**, *5*, 932-941.
- (3) Dzhardimalieva, G. I.; Yadav, B. C.; Singh, S.; Uflyand, I. E. Self-healing and shape memory metallopolymers: state-of-the-art and future perspectives. *Dalton Trans.* **2020**, *49*, 3042-3087.
- (4) Shi, H.; Ma, X.; Zhao, Q.; Liu, B.; Qu, Q.; An, Z.; Zhao, Y.; Huang, W. Ultrasmall Phosphorescent Polymer Dots for Ratiometric Oxygen Sensing and Photodynamic Cancer Therapy. *Adv. Funct. Mater.* **2014**, *24*, 4823-4830.
- (5) Zhao, Q.; Zhou, X.; Cao, T.; Zhang, K. Y.; Yang, L.; Liu, S.; Liang, H.; Yang, H.; Li, F.; Huang, W. Fluorescent/phosphorescent dual-emissive conjugated polymer dots for hypoxia bioimaging. *Chem. Sci* **2015**, *6*, 1825-1831.
- (6) Hu, C.-W.; Sato, T.; Zhang, J.; Moriyama, S.; Higuchi, M. Multi-colour electrochromic properties of Fe/Ru-based bimetallo-supramolecular polymers. *J. Mater. Chem. C* **2013**, *1*, 3408-3413.
- (7) Zeng, Q.; McNally, A.; Keyes, T. E.; Forster, R. J. Three colour electrochromic metallopolymer based on a ruthenium phenolate complex bound to poly(4-vinyl)pyridine. *Electrochem. Commun.* **2008**, *10*, 466-470.
- (8) Napierała, S.; Kubicki, M.; Wałęsa-Chorab, M. Toward Electrochromic Metallopolymers: Synthesis and Properties of Polyazomethines Based on Complexes of Transition-Metal Ions. *Inorg. Chem.* **2021**, *60*, 14011-14021.
- (9) Chatir, E.; Khettabi, A.; Lafalet, F.; Jouvenot, D.; Royal, G.; Saint-Aman, E.; Cobo, S. Photochromic Metallopolymer Based on Dithienylethene as a Molecular Calculator. *Chem. Mater.* **2022**, *34*, 5912-5918.
- (10) Sakurai, H.; Jacquet, M.; Lafalet, F.; Loiseau, F.; Saint-Aman, E.; Royal, G.; Cobo, S. Photochemical and photophysical properties of photochromic osmium terpyridine-dimethyldihydropyrene complexes. *Dyes Pigm.* **2019**, *160*, 93-98.

- (11) de Hatten, X.; Bell, N.; Yufa, N.; Christmann, G.; Nitschke, J. R. A Dynamic Covalent, Luminescent Metallopolymer that Undergoes Sol-to-Gel Transition on Temperature Rise. *J. Am. Chem. Soc.* **2011**, *133*, 3158-3164.
- (12) Asil, D.; Foster, J. A.; Patra, A.; de Hatten, X.; del Barrio, J.; Scherman, O. A.; Nitschke, J. R.; Friend, R. H. Temperature- and voltage-induced ligand rearrangement of a dynamic electroluminescent metallopolymer. *Angew. Chem. Int. Ed. Engl.* **2014**, *53*, 8388-8391.
- (13) Miyata, K.; Konno, Y.; Nakanishi, T.; Kobayashi, A.; Kato, M.; Fushimi, K.; Hasegawa, Y. Chameleon Luminophore for Sensing Temperatures: Control of Metal-to-Metal and Energy Back Transfer in Lanthanide Coordination Polymers. *Angew. Chem. Int. Ed.* **2013**, *52*, 6413-6416.
- (14) Pinaud, F.; Russo, L.; Pinet, S.; Gosse, I.; Ravaine, V.; Sojic, N. Enhanced Electrogenerated Chemiluminescence in Thermoresponsive Microgels. *J. Am. Chem. Soc.* **2013**, *135*, 5517-5520.
- (15) Granqvist, C. G.; Arvizu, M. A.; Bayrak Pehlivan, İ.; Qu, H. Y.; Wen, R. T.; Niklasson, G. A. Electrochromic materials and devices for energy efficiency and human comfort in buildings: A critical review. *Electrochim. Acta* **2018**, *259*, 1170-1182.
- (16) Rai, V.; Singh, R. S.; Blackwood, D. J.; Zhili, D. A Review on Recent Advances in Electrochromic Devices: A Material Approach. *Adv. Eng. Mater.* **2020**, *22*, 2000082.
- (17) Liu, S.; Zhang, P.; Fu, J.; Wei, C.; Cai, G. A Mini-Review: Pyridyl-Based Coordination Polymers for Energy Efficient Electrochromic Application. *Front. Energy Res.* **2021**, *9*.
- (18) Chen, B.-H.; Kao, S.-Y.; Hu, C.-W.; Higuchi, M.; Ho, K.-C.; Liao, Y.-C. Printed Multicolor High-Contrast Electrochromic Devices. *ACS Appl. Mater. Interfaces* **2015**, *7*, 25069-25076.
- (19) Higuchi, M. Electrochromic Organic–Metallic Hybrid Polymers: Fundamentals and Device Applications. *Polym. J.* **2009**, *41*, 511-520.
- (20) Tran, M.; Kline, K.; Qin, Y.; Shen, Y.; Green, M. D.; Tongay, S. 2D coordination polymers: Design guidelines and materials perspective. *Appl. Phys. Rev.* **2019**, *6*.
- (21) Hu, C.-W.; Sato, T.; Zhang, J.; Moriyama, S.; Higuchi, M. Three-Dimensional Fe(II)-based Metallo-Supramolecular Polymers with Electrochromic Properties of Quick Switching, Large Contrast, and High Coloration Efficiency. *ACS Appl. Mater. Interfaces* **2014**, *6*, 9118-9125.
- (22) Mondal, S.; Ninomiya, Y.; Yoshida, T.; Mori, T.; Bera, M. K.; Ariga, K.; Higuchi, M. Dual-Branched Dense Hexagonal Fe(II)-Based Coordination Nanosheets with Red-to-Colorless

Electrochromism and Durable Device Fabrication. *ACS Appl. Mater. Interfaces* **2020**, *12*, 31896-31903.

(23) Narayana, Y. S. L. V.; Mondal, S.; Rana, U.; Ninomiya, Y.; Santra, D. C.; Yoshida, T.; Higuchi, M. One-Step Synthesis of a Three-Dimensionally Hyperbranched Fe(II)-Based Metallo-Supramolecular Polymer Using an Asymmetrical Ditopic Ligand for Durable Electrochromic Films with Wide Absorption, Large Optical Contrast, and High Coloration Efficiency. *ACS Appl. Electron. Mater.* **2021**, *3*, 2044-2055.

(24) Kuai, Y.; Li, W.; Dong, Y.; Wong, W.-Y.; Yan, S.; Dai, Y.; Zhang, C. Multi-color electrochromism from coordination nanosheets based on a terpyridine-Fe(ii) complex. *Dalton Trans.* **2019**, *48*, 15121-15126.

(25) Liu, Y.; Sakamoto, R.; Ho, C.-L.; Nishihara, H.; Wong, W.-Y. Electrochromic triphenylamine-based cobalt(ii) complex nanosheets. *J. Mater. Chem. C* **2019**, *7*, 9159-9166.

(26) Yao, C.-J.; Zhong, Y.-W.; Yao, J. Five-Stage Near-Infrared Electrochromism in Electropolymerized Films Composed of Alternating Cyclometalated Bisruthenium and Bis-triarylamine Segments. *Inorg. Chem.* **2013**, *52*, 10000-10008.

(27) Fan, C.; Ye, C.; Wang, X.; Chen, Z.; Zhou, Y.; Liang, Z.; Tao, X. Synthesis and Electrochromic Properties of New Terpyridine-Triphenylamine Hybrid Polymers. *Macromolecules* **2015**, *48*, 6465-6473.

(28) Mukkatt, I.; Mohanachandran, A. P.; Nirmala, A.; Patra, D.; Sukumaran, P. A.; Pillai, R. S.; Rakhi, R. B.; Shankar, S.; Ajayaghosh, A. Tunable Capacitive Behavior in Metallopolymer-based Electrochromic Thin Film Supercapacitors. *ACS Appl. Mater. Interfaces* **2022**, *14*, 31900-31910.

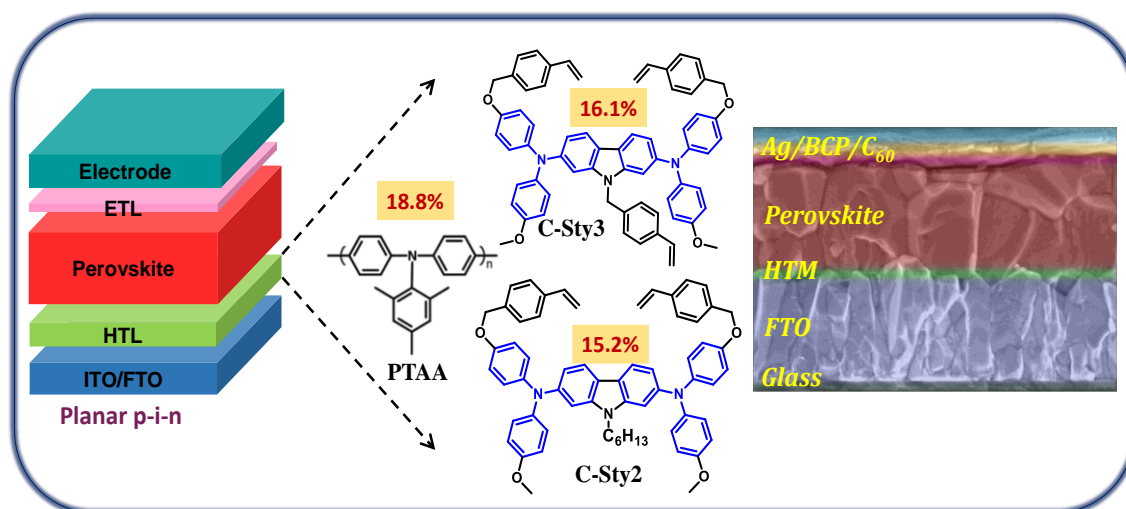
(29) Mukkatt, I.; Nirmala, A.; Madhavan, N. D.; Shankar, S.; Deb, B.; Ajayaghosh, A. Ligand-Controlled Electrochromic Diversification with Multilayer Coated Metallosupramolecular Polymer Assemblies. *ACS Appl. Mater. Interfaces* **2021**, *13*, 5245-5255.

(30) González-Meza, O. A.; Larios-Durán, E. R.; Gutiérrez-Becerra, A.; Casillas, N.; Escalante, J. I.; Bárcena-Soto, M. Development of a Randles-Ševčík-like equation to predict the peak current of cyclic voltammetry for solid metal hexacyanoferrates. *J. Solid State Electrochem.* **2019**, *23*, 3123-3133.

(31) Langhus, D. L. Fundamentals of Electroanalytical Chemistry (Monk, Paul M. S.). *J. Chem. Educ.* **2002**, *79*, 1207.

- (32) Sun, X.; Zhao, L.; Han, X.; Liu, H.; Gao, Y.; Tao, Y.; Zhang, H.; Yang, B.; Lu, P. Preparation of Cyano-Substituted Tetraphenylethylene Derivatives and Their Applications in Solution-Processable OLEDs. *Molecules* [Online early access] **2018**.
- (33) Sasaki, S.; Drummen, G. P. C.; Konishi, G.-i. Recent advances in twisted intramolecular charge transfer (TICT) fluorescence and related phenomena in materials chemistry. *J. Mater. Chem. C* **2016**, *4*, 2731-2743.
- (34) Mondal, S.; Chandra Santra, D.; Ninomiya, Y.; Yoshida, T.; Higuchi, M. Dual-Redox System of Metallo-Supramolecular Polymers for Visible-to-Near-IR Modulable Electrochromism and Durable Device Fabrication. *ACS Appl. Mater. Interfaces* **2020**, *12*, 58277-58286.
- (35) Lashgari, N.; Badiiei, A.; Mohammadi Ziarani, G. A Fluorescent Sensor for Al(III) and Colorimetric Sensor for Fe(III) and Fe(II) Based on a Novel 8-Hydroxyquinoline Derivative. *J. Fluoresc.* **2016**, *26*, 1885-1894.
- (36) Baskin, M.; Maayan, G. Chiral Cu(ii), Co(ii) and Ni(ii) complexes based on 2,2'-bipyridine modified peptoids. *Dalton Trans.* **2018**, *47*, 10767-10774.
- (37) Brown, A. M.; McCusker, C. E.; McCusker, J. K. Spectroelectrochemical identification of charge-transfer excited states in transition metal-based polypyridyl complexes. *Dalton Trans.* **2014**, *43*, 17635-17646.
- (38) Österholm, A. M.; Shen, D. E.; Kerszulis, J. A.; Bulloch, R. H.; Kuepfert, M.; Dyer, A. L.; Reynolds, J. R. Four Shades of Brown: Tuning of Electrochromic Polymer Blends Toward High-Contrast Eyewear. *ACS Appl. Mater. Interfaces* **2015**, *7*, 1413-1421.
- (39) Padhy, H.; Sahu, D.; Chiang, I. H.; Patra, D.; Kekuda, D.; Chu, C.-W.; Lin, H.-C. Synthesis and applications of main-chain Ru(ii) metallo-polymers containing bis-terpyridyl ligands with various benzodiazole cores for solar cells. *J. Mater. Chem.* **2011**, *21*, 1196-1205.
- (40) Bera, M. K.; Mori, T.; Yoshida, T.; Ariga, K.; Higuchi, M. Construction of Coordination Nanosheets Based on Tris(2,2'-bipyridine)-Iron (Fe<sup>2+</sup>) Complexes as Potential Electrochromic Materials. *ACS Appl. Mater. Interfaces* **2019**, *11*, 11893-11903.
- (41) Roy, S.; Chakraborty, C. Metallo-Macrocyclic Camouflages: Multicolored Electrochromism in a Fe(II) Based Metallo-Supramolecular Macrocyclic Utilizing the Redox of Metal Centers and Carbazole Containing Ligand. *ACS Appl. Electron. Mater.* **2019**, *1*, 2531-2540.

## Cross-linkable, Carbazole-Diphenylamine Derivatives as Dopant Free, Hole Transporting Materials for Perovskite Solar Cells



### 4A.1. Abstract

Hole-transporting layer (HTL) with a stable film structure, appropriate energy level, excellent hole mobility and optical transparency is essential for achieving high-performance Perovskite solar cells (PSC) with long-term stability. The development of a cross-linkable HTL, with high thermal stability and solvent resistance, which can perform effective hole extraction while serving as a protective barrier, is a promising approach. HTMs based on triphenylamine (TPA)-derivatives are extensively utilized to increase the stability and performance of Perovskite solar cells due to their superior thermal stability and tunable optoelectronic properties. The current Chapter focuses on the application of styrene attached carbazole-diphenylamine derivatives,

**C-Sty2** and **C-Sty3** (previously discussed in Chapter 2) as thermally cross-linkable, hole-transport materials for Perovskite solar cells. These molecules are specifically designed to exhibit thermal cross-linking properties, which allows for the formation of stable and durable hole-transporting layers in PSC devices. The performance of the PSC devices were optimized by varying several parameters, including weight percentage of the hole-transporting material, spin-coating speed (rpm) and annealing temperature. Optimized p-i-n PSC devices of **C-Sty3** and **C-Sty2** showed power conversion efficiencies (PCE) of 16.1% and 15.2%, respectively in comparison with the standard HTM, PTAA based device with PCE of 18.8%. The device incorporating **C-Sty3** derivative demonstrated higher performance compared to **C-Sty2** derivative, which can be attributed to the lower charge transfer resistance and higher conductivity across the hyper-cross-linked **C-Sty3**-based films. This chapter highlights the influence of different parameters on PSC device performance and demonstrates the potential of these materials to enhance the efficiency of PSCs through the formation of stable and conductive hole-transporting layers.



## 4A.2. Introduction

Perovskite solar cells exhibit remarkable photovoltaic performance, with high power conversion efficiencies achieved in a relatively short period of development. This has piqued a great interest in investigating their potential for wide usage in solar energy applications. Currently, the PCE of perovskite-based solar cells has made significant progress, reaching up to 26%. Furthermore, the development of tandem solar cells combining perovskite with silicon (Si) has achieved 33.7% according to NREL.<sup>1</sup> The PSCs are divided into n-i-p and p-i-n architectures depending on the arrangement of the layers in the devices. In n-i-p devices, the HTM is positioned over the perovskite layer. Due to the rough surface of the perovskite layer and the need to prevent metal diffusion into the perovskite, a thick HTM film (typically in the 200 - 370 nm range) is required to achieve full coverage and protection.<sup>2-4</sup> In this configuration, high mobility becomes particularly important for the HTM, along with other general requirements such as suitable energy levels, good solubility, smooth film morphology, and thermal stability. The choice of HTM for each device can differ according to the requirements.<sup>5</sup> Representative examples for n-i-p and p-i-n devices are given in Figure 4A. Presently, the highest PCE of 26% is achieved by an n-i-p structured PSC, based on Spiro-OMeTAD hole transporting material (Figure 4A.1A).<sup>6</sup> Spiro-OMeTAD based n-i-p PSC typically needs to be doped with additives such as t-BP, Li-TFSI, and cobalt complexes to enhance its performance due to its low mobility. The hygroscopic nature of the dopants affects the stability of the device.<sup>7</sup> On the other hand, in p-i-n devices, the HTM film can be much thinner and as a result, mobility is not the most important requirement in this configuration, whereas energy level alignment, solvent resistance, transparency and stable film formation become more

important.<sup>8</sup> Polymeric, dopant free arylamine derivatives, for example PTAA and Poly-TPD have been widely used as p-i-n device HTMs due to wide bandgaps, good hole mobility, thermal stability and solution processability.<sup>9,10</sup> High solubility can both be an advantage and disadvantage during the solution based device fabrication process. Initial solution-based film formation is facilitated by good solubility, whereas the fabrication of subsequent layers by solution processing can perturb the film quality by partial dissolution of the HTL. The highest published power conversion efficiency value reported so far for p-i-n PSCs is 25.0% by Li *et al.* (Figure 4A.1B).<sup>11</sup> They enhanced the performance and stability of inverted perovskite solar cells through the functionalization of multi-cation and halide perovskite interfaces using a ferrocene based organometallic compound. The devices maintained over 98% of their initial efficiency after continuous operation at the maximum power point for 1500 hours under simulated sunlight. This indicates that p-i-n PSCs have made significant progress and are approaching the performance levels of the best regular, n-i-p PSCs.

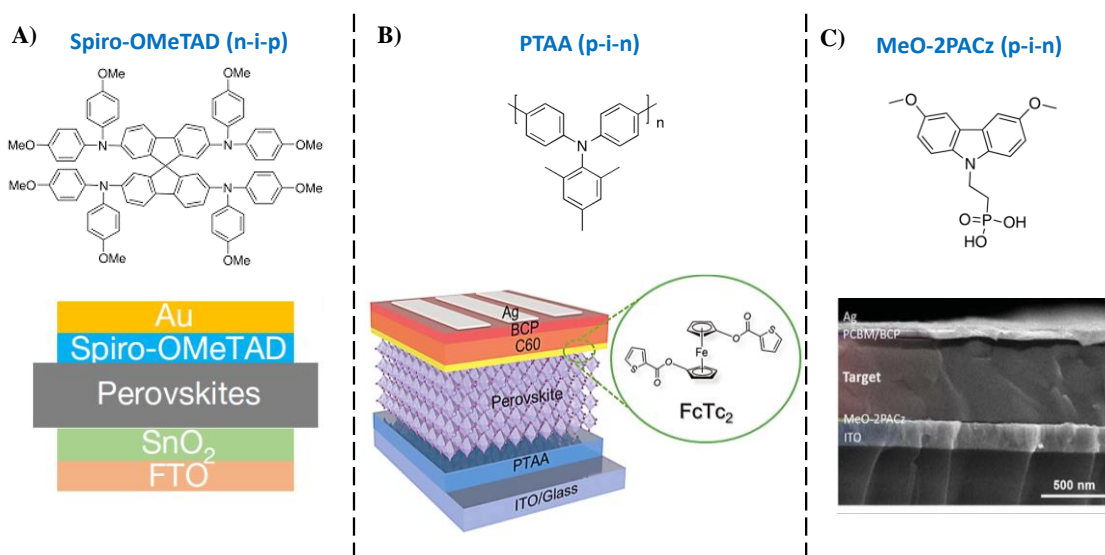


**Figure 4A.1.** Device structures and HTMs used in highest PCE Perovskite solar cells based on (A) n-i-p and (B) and (C) p-i-n structures. (Adapted from reference 6,11 and 15)

The exploration of the p-i-n configuration offers new possibilities for improving the efficiency and overall performance of perovskite solar cells. However, as indicated, the solubility of HTMs make them susceptible to partial dissolution or etching when exposed to certain solvents used in subsequent steps of the fabrication process, such as DMF and DMSO. The synthetic cost of these materials also can impact the commercial viability and large-scale applications. Techniques such as cross-linking of small molecules and self-assembled monolayers (SAM) are widely used to develop stable HTM layers on the substrates, which can perform effective hole extraction while serving as a protective barrier.<sup>12-14</sup> The best p-i-n Perovskite solar cell efficiency achieved among SAM based techniques is 24.6%, which used a self-assembled monolayer of MeO-2PACz ((2-(3,6-Dimethoxy-9*H*-carbazol-9-yl)ethyl)phosphonic acid) as the HTM (Figure 4A.1C).<sup>15</sup>

Wakamiya's group reported two p-i-n perovskite solar cells fabricated using two triple-cation, mixed halide lead Perovskites (low-Br material (Br/I 1:11) with a bandgap of 1.57 eV and a high-Br formulation (Br/I 1:2) with a bandgap of 1.72 eV) and compared their device properties.<sup>16</sup> A self-assembled monolayer (MeO-2PACz) was used as hole extraction layer with a focus on ambient light-harvesting applications. The perovskite with lower bromide content exhibited higher power conversion efficiency of 19.1% and operational stability (Figure 4A.2A). Geguziene *et al.* demonstrated the hole transporting properties of two cross-linkable carbazole-diphenylamine derivatives.<sup>17</sup> Compound with three carbazole units and two methoxy groups named as V1205, whereas compound with five carbazole moieties without methoxy group named as V1206. The cross-linked films of HTMs displayed good resistance towards organic solvents and V1205 based device exhibited a PCE of 16.9% (Figure 4A.2B).

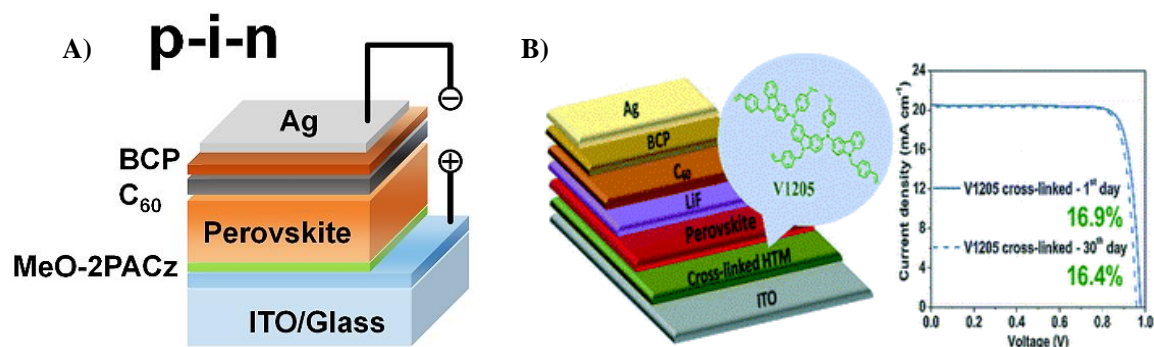


**Figure 4A.2.** p-i-n structure-based Perovskite solar cell devices with (A) self-assembled monolayer of MeO-2PACz and (B) thermally cross-linked carbazole-styrene derivatives. (Adapted from reference 16 and 17)

#### 4A.2.1. Mixed Halide Hybrid Perovskites for Perovskite Solar Cells

Methylammonium lead iodide (MAPbI<sub>3</sub>) is one of the most widely studied and extensively utilized Perovskite materials in the field of Perovskite solar cells. Presently, the efficiency of MAPbI<sub>3</sub> falls within the approximate range of 20%. Researchers have been exploring various strategies to further enhance the performance of PSCs by replacing or mixing of different cations and anions in the Perovskite lattice.<sup>18-20</sup> By introducing different cation and anion species into the Perovskite structure, the bandgap of the materials can be tuned, which allows better matching of the solar spectrum and improved light absorption. Additionally, changing the composition can also affect the charge transporting energy levels within the Perovskite, influencing charge carrier mobility and reducing recombination losses.<sup>21</sup> Formamidinium lead iodide (FAPbI<sub>3</sub>) is known to have a narrower bandgap which makes it potentially suitable for improved light harvesting and absorption of a broader range of solar radiation. However, FAPbI<sub>3</sub> faces stability issues as it undergoes a spontaneous phase transition at room temperature, shifting from its light-absorbing black  $\alpha$ -phase Perovskite form to a non-perovskite yellow  $\delta$ -phase that is not photoactive.<sup>22,23</sup> In 2015, Seok and group demonstrated that the stability of

the  $\alpha$ -phase  $\text{FAPbI}_3$  perovskite can be improved by incorporating a small amount of  $\text{MAPbBr}_3$  into the  $\text{FAPbI}_3$  lattice  $(\text{FAPbI}_3)_{1-x}(\text{MAPbBr}_3)_x$  to form a mixed composition perovskite.<sup>24</sup> Michael Saliba and his research team have successfully formulated an efficient Perovskite material with a mixed composition  $(\text{Cs}_{0.05}\text{MA}_{0.16}\text{FA}_{0.79}\text{PbI}_{2.49}\text{Br}_{0.51})$ .<sup>25</sup> They introduced caesium ions which improved the stability of the Perovskite by reducing the transition from the  $\alpha$  to  $\delta$ -phase, which enhanced the long-term performance and durability of the Perovskite solar cells with 21.1% PCE and  $\sim 18\%$  after 250 hours under operational conditions.

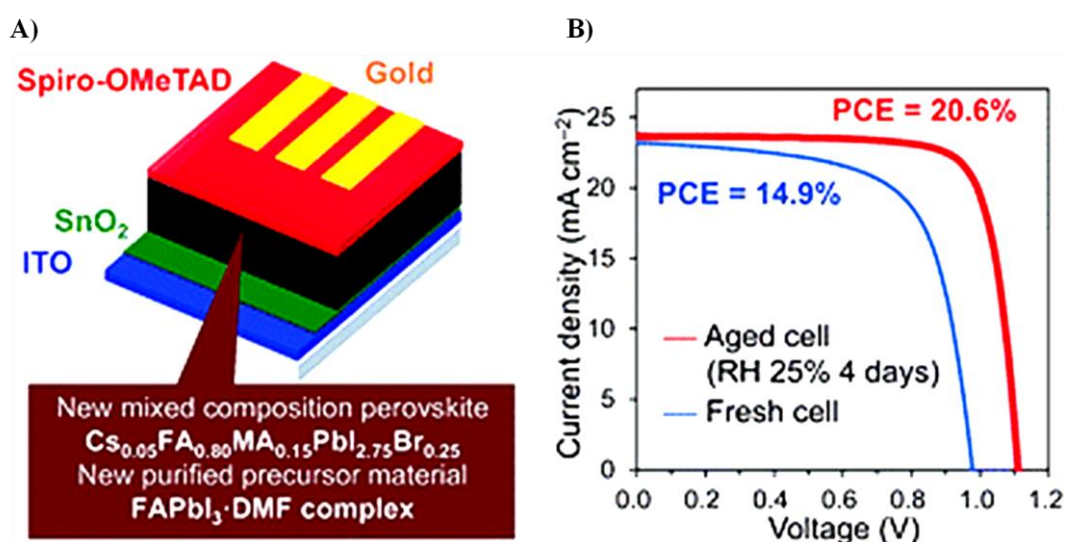


**Figure 4A.3.** (A) Device structure and (B) current density vs voltage graph showing the efficiency change after several days of iodine-rich mixed composition metal-halide perovskite ( $\text{Cs}_{0.05}\text{FA}_{0.80}\text{MA}_{0.15}\text{PbI}_{2.75}\text{Br}_{0.25}$ ) based Perovskite solar cells. (Adapted from reference 8)

An iodine-rich mixed composition Perovskite ( $\text{Cs}_{0.05}\text{FA}_{0.80}\text{MA}_{0.15}\text{PbI}_{2.75}\text{Br}_{0.25}$ ) with 11:1 ratio of iodide to bromide ions and bandgap of 1.57 eV was used for the PSC in the current chapter.<sup>26,27</sup> The composition ratio of the Perovskite materials is usually analysed using neutron activation analysis (NAA) technique. Wakamiya and team used this type of Perovskites into devices that utilized tin(IV) oxide substrates

for electron transport layers and resulted in enhanced device performance.<sup>28</sup> Aging the Perovskite solar cells in the ambient atmosphere over several days enhanced the device performance from 14.9% to 20.6% due to the shift in the energy levels within the Perovskite material that improved charge transport and reduced charge carrier recombination (Figure 4A.3).

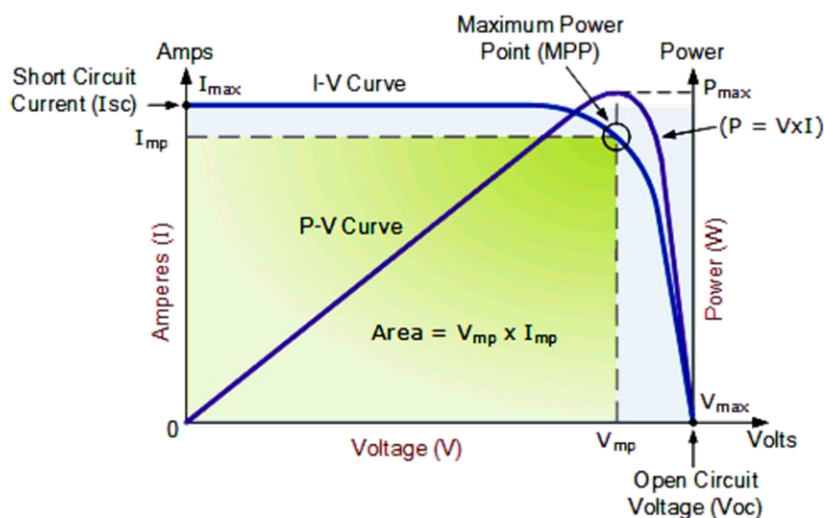


**Figure 4A.4.** I-V characteristic curve of a solar cell showing open-circuit voltage ( $V_{oc}$ ), short-circuit current ( $J_{sc}$ ), maximum power point (mpp), voltage at maximum power ( $V_{mp}$ ) and current at maximum power ( $J_{mp}$ ). (Adapted from reference 29)

Perovskite solar cells have several key parameters that are used to evaluate their performance. Figure 4A.4 shows the current-voltage characteristics of solar cells.<sup>29</sup> Commonly measured parameters are:

- (i) **Open-circuit voltage ( $V_{oc}$ ):**  $V_{oc}$  is the maximum voltage that can be obtained from the solar cell when there is no external load connected. It represents the potential difference across the terminals of the solar cell.
- (ii) **Short-circuit current ( $J_{sc}$ ):**  $J_{sc}$  is the current flowing through the solar cell when the terminals are shorted together (i.e., no voltage across the terminals). It represents the maximum current that the solar cell can deliver under short-

circuit conditions. Short-circuit current depends on the incident photon on the solar cell.

**(iii) Fill factor (FF):** FF is a measure of how effectively the solar cell can convert incident light into electrical power. It is calculated by dividing the maximum power output ( $P_{\max}$ ) of the solar cell by the product of  $V_{oc}$  and  $J_{sc}$  (Equation 4A.1).  $P_{\max}$  can be expressed as the product of  $J_{mpp}$  and  $V_{mpp}$ , where mpp is maximum power point of the cell.

$$FF = \frac{J_{mpp} V_{mpp}}{J_{sc} V_{oc}} \quad \text{Equation 4A.1}$$

**(iv) Power conversion efficiency (PCE%):** PCE is a critical measure for solar cells that reflects the proportion of incident sunlight converted into usable electrical energy. It is calculated by dividing the solar cell's maximum power output ( $P_{\max}$ ) by the incident solar power ( $P_{in}$ ) (Equation 4A.2).

$$PCE\% = \frac{P_{max}}{P_{in}} = \frac{J_{mpp} V_{mpp}}{P_{in}} = \frac{FF J_{sc} V_{oc}}{P_{in}} \quad \text{Equation 4A.2}$$

In this chapter, two thermally cross-linkable, hole-transporting materials derived from carbazole and diphenylamine moieties, namely **C-Sty3** and **C-Sty2** (Figure 4A.5), are discussed. Carbazole-based derivatives have already found successful applications in OLEDs, OFETs, and DSSCs due to excellent charge-transport properties, high chemical stability, and the ability to easily modify its structure with various functional groups.<sup>30-33</sup> The performance of Perovskite solar cell incorporating these materials was optimized by adjusting several parameters such as weight percentage of the hole-transporting material, spin-coating speed (rpm), and annealing temperature. By varying these parameters, we were able to enhance the performance of the PSC devices. The power conversion efficiencies achieved by the

optimized **C-Sty3** and **C-Sty2** devices were 16.1% and 15.2%, respectively. These efficiencies were compared to a reference device based on widely used hole-transporting material, PTAA, which exhibited a PCE of 18.8%. The device containing **C-Sty3** derivative outperformed the **C-Sty2** derivative due to increased conductivity and ion diffusion across the hyper-cross-linked **C-Sty3**-based films. The chapter also highlights the impact of various factors on the performance of the PSC devices and demonstrates how thermally cross-linkable hole-transporting materials can be used to form stable and conductive hole-transporting layers.

### 4A.3. Results and Discussion

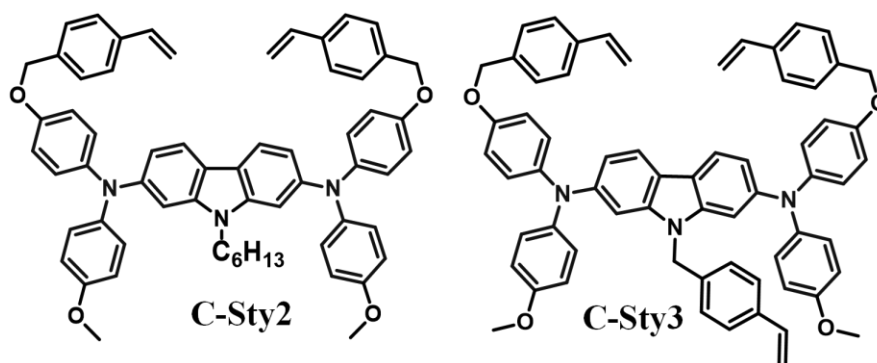


**Figure 4A.5.** Chemical structures of **C-Sty2** and **C-Sty3**.

The hole transporting materials **C-Sty2** and **C-Sty3** (Figure 4A.5) have two or three styryl units which can undergo thermal polymerization. Both HTMs showed good solubility in common organic solvents, which benefitted the solution processing of these materials. The synthesis and detailed characterization of **C-Sty2** and **C-Sty3** have been explained in Chapter 2 (Session 2.5.4; Page 33).

#### 4A.3.1. Thermal, Photophysical and Electrochemical Properties

Both carbazole derivatives, **C-Sty3** and **C-Sty2**, exhibited minimal absorption beyond 450 nm. The enhanced transparency of the cross-linked films formed from three weight percentage solutions (3 mg/ml, 5 mg/ml and 10 mg/ml) showed >95%



transmittance in the visible region as shown in Figure 4A.6. This makes the hole-transporting material layer to allow incident light to pass through without significant absorption loss. In the p-i-n architecture of Perovskite solar cells, the light first traverses the thin HTM layer before reaching the Perovskite layer. Transparent HTM layers ensure maximum light absorption by the Perovskite layer, increasing the overall efficiency of the PSC device.

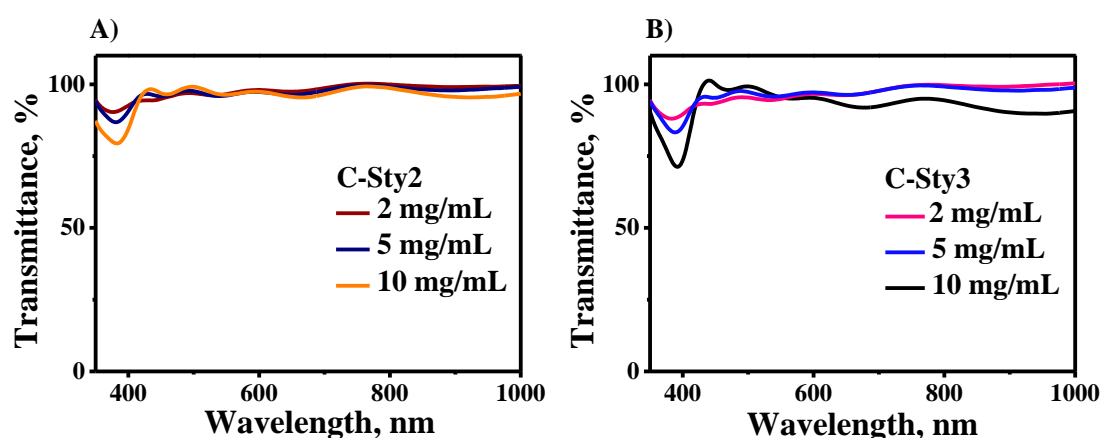


**Figure 4A.6.** Transmittance plots of cross-linked (A) **C-Sty2** and (B) **C-Sty3** films formed from different weight percentage solutions.

The thermal stability of the materials were investigated through TGA analysis in nitrogen atmosphere (Chapter 2; Figure 2.11). TGA showed excellent thermal stability with decomposition temperature at 410 °C and 427 °C for **C-Sty2** and **C-Sty3**, respectively, which is high enough to tolerate normal PSC processing conditions. The cross-linking ability and the insoluble polymeric films were thoroughly characterized using techniques like FT-IR, WAXD, UV-Vis, AFM analyses (Chapter 2; Figures 2.6, 2.7 and 2.10). Electrochemical impedance spectroscopy was used to study the electrical conductivity and ion transport of the cross-linked films (Chapter 2; Figure 2.21). The hyperbranched **C-Sty3** films showed low charge transfer resistance compared to **C-Sty2** indicating the improved conductivity. The details of these experiments and

characterizations are given in Chapter 2. Table 4A.1 presents a concise summary of the photophysical and thermal studies conducted on these materials.

**Table 4A.1.** Photophysical and thermal properties of carbazole-diphenylamine derivatives. (CB: Chlorobenzene,  $\Phi_F$ : Fluorescence quantum yield in solid state)

Compounds	$\lambda_{\text{abs}}$ (nm) $\epsilon$ ( $M^{-1} \text{cm}^{-1}$ )				$\lambda_{\text{em}}$ (nm)				$\Phi_F$ (%)	$T_d$ ( $^{\circ}\text{C}$ )
	DMF	THF	CB	Tol	DMF	THF	CIB	Tol		
<b>C-Sty2</b>	386 ( $2.5 \times 10^4$ )	388 ( $3.5 \times 10^4$ )	390 ( $2.6 \times 10^4$ )	392 ( $3.9 \times 10^4$ )	424	419	415	413	$2.5 \pm 0.02$	410
<b>C-Sty3</b>	386 ( $2.1 \times 10^4$ )	390 ( $3.3 \times 10^4$ )	392 ( $2.4 \times 10^4$ )	394 ( $3.5 \times 10^4$ )	425	420	417	415	$0.98 \pm 0.02$	427

The redox potentials of the polymers were calculated by utilizing the experimental data from solid-state UV-vis absorption spectra and CV using -4.8 eV as the HOMO of ferrocene against vacuum vs the Ag/AgCl reference electrode. We have used the longest absorption wavelength,  $\lambda_{\text{onset}}$  to determine the optical band gap energy using the equation,  $\Delta E = 1242/\lambda_{\text{onset}}$ . The oxidation potentials ( $E_{\text{ox}}$ ) were obtained from cyclic voltammetry and the molecule's HOMO energy levels using Equation 4A.3.

$$E_{\text{HOMO}} = - [(4.8 - E_{\text{OX.Ferrocene}}) + E_{\text{OX.}}] \quad \text{Equation 4A.3}$$

where,  $E_{\text{OX.Ferrocene}}$  and  $E_{\text{OX.}}$  are the onset oxidation potential of ferrocene and material, respectively. 4.8 eV is the absolute oxidation potential of ferrocene with respect to vacuum. LUMO values are obtained by adding the HOMO energy to  $\Delta E$  value. **C-Sty2** and **C-Sty3** in solution state showed HOMO energy values of -4.9 eV and -4.95 eV, respectively, whereas cross-linked polymers display marginally deeper HOMO energy levels of 5.01 eV and 5.11 eV by **C-Sty2** and **C-Sty3**, respectively. The deeper HOMO energy level of cross-linked polymers likely reduces potential voltage loss, implying a greater  $V_{\text{oc}}$  in the related Perovskite solar cell devices.<sup>8</sup> The stabilized structure of the

molecules was theoretically computed using DFT calculations with the B3LYP exchange-correlation functional and a 6-311G basis set using Gaussian 09W.<sup>34</sup> The HOMO-LUMO energy distribution and the calculated energy levels are given in Figure 4A.7. Both the HTMs exhibited suitable energy levels with respect to the valence band energy of the Perovskite materials used (VB= -5.56 eV and CB= -3.9 eV).

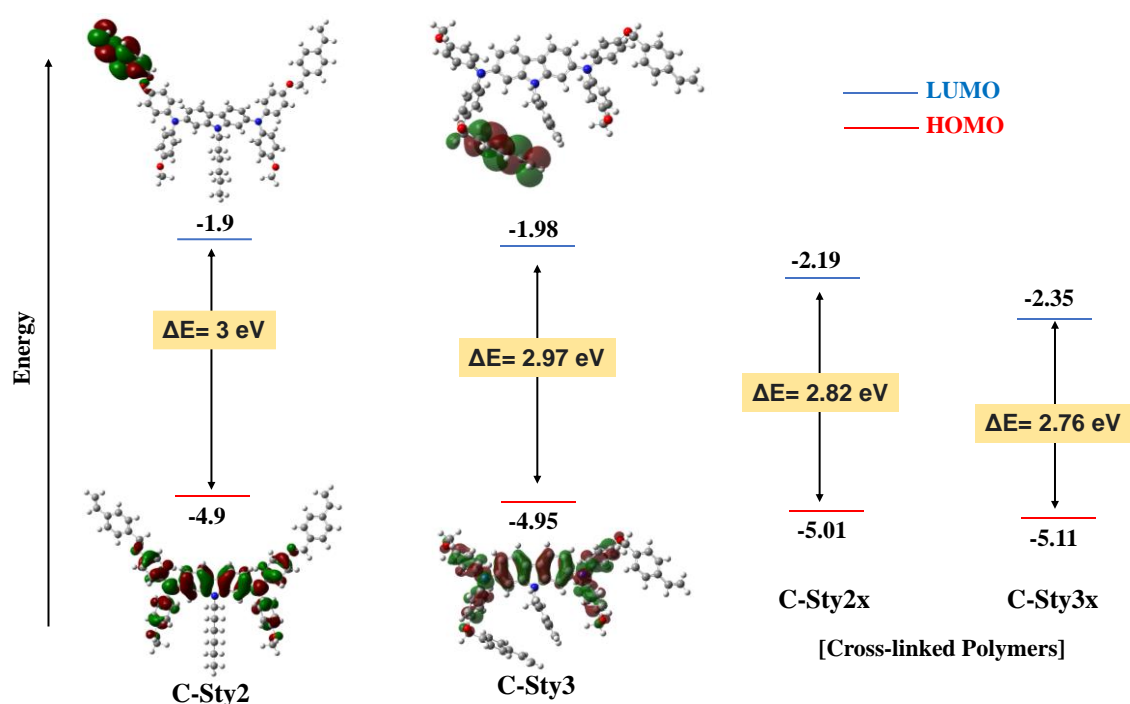


**Figure 4A.7.** HOMO-LUMO energy distribution on stabilized structures and the optically calculated energy values of monomers and cross-linked polymers.

In Perovskite solar cells, DMF is the commonly used solvent for Perovskite precursor preparation and film deposition, and hence it is important to consider the resistance of the HTM layer towards DMF. In p-i-n device structure of PSCs, Perovskite is coated over the thin HTM layer. A stable, solvent resistive HTM gives more stability to the PSC devices by avoiding partial washing or etching when exposed to certain solvents used in subsequent steps of the fabrication process. In this context, we examined the solvent (DMF) resistance of the cross-linked films (200° annealing

temperature) formed from three weight percentage solutions (3 mg/ml, 5 mg/ml and 10 mg/ml) by comparing the UV-Vis absorption of the cross-linked materials before and after washing with DMF. The results showed an improved solvent resistance after cross-linking (Figures 4A.8A and 4A.8B).

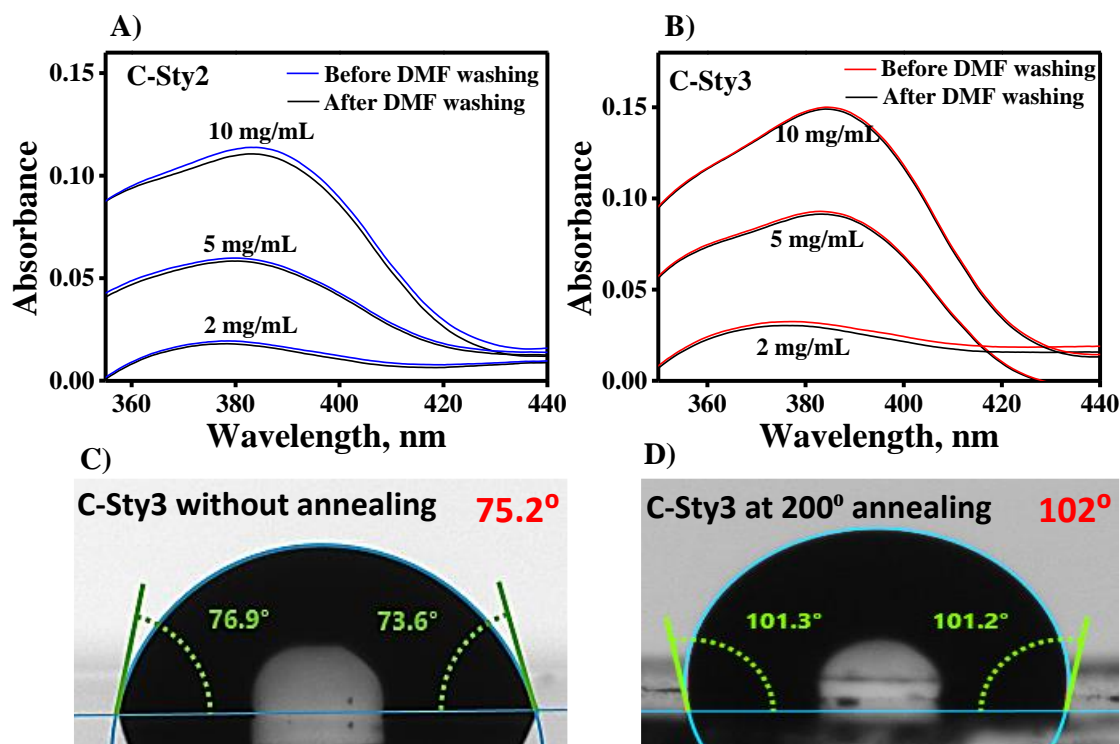


**Figure 4A.8.** Absorbance spectra of the cross-linked films of (A) **C-Sty2** and (B) **C-Sty3** before and after rinsing with DMF; Water contact angle of the films of **C-Sty3** (C) before and (D) after annealing.

We further determined the hydrophobicity of the **C-Sty3** polymer through water contact angle measurements. As shown in Figures 4A.8C and 4A.8D, cross-linked films exhibited a significantly increased contact angle of  $\approx 101.2^\circ$ , which is larger than commercially used PEDOT:PSS ( $\approx 7.9^\circ$ ), PTAA ( $\approx 85^\circ$ ) and spiro-OMeTAD ( $\approx 76.1^\circ$ ).<sup>35,36</sup> This result confirms the hydrophobic nature of the synthesized HTMs. While such an enhanced hydrophobic character of HTM films is highly beneficial in n-i-p

architecture, it could adversely affect the p-i-n devices due to poor wetting of the Perovskite precursor solutions leading to lower quality Perovskite films.

#### 4A.3.2. Photovoltaic Performance of Devices

To analyse the photovoltaic device performance of the developed HTMs, we fabricated the Perovskite solar cells with a typical planar p-i-n device configuration of FTO/HTM/Perovskite( $\text{Cs}_{0.05}\text{FA}_{0.80}\text{MA}_{0.15}\text{PbI}_{2.75}\text{Br}_{0.25}$ )/ $\text{C}_{60}$ /BCP/Ag, without any dopants/additives to HTM layer. The Experimental Section provides detailed information on device fabrication. The device architecture and energy level diagram of the fabricated devices are shown in Figure 4A.9.

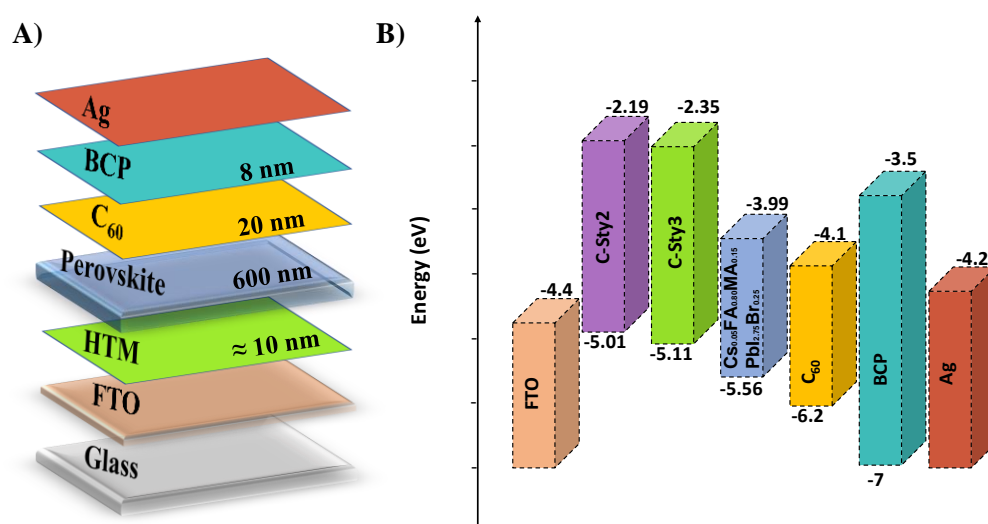


**Figure 4A.9.** (A) Schematic representation of the layered Perovskite device architecture and (B) Energy band diagram.

A mixed-composition perovskite material was used, with cesium, formamidinium (FA), and methylammonium (MA) cations and a I/Br ratio of 11:1. As shown in Figure 4A.9B, the HOMO levels of cross-linked HTL match the valence band energy of Perovskite (-5.56), implying that effective hole extraction from Perovskite to HTL is achievable. Furthermore, the cross-linked HTL's high LUMO values may efficiently block electrons, enabling higher charge selectivity while preventing charge

recombination and current leakage. A BCP layer was utilized as a hole-blocking layer, and an additional C<sub>60</sub> layer was added in order to facilitate improved electron extraction at the Perovskite/TiO<sub>2</sub> interface.<sup>37,38</sup>

To optimize the PSC device fabrication, we have used **C-Sty3**, by systematically varying various factors such as weight percentage, spin coating speed (rpm) and annealing temperature of the hole transporting material. Careful analysis of the results enabled us to identify the optimal conditions for the HTM layer, leading to notable enhancements in various device parameters, including power conversion efficiency (PCE), short-circuit current density (J<sub>sc</sub>), open-circuit voltage (V<sub>oc</sub>), and fill factor (FF). This investigation revealed the substantial impact of these variables on the performance of Perovskite solar cells.

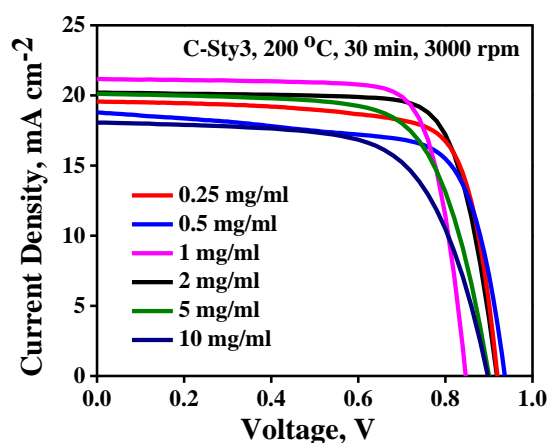


**Figure 4A.10.** J-V characteristics of devices based on different weight percentage of **C-Sty3** HTM recorded under irradiation of AM 1.5G light.

The weight percentage of the HTM solution affects the film thickness and morphology of the HTM layer. An optimal HTM thickness ensures increased performance of the devices and it can have effect on hole extraction, series resistance, film morphology, surface coverage and light absorption. Evaluation of the PSC device performance was performed by using different weight percentage solutions of **C-Sty3**

(0.25 mg, 0.5 mg, 1 mg, 2 mg, 5 mg and 10 mg) per ml of the chlorobenzene solutions at 3000 rpm, 200 °C annealing temperature and 30 min annealing time (Figure 4A.10). The best efficiency was shown by the device prepared from 2 mg/ml solution with a champion cell PCE of 14.28%,  $V_{oc}$  of 0.92 V,  $J_{sc}$  of 20.20 mA cm<sup>-2</sup> and a FF of 0.77. The photocurrent density-voltage (J-V) plot of the PSCs and the performance parameters obtained are given in Figure 4A.10 and Table 4A.2.

**Table 4A.2.** J-V curve parameters of Perovskite solar cells fabricated from different weight percentage of **C-Sty3** HTM.

Weight (mg/ml)	$J_{sc}$ (mA/cm <sup>2</sup> )	$V_{oc}$ (V)	FF	PCE (%)
0.25	19.57	0.92	0.75	13.51
0.5	18.79	0.94	0.71	12.47
1	21.18	0.85	0.78	13.94
2	20.20	0.92	0.77	14.28
5	20.12	0.90	0.70	12.61
10	18.06	0.90	0.66	10.69

In the subsequent stage of the optimization of the fabrication process, we varied the spin-coating speed of the **C-Sty3** HTM deposition (1000 rpm, 3000 rpm, and 5000 rpm) and used 2 mg/ml of the material, annealing temperature of 200 °C and annealing duration of 30 minutes. Higher spin-coating speeds were expected to yield thinner and more uniform HTM films, which could facilitate efficient hole extraction. On the other hand, lower spin-coating speeds can lead to thicker films, potentially increasing the likelihood of charge recombination. All the PSC devices fabricated during these experiments showed PCEs in the 14%-16% range and the device with **C-Sty3** spin coated at 5000 rpm exhibited the highest PCE value of 15.22% (Figure 4A.11 and Table 4A.3). Although the  $V_{oc}$  of the 5000-rpm PSC device (0.91 V) was slightly lower compared to the devices spun at 3000 and 1000 rpm (0.92 V and 0.94

V, respectively), the 5000-rpm devices demonstrated a higher PCE% with a Fill Factor (FF) of 0.79 and  $J_{sc}$  of 21.08 mA cm<sup>-2</sup>. The film thickness attained at these optimum conditions measured using a profilometer was  $\approx$ 10 nm.

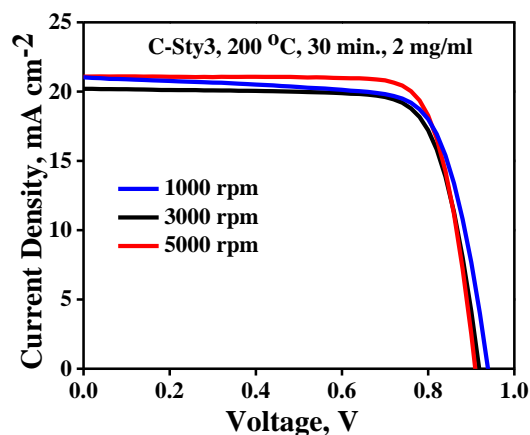


**Figure 4A.11.** J-V characteristics of devices based on different spinning rate of HTM coating, recorded under irradiation of AM 1.5G light.

**Table 4A.3.** J-V curve parameters of Perovskite solar cells fabricated from different spinning rate (rpm) of HTM.

rpm	$J_{sc}$ (mA/cm <sup>2</sup> )	$V_{oc}$ (V)	FF	PCE (%)
1000	21.03	0.94	0.74	14.60
3000	20.20	0.92	0.77	14.28
5000	21.08	0.91	0.79	15.22

The performance of the devices showed a significant improvement after being stored in ambient air conditions (<25% relative humidity) without encapsulation for a period of 3-4 days.<sup>28</sup> This aging effect is demonstrated in Figure 4A.12 and Table 4. The initial PCE by the devices at 1000, 3000 and 5000 rpm were 10.32%, 11.66% and 12.64%, respectively. The devices showed great improvement in PCE upon aging and the third day measurements showed values of 14.60% (1000rpm), 14.28% (3000 rpm) and 15.22% (5000 rpm).



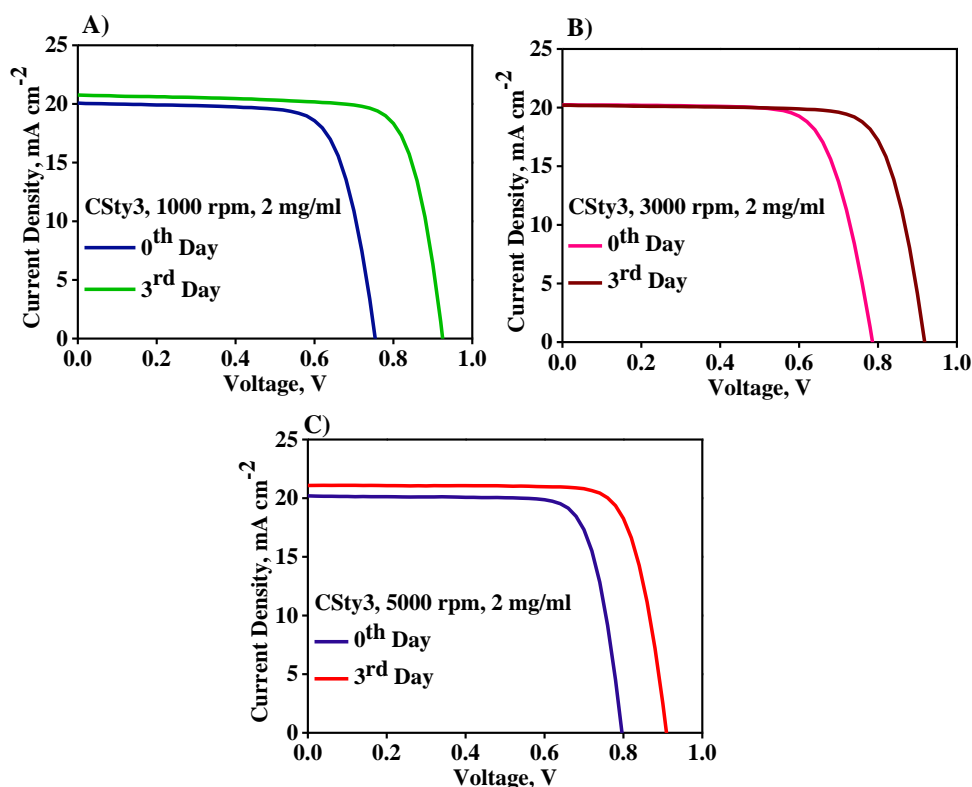


**Figure 4A.12.** J-V characteristics of devices fabricated using the HTMs prepared from (A) 1000; (B) 3000 and (C) 5000 rpm, as fabricated and after 3 days of aging. The measurements were recorded under irradiation of AM 1.5G light.

**Table 4A.4.** J-V curve parameters of Perovskite solar cells fabricated from different spinning rate (rpm) of HTM as fabricated and after 3 days of aging.

rpm	Day	Jsc (mA/cm <sup>2</sup> )	Voc (V)	FF	PCE (%)	Rs (Ω cm <sup>2</sup> )	Rsh (Ω cm <sup>2</sup> )
1000	0	20.08	0.73	0.71	10.32	4.42	445.44
	3	21.03	0.94	0.74	14.60	4.70	509.61
3000	0	20.24	0.79	0.73	11.66	4.89	737.28
	3	20.20	0.92	0.77	14.28	4.57	765.90
5000	0	20.20	0.80	0.79	12.64	3.80	797.18
	3	21.08	0.91	0.79	15.22	3.83	947.22

When perovskite layers are annealed, a substantial amount of surface PbI<sub>2</sub> is formed, which can have a passivation effect on the Perovskite layer. This excess PbI<sub>2</sub> interacts with the perovskite structure and helps to passivate defects and grain boundaries, reducing recombination and improving charge transport. Thus, the

enhanced performance of the PSC devices upon aging can be attributed to the increased  $R_{sh}$  (small leakage in current caused by material defects, impurities, or non-uniformity in the device structure, known as shunt resistance), which is generally considered as a recombination resistance under strong illumination. The recombination resistance increased in all the cases from  $445.44 \Omega \text{ cm}^2$  to  $509.61 \Omega \text{ cm}^2$  (1000 rpm),  $737.28 \Omega \text{ cm}^2$  to  $765.90 \Omega \text{ cm}^2$  (3000 rpm) and  $797.18 \Omega \text{ cm}^2$  to  $947.22 \Omega \text{ cm}^2$  (5000 rpm) due to the reduction in charge recombination effects. The energy level alignment shift between the valence and conduction bands of the perovskite layer also played a crucial role in enhancing the performance of the device by influencing the charge extraction process.<sup>28,39</sup>

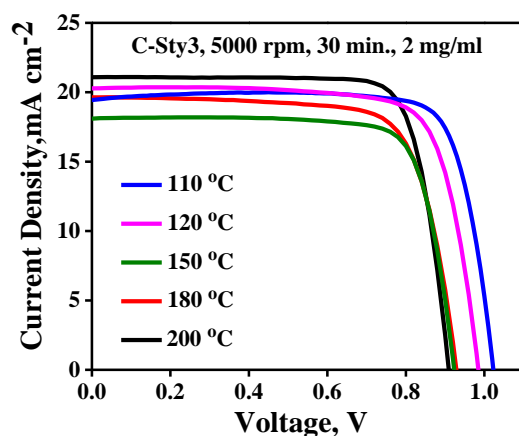


**Figure 4A.13.** J-V characteristics of devices based on different annealing temperature of HTM, recorded under irradiation of AM 1.5G light.

**Table 4A.5.** J-V curve parameters of Perovskite solar cell fabricated from different annealing temperature of HTM.

Annealing temperature (°C)	Jsc (mA/cm <sup>2</sup> )	Voc (V)	FF	PCE (%)
200	21.08	0.91	0.79	15.22
180	19.63	0.93	0.74	13.48
150	18.10	0.92	0.78	13.08
120	20.28	0.98	0.76	15.21
110	19.44	1.02	0.81	16.12

The degree of thermal annealing plays a crucial role in the cross-linking reaction process of hole transporting materials and significantly affects the quality of HTM films. To determine the optimal cross-linking temperature, J-V curves of solar cells incorporating **C-Sty3** as the HTM were analysed at different cross-linking temperatures. The results, shown in Figure 4A.13 and Table 4A.5, indicated that the solar cells achieved the highest PCE of 16.12% with a remarkable FF value of 0.81,  $V_{oc}$  of 1.02 V, and  $J_{sc}$  of  $19.44 \text{ mA cm}^{-2}$  at an optimum annealing temperature of  $110^\circ\text{C}$ . It is noteworthy that this annealing temperature was significantly lower than the crosslinking temperature ( $\approx 170^\circ\text{C}$ ). The observed differences in device parameters can be attributed to the dewetting of the Perovskite precursor solutions over HTM films at higher thermal annealing temperatures leading to poor quality films. Optimized PSC fabrication conditions with higher temperature annealing at  $200^\circ\text{C}$  for 30 min, yielded slightly lower PCE of 15.22%.

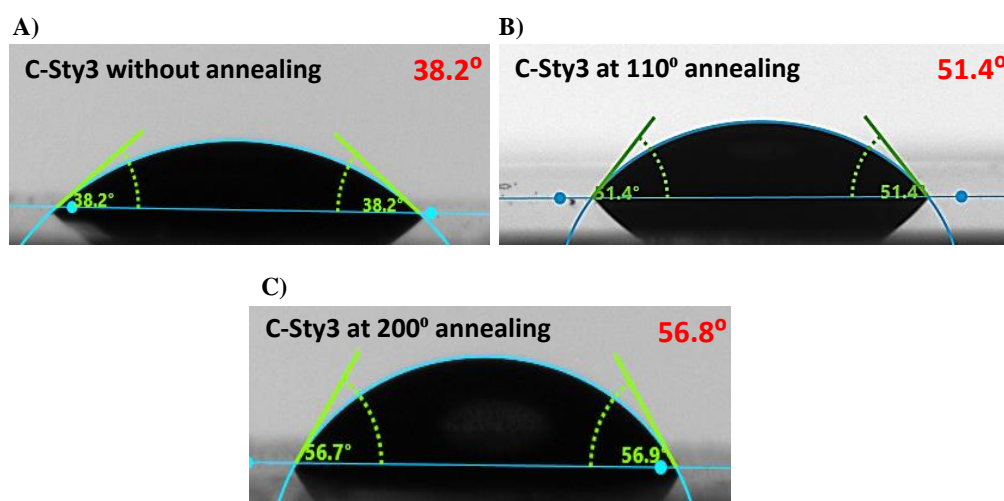


**Figure 4A.14.** Contact angles of DMF on (A) **C-Sty3** film without thermal cross-links; (B) **C-Sty3** film cross-linked at  $110^\circ\text{C}$  and (C) **C-Sty3** film cross-linked at  $200^\circ\text{C}$ .

To further investigate the effect of annealing temperature, DMF contact angle measurements were conducted on HTM films prepared at  $200^\circ\text{C}$  and  $110^\circ\text{C}$

annealing temperatures, using 2 mg/ml HTM solutions and a spin-coating speed of 5000 rpm (Figure 4A.14). The HTMs subjected to the lower annealing temperature of 110 °C displayed a lower contact angle value of 51.4° compared to those annealed at 200 °C (contact angle of 56.8°). The film without thermal cross-linking exhibited a DMF contact angle of 38.2°. These experiments demonstrated the change in the contact angle with the annealing temperature and subsequent correlation with the performance of the perovskite solar cells incorporating these HTMs. The devices using HTMs with higher contact angle (from the 200 °C annealing) demonstrated lower PCE% compared to the devices using HTMs with lower contact angles (from the 110 °C annealing). The lower PCE% could be attributed to the dewetting of the Perovskite precursor solution on the HTM surface leading to visible imperfections during the Perovskite film formation. Dewetting refers to the incomplete spreading and coverage of a liquid on a substrate, resulting in the formation of droplets or beads instead.<sup>35</sup>

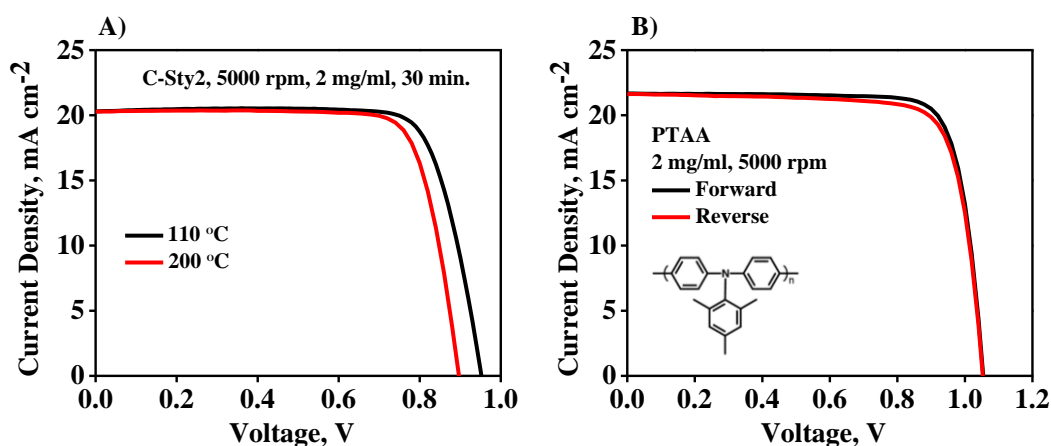


**Figure 4A.15.** J-V characteristics of (A) C-Sty2 devices based on different annealing temperature of HTM; (B) PTAA based devices recorded under irradiation of AM 1.5G light.

Under the same optimized conditions (2 mg/ml; 5000 rpm & 110 °C thermal annealing for 30 min), we have fabricated Perovskite solar cells using C-Sty2 as the

HTM. The device with 110 °C thermal annealing of the **C-Sty2** HTM exhibited a slightly lower PCE of 15.16% compared to **C-Sty3**, with a FF of 0.78,  $V_{oc}$  of 0.95 V, and  $J_{sc}$  of 20.3 mA/cm<sup>2</sup>. These results are shown in Figure 4A.15A and Table 4A.6.

**Table 4A.6.** J-V curve parameters of Perovskite solar cell fabricated from **C-Sty2** at different annealing temperature.

Annealing temperature (°C)	$J_{sc}$ (mA/cm <sup>2</sup> )	$V_{oc}$ (V)	FF	PCE (%)
110	20.30	0.95	0.78	15.16
200	20.28	0.90	0.79	14.39

**Table 4A.7.** J-V curve parameters of Perovskite solar cell using standard PTAA as HTM, fabricated under the similar conditions (5000 rpm, 2 mg/ml).

PTAA	$J_{sc}$ (mA/cm <sup>2</sup> )	$V_{oc}$ (V)	FF	PCE (%)
Forward	22.59	1.04	0.80	18.82
Reverse	22.40	1.05	0.80	18.79

To provide a reference point, we compared the performance of the **C-Sty2** and **C-Sty3** devices to PSC devices fabricated with commercially available and widely used HTM, PTAA under similar fabrication conditions. The PTAA-based devices demonstrated a PCE of 18.8% with a FF of 0.8,  $V_{oc}$  of 1 V, and  $J_{sc}$  of 22.5 mA/cm<sup>2</sup>, which is comparable to that of the **C-Sty3**-based devices (Figure 4A.15B and Table 4A.7), providing insights into the relative performance of the different HTM materials. Major differences between the **C-Sty3** / **C-Sty2** based devices and standard PTAA device is in the  $V_{oc}$ , which could be due to the better band alignment of PTAA with the Perovskite material we used.<sup>40,41</sup>

Figure 4A.16A presents a cross-sectional SEM image of the **C-Sty3** device architecture. The thickness of each layer may be approximately estimated as follows:

the HTL layer appears to be in the range of 10-15 nm (not clearly resolved), the Perovskite layer is approximately 550-600 nm thick, the C<sub>60</sub> layer measures around 20 nm, and the BCP layer has a thickness of approximately 8 nm. The C<sub>60</sub> and BCP layers formed a 30 nm crust on the top surface of the perovskite. The Ag electrode exhibited partial delamination, which likely occurred during the cutting process conducted prior to the SEM measurements.<sup>16</sup>

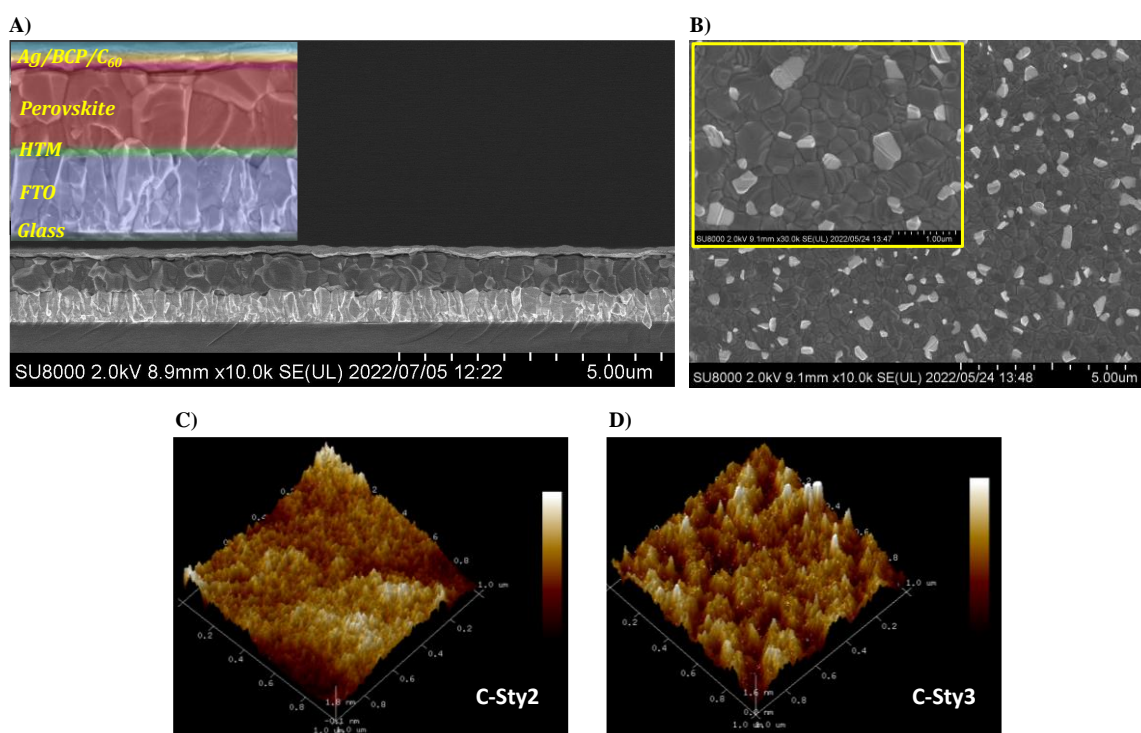


**Figure 4A.16.** (A) Cross sectional SEM image of p-i-n based device with cross-linked **C-Sty3** HTM (inset shows the zoomed image of the separate layers in the device); (B) Top-view SEM images of perovskite films spin coated on cross-linked **C-Sty3** HTM. (The inset shows the zoomed (1 μm) scale bar image) and (C-D) AFM images of the cross-linked films of **C-STy2** and **C-STy3** at the optimum conditions (2mg/ml, 5000 rpm, 110°C, ≈15 nm thickness).

Figure 4A.16B shows top-view SEM images of the Perovskite layer coated on top of cross-linked **C-Sty3** HTM. The homogeneous morphology of the film with the entire surface coverage demonstrated the benefit of crosslinked HTMs in generating

compact and homogeneous films. Further, AFM was used to investigate the morphology of the cross-linked films. The films featured a consistently dispersed grain-like structure and a uniform surface morphology (Figure 4A.16C).

#### 4A.4. Conclusions

Two cross-linkable carbazole - diphenylamine derivatives were utilized as HTMs in planar p-i-n type Perovskite solar cells. Different parameters, such as the weight percentage of the hole-transporting material, spin-coating speed (rpm), and annealing temperature, were optimized to enhance the performance of PSC devices. The dopant free PSCs of **C-Sty3** and **C-Sty2** showed power conversion efficiencies (PCE) of 16.1% and 15.2%, respectively in comparison with the standard HTM, PTAA based device with PCE of 18.8%. The improved performance observed in the device containing the **C-Sty3** derivative compared to **C-Sty2**, can be attributed to the enhanced conductivity and superior ion diffusion within the hyper-cross-linked **CSty3**-based films. This chapter emphasizes the impact of various factors on the performance of PSC devices and highlights the promising use of low-cost, cross-linkable triphenylamine-based compounds as dopant-free hole-transport materials for efficient and stable PSCs.

#### 4A.5. Experimental Section

##### 4A.5.1. Materials and Methods

Synthesis, photophysical and electrochemical studies were conducted in CSIR-NIIST, whereas the Perovskite solar cells were fabricated in Kyoto University, Japan under the guidance of Prof. Atsushi Wakamiya. Chapter 2 provides a comprehensive explanation of the synthesis and detailed characterization of **C-Sty2** and **C-Sty3**. Cyclic voltammetry measurements were conducted on a PARSTAT 4000A Potentiostat to

study the electrochemical properties. The experiments were performed under Argon using 0.1 M tetrabutylammonium hexafluorophosphate (TBAPF<sub>6</sub>) in acetonitrile as the supporting electrolyte. A reference electrode of Ag/AgCl and a platinum wire counter electrode were employed. The scan rate used was 50 mV/s. Optical estimation of energy levels was carried out using UV-Vis spectra obtained from a Shimadzu UV-Vis spectrophotometer (UV-2600) and cyclic voltammetry. The AFM images of the films were acquired using an AFM-Bruker Multitop Nanoscope V instrument operating in tapping mode. The transmittance of the cross-linked films were recorded using an Ocean Optics Spectrometer DH-2000-BAL. Contact angles were measured using a DSA30E-contact angle goniometer instrument. The materials used for device fabrication were utilized as received without undergoing additional purification steps. Cesium iodide (CsI), methylammonium bromide (MABr, >98.0%), lead(II) bromide (PbBr<sub>2</sub>, >98.0%), lead(II) iodide (PbI<sub>2</sub>, 99.99%, trace metals basis), formamidinium lead iodide ( $\delta$ -FAPbI<sub>3</sub>), and bathocuproine (BCP) were procured from Tokyo Chemical Industry Co., Ltd. (TCI). ATR Company provided the sublimed fullerene C<sub>60</sub> (99.99% purity). Sigma-Aldrich supplied poly[bis(4-phenyl)(2,4,6-trimethylphenyl)amine] (PTAA), while dehydrated dimethylsulfoxide (DMSO, super dehydrated) was purchased from FUJIFILM Wako Pure Chemical Co., Ltd. Dimethylformamide (DMF) and chlorobenzene were obtained from Kanto Chemical Co., Inc. All solvents were degassed by bubbling Ar gas for 1 hour and further dried using molecular sieves in an Ar-filled glove box (O<sub>2</sub>, H<sub>2</sub>O < 0.1 ppm) prior to usage. Scanning electron microscopy (SEM) analysis was conducted using a Hitachi S8010 ultra-high-resolution scanning electron microscope (Hitachi High-Tech Corporation). AM1.5G light was generated with a Bunkoukeiki SMO-250PV solar simulator via a 150 W Xe lamp. Bunkoukeiki BS-520BK reference silicon photodiode with an IR-cut filter



was used to calibrate the light intensity. Attenuation over a wide range of intensity was enabled by using various neutral density filters (100, 40, 20, 10, 5, and 1% transmittance) in combination with the variable aperture built into the solar simulator.  $J$ - $V$  curves were obtained using a Keithley 2450 source meter. Forward and reverse scans were measured between -0.1 and 1.2 V at a scan rate of 50 mV s<sup>-1</sup>.

#### 4A.5.2. Preparation of Cs<sub>0.05</sub>FA<sub>0.80</sub>MA<sub>0.15</sub>PbI<sub>2.75</sub>Br<sub>0.25</sub> Solution

The precursor solution was prepared by dissolving CsI (34 mg, 0.14 mmol), MABr (45 mg, 0.40 mmol), PbBr<sub>2</sub> (51 mg, 0.14 mmol), PbI<sub>2</sub> (187 mg, 0.41 mmol), and  $\delta$ -FAPbI<sub>3</sub> (1380 mg, 2.18 mmol) in a mixture of DMF (1.6 mL) and DMSO (0.48 mL) in a 3:1 ratio. The solution was then stirred at 70 °C for 5 min. and then at 40 °C for 30 minutes and subsequently filtered using a 0.45  $\mu$ m PTFE filter.

#### 4A.5.3. p-i-n Device Fabrication

Glass/FTO substrates (with a sheet resistance of 10  $\Omega$  sq<sup>-1</sup>, AGC Inc.) underwent a series of cleaning steps. First, they were etched using zinc powder and HCl (6 M in de-ionized water). Then, the substrates are sequentially cleaned by immersing them in water, acetone, detergent solution (Semico Clean 56, Furuuchi chemical), water, and isopropanol, followed by ultrasonic treatment for 15 minutes. Afterward, the substrates were dried using an air gun and subjected to plasma treatment immediately before the deposition of HTM.

To deposit the hole transporting material, a solution of chlorobenzene was spin-coated onto the plasma-treated FTO substrates, followed by heating on a hot plate at various temperatures for 30 minutes. For the PTAA devices, the hole transporting material PTAA (2 mg mL<sup>-1</sup> in anhydrous toluene) was spin-coated (5000 rpm) onto

the substrates and then heated on a hot plate at 100 °C for 10 minutes. The detailed profile of the spin coating program is shown in Figure 4A.17.

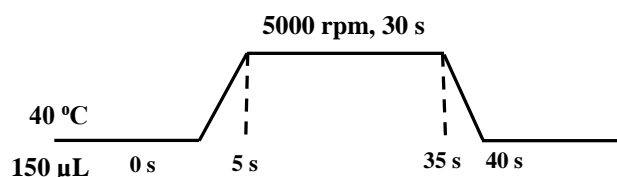


**Figure 4A.17.** Profile for the spin coating program of HTM layer deposition.

100 μL DMF was added to slides prior to spin coating for increasing the wettability of Perovskite precursor solution. A thin film of Perovskite layer was prepared by spin-coating 190 μL Perovskite precursor solution onto the **C-Sty2/C-Sty2**/PTAA coated FTO substrate and spread evenly. Just before completing the spin-coating process at 3000 rpm, 300 μL of chlorobenzene antisolvent was dripped onto the rotating substrate. The films were subsequently annealed on a hot plate at 150 °C for 10 minutes. The detailed profile of the spin coating program is shown in Figure 4A.18.

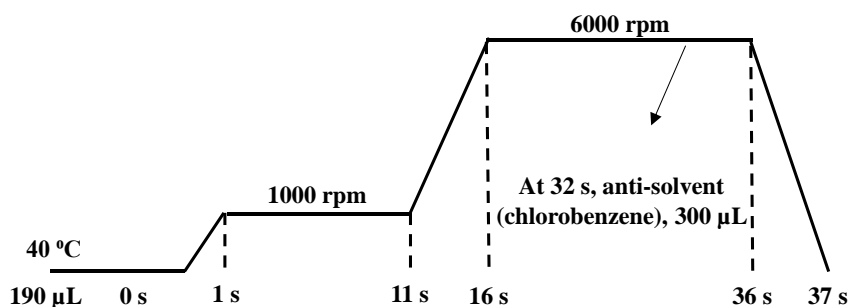


**Figure 4A.18.** Profile for the spin coating program of Perovskite layer deposition.

Under an inert atmosphere, the samples were transferred to a vacuum deposition chamber, where thermal evaporation was used to deposit 20 nm of C<sub>60</sub> (deposition rate: 0.05 nm s<sup>-1</sup>) and 8 nm of BCP (deposition rate: 0.01 nm s<sup>-1</sup>). Finally, a top electrode was created by depositing 100 nm of silver (deposition rate: 0.005 nm s<sup>-1</sup>) through a shadow mask.

## 4A.6. References

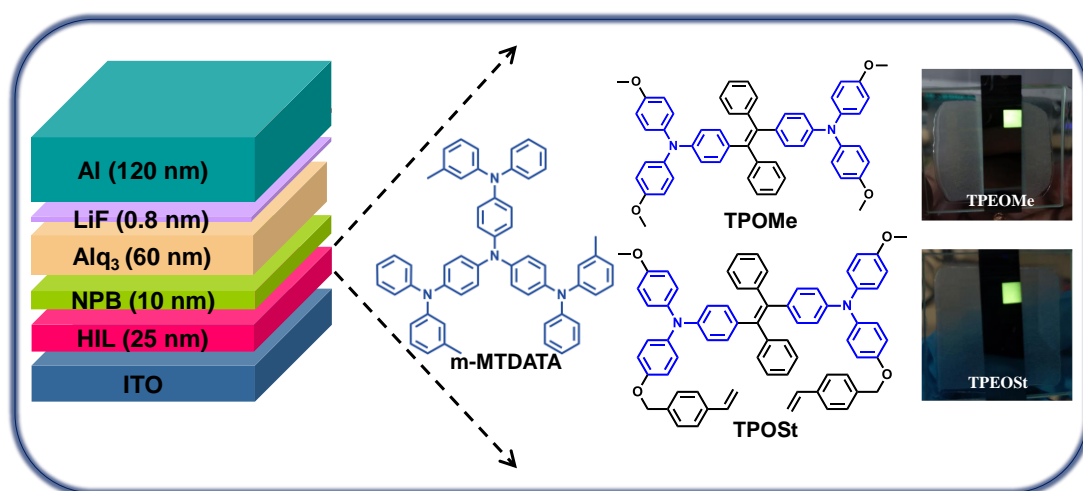
- (1) <https://www.nrel.gov/pv/cell-efficiency.html-july-2023>.
- (2) Grill, I.; Aygüler, M. F.; Bein, T.; Docampo, P.; Hartmann, N. F.; Handloser, M.; Hartschuh, A. Charge Transport Limitations in Perovskite Solar Cells: The Effect of Charge Extraction Layers. *ACS Appl. Mater. Interfaces* **2017**, *9*, 37655-37661.
- (3) Kim, G.-W.; Shinde, D. V.; Park, T. Thickness of the hole transport layer in perovskite solar cells: performance versus reproducibility. *RSC Adv.* **2015**, *5*, 99356-99360.
- (4) Marinova, N.; Tress, W.; Humphry-Baker, R.; Dar, M. I.; Bojinov, V.; Zakeeruddin, S. M.; Nazeeruddin, M. K.; Grätzel, M. Light Harvesting and Charge Recombination in CH<sub>3</sub>NH<sub>3</sub>PbI<sub>3</sub> Perovskite Solar Cells Studied by Hole Transport Layer Thickness Variation. *ACS Nano* **2015**, *9*, 4200-4209.
- (5) Rombach, F. M.; Haque, S. A.; Macdonald, T. J. Lessons learned from spiro-OMeTAD and PTAA in perovskite solar cells. *Energy Environ. Sci.* **2021**, *14*, 5161-5190.
- (6) Park, J.; Kim, J.; Yun, H.-S.; Paik, M. J.; Noh, E.; Mun, H. J.; Kim, M. G.; Shin, T. J.; Seok, S. I. Controlled growth of perovskite layers with volatile alkylammonium chlorides. *Nature* **2023**, *616*, 724-730.
- (7) Schloemer, T. H.; Christians, J. A.; Luther, J. M.; Sellinger, A. Doping strategies for small molecule organic hole-transport materials: impacts on perovskite solar cell performance and stability. *Chem. Sci* **2019**, *10*, 1904-1935.
- (8) Wang, L.; Zhang, F.; Liu, T.; Zhang, W.; Li, Y.; Cai, B.; He, L.; Guo, Y.; Yang, X.; Xu, B.; Gardner, J. M.; Kloo, L.; Sun, L. A crosslinked polymer as dopant-free hole-transport material for efficient n-i-p type perovskite solar cells. *J. Energy Chem.* **2021**, *55*, 211-218.
- (9) Heo, J. H.; Im, S. H.; Noh, J. H.; Mandal, T. N.; Lim, C.-S.; Chang, J. A.; Lee, Y. H.; Kim, H.-j.; Sarkar, A.; Nazeeruddin, M. K.; Grätzel, M.; Seok, S. I. Efficient inorganic-organic hybrid heterojunction solar cells containing perovskite compound and polymeric hole conductors. *Nat. Photonics* **2013**, *7*, 486-491.
- (10) Xie, Y.-M.; Yao, Q.; Xue, Q.; Zeng, Z.; Niu, T.; Zhou, Y.; Zhuo, M.-P.; Tsang, S.-W.; Yip, H.-L.; Cao, Y. Subtle side chain modification of triphenylamine-based polymer hole-transport layer materials produces efficient and stable inverted perovskite solar cells. *Int. J. Surf. Eng. Interdiscip. Mater. Sci.* **2022**, *1*, 281-293.
- (11) Li, Z.; Li, B.; Wu, X.; Sheppard, S. A.; Zhang, S.; Gao, D.; Long, N. J.; Zhu, Z. Organometallic-functionalized interfaces for highly efficient inverted perovskite solar cells. *Science* **2022**, *376*, 416-420.

- (12) Watson, Brian L.; Rolston, N.; Bush, K. A.; Taleghani, L.; Dauskardt, R. H. Synthesis and use of a hyper-connecting cross-linking agent in the hole-transporting layer of perovskite solar cells. *J. Mater. Chem. A* **2017**, *5*, 19267-19279.
- (13) Magomedov, A.; Al-Ashouri, A.; Kasparavičius, E.; Strazdaite, S.; Niaura, G.; Jošt, M.; Malinauskas, T.; Albrecht, S.; Getautis, V. Self-Assembled Hole Transporting Monolayer for Highly Efficient Perovskite Solar Cells. *Adv. Energy Mater.* **2018**, *8*, 1801892.
- (14) Guo, H.; Liu, C.; Hu, H.; Zhang, S.; Ji, X.; Cao, X.-M.; Ning, Z.; Zhu, W.-H.; Tian, H.; Wu, Y. Neglected acidity pitfall: boric acid-anchoring hole-selective contact for perovskite solar cells. *Natl. Sci.* **2023**, *10*.
- (15) Li, G.; Su, Z.; Canil, L.; Hughes, D.; Aldamasy, M. H.; Dagar, J.; Trofimov, S.; Wang, L.; Zuo, W.; Jerónimo-Rendon, J. J.; Byranvand, M. M.; Wang, C.; Zhu, R.; Zhang, Z.; Yang, F.; Nasti, G.; Naydenov, B.; Tsoi, W. C.; Li, Z.; Gao, X.; Wang, Z.; Jia, Y.; Unger, E.; Saliba, M.; Li, M.; Abate, A. Highly efficient p-i-n perovskite solar cells that endure temperature variations. *Science* **2023**, *379*, 399-403.
- (16) Murdey, R.; Ishikura, Y.; Matsushige, Y.; Hu, S.; Pascual, J.; Truong, M. A.; Nakamura, T.; Wakamiya, A. Operational stability, low light performance, and long-lived transients in mixed-halide perovskite solar cells with a monolayer-based hole extraction layer. *Sol. Energy Mater. Sol. Cells* **2022**, *245*, 111885.
- (17) Daskeviciute-Geguziene, S.; Magomedov, A.; Daskeviciene, M.; Genevičius, K.; Nekrašas, N.; Jankauskas, V.; Kantminiene, K.; McGehee, M. D.; Getautis, V. Cross-linkable carbazole-based hole transporting materials for perovskite solar cells. *Chem. Commun.* **2022**, *58*, 7495-7498.
- (18) Yang, W.; Long, H.; Sha, X.; Sun, J.; Zhao, Y.; Guo, C.; Peng, X.; Shou, C.; Yang, X.; Sheng, J.; Yang, Z.; Yan, B.; Ye, J. Unlocking Voltage Potentials of Mixed-Halide Perovskite Solar Cells via Phase Segregation Suppression. *Adv. Funct. Mater.* **2022**, *32*, 2110698.
- (19) Mahesh, S.; Ball, J. M.; Oliver, R. D. J.; McMeekin, D. P.; Nayak, P. K.; Johnston, M. B.; Snath, H. J. Revealing the origin of voltage loss in mixed-halide perovskite solar cells. *Energy Environ. Sci.* **2020**, *13*, 258-267.
- (20) Gil-Escrig, L.; Dreessen, C.; Palazon, F.; Hawash, Z.; Moons, E.; Albrecht, S.; Sessolo, M.; Bolink, H. J. Efficient Wide-Bandgap Mixed-Cation and Mixed-Halide Perovskite Solar Cells by Vacuum Deposition. *ACS Energy Lett.* **2021**, *6*, 827-836.
- (21) Tong, Y.; Najar, A.; Wang, L.; Liu, L.; Du, M.; Yang, J.; Li, J.; Wang, K.; Liu, S. Wide-Bandgap Organic-Inorganic Lead Halide Perovskite Solar Cells. *Adv. Sci.* **2022**, *9*, 2105085.

- (22) Cordero, F.; Craciun, F.; Paoletti, A. M.; Zanotti, G. Structural Transitions and Stability of FAPbI<sub>3</sub> and MAPbI<sub>3</sub>: The Role of Interstitial Water. *Nanomaterials* **2021**, *11*, 1610..
- (23) Zheng, Z.; Wang, S.; Hu, Y.; Rong, Y.; Mei, A.; Han, H. Development of formamidinium lead iodide-based perovskite solar cells: efficiency and stability. *Chem. Sci* **2022**, *13*, 2167-2183.
- (24) Jeon, N. J.; Noh, J. H.; Yang, W. S.; Kim, Y. C.; Ryu, S.; Seo, J.; Seok, S. I. Compositional engineering of perovskite materials for high-performance solar cells. *Nature* **2015**, *517*, 476-480.
- (25) Saliba, M.; Matsui, T.; Seo, J.-Y.; Domanski, K.; Correa-Baena, J.-P.; Nazeeruddin, M. K.; Zakeeruddin, S. M.; Tress, W.; Abate, A.; Hagfeldt, A.; Grätzel, M. Cesium-containing triple cation perovskite solar cells: improved stability, reproducibility and high efficiency. *Energy Environ. Sci.* **2016**, *9*, 1989-1997.
- (26) Truong, M. A.; Funasaki, T.; Ueberricke, L.; Nojo, W.; Murdey, R.; Yamada, T.; Hu, S.; Akatsuka, A.; Sekiguchi, N.; Hira, S.; Xie, L.; Nakamura, T.; Shioya, N.; Kan, D.; Tsuji, Y.; Iikubo, S.; Yoshida, H.; Shimakawa, Y.; Hasegawa, T.; Kanemitsu, Y.; Suzuki, T.; Wakamiya, A. Tripodal Triazatruxene Derivative as a Face-On Oriented Hole-Collecting Monolayer for Efficient and Stable Inverted Perovskite Solar Cells. *J. Am. Chem. Soc.* **2023**, *145*, 7528-7539.
- (27) Jegorovė, A.; Minh Anh, T.; Murdey, R.; Daskeviciene, M.; Malinauskas, T.; Kantminiene, K.; Jankauskas, V.; Getautis, V.; Wakamiya, A. Starburst Carbazole Derivatives as Efficient Hole Transporting Materials for Perovskite Solar Cells. *Sol. RRL* **2021**, *6*.
- (28) Ozaki, M.; Ishikura, Y.; Truong, M. A.; Liu, J.; Okada, I.; Tanabe, T.; Sekimoto, S.; Ohtsuki, T.; Murata, Y.; Murdey, R.; Wakamiya, A. Iodine-rich mixed composition perovskites optimised for tin(IV) oxide transport layers: the influence of halide ion ratio, annealing time, and ambient air aging on solar cell performance. *J. Mater. Chem. A* **2019**, *7*, 16947-16953.
- (29) Tesoro, G. Aromatic high-strength fibers, H. H. Yang, John Wiley & Sons, Inc., New York, 1989, 873 pp. **1990**, *28*, 264-265.
- (30) Kato, S.-i.; Noguchi, H.; Kobayashi, A.; Yoshihara, T.; Tobita, S.; Nakamura, Y. Bicarbazoles: Systematic Structure–Property Investigations on a Series of Conjugated Carbazole Dimers. *J. Org. Chem* **2012**, *77*, 9120-9133.
- (31) Wex, B.; Kaafarani, B. R. Perspective on carbazole-based organic compounds as emitters and hosts in TADF applications. *J. Mater. Chem. C* **2017**, *5*, 8622-8653.

- (32) Reig, M.; Puigdollers, J.; Velasco, D. Molecular order of air-stable p-type organic thin-film transistors by tuning the extension of the  $\pi$ -conjugated core: the cases of indolo[3,2-b]carbazole and triindole semiconductors. *J. Mater. Chem. C* **2015**, *3*, 506-513.
- (33) Xiao, Z.; Chen, B.; Cheng, X. Novel Red Light-Absorbing Organic Dyes Based on Indolo[3,2-b]carbazole as the Donor Applied in Co-Sensitizer-Free Dye-Sensitized Solar Cells. *Materials* **2021**, *14*, 1716.
- (34) Abdulnaby Abdulzahra, R. A. A.; I. Abbood, H. I. A. Geometry Optimization And Energies of Donor-Bridge-Acceptor Molecular System:B3LYP/DFT Calculations. *J. Kufa phys.* **2014**, *6*.
- (35) Zhang, Y.; Kou, C.; Zhang, J.; Liu, Y.; Li, W.; Bo, Z.; Shao, M. Crosslinked and dopant free hole transport materials for efficient and stable planar perovskite solar cells. *J. Mater. Chem. A* **2019**, *7*, 5522-5529.
- (36) Safari, Z.; Zarandi, M. B.; Giuri, A.; Bisconti, F.; Carallo, S.; Listorti, A.; Esposito Corcione, C.; Nateghi, M. R.; Rizzo, A.; Colella, S. Optimizing the Interface between Hole Transporting Material and Nanocomposite for Highly Efficient Perovskite Solar Cells. *Nanomaterials* **2019**, *9*, 1627.
- (37) Chen, L.-C.; Tseng, Z.-L.; Huang, J.-K.; Chen, C.-C.; Chang, S. H. Fullerene-Based Electron Transport Layers for Semi-Transparent MAPbBr<sub>3</sub> Perovskite Films in Planar Perovskite Solar Cells. *Coatings* **2016**, *6*, 53.
- (38) Yang, J.; Luo, X.; Zhou, Y.; Li, Y.; Qiu, Q.; Xie, T. Recent Advances in Inverted Perovskite Solar Cells: Designing and Fabrication. *Int. J. Mol. Sci.* **2022**, *23*, 11792.
- (39) Busby, Y.; Agresti, A.; Pescetelli, S.; Di Carlo, A.; Noel, C.; Pireaux, J.-J.; Houssiau, L. Aging effects in interface-engineered perovskite solar cells with 2D nanomaterials: A depth profile analysis. *Mater. Today Energy* **2018**, *9*, 1-10.
- (40) Luo, D.; Yang, W.; Wang, Z.; Sadhanala, A.; Hu, Q.; Su, R.; Shivanna, R.; Trindade, G. F.; Watts, J. F.; Xu, Z.; Liu, T.; Chen, K.; Ye, F.; Wu, P.; Zhao, L.; Wu, J.; Tu, Y.; Zhang, Y.; Yang, X.; Zhang, W.; Friend, R. H.; Gong, Q.; Snaith, H. J.; Zhu, R. Enhanced photovoltage for inverted planar heterojunction perovskite solar cells. *Science* **2018**, *360*, 1442-1446.
- (41) Bi, C.; Wang, Q.; Shao, Y.; Yuan, Y.; Xiao, Z.; Huang, J. Non-wetting surface-driven high-aspect-ratio crystalline grain growth for efficient hybrid perovskite solar cells. *Nat. Commun.* **2015**, *6*, 7747.

## TPE-Diphenylamine Derivatives as Solution-Processable Hole Injectors with Better Charge Balance for Organic Light Emitting Diodes (OLEDs)



### 4B.1. Abstract

Charge injection and transport layers with optimum carrier transport properties are essential for stable and efficient OLED devices. In this Chapter, we discuss two tetraphenylethylene-diphenylamine derivatives, **TPOMe** and **TPOSt** having four and two methoxy substituents, respectively and explored their potential as solution processable hole injection layers (HILs) for OLEDs. Standard, Alq<sub>3</sub>-based green OLEDs with a simple device design were used to demonstrate the properties of the synthesized HILs, in comparison with a commercially available standard HIL, m-MTDATA. **TPOMe** based device exhibited a current efficiency of 4.2 cd/A, while **TPOSt** based device showed 3.81 cd/A at 10 mA/cm<sup>2</sup>. Both the above devices showed better

performance compared to a control device fabricated with the standard HIL, m-MTDATA which showed a relatively lower current efficiency value (1.70 cd/A at 10 mA/cm<sup>2</sup>). Similarly, the maximum EQE of **TPOMe** (1.77%) and **TPOSt** (1.55%) were higher than that of the m-MTDATA based device (1.40%). Although m-MTDATA device has better luminance and hole mobility compared to **TPOMe** and **TPOSt** devices, the optimum charge balance in the latter devices lead to better current efficiency and EQE. This study signifies the importance of device engineering with compatible layers and optimum charge transport properties for efficient OLED devices.



## 4B.2. Introduction

Organic light-emitting diodes (OLEDs) have been the subject of intense research for quite a few decades due to their possible applications as emissive components in displays and solid-state lighting. Multi-layer structured devices exhibit higher performance and device efficiency than single-layered devices.<sup>1,2</sup> Each layer serves a specific purpose, such as charge injection through a hole or electron injection layer, charge transport through a hole or electron transport layer, carrier blocking layers, and the emissive layer emits light as the holes and electrons recombine. There are mainly two types of processing technologies for OLEDs, vacuum deposition and solution processing,<sup>3</sup> the former being the most common technique since it offers easy fabrication of multi-layered devices and offers high purity. Whereas conditions such as high vacuum, high temperature, and material wastage increase the complexity of the device fabrication, hindering the growth of large area fabrication of OLED devices.<sup>4,5</sup> In the present scenario, solution processed small molecular OLEDs are drawing much more research attention, since they have advantages like low-cost and large area fabrication, high processing efficiency, low material consumption and possible fabrication on flexible substrates.<sup>6</sup>

The hole injection layer in OLED is an interface between the hole transport layer (HTL) and indium tin oxide (ITO) anode, which is used to modify the charge injection from the electrode to improve the injection of holes and electrons into the organic layers. It can also influence the current efficiency, operational voltage, and stability of the devices.<sup>7,8</sup> To date, several kinds of organic and inorganic based materials have been reported for the HIL in OLEDs.<sup>9-12</sup> HILs based on triphenylamine (TPA), such as 4,4',4''-tris[N-(naphthalene-2-yl)-N-phenyl-amino]triphenylamine (2-TNATA),

4,4',4''-tris(N-3-methylphenyl-N-phenyl-amino)triphenylamine (m-MTDATA) and several other materials like (hexaazatriphenylene-hexacarbonitrile (HATCN), Spiro-OMeTAD, NiO<sub>x</sub>, CuSCN, and modified PEDOT:PSS have been used as HILs in OLEDs.<sup>13-17</sup> TPA has been extensively used as HTM/HTL because of their excellent electron donating ability, low ionisation potential, high hole mobility, stable morphology and attractive thermal properties.<sup>18,19</sup> Recently, TPE-bearing triphenylamine end caps have proven their potential as efficient HTMs in perovskite solar cells.<sup>20-23</sup>

#### **4B.2.1. Charge Balance in OLEDs**

The hole-electron balance in the emissive zone is also crucial for the development of high-efficiency OLEDs, which could be attained by fine-tuning the charge injection barriers in OLEDs.<sup>24-26</sup> It refers to maintaining an equilibrium between the injection of electrons and holes into the emissive layer of the OLED, ensuring that recombination and light emission occur with high efficiency. In OLEDs, electrons are injected from the cathode (negative electrode) and holes are injected from the anode (positive electrode) into the emissive layer, which consists of organic materials capable of emitting light. To achieve charge balance, the total electrical current flowing into the device should be balanced. This means that the rate of electron injection should be equal to the rate of hole injection. The choice of organic emitter materials plays a crucial role in achieving the charge balance. The energy levels and electron and hole mobilities of the emitter material should be compatible with the adjacent transport layers, allowing for efficient charge injection and recombination. If the energy alignment is shifted too much towards one type of carrier, it can result in an imbalance in charge carriers. Improving the injection of carriers that are already in excess can increase the absolute luminance of an OLED

device by promoting a higher probability of charge recombination, but it can have a negative impact on the efficiency of the device due to an imbalanced distribution of charge carriers.

Yu-Tai Tao *et al.* discovered the significance of fine-tuning the work function of ITO in OLED devices using self-assembled monolayers of 1-butylphosphonic acid, 4,4',4''-trifluoro-1-butylphosphonic acid and a binary mixture of them for understanding and optimising charge carrier balance.<sup>27</sup> When ITO was treated with single-component monolayer of 4,4',4''-trifluorobutyl-1-phosphonic acid, the injection barrier between the electrode and the hole transport layer was the lowest. Depending on HTL or HIL utilized, different anode modifications led to varying maximum device currents and luminance efficiencies because of the shift in hole/electron carrier balance. They showed that, it was preferable to increase the number of minor carriers rather than major carriers in situations where charge carrier balance could not be reached to enhance both luminance efficiency and power efficiency. Figure 4B.1A shows the energy level distribution of OLED devices with modified ITO. Byungmin Ahn and group demonstrated that the charge balance in the emission layer of an efficient device employing an exciplex system can be regulated by controlling the mixing ratio of electron (ET) and hole (HT) transporting host materials based on their respective charge transport properties.<sup>28</sup> They have identified the optimal conditions for achieving both efficient charge balance and enhanced device lifetime in exciplex-based OLED systems by carefully considering the transport properties of each layer, optimizing the mixing ratio of host materials and understanding the energy level alignment. Figure 4B.1B shows the proposed energy level diagram and chemical structure of HT hosts, such as DP-BCZ and BPP-BCZ, ET hosts, including PTZP-PCZ, BTPP-PCZ, and PTZP-BCZ and Ir-complex dopant.

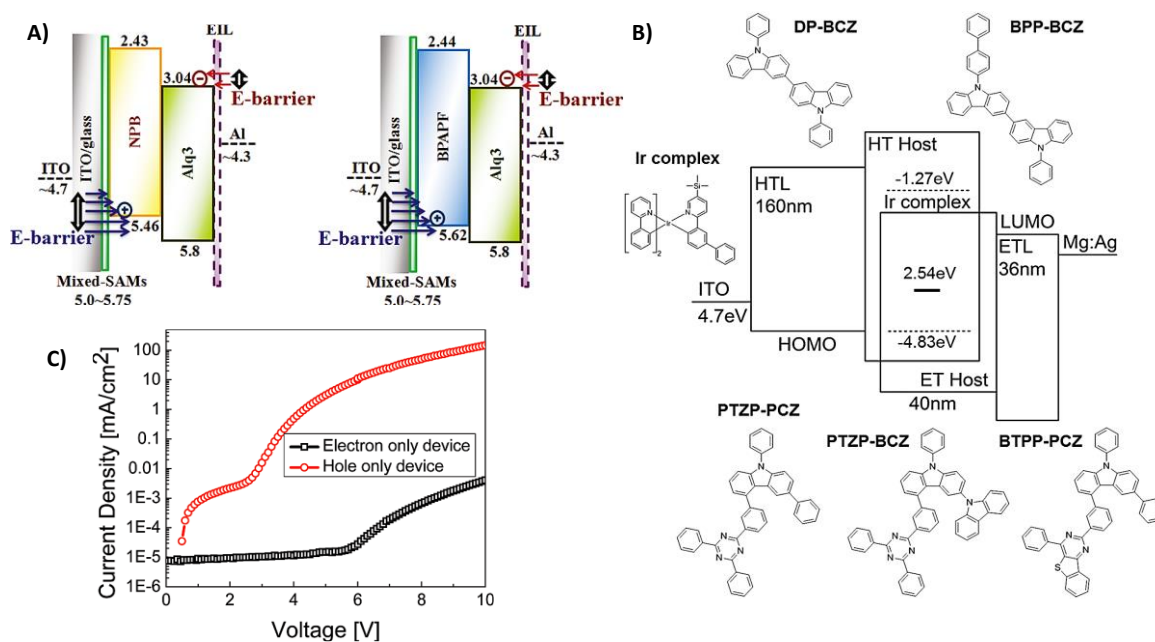


**Figure 4B.1.** (A) Energy level distribution of OLED devices with modified ITO; (B) Energy level diagram and chemical structure of HT hosts and Ir-complex dopant and (C) J-V curves of hole only and electron only devices showing the current density difference. (Adapted from references 27, 28 and 29)

Won Ho Lee *et al.* reported that optimised thickness of the electron transporting layer is essential for achieving charge balancing and recombination zone confinement in the emissive layer for improved efficiency in green phosphorescent-OLEDs.<sup>29</sup> A 40 nm thick 2,2',2''-(1,3,5-Benzinetriyl)-tris(1-phenyl-1-*H*-benzimidazole) (TPBi) - incorporated device displayed greater exciton confinement and charge balance, resulting in an improved EQE of 23.4% at 1000 cd/m<sup>2</sup>. Franky So *et al.* used a single-carrier device to evaluate the charge balance in blue-phosphorescent devices and discovered that carrier transport is considerably hole dominated. The hole mobility of TAPC is approximately 10,000 times higher ( $\sim 1.0 \times 10^{-2} \text{ cm}^2 \text{ V}^{-1} \text{ s}^{-1}$ ) than the electron mobility of BCP ( $5.5 \times 10^{-6} \text{ cm}^2 \text{ V}^{-1} \text{ s}^{-1}$ ), representing a significant difference in their charge transport properties (Figure 4B.1C).<sup>30</sup> Thus, they enhanced the charge balance and maximum current efficiency to 60 cd A<sup>-1</sup> at a luminance of 500 cd m<sup>-2</sup> by

using a high-mobility, high triplet-energy electron transporting material (3TPYMB  $\sim 6.77 \times 10^{-5} \text{ cm}^2 \text{ V}^{-1} \text{ s}^{-1}$ ).

In this work, we introduce two solution-processable hole injection layers derived from tetraphenylethylene - diphenylamine moieties equipped with methoxy groups in the periphery arms, and discovered that the hole injection layer has a considerable influence on the OLED efficiency. The derivatives satisfied the conditions for a good HIL used in OLEDs, such as, high thermal stability, suitable energy levels, transmittance above 80%, and reasonable hole mobility. Furthermore, the HIL properties were compared with those of a commercially available HIL, 4,4',4''-Tris[(3-methylphenyl)phenylamino]triphenylamine (m-MTDATA) and the OLED devices using the synthesised molecules exhibited better current efficiency and external quantum efficiency (EQE) compared to m-MTDATA-based devices. The results give new insights into the design principles of novel HIL materials for OLEDs.

### 4B.3. Results and Discussion

TPE-diphenylamine derivatives, **TPOMe** and **TPOSt** (Figure 4B.2) were synthesised by modified Buchward-Hartwig coupling reactions as reported earlier.<sup>31</sup> The core moiety, 1,2-bis(4-bromophenyl)-1,2-diphenylethene, was synthesised by the McMurry reaction and **TPOMe** was synthesised in good yields by the palladium-catalysed coupling of 1,2-bis(4-bromophenyl)-1,2-diphenylethene with 4,4'-dimethoxydiphenylaniline in toluene. On the other hand, **TPOSt** was synthesised by the reaction of 1,2-bis (4-bromophenyl)-1,2-diphenylethene with 4-methoxy-N-(4-(4-vinylbenzyloxy)phenyl)aniline.<sup>31</sup>

For both derivatives, A mixture of E-Z isomers were obtained from the final reaction step and were used for optoelectronic studies without further separation.

The obtained TPE derivatives were soluble in most of the organic solvents. The materials showed high melting transition temperatures and thermal decomposition temperatures ( $T_{d5\%}$ ), defined as the temperature at which 5% mass loss occurs. The basic photophysical, and electrochemical and thermal properties of these molecules were studied in detail and reported by our group earlier (Table 4B.1), where **TPOSt** was used as an electrochromic material.<sup>31</sup>

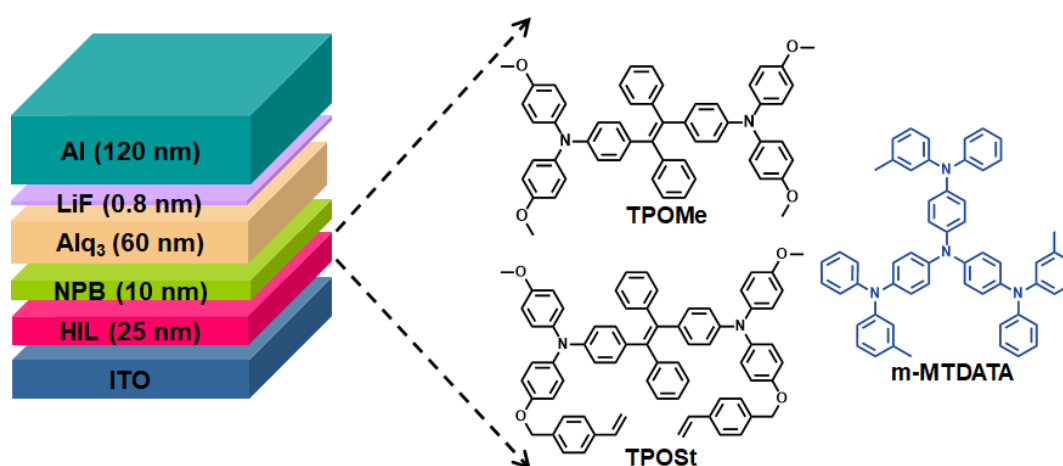


**Figure 4B.2.** Device configuration for the OLED with **TPOMe**, **TPOSt**, and m-MTDATA layer and their chemical structures.

**Table 4B.1.** Photophysical, thermal and electrochemical properties of the synthesized molecules.\*

Compound	$\lambda_{\text{abs}}$ (nm), ( $\epsilon$ , $\text{cm}^{-1}\text{M}^{-1}$ )			$\lambda_{\text{em}}$ film state (nm)	$\Phi_{\text{F}}$ (%)	$T_{d5\%}$ ( $^{\circ}\text{C}$ )	Optically Calculated (eV)		Theoretically Calculated (eV)	
	Toluene	Chlorobenzene	DMF				HOMO	LUMO	HOMO	LUMO
TPOMe	375 ( $3.08 \times 10^4$ )	370 ( $2.99 \times 10^4$ )	363 ( $3.34 \times 10^4$ )	543	$0.50 \pm 0.02$	384	-5.0	-1.9	-4.75	-1.38
TPOSt	379 ( $2.80 \times 10^4$ )	369 ( $2.61 \times 10^4$ )	367 ( $3.06 \times 10^4$ )	540	$0.47 \pm 0.02$	336	-5.03	-2.0	-4.77	-1.33

\* (Taken from reference 31)  $\lambda_{\text{abs}}$ : absorption maximum,  $\epsilon$ : molar extinction coefficient,  $\lambda_{\text{em}}$ : emission maximum of thin film,  $\Phi_{\text{F}}$ : quantum yield of fluorescence in film state  $T_{\text{d}}$ : decomposition temperature.

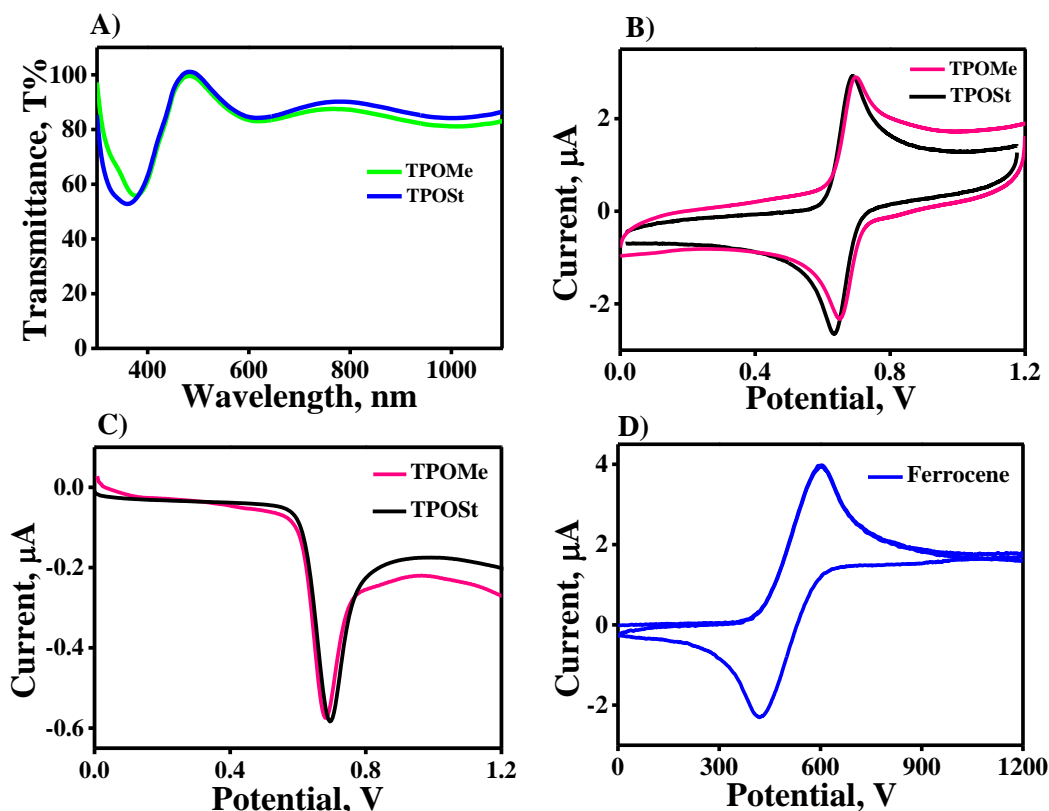


**Figure 4B.3.** (A) Transmittance spectra of **TPOMe** and **TPOSt** films; (B) CV and (C) Square wave analyses of **TPOMe** and **TPOSt** in chlorobenzene with supporting electrolyte 0.1 M TBAPF<sub>6</sub> and (D) CV of ferrocene in acetonitrile with supporting electrolyte 0.1 M TBAPF<sub>6</sub>.

The UV-VIS absorption maxima of **TPOMe** and **TPOSt** in solution state showed two maxima around 279 and 369 nm, and the absorption ranges of the materials in both solid and solution state showed negligible absorption beyond 450 nm, which is optimal for a good HIL.<sup>31</sup> Also, the transmittance spectra of the molecules exhibited moderate transmittance (above 55%) from 350 to 490 nm, and beyond that a higher transmittance of above 80% was observed (Figure 4B.3A). Electrochemical analyses of **TPOMe** and **TPOSt** were conducted using cyclic voltammetry and square wave analysis. CV showed the characteristic two electron oxidation peaks of triphenylamine at 0.68 V and 0.69 V by **TPOMe** and **TPOSt**, respectively, whereas square wave analyses of **TPOMe** and **TPOSt** showed peaks with potentials around

0.69 V and 0.7 V, respectively (Figures 4B.3B & 4B.3C).<sup>31</sup> The band-gap energies of the molecules in eV were obtained from the longest absorption wavelength,  $\lambda_{\text{onset}}$  using the equation,  $\Delta E = 1242/\lambda_{\text{onset}}$  and then the HOMO energy levels were calculated from the oxidation potential by taking ferrocene as the standard with an energy level value of 4.8 eV against vacuum vs the Ag/AgCl reference electrode (CV of ferrocene is shown in Figure 4B.3D for reference). The LUMO energy level was then derived from the HOMO and bandgap values (Table 4B.1). The optically determined HOMO and LUMO energy values were subsequently utilized in the OLED device design in this chapter. Further, the geometry optimizations and theoretical calculations of the energy levels were performed at the DFT level with the B3LYP exchange-correlation functional and a 6-311G basis set using Gaussian 09W. Both the molecules showed well separated HOMO and LUMO energy levels with HOMO orbitals mainly located over the triphenylamine moiety, and LUMO orbitals mostly distributed over the TPE core (Figure 4B.4A). **TPOMe** and **TPOSt** showed theoretically calculated HOMO energies of -4.75 eV and -4.77 eV, and LUMO energies of -1.38 eV and -1.33 eV, respectively. AFM analysis was used to investigate the morphology of the films spin-coated from chlorobenzene solutions. These films displayed a uniform and smooth surface with low roughness values, fewer crystalline islands and pinholes (image Rq values of 2.77 nm for **TPOMe** and 2.45 nm for **TPOSt**, and image Ra values of 2.32 nm and 2.07 nm for **TPOMe** and **TPOSt**, respectively), demonstrating good film-forming ability by the material (Figures 4B.4B & 4B.4C).

Water contact angle measurements of the spin coated films on ITO were conducted. Both showed an intermediate non-wettability with the water having contact angle values higher than 70° (**TPOMe** - 72.6° & **TPOSt** - 73.7°), which prevents



the water absorption from the environment and thus helps to improve the device stability (Figures 4B.4D & 4B.4E).

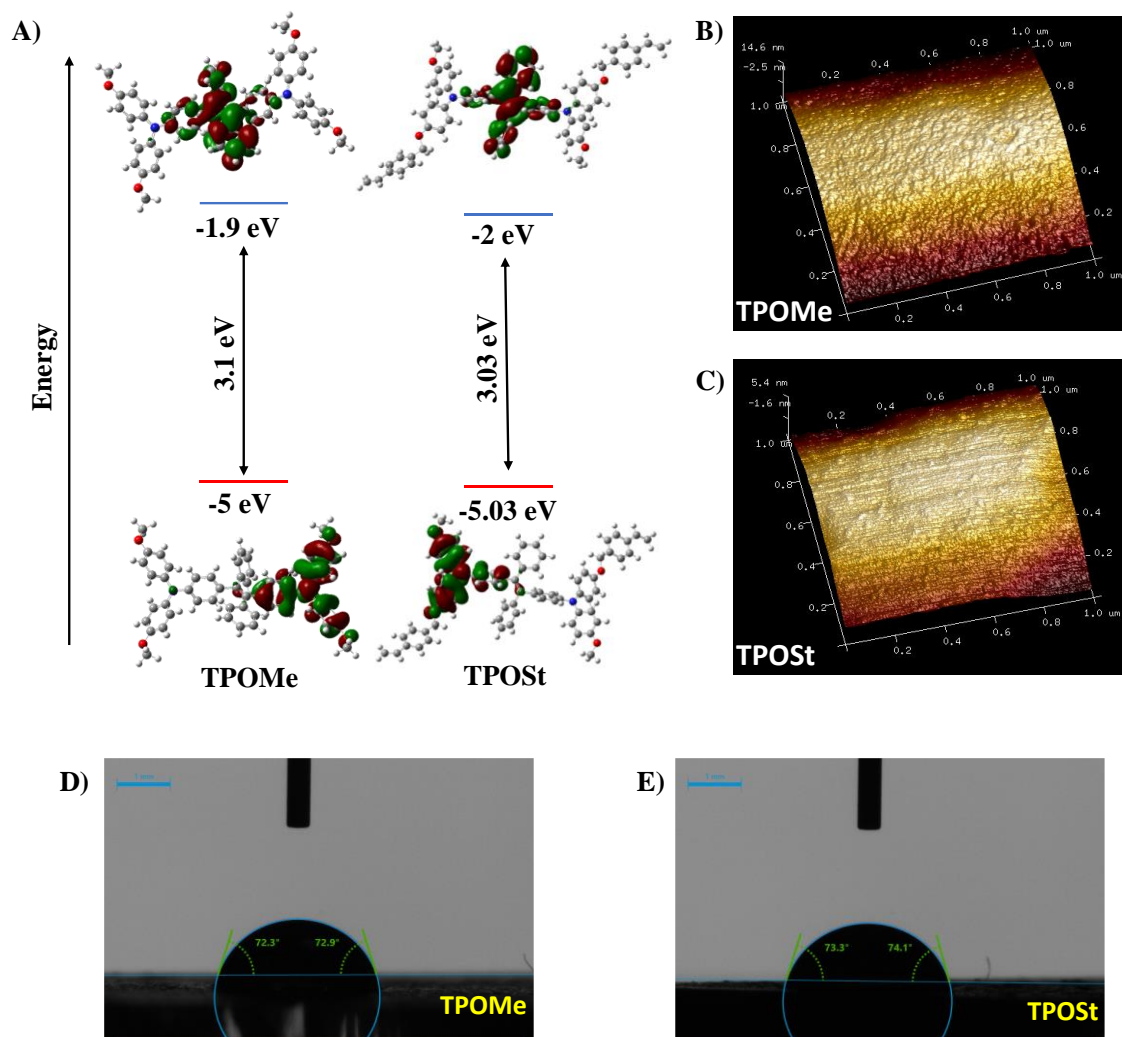


**Figure 4B.4.** (A) Electron density distributions for frontier molecular orbitals of **TPOMe** and **TPOSt** based on DFT B3LYP/6-311G(d,p) level calculations; Tapping mode AFM images (3D) of (B) **TPOMe** and (C) **TPOSt** films on ITO substrates, spin coated from chlorobenzene solutions; water contact angle measurements of the spin coated (D) **TPOMe** and (E) **TPOSt** films.

In order to understand the hole-injecting capability of the materials, we fabricated the classical single carrier devices based with the following structure: ITO/HIL (100 nm)/N,N'-Bis(naphthalen-1-yl)-N,N'-bis(phenyl)-benzidine (NPB) (60 nm)/Al (100 nm) as shown in Figure 4B.5A.

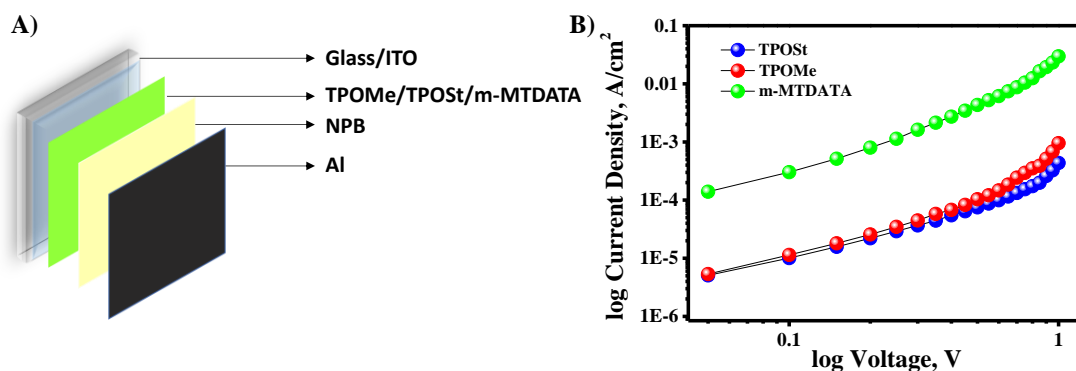


**Figure 4B.5.** (A) Schematic representation of hole only device architecture and (B) Current density–voltage (J–V) characteristics of the hole-only devices.

We have chosen a commercially available standard material, m-MTDATA, and the devices based on m-MTDATA were used as the reference devices.<sup>32,33</sup> m-MTDATA is a star-burst amine used as a hole injecting layer between the hole transport layer (HTL) and the transparent anode, usually ITO, that possesses similar HOMO-LUMO values as the synthesised HIL materials. The hole mobility of the pristine m-MTDATA is in the range of  $(2-4) \times 10^{-5} \text{ cm}^2 \text{ V}^{-1} \text{ s}^{-1}$  with a HOMO energy level of -5.1 eV and a LUMO level of -2 eV, making it a suitable hole injecting layer for OLED applications.<sup>2,34</sup> Hole-only devices of the synthesised materials and m-MTDATA could give more information about the hole transporting properties. The J–V characteristics of the m-MTDATA based hole-only device showed increased current density and better performance than the devices with **TPOMe** and **TPOSt**, indicating the better hole transporting ability of m-MTDATA compared to our molecules (Figure 4B.5B). The values of hole mobility of the materials were calculated according to the SCLC model, where the current,  $I$  can be expressed as shown in Equation 4B.1

$$I = \frac{9}{8} \mu_{eff} \epsilon_0 \epsilon_r A \frac{V^2}{d^3} \quad \text{Equation 4B.1}$$

where  $\mu_{eff}$  is the charge carrier mobility at zero field,  $\epsilon_0 = 8.854 \times 10^{-12} \text{ Fm}^{-1}$  is the permittivity of free space,  $\epsilon_r$  is the relative dielectric constant of the thin film ( $\epsilon_r = 3$  for conventional semiconductors), and  $d$  is the thickness of the thin film. Using Equation 4B.1, m-MTDATA is found to have a hole mobility of  $5.95 \times 10^{-5} \text{ cm}^2 \text{ V}^{-1} \text{ s}^{-1}$ , while **TPOMe** and **TPOSt** exhibited slightly lower values of  $1.46 \times 10^{-6} \text{ cm}^2 \text{ V}^{-1} \text{ s}^{-1}$ , and  $1.06 \times 10^{-6} \text{ cm}^2 \text{ V}^{-1} \text{ s}^{-1}$ , respectively. The results indicate that the synthesised materials have approached the charge transport properties of m-MTDATA. However, the external quantum efficiency (EQE,  $\eta_{ext}$ ) of OLED is given by Equation 4B.2,

$$\eta_{ext} = \gamma \eta_{fl} \cdot \eta_{oc} \quad \text{Equation 4B.2}$$

where,  $\gamma$  is the charge balance factor,  $\eta_{fl}$  is the fluorescence efficiency, and  $\eta_{oc}$  is the outcoupling efficiency. It means the performance of an OLED is not only determined by the conductivity of the injection and transport layers, and the fluorescence efficiency of the emitter but also by the balanced charge transport and carrier confinement or carrier blocking. In this work, calculations for EQE were made using the relations obtained from previous reports.<sup>35-37</sup>

Figures 4B.6A, 4B.6B & 4B.6C show the energy level diagrams of the OLED devices fabricated using **TPOMe**, **TPOSt**, and m-MTDATA, as HIL. Both of the newly designed materials show similar HOMO and LUMO values lying between the HOMO of ITO (-4.7 eV) and that of NPB (-5.5 eV), which are appropriate for the HOMO of a hole injecting layer. All devices had a configuration, ITO/ HIL (25 nm)/ NPB (10 nm)/ Alq3 (60 nm)/ LiF (0.8 nm)/ Al (120 nm). *N,N'*-Di(1-naphthyl)-*N,N'*-diphenyl-(1,1'-biphenyl)-4,4'-diamine (NPB) acts as the hole transporting material, tris(8-hydroxyquinoline) aluminum(III) (Alq3) serves as both emissive layer (EML) and the

electron transport layer (ETL), lithium fluoride (LiF) forms the EIL and ITO and Al act as anode and cathode, respectively.

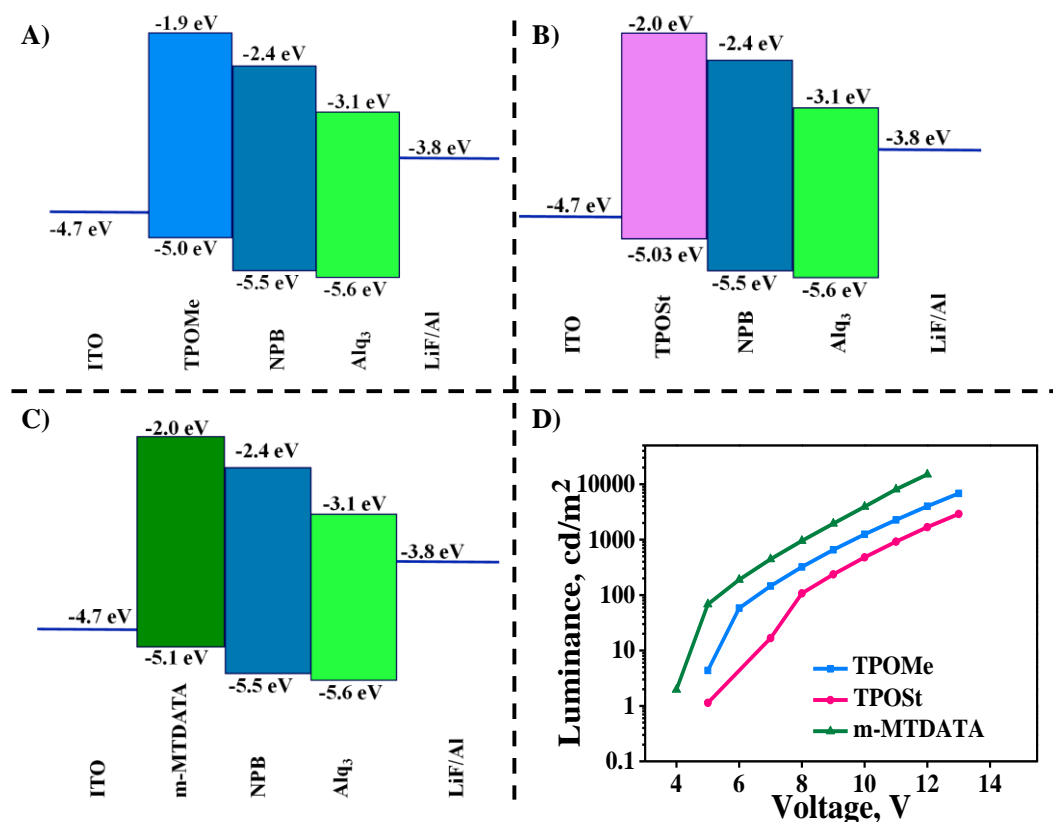


**Figure 4B.6.** Energy level diagrams of (A) **TPOMe**; (B) **TPOSt** and (C) **m-MTDATA** based OLED devices and (D) Luminance of the OLED devices with respect to voltage.

Device with **m-MTDATA** as the HIL showed higher luminance compared to the devices with **TPOMe** and **TPOSt**. Maximum luminance of 15,000  $\text{cd}/\text{m}^2$  at 14 V was obtained for **m-MTDATA** based device, whereas devices with **TPOMe** and **TPOSt** as HILs had a maximum luminance of nearly 9000  $\text{cd}/\text{m}^2$  and 7000  $\text{cd}/\text{m}^2$ , respectively at 15 V (Figure 4B.6D). Higher luminance in **m-MTDATA** device may be due to the higher hole mobility and enhanced carrier transport in the HIL.

The electroluminescence spectra of **TPOMe**, **TPOSt** and **m-MTDATA** devices showed respective maxima at 540 nm, 548 nm and 532 nm, with Commission Internationale de L'Eclairage (CIE) coordinates of  $x = 0.38$  and  $y = 0.53$  for **TPOMe**

device,  $x = 0.37$  and  $y = 0.53$  for **TPOSt** device and  $x = 0.34$  and  $y = 0.56$  for m-MTDATA device (Figures 4B.7A & 4B.7B). Shifts in the peak emission wavelengths can be attributed to weak microcavity effects and shifts in the recombination zone within the OLED device stack.<sup>38</sup> Images of the fabricated OLED devices are shown in Figure 4B.7C.

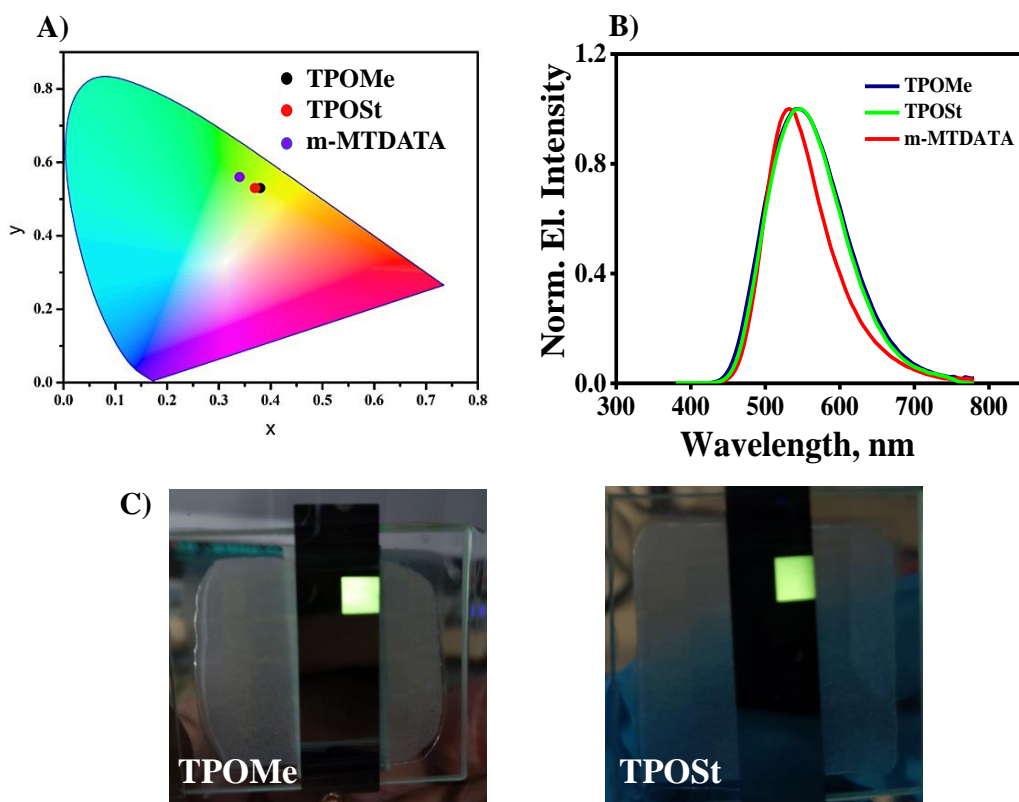


**Figure 4B.7.** (A) CIE chromaticity diagram, and (B) Electroluminescence spectra of the **TPOMe**, **TPOSt** and m-MTDATA based OLED devices and (C) Photographs of the **TPOMe**, **TPOSt** based OLED devices.

A comparison of the current density, external quantum efficiency (EQE), and current efficiency of the devices are shown in Figure 4B.8. Device with m-MTDATA as the HIL showed higher current density and lower turn on voltage. However, the EQE and current efficiency of m-MTDATA device was lower compared to devices with **TPOMe** and **TPOSt**. Device based on **TPOMe** exhibited a maximum EQE of 1.77%, which was higher than the EQE maxima of **TPOSt** device (1.55%) and m-MTDATA

device (1.40%). The current efficiency of the devices fabricated with TPE-diphenylamine derivatives displayed a value of 4.2 cd/A and 3.81 cd/A at 10 mA/cm<sup>2</sup> for **TPOMe** and **TPOSt** devices, respectively, and both were much better than device with m-MTDATA (1.70 cd/A at 10 mA/cm<sup>2</sup>).

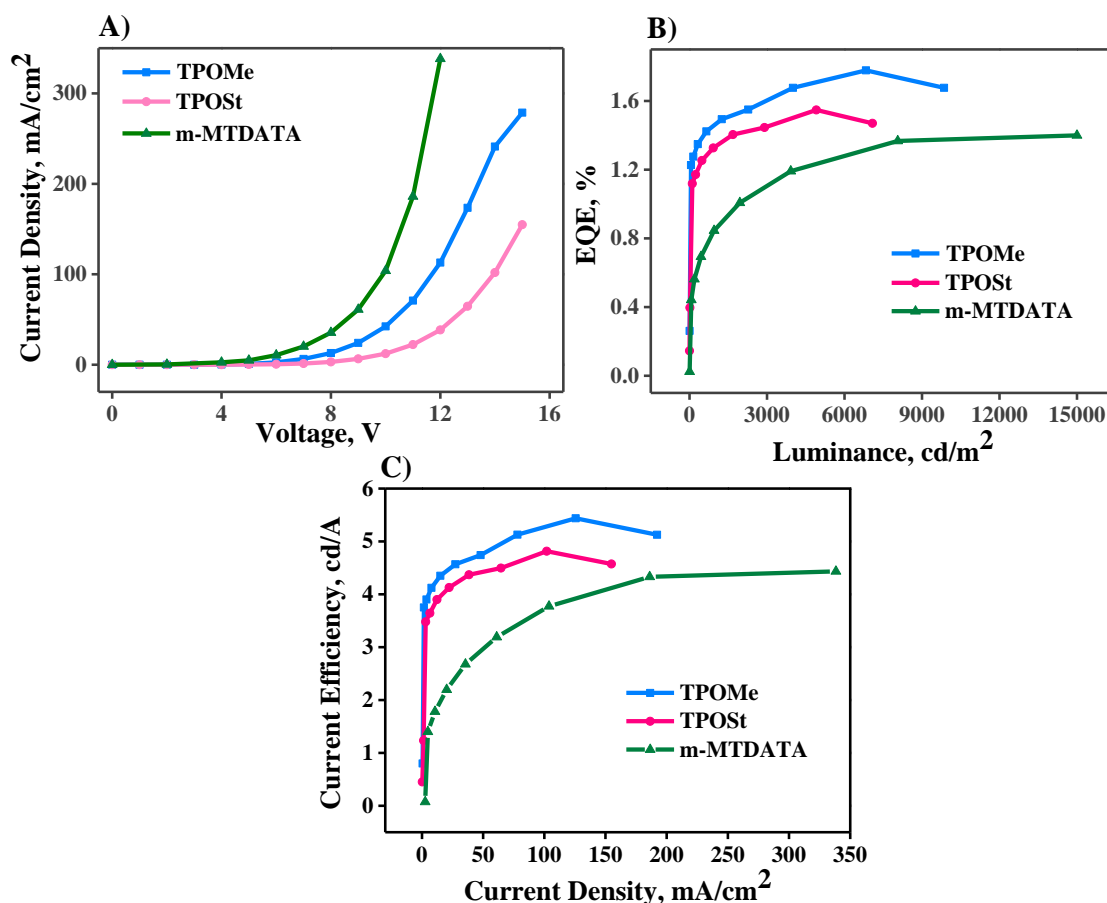


**Figure 4B.8.** Plots of (A) Current density vs voltage; (B) EQE vs luminance and (C) Current efficiency vs current density of **TPOMe**, **TPOSt** and m-MTDATA based OLED devices.

In 2017, Shan *et al.* reported a device that used m-MTDATA as HIL with a 40 nm thickness and has the device structure as ITO/ m-MTDATA (40 nm)/ NPB (10 nm)/ Alq3 (60 nm)/ LiF (0.8 nm)/ Al (120 nm). This device achieved a maximum current efficiency of approximately 4 cd/A. Our m-MTDATA device, which has the same device architecture but a different m-MTDATA layer thickness of 25 nm, demonstrated greater current efficiency (4.45 cd/A) than the device reported by Shan *et al.* They

further improved the current efficiency to 10.40 cd/A by using CuI-doped m-MTDATA HIL and fluorescent dopants like C-545T in the emissive Alq3 layer.<sup>10</sup>

The better performance in the current and external quantum efficiencies of the TPE-diphenylamine derivatives than the m-MTDATA based reference device originates from the excellent charge balance happening in the emissive layer. Air stable and solution processable molecules like **TPOMe** and **TPOST** are important for fabricating cost effective and stable device structures.

#### 4B.4. Conclusions

In summary, we have reported two tetraphenylethylene-diphenylamine derivatives with four and two methoxy substituents (**TPOMe** and **TPOST**) and demonstrated their potential as hole injection layers for OLEDs. Alq3 based green OLEDs were fabricated with the newly synthesized HILs and with a commercially available standard HIL, m-MTDATA. The devices with **TPOMe** and **TPOST** exhibited improved current efficiency and EQE than m-MTDATA based device although m-MTDATA based device has better luminance and hole mobility. This indicates that a better charge balance occurs in the emissive layer of TPE-diphenylamine based OLED devices. The present results may serve as guidelines for designing suitable HIL materials with better charge balance factor. Most importantly, molecules with good stability in air and solution processable properties can be explored for cost-effective and stable device architectures. The OLED used in the current study has a simple design meant only for the comparison of the HIL materials, and the device performance can be further improved by modifying the active layers with the addition of dopants.

## **4B.5. Experimental Section**

### **4B.5.1. Materials and Methods**

The synthesis and detailed characterization of **TPOMe** and **TPOSt** have been explained in the previously reported literature from our group.<sup>31</sup> The redox potentials of the materials were obtained by using cyclic voltammetry (BASI CV-50W) at room temperature with 0.1 M tetrabutylammonium hexafluorophosphate (TBAPF<sub>6</sub>) in acetonitrile as a supporting electrolyte, Ag/AgCl and platinum wire as the reference and counter electrode, respectively. The working electrode was prepared by spin-coating the materials onto FTO substrates. The energy levels were estimated optically from UV-Vis spectra (Shimadzu UV-Vis spectrophotometer, UV-2600) and cyclic voltammetry. AFM images of the films were recorded using an AFM-Bruker Multitop Nanoscope V instrument operating in tapping mode, and the roughness of the films was found using Nanoscope Analysis 1.5 software. The thickness of the films was measured using a Dektak XT profilometer. Thermal evaporation of the materials on the cleaned substrates was done under high vacuum condition (pressure < 2×10<sup>-6</sup> Torr) in an Angstrom Engineering Thermal Evaporation System. Device parameters were measured by using a Spectroradiometer SpectraScan PR655 interfaced with a Keithely 2400. Spectrofluorometer FLUOROLOG-3 was used for photoluminescence measurements. All chemicals and solvents were purchased from Sigma-Aldrich, Merck, Spectrochem Pvt Ltd. and Luminescence Technology Corp., Taiwan. Patterned ITO glasses were purchased from KINTEC, Hong Kong.

### **4B.5.2. Device Fabrication**

OLEDs were fabricated on pre-patterned ITO substrates, which act as the anode. Cleaning of substrates has been done with detergent and sonication with chloroform,



iso propyl alcohol, and deionized water for 15 minutes each. After UV ozone treatment for 15 minutes, hole injection layers **TPOMe** and **TPOSt** dissolved in chlorobenzene (25 mg/ml) were spin coated on the pre-patterned ITO substrates. Subsequently, the samples were dried for 1 hour at 60 °C in air. In m-MTDATA based OLED device, m-MTDATA layer was deposited by thermal evaporation. For each device, subsequent organic layers and an Al electrode were deposited by thermal evaporation under high vacuum conditions. In order to resist possible degradation of devices in the air, encapsulation of the devices has been done with UV curable EPOTEK epoxy and cover glass. Encapsulated devices were measured in air using a Spectrascan PR-655 spectroradiometer ((Photo Research Inc.) integrated with the Keithley 2400 source meter and a PC. Hole-only devices (HODs) were prepared by the same procedure. All of the measurements were carried out at room temperature.

#### 4B.6. References

- (1) Thejo Kalyani, N.; Dhoble, S. J. Organic light emitting diodes: Energy saving lighting technology-A review. *Renew. Sust. Energ. Rev.* **2012**, *16*, 2696-2723.
- (2) Shahnawaz; Sudheendran Swayamprabha, S.; Nagar, M. R.; Yadav, R. A. K.; Gull, S.; Dubey, D. K.; Jou, J.-H. Hole-transporting materials for organic light-emitting diodes: an overview. *J. Mater. Chem. C* **2019**, *7*, 7144-7158.
- (3) Wang, Z.; Lou, Y.; Naka, S.; Okada, H. Direct Comparison of Solution- and Vacuum-Processed Small Molecular Organic Light-Emitting Devices with a Mixed Single Layer. *ACS Appl. Mater. Interfaces* **2011**, *3*, 2496-2503.
- (4) Luo, D.; Yang, W.; Wang, Z.; Sadhanala, A.; Hu, Q.; Su, R.; Shivanna, R.; Trindade, G. F.; Watts, J. F.; Xu, Z.; Liu, T.; Chen, K.; Ye, F.; Wu, P.; Zhao, L.; Wu, J.; Tu, Y.; Zhang, Y.; Yang, X.; Zhang, W.; Friend, R. H.; Gong, Q.; Snaith, H. J.; Zhu, R. Enhanced photovoltage for inverted planar heterojunction perovskite solar cells. *Science* **2018**, *360*, 1442-1446.
- (5) Shibata, M.; Sakai, Y.; Yokoyama, D. Advantages and disadvantages of vacuum-deposited and spin-coated amorphous organic semiconductor films for organic light-emitting diodes. *J. Mater. Chem. C* **2015**, *3*, 11178-11191.

- (6) Tang, Y.; Zhuang, J.; Xie, L.; Chen, X.; Zhang, D.; Hao, J.; Su, W.; Cui, Z. Thermally Cross-Linkable Host Materials for Solution-Processed OLEDs: Synthesis, Characterization, and Optoelectronic Properties. *Eur. J. Org. Chem.* **2016**, *2016*, 3737-3747.
- (7) Shih, H.-K.; Chu, Y.-L.; Chang, F.-C.; Zhu, C.-Y.; Kuo, S.-W. A cross-linkable triphenylamine derivative as a hole injection/transporting material in organic light-emitting diodes. *Polym. Chem.* **2015**, *6*, 6227-6237.
- (8) Yang, Z.; Cheng, C.; Pan, X.; Pan, F.; Wang, F.; Tian, M.; Zhang, H. Effects of hole injection layer on performance of green OLEDs based on flexible ITO. *Mater. Chem. Phys.* **2020**, *239*, 121828.
- (9) Krucaite, G.; Blazelevicius, D.; Tavgeniene, D.; Grigalevicius, S.; Lin, C.-H.; Shao, C.-M.; Chang, C.-H. Tetramer of triphenylamine and similar derivatives with bromine atoms as hole injecting/transporting materials for efficient red phosphorescent OLEDs. *Opt. Mater.* **2020**, *108*, 110225.
- (10) Shan, M.; Jiang, H.; Guan, Y.; Sun, D.; Wang, Y.; Hua, J.; Wang, J. Enhanced hole injection in organic light-emitting diodes utilizing a copper iodide-doped hole injection layer. *RSC Adv.* **2017**, *7*, 13584-13589.
- (11) Xiao, H.; Rungo, B. A.; Wang, S.; Li, X.; Liu, H. Controllable and efficient hole-injection layers with molybdenum oxide units by solution-processed procedure for OLEDs. *Org. Electron.* **2020**, *85*, 105868.
- (12) Zhang, X.; Wu, Z.; Wang, D.; Wang, D.; Hou, X. Improving the stability of organic light-emitting devices using a solution-processed hole-injecting layer. *Appl. Surf. Sci.* **2009**, *255*, 7970-7973.
- (13) Chavhan, S. D.; Ou, T. H.; Jiang, M.-R.; Wang, C.-W.; Jou, J.-H. Enabling High-Efficiency Organic Light-Emitting Diode with Trifunctional Solution-Processable Copper(I) Thiocyanate. *J. Phys. Chem. C* **2018**, *122*, 18836-18840.
- (14) Chen, W.-S.; Yang, S.-H.; Tseng, W.-C.; Chen, W. W.-S.; Lu, Y.-C. Utilization of Nanoporous Nickel Oxide as the Hole Injection Layer for Quantum Dot Light-Emitting Diodes. *ACS Omega* **2021**, *6*, 13447-13455.
- (15) Jaramillo-Quintero, O. A.; Sanchez, R. S.; Rincon, M.; Mora-Sero, I. Bright Visible-Infrared Light Emitting Diodes Based on Hybrid Halide Perovskite with Spiro-OMeTAD as a Hole-Injecting Layer. *J. Phys. Chem. Lett* **2015**, *6*, 1883-1890.

- (16) Lin, H.-W.; Lin, W.-C.; Chang, J.-H.; Wu, C.-I. Solution-processed hexaazatriphenylene hexacarbonitrile as a universal hole-injection layer for organic light-emitting diodes. *Org. Electron.* **2013**, *14*, 1204-1210.
- (17) Zhong, Z.; Ma, Y.; Liu, H.; Peng, F.; Ying, L.; Wang, S.; Li, X.; Peng, J.; Cao, Y. Improving the Performance of Blue Polymer Light-Emitting Diodes Using a Hole Injection Layer with a High Work Function and Nanotexture. *ACS Appl. Mater. Interfaces* **2020**, *12*, 20750-20756.
- (18) Fong, H. H.; Papadimitratos, A.; Hwang, J.; Kahn, A.; Malliaras, G. G. Hole Injection in a Model Fluorene-Triarylamine Copolymer. *Adv. Funct. Mater.* **2009**, *19*, 304-310.
- (19) Jiang, Z.; Ye, T.; Yang, C.; Yang, D.; Zhu, M.; Zhong, C.; Qin, J.; Ma, D. Star-Shaped Oligotriarylaminines with Planarized Triphenylamine Core: Solution-Processable, High-Tg Hole-Injecting and Hole-Transporting Materials for Organic Light-Emitting Devices. *Chem. Mater.* **2011**, *23*, 771-777.
- (20) Muniyasamy, H.; Muthusamy, K.; Chinnamadhayan, M.; Sepperumal, M.; Ayyanar, S.; Selvaraj, M. Molecular Design and Cost-Effective Synthesis of Tetraphenylethene-Based Hole-Transporting Materials for Hybrid Solar Cell Application. *Energy Fuels* **2022**, *36*, 3909-3919.
- (21) Zhang, X.; Liu, X.; Ghadari, R.; Li, M.; Zhou, Z. a.; Ding, Y.; Cai, M.; Dai, S. Tetraphenylethylene-Arylamine Derivatives as Hole Transporting Materials for Perovskite Solar Cells. *ACS Appl. Mater. Interfaces* **2021**, *13*, 12322-12330.
- (22) Zhang, X.; Zhou, Z. a.; Ma, S.; Wu, G.; Liu, X.; Mateen, M.; Ghadari, R.; Wu, Y.; Ding, Y.; Cai, M.; Dai, S. Fused tetraphenylethylene-triphenylamine as an efficient hole transporting material in perovskite solar cells. *Chem. Commun.* **2020**, *56*, 3159-3162.
- (23) Ke, W.; Priyanka, P.; Vegiraju, S.; Stoumpos, C. C.; Spanopoulos, I.; Soe, C. M. M.; Marks, T. J.; Chen, M.-C.; Kanatzidis, M. G. Dopant-Free Tetrakis-Triphenylamine Hole Transporting Material for Efficient Tin-Based Perovskite Solar Cells. *J. Am. Chem. Soc.* **2018**, *140*, 388-393.
- (24) Jou, J.-H.; Kumar, S.; Singh, M.; Chen, Y.-H.; Chen, C.-C.; Lee, M.-T. Carrier Modulation Layer-Enhanced Organic Light-Emitting Diodes. *Molecules* **2015** *20*, 13005-13030.
- (25) Mentado-Morales, J.; Ximello-Hernández, A.; Salinas-Luna, J.; Freitas, V. L. S.; Ribeiro da Silva, M. D. M. C. A Promising Thermodynamic Study of Hole Transport Materials to Develop Solar Cells: 1,3-Bis(N-carbazolyl)benzene and 1,4-Bis(diphenylamino)benzene. *Molecules* **2022**, *27*, 381.
- (26) Benor, A.; Takizawa, S.-y.; Pérez-Bolivar, C.; Anzenbacher, P., Jr. Energy barrier, charge carrier balance, and performance improvement in organic light-emitting diodes. *Appl. Phys. Lett.* **2010**, *96*.

- (27) Yu, S.-Y.; Huang, D.-C.; Chen, Y.-L.; Wu, K.-Y.; Tao, Y.-T. Approaching Charge Balance in Organic Light-Emitting Diodes by Tuning Charge Injection Barriers with Mixed Monolayers. *Langmuir* **2012**, *28*, 424-430.
- (28) Lee, S.; Koo, H.; Kwon, O.; Jae Park, Y.; Choi, H.; Lee, K.; Ahn, B.; Min Park, Y. The Role of Charge Balance and Excited State Levels on Device Performance of Exciplex-based Phosphorescent Organic Light Emitting Diodes. *Sci. Rep.* **2017**, *7*, 11995.
- (29) Lee, W. H.; Kim, D. H.; Justin Jesuraj, P.; Hafeez, H.; Lee, J. C.; Choi, D. K.; Bae, T.-S.; Yu, S. M.; Song, M.; Kim, C. S.; Ryu, S. Y. Improvement of charge balance, recombination zone confinement, and low efficiency roll-off in green phosphorescent OLEDs by altering electron transport layer thickness. *Mater. Res. Express* **2018**, *5*, 076201.
- (30) Chopra, N.; Lee, J.; Zheng, Y.; Eom, S.-H.; Xue, J.; So, F. Effect of the Charge Balance on High-Efficiency Blue-Phosphorescent Organic Light-Emitting Diodes. *ACS Appl. Mater. Interfaces* **2009**, *1*, 1169-1172.
- (31) Abraham, S.; Mangalath, S.; Sasikumar, D.; Joseph, J. Transmissive-to-Black Electrochromic Devices Based on Cross-Linkable Tetraphenylethene-Diphenylamine Derivatives. *Chem. Mater.* **2017**, *29*, 9877-9881.
- (32) Nayak, D.; Choudhary, R. B. A survey of the structure, fabrication, and characterization of advanced organic light emitting diodes. *Microelectron. Reliab.* **2023**, *144*, 114959.
- (33) Zeng, X.-Y.; Tang, Y.-Q.; Cai, X.-Y.; Tang, J.-X.; Li, Y.-Q. Solution-processed OLEDs for printing displays. *Mater. Chem. Front.* **2023**, *7*, 1166-1196.
- (34) Bauri, J.; Choudhary, R. B.; Mandal, G. Recent advances in efficient emissive materials-based OLED applications: a review. *J. Mater. Sci.* **2021**, *56*, 18837-18866.
- (35) Forrest, S. R.; Bradley, D. D. C.; Thompson, M. E. Measuring the Efficiency of Organic Light-Emitting Devices. *Adv. Mater.* **2003**, *15*, 1043-1048.
- (36) Wu, L.; Xu, H.; Yang, H. Realization of Efficient Phosphorescent Organic Light-Emitting Devices Using Exciplex-Type Co-Host. *Micromachines* **2021**, *13*.
- (37) Tanaka, I.; Tokito, S. Precise Measurement of External Quantum Efficiency of Organic Light-Emitting Devices. *Jpn. J. Appl. Phys.* **2004**, *43*, 7733.
- (38) Wei, M. K.; Lin, C. W.; Yang, C. C.; Kiang, Y. W.; Lee, J. H.; Lin, H. Y. Emission characteristics of organic light-emitting diodes and organic thin-films with planar and corrugated structures. *Int. J. Mol. Sci.* **2010**, *11*, 1527-1545.

## ABSTRACT

Name of the Student: **Ms. Shibna Balakrishnan**  
Faculty of Study: Chemical Sciences  
AcSIR academic centre/CSIR Lab: CSIR-National  
Institute for Interdisciplinary Science  
and Technology (CSIR-NIIST)

Registration No.: 10CC17A39003  
Year of Submission: 2023

Name of the Supervisor: Dr. Joshy Joseph

Title of the thesis: **Design of Triphenylamine Derivatives for Organic Electronics Applications: Synthesis, Photophysics and Device Studies**

Organic materials have garnered a lot of attention in the past couple of decades, owing to advancements in material design and purification, which have strengthened material performance in various organic electronic devices. Charge injection/transport materials and electroactive materials compatible with device fabrication conditions are essential components in many organic electronic devices such as electrochromic devices, Perovskite solar cells and organic light emitting diodes. In this sense, triphenylamine derivatives with twisted molecular conformations and multiple amine centres have drawn specific interest as organic charge transport materials. The triphenylamine moiety acts as a good electron donor unit with easy oxidizability, hole mobility, and compatible energy levels, color tunability and redox stability enabling TPA derivatives to achieve the highest efficiency and performance among photovoltaics, OLEDs and electrochromic systems. In this regard, the design and development of triphenylamine-based derivatives with features that could potentially enhance device performance are essential for improving the capabilities of organic materials for future applications. The **Chapter 1** provides an overview on triphenylamine based organic compounds, their synthesis, optical and electronic properties and classifications based on specific literature survey. It also discusses the role of triphenylamine derivatives as hole transporting/injecting and electrochromic materials in solar cells, OLEDs and electrochromic devices, respectively.

In **chapter 2**, We successfully developed two cross-linkable, triphenylamine derivatives based on a donor- $\pi$ -donor (D- $\pi$ -D) type molecular design (**C-Sty2** and **C-Sty3**) and investigated of the effects of  $\pi$ -core and hyper-cross-linking on the electrochromic properties of the thin films and devices. The hyper-cross-linked films of **C-Sty3** demonstrated enhanced coloration efficiency, optical contrast, and open-circuit memory compared to **C-Sty2**. Electrochemical impedance spectroscopy analysis showed lower solution and charge-transfer resistances for hyper-cross-linked films of **C-Sty3**, indicating higher conductivity and ion diffusion compared to **C-Sty2**.

Designing ligands with varying numbers of coordination sites can result in metallopolymers with linear and branched structures and these structural differences can have a significant impact on their photophysical, thermal, morphological, and electrochromic characteristics. In this regard, in **Chapter 3**, two tetraphenylethylene-diphenylamine-terpyridine based ligands, **TPE-TPy2** and **TPE-TPy4**, having two and four terpyridine units attached to the diphenylamine moiety, were synthesised, and their photophysical, electrochemical, and metal interaction properties were investigated. Hyperbranched metallo-polymers of **TPE-TPy4-Fe** exhibited better colouration efficiency and shorter electrochromic switching times compared to linear metallopolymers of **TPE-TPy2-Fe**.

To understand the structure-property relations of triphenylamine derivatives with carbazole (**C-Sty2** and **C-Sty3**) or tetraphenylethylene core (**TPOMe** and **TPOSt**) groups, we used two sets of triphenylamine derivatives as hole transport/injection materials for Perovskite Solar Cells and Organic Light Emitting Diodes in **Chapter4A** and **Chapter4B**, respectively. The devices incorporating the synthesized materials demonstrated efficient hole transporting/injecting properties in Perovskite solar cells and OLEDs, respectively and indicated their versatile applications in organic electronics.

## List of Publications Emanating from the Thesis

1. **Shibna Balakrishnan**, Ranjana Venugopal, Aswathi Harikumar, Biswapriya Deb\*, and Joshy Joseph\* Effect of Hyper-Cross-Linking on the Electrochromic Device Properties of Cross-Linkable Carbazole–Diphenylamine Derivatives, *ACS Appl. Polym. Mater.* 2023, 5, 4170-4179.
2. **Shibna Balakrishnan**, Pavithra V. Prabhu, C. K. Vipin, Vibhu Darshan, K. N. Narayanan Unni\* and Joshy Joseph\*, TPE-Diphenylamine derivatives as solution-processable hole injectors with better charge balance for organic light emitting diodes (OLEDs) (Manuscript submitted, under revision).
3. **Shibna Balakrishnan** and Joshy Joseph\*, Two Tetraphenylethylene-Diphenylamine-Terpyridine Ligands and their Iron Metallopolymers: Effect of Hyperbranching on Electrochromic Properties (Manuscript completed and to be submitted).
4. **Shibna Balakrishnan**, Richard Murdey, Minh Anh Truong and Tomoya Nakamura Atsushi Wakamiya\* and Joshy Joseph\*, Carbazole-diphenylamine derivatives as hole transporting materials for perovskite solar cells. (Manuscript to be submitted).

## List of Publications not Related to Thesis Work

1. Silja Abraham, **Shibna Balakrishnan** and Joshy Joseph\*, Transmissive-to- Gray-Near-IR Switching Electrochromic Device (*Manuscript completed and to be submitted*).

## List of Papers/Posters Presented in Conferences

1. *Terpyridine Appended Tetraphenylethylene Derivatives: Stimuli-responsive Self-Assembly and Optoelectronic Properties*, **Shibna Balakrishnan**, Sreejith Mangalath, Anjali Cheruvalath and Joshy Joseph\*, ICMST-2018 at VSSC-Trivandrum, 10<sup>th</sup> October, 2018 (Poster Presentation).
2. *Cross-linkable, TPE-Diphenylamine Derivatives as Hole Transporting Materials For Perovskite Solar Cells*, **Shibna Balakrishnan**, Silja Abraham, Vibhu Darsan, K. N. Narayanan Unni\* and Joshy Joseph\*, ICAFM-2019 at CSIR-NIIST, Thiruvananthapuram, December 10, 2019 (Poster Presentation).
3. *Design of Cross-linkable, TPE-Diphenylamine Based Hole Transporting Materials For Perovskite Solar Cells*, **Shibna Balakrishnan**, Silja Abraham, Vibhu Darsan, K. N. Narayanan Unni\* and Joshy Joseph\*, 14<sup>th</sup> International Conference on Ecomaterials (ICEM) at CSIR-National Institute for Interdisciplinary Science and Technology (NIIST), Trivandrum, February 7, 2020 (Poster Presentation).
4. *Design of Cross-linkable Carbazole-Diphenylamine Electrochromic Materials and Devices*, **Shibna Balakrishnan**, Ranjana Venugopal, Aswathi Harikumar, Biswapriya Deb\* and Joshy Joseph\*, NCMST-2021 at IIST, Trivandrum, December 7-9, 2021 (**Best Poster Award**)
5. *Electrochromic Properties of Cross-Linkable Carbazole-Diphenylamine Derivatives and Devices*, **Shibna Balakrishnan**, Ranjana Venugopal, Aswathi Harikumar, Biswapriya Deb\* and Joshy Joseph\*, EFCS-2021 at Farook College, Kozhikode, October 29-31, 2021(**Best Poster Award**)
6. *Electrochromic Properties of Cross-Linkable Carbazole-Diphenylamine Derivatives and Devices*, **Shibna Balakrishnan**, Ranjana Venugopal, Aswathi Harikumar, Biswapriya Deb\* and Joshy Joseph\*, National Symposium on Recent Advances in the Physics of Materials

(RAPM-2021) at National Institute for Interdisciplinary Science and Technology (NIIST), Thiruvananthapuram, December, 2021, (Poster Presentation).

7. *Cross-Linkable Carbazole-Diphenylamine Derivatives for Electrochromic Devices*. **Shibna Balakrishnan**, Ranjana Venugopal, Biswapriya Deb\* and Joshy Joseph\*, Indian Analytical Science Congress 2022 at Tea County Hill Resort, Munnar, March 10-12, 2022. (Poster Presentation).
8. *Cross-Linkable Carbazole-Diphenylamine Derivatives for Electrochromic Applications*, **Shibna Balakrishnan**, Ranjana Venugopal, Biswapriya Deb\* and Joshy Joseph\*, 16<sup>th</sup> JNCASR research conference on chemistry of materials at Jawaharlal Nehru Centre for Advanced Scientific Research (JNCASR), Bengaluru, October 2022 (Poster Presentation).
9. *Effect of Hyper-crosslinking on the Electrochromic Device Properties of Carbazole–Diphenylamine Derivatives*, **Shibna Balakrishnan**, Ranjana Venugopal, Aswathi Harikumar, Biswapriya Deb\* and Joshy Joseph\*, Materials Research Society of India (MRSI-2023, Trivandrum Chapter) at University of Kerala, Trivandrum, May 20,2023 (Oral Presentation).



# Effect of Hyper-Cross-Linking on the Electrochromic Device Properties of Cross-Linkable Carbazole–Diphenylamine Derivatives

Shibna Balakrishnan, Ranjana Venugopal, Aswathi Harikumar, Biswapriya Deb,\* and Joshy Joseph\*

Cite This: *ACS Appl. Polym. Mater.* 2023, 5, 4170–4179

Read Online

ACCESS |

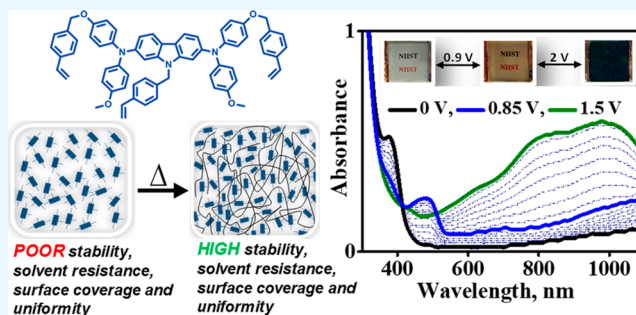
Metrics &amp; More

Article Recommendations

Supporting Information

**ABSTRACT:** Triphenylamine derivatives are promising organic electrochromic (EC) materials due to their easy synthesis, low oxidation potentials, high charge-carrier mobilities, electrochemical stability, coloration efficiency, and tunability of EC properties via substitution. Further, the cross-linking strategy provides an added advantage to the small-molecule-based EC devices in terms of better-quality EC films with enhanced EC properties. Herein, we discuss the EC properties of two carbazole–diphenylamine derivatives, C-Sty2 and C-Sty3, with two and three thermally cross-linkable styryl units, respectively, following a donor– $\pi$ –donor (D– $\pi$ –D) design, where both the carbazole moiety and cross-linking styrene groups modulate the photophysical and EC properties. Both styryl derivatives formed rigid, uniform, and transparent films with high solvent resistance and exhibited excellent thermal and electrochemical stability upon cross-linking. C-Sty3, with three cross-linkable styryl units, could form more extended cross-links, leading to hyper-cross-linked films with distinct, regular, and porous morphology compared to C-Sty2. Spectroelectrochemical studies of the films showed a color change from a transparent colorless state to an initial light-yellow color and then a final dark-blue color with a color contrast of 65% at 890 nm for C-Sty2 and 78% at 850 nm for C-Sty3. The hyper-cross-linked films of C-Sty3 demonstrated enhanced coloration efficiency (248 cm<sup>2</sup>/C), optical contrast, and open-circuit memory compared to C-Sty2. Electrochemical impedance spectroscopy analysis showed lower solution and charge-transfer resistances ( $R_s$  and  $R_{ct}$ , respectively) for hyper-cross-linked films of C-Sty3, indicating higher conductivity and ion diffusion compared to C-Sty2. Thus, a comparison of the EC properties of two polymers with the same electroactive groups reveals the significance of hyper-cross-linking in the EC properties of these cross-linked polymers. Furthermore, the EC properties of the hyper-cross-linked D– $\pi$ –D derivative, C-Sty3, were compared to those of previously reported molecules, demonstrating the importance of highly branched conducting polymers for EC applications.

**KEYWORDS:** electrochromism, triphenylamine, carbazole, styrene, thermal polymerization, hyper-cross-linking, electrochromic devices, electrochemical impedance spectroscopy



**POOR stability, solvent resistance, surface coverage and uniformity**

**HIGH stability, solvent resistance, surface coverage and uniformity**

## 1. INTRODUCTION

Electrochromic (EC) devices respond to the applied voltage through changes in their optical properties such as transmittance, reflectance, and absorbance. Novel materials are being developed for EC devices due to their applications in smart windows, antiglazing mirrors, e-papers, display devices, etc.<sup>1–3</sup> Among the various classes of materials exhibiting EC properties, organic small molecules possess beneficial features like ease of structural tuning, solution processability, intense coloration, and fast switching.<sup>4,5</sup> Despite these advantages, EC device fabrication with small organic molecules suffers from poor film and device quality, which detrimentally affects their overall EC performance. In the recent past, we and several other groups utilized the cross-linking strategy with small organic molecules to overcome film and device stability issues.<sup>6–10</sup> Hence, the attachment of cross-linking groups like siloxane, oxetane, benzocyclobutene, benzoxazine, and styrene

endows the films of these molecules with excellent solvent resistance. Previously, we demonstrated the multicolor electrochromism of fluorene–diphenylamine derivatives<sup>6</sup> and transmissive-to-black EC and fluorescent-to-dark electrofluorochromic dual behavior of a tetraphenylethene–diphenylamine derivative.<sup>7</sup> All of these derivatives were incorporated with two thermally cross-linkable styryl moieties that ensured flawless film formation with excellent color contrast and EC switching stabilities. Introducing more than two cross-linkable groups in the monomer molecules can result in extensively

Received: February 28, 2023

Accepted: April 21, 2023

Published: May 8, 2023

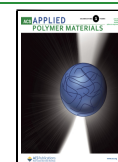
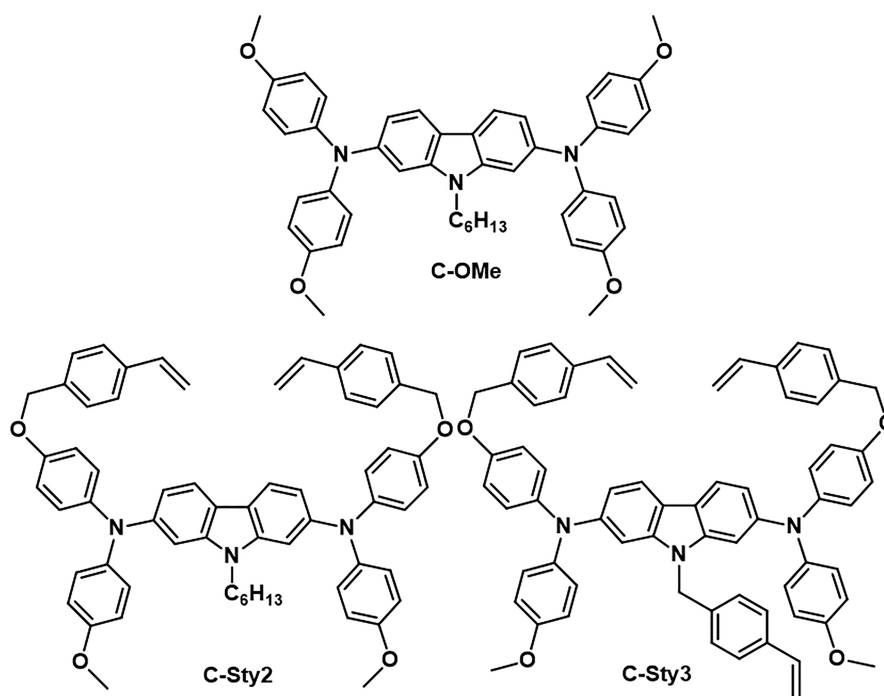


Chart 1. Molecular Structures of C-OMe, C-Sty2, and C-Sty3



cross-linked polymers with improved charge-transfer and conductivity properties, resulting in subsequent enhancement in EC properties such as coloration efficiency, contrast ratios, lifetimes, and response times. Hyper-cross-linked polymers are reported to have greater ionic and electron conductivity due to their highly branched and microporous structure.<sup>11–13</sup> For example, Wang's group compared the EC properties of linear- and star-structured poly(3,4-ethylenedioxythiophene–didodecyloxybenzenes) and demonstrated that the star polymer has superior thermal stability, processability, and durability in addition to the EC qualities of its linear parent.<sup>14</sup> Ak's group discovered the superior optoelectronic and EC properties of a star-shaped polymer,  $N^1, N^3, N^5$ -tris(2,5-di(thiophen-2-yl)-1H-pyrrol-1-yl)benzene-1,3,5-tricarboxamide (TCA) due to its more conjugated three-dimensional shape and extremely branched structure in comparison with linear analogues.<sup>15</sup>

Another challenge in the EC technology for applications like smart windows, eyewear, display devices, etc., is the development of darker shades from a thin film with a transparent initial state. Several attempts of fine-tuning of the optoelectronic properties of electroactive materials and devices have been reported in the past decade by leading research groups around the globe.<sup>16–18</sup> Reynolds' group have uncovered many elements affecting the EC properties like coloration, switching kinetics, and optical contrast in organic EC polymers.<sup>2,19–23</sup> Hou et al. reported an organic–inorganic hybrid EC material (PDPAP-TEOSPU), which switched from the initial colorless state to dark blue, with an optical transmittance change of up to 84% and a coloration efficiency of 188  $\text{cm}^2/\text{C}$ .<sup>24</sup> Similarly, a conjugated polymer based on cross-linked poly(4-vinyltriphenylamine) and tungsten trioxide<sup>25</sup> and widely used EC polymers like PANI, PolyProDOT-Me2,<sup>26</sup> and polyimides<sup>27</sup> are reported to exhibit transparent-to-dark switching with high contrast ratios.

Wide-band-gap triphenylamine derivatives are a well-studied class of organic EC materials due to their high charge-carrier

mobilities, low oxidation potentials, reversible redox properties, transparent-to-visible color switching with high optical contrast, thermal and electrochemical stability, and tunability of the EC properties via easy substitution.<sup>28–30</sup> In our earlier work, we adopted a donor– $\pi$ –donor (D– $\pi$ –D) design strategy for the design of cross-linkable EC molecules, with two diphenylamine donor groups bridged by a  $\pi$  core, such as fluorene and tetraphenylethylene, and two styrene moieties that can be cross-linked attached to the diphenylamine groups.<sup>6,7</sup> The  $\pi$  core in these derivatives influence the EC properties via differential electronic coupling of the donor units in the neutral and oxidized states. In the current design, we introduced N-substituted carbazole as the  $\pi$  core, and two and three styrene groups are attached to the diphenylamine and carbazole parts, which is shown to have a significant role in controlling the EC parameters in both film and device conditions (Chart 1). Carbazole provides through-bond conjugation enabling efficient coupling of the two donor units and an easy derivatization route to attach alkyl or other cross-linkable moieties as pendent groups. Carbazole derivatives are widely used as hole-transporting materials in organic photovoltaics<sup>31–35</sup> and as host and active materials in light-emitting-diode applications.<sup>36–39</sup> EC polymer materials based on carbazole have been explored in many ways as electroactive films. For example, electrochemically polymerized long polycarbazole chains,<sup>40–42</sup> copolymers from carbazole and different monomers like thiophene, bithiophene, and 3,4-ethylenedioxythiophene,<sup>43,44</sup> and small molecules and polymers of carbazole as the center core and side chain have been studied for their EC properties.<sup>45–49</sup> Although cross-linkable, carbazole–triarylamine derivatives are used as hole-transporting materials for Perovskite solar cells,<sup>50</sup> EC applications of these derivatives are not reported. In the present work, we report three carbazole–diphenylamine derivatives (Chart 1; C-OMe, C-Sty2, and C-Sty3), which were synthesized via palladium-catalyzed Buchwald–Hartwig cross-coupling amina-

tion reactions and characterized through  $^1\text{H}$  and  $^{13}\text{C}$  NMR, electrospray ionization mass spectrometry (ESI-MS), Fourier transform infrared (FT-IR) spectroscopy, and CHN elemental analysis. The optical, electrochemical, and EC properties of these derivatives were thoroughly investigated in solution, film, and device states. Among the three derivatives, **C-OMe** has no styrene group attached to it and acts as a model compound for comparing the properties with **C-Sty2** and **C-Sty3**. A comparative analysis of the EC properties of cross-linked **C-Sty2** and hyper-cross-linked **C-Sty3** polymers with the same electroactive groups highlights the significance of hyper-cross-linking in the EC films. **C-Sty3**, with three styryl subunits, forms rigid and smoother films with reduced roughness, compact surface, better coloration efficiency, optical contrast, and open-circuit memory compared to **C-Sty2**.

## 2. EXPERIMENTAL SECTION

All chemicals and solvents were purchased from Sigma-Aldrich, TCI-India Pvt. Ltd., Merck, and Spectrochem Pvt. Ltd. and used as received. The fluorine-doped tin oxide (FTO) substrate with a surface resistivity of  $8\ \Omega/\text{sq}$  was purchased from Sigma-Aldrich and cleaned by ultrasonication with water, acetone, and isopropyl alcohol for 15 min each. Moisture- and oxygen-sensitive reactions were carried out under an argon atmosphere in dry solvents. Details of the synthetic procedures and characterization are described in the [Supporting Information](#).

$^1\text{H}$  and  $^{13}\text{C}$  NMR spectra were recorded at 300 K on a DPX 500 MHz spectrometer with tetramethylsilane as the internal standard. Electrospray ionization high-resolution mass spectrometry (ESI-HRMS) spectra were recorded with a JEOL JSM 600 spectrometer. IR spectra were recorded in the solid state (KBr) using a Shimadzu IR Prestige-21 FT-IR spectrophotometer. The solution-state absorbance measurements were done on a Shimadzu UV-vis spectrophotometer (UV-2600), and the film-state absorbance and transmittance measurements were done using an Ocean Optics UV-vis modular spectrometer (DH-2000-BAL). The fluorescence quantum yield of the powder samples was calculated using a calibrated integrating sphere in a SPEX Fluorolog spectrofluorometer. The absolute quantum yield was determined on the basis of the de Mello method. Differential scanning calorimetry (DSC) analyses were done using a TA Instruments DSC Q2000 model with an intracooler facility. Thermogravimetric analysis (TGA) was performed on a Shimadzu DTG-60 instrument under a nitrogen atmosphere at a heating rate of  $10\ ^\circ\text{C}/\text{min}$ . Wide-angle X-ray diffraction (WAXD) analysis was done using a XEUSS small-angle X-ray scattering (SAXS)/wide-angle scattering (WAXS) system by Xenocs using Ni-filtered  $\text{Cu}\ K\alpha$  radiation ( $\lambda = 0.15405\ \text{nm}$ ), and a one-dimensional pattern was generated from the two-dimensional images using *Fit2D* software. The thickness of the samples was measured using the Dektak XT profilometer. Atomic force microscopy (AFM) images of the films before and after annealing were recorded using an AFM-Bruker Multitop Nanoscope V instrument operating under tapping mode, and the roughness of the films was found using *Nanoscope Analysis 1.5* software. Cyclic voltammetry (CV; BASI CV-50W) for liquid-state samples was performed under an argon atmosphere using 0.1 M tetrabutylammonium hexafluorophosphate (TBAPF<sub>6</sub>) in acetonitrile as the supporting electrolyte, glassy carbon as the working electrode, Ag/AgCl electrode as the reference electrode, and platinum wire as the counter electrode under an argon atmosphere with a scan rate of  $50\ \text{mV}/\text{s}$ . Cyclic voltammograms of the films and devices were obtained on a PARSTAT 4000A potentiostat. The spectroelectrochemistry of EC devices and films was recorded on an Ocean Optics DH-2000-BAL spectrometer using a PARSTAT 4000A potentiostat for the electrochemical redox process. Spectroelectrochemical responses of the films were done by dipping the cross-linked films in a 0.1 M TBAPF<sub>6</sub> in dry acetonitrile solution using Ag/AgCl and platinum wire as the reference and counter electrodes, respectively. The blank was done using bare FTO in a 0.1 M

TBAPF<sub>6</sub> in dry acetonitrile solution in a cuvette having a 1 cm path length. The  $L^*a^*b^*$  values for the colors under different applied voltages were found using a Bench Top Color spectrophotometer with an UltraScan vis sensor, 110 V/220 V w/SAV and UV control, and *EasyMatch QC*, version 4.0, software. Electrochemical impedance spectroscopy (EIS) was measured in the frequency range of 100 kHz to 10 mHz. An electrochemical cell of a three-electrode system using Ag/AgCl as the reference electrode, platinum wire as the counter electrode, and films coated on FTO substrates as the working electrode in a 0.1 M TBAPF<sub>6</sub>/acetonitrile electrolyte was used. The measurements were conducted in a CHI660E series electrochemical workstation.

**2.1. Electrolyte Preparation.** The electrolyte used for the EC devices was prepared by adding 20 wt % LiClO<sub>4</sub> and 30 wt % propylene carbonate to the measured amount of poly(methyl methacrylate) (PMMA;  $M_w = 120000$ ), dissolved in tetrahydrofuran (2 g of PMMA + 0.2 g of LiClO<sub>4</sub> + 300  $\mu\text{L}$  of propylene carbonate in 20 mL of THF), and stirred at  $80\ ^\circ\text{C}$  until complete dissolution, followed by stirring at room temperature overnight. PMMA and LiClO<sub>4</sub> were dried under vacuum for 12 h at  $90$  and  $110\ ^\circ\text{C}$ , respectively, before use. The mixture was poured into a clean Petri dish, and the solvent was allowed to evaporate at room temperature. The required amount of electrolyte film was peeled from the Petri dish and used.

**2.2. EC Device Fabrication.** The EC devices were fabricated using FTO-coated glass substrates as the working electrodes and followed the architecture glass/FTO/electrolyte/EC layer/FTO/glass. After cleaning of the electrodes (2.5 cm  $\times$  2.5 cm FTO-coated glass slide) by sonicating with water, acetone, and isopropyl alcohol for 15 min each, the electrodes were annealed at  $500\ ^\circ\text{C}$ , followed by UV-ozone treatment. Solutions of **C-Sty2** or **C-Sty3** (150 mg/mL) in chlorobenzene were spin-coated at 1500 rpm for 30 s. The spin-coated transparent thin films were then kept for polymerization in a glovebox by annealing at the respective temperatures for 30 min. The prepared solid electrolyte was sandwiched between the cross-linked film and FTO counter electrode. To prevent the diffusion of oxygen and moisture into the fabricated device, commercial epoxy was used to seal the edges of the devices. Copper tape was applied to both sides of the bare FTO for efficient and uniform electrical contact while connected to the potentiostat.

## 3. RESULTS AND DISCUSSION

The carbazole-diphenylamine derivatives were synthesized in good yields by a modified Buchwald-Hartwig coupling reaction as per [Scheme S1](#). 9-Hexyl- $N^2,N^2,N^7,N^7$ -tetrakis(4-methoxyphenyl)-9H-carbazole-2,7-diamine (**C-OMe**) and 9-hexyl- $N^2,N^7$ -bis(4-methoxyphenyl)- $N^2,N^7$ -bis[4-[(4-vinylbenzyl)oxy]phenyl]-9H-carbazole-2,7-diamine (**C-Sty2**) were synthesized from the reaction between 2,7-dibromo-9-hexyl-9H-carbazole and the corresponding diphenylamine derivatives.  $N^2,N^7$ -bis(4-methoxyphenyl)-9-(4-vinylbenzyl)- $N^2,N^7$ -bis[4-[(4-vinylbenzyl)oxy]phenyl]-9H-carbazole-2,7-diamine (**C-Sty3**) was synthesized from the coupling reaction between 2,7-dibromo-9-(4-vinylbenzyl)-9H-carbazole and 4-methoxy- $N$ -[4-(4-vinylbenzyloxy)phenyl]aniline. The structures of **C-OMe**, **C-Sty2**, and **C-Sty3** were characterized by  $^1\text{H}$  and  $^{13}\text{C}$  NMR, ESI-MS ([Figures S1–S4](#)), FT-IR, and CHN elemental analysis techniques.

The solution-state absorption properties of **C-OMe**, **C-Sty2**, and **C-Sty3** were studied in different solvents like  $N,N$ -dimethylformamide (DMF), THF, chlorobenzene, and toluene ([Figure S5](#) and [Table S1](#)). Absorption spectra of these D- $\pi$ -D derivatives showed slight negative solvatochromism, indicating minor perturbations in the dipole moments during the excitation process. For example, **C-Sty3** showed an absorption maximum of 394 nm in toluene, with a blue shift of 8 nm in the more polar DMF. The observed negative



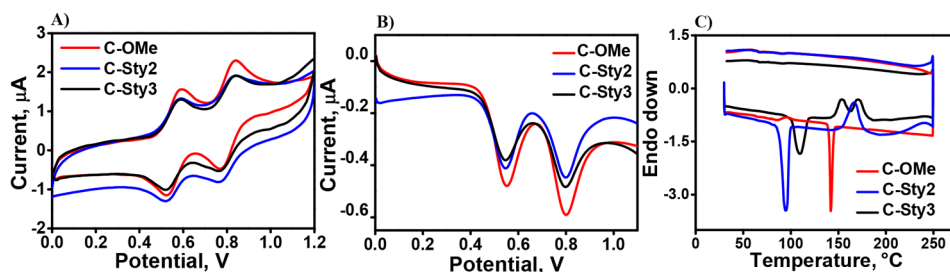


**Figure 1.** (A) Cyclic voltammograms of C-OMe, C-Sty2, and C-Sty3 in chlorobenzene (supporting electrolyte 0.1 M TBAPF<sub>6</sub>; scan rate 50 mV/s). (B) Square-wave voltammograms of C-OMe, C-Sty2, and C-Sty3 in chlorobenzene (supporting electrolyte 0.1 M TBAPF<sub>6</sub>). (C) DSC heating curves of C-OMe, C-Sty2, and C-Sty3 with a heating rate of 10 °C/min under a nitrogen atmosphere.

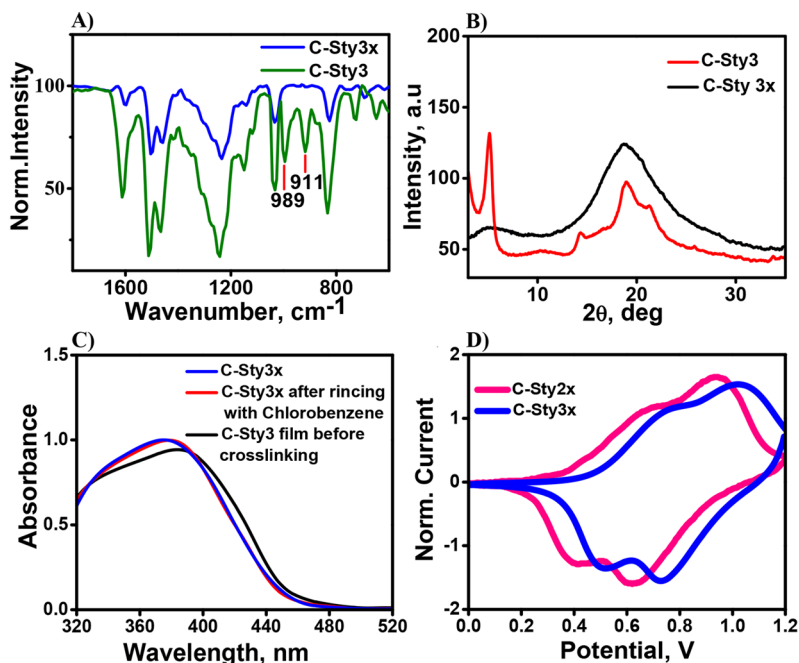


**Figure 2.** (A) Normalized FT-IR spectra of C-Sty3 before and after cross-linking. (B) WAXD pattern of C-Sty3 before and after cross-linking. (C) UV-vis absorption spectra of C-Sty3 before and after cross-linking and after rinsing with chlorobenzene. (D) Cyclic voltammograms of C-Sty2x and C-Sty3x films on FTO in 0.1 M TBAPF<sub>6</sub>/acetonitrile (scan rate 50 mV/s).

solvatochromism could be due to a larger dipole moment and better stabilization of the ground state in polar solvents, which is observed prior to 2,7-donor-substituted carbazole derivatives.<sup>51,52</sup> These derivatives showed negligible absorption beyond 450 nm, ensuring complete transparency in the visible range. Further, these derivatives were moderately fluorescent in both the solid state and solution with emission maxima in the 410–425 nm range and 1–10% solid-state fluorescence quantum yields (Figure S6 and Table S1). However, their fluorescence were significantly quenched in annealed amorphous films and devices due to self-quenching. Solution-state CV and square-wave voltammetry analysis of all of the carbazole–diphenylamine derivatives showed two reversible anodic peaks corresponding to the formation of polarons and bipolarons at 0.55 and 0.8 V, respectively (Figure 1A,B).

In general, organic small molecules form poor quality films on glass, indium-doped tin oxide, and FTO substrates, which is unfavorable for the fabrication of efficient EC devices. Thermal cross-linking of small molecules is shown to be an effective strategy to improve the film, thermal, electrochemical, and long-term operational stabilities of EC devices. Two/three styrene moieties were introduced in a C-Sty2/C-Sty3

structural design to understand the effect of cross-linkable functionalities in the film formation and EC device properties. The formation of stable, thermally cross-linked films was confirmed via DSC, FT-IR, WAXD, UV-vis, and AFM analyses. Here onward, the films formed via thermal cross-linking of C-Sty2 and C-Sty3 are represented as C-Sty2x and C-Sty3x, respectively. DSC analysis showed an endothermic melting curve at 141 °C for C-OMe, whereas the melting temperature shifted to lower temperatures for the other two derivatives (C-Sty2 at 94 °C and C-Sty3 at 109 °C). The cross-linking temperature was observed after melting transitions at 166 °C for C-Sty2 and 153 and 170 °C for C-Sty3, which was absent for C-OMe (Figure 1C). FT-IR spectra of the compounds before and after thermal cross-linking displayed the absence of peaks attributed to the out-of-plane deformation vibration of the vinyl group present in the monomer. The peaks at 991 and 909 cm<sup>-1</sup> of C-Sty2 and 989 and 911 cm<sup>-1</sup> of C-Sty3 were significantly attenuated after polymerization, indicating efficient cross-linking of the films (Figures 2A and S7A). WAXD studies of C-Sty2 and C-Sty3, before and after thermal cross-linking, showed a change from a more crystalline phase to an amorphous phase after thermal

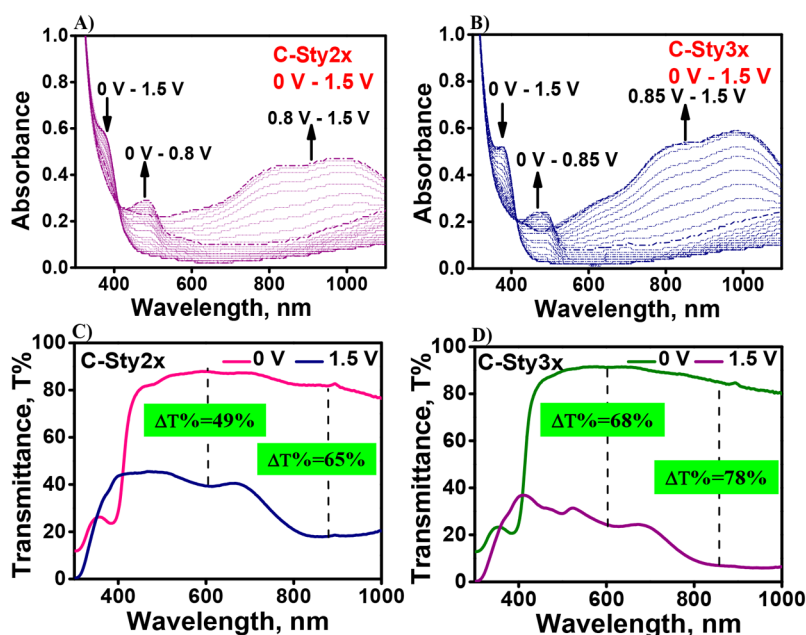


**Figure 3.** Spectroelectrochemical responses of (A) C-Sty2x and (B) C-Sty3x films on FTO (the thicknesses of the films used are  $150 \pm 10$  and  $130 \pm 10$  nm for C-Sty2x and C-Sty3x, respectively) and transmittance spectra of (C) C-Sty2x and (D) C-Sty3x films at the colored (1.5 V) and bleached (0 V) states. The thicknesses of the C-Sty2x and C-Sty3x films used for transmittance study are  $245 \pm 10$  and  $230 \pm 10$  nm, respectively.

annealing (Figures 2B and S7B). The UV–vis absorption spectra of thin films of C-Sty2 and C-Sty3 on quartz substrates with and without thermal annealing above  $150$  °C showed slight changes in absorbance with apparent hypsochromic shift after cross-linking. These changes indicate reorganization of the chromophores in the amorphous state, leading to better surface coverage after cross-linking.<sup>7</sup> The absorption spectra of cross-linked films before and after washing with chlorobenzene showed negligible changes in absorbance, indicating a high solvent resistance of the cross-linked films (Figures 2C and S8). On the other hand, non-cross-linked films of all derivatives are readily dissolved in most organic solvents. Square-wave voltammetry analysis displayed two reversible peaks with half-wave potentials at 0.5 and 0.76 V for C-Sty2x and 0.56 and 0.8 V for C-Sty3x, which are attributed to successive one-electron oxidations of the two diphenylamine units (Figure S9), leading to mono- and dicationic oxidized states. The cyclic voltammograms of the films are shown in Figure 2D. The electrochemical stability of the cross-linked films was determined by performing continuous 500 switching cycles in 0.1 M TBAPF<sub>6</sub>/acetonitrile, and both films demonstrated very good switching stability with negligible changes at 20 s pulse width with a transmittance loss of 3% for C-Sty2x and 1% for C-Sty3x at 890 and 850 nm, respectively, indicating the materials' stability toward voltage switching (Figure S10). Both materials showed comparable switching stability with reported triphenylamine-based EC materials prepared by electropolymerization and thermal annealing methods.<sup>53,54</sup> The film morphology plays an important role in modifying the EC properties of the polymer. The surface morphology changes upon thermal cross-linking were further probed by AFM analysis (Figure S11), which showed better surface alignment upon cross-linking with an apparent reduction in surface roughness values. For example, for C-Sty2/C-Sty2x, the arithmetic roughness average of the surface ( $R_a$ ) changed from 2.76 to 1.97 nm and the root-mean-square surface roughness ( $R_q$ ) changed from 3.4 to 2.51 nm, while for

C-Sty3/C-Sty3x,  $R_a$  changed from 0.357 to 0.141 nm and  $R_q$  changed from 0.449 to 0.172 nm. C-Sty3 after polymerization formed cross-linked films with lower roughness and thickness than C-Sty2. Both films exhibited rigid and regular morphology, with C-Sty3x having clear grains and a compact surface compared to C-Sty2x (Figure S11C,F). The thermal stability of these derivatives were probed via TGA, and the decomposition temperature ( $T_d$ ) at 5% weight loss under nitrogen was found to be 380, 410, and 427 °C for C-OMe, C-Sty2, and C-Sty3, respectively (Figure S12). Both cross-linkable derivatives, C-Sty2 and C-Sty3, displayed good thermal stability without much weight loss up to 400 °C. The film-state photoluminescence spectra of C-Sty2 and C-Sty3, before and after thermal cross-linking, exhibited complete quenching of the fluorescence after cross-linking, due to enhanced aggregation-induced quenching in the amorphous, cross-linked polymer (Figure S13).

The spectroelectrochemical responses of the films on FTO substrates were studied by applying different potentials from 0 to 1.5 V (Figure 3A,B). C-Sty2x and C-Sty3x showed similar absorption changes against the applied potentials. For C-Sty2x, the initial neutral state has an absorption maximum of around 372 nm, the absorbance of which gradually decreases with an increase in the applied potential from 0 to 1.5 V. From 0 to 0.8 V, absorption around 483 nm and a long-wavelength absorption band above 1000 nm developed, which correspond to monocation formation, and the film color changed from a transmissive colorless to a transparent light-yellow state. From 0.8 to 1.5 V, a broad absorption covering from 600 to 1100 nm with two peaks around 830 and 987 nm was formed, and the color of the film changed from yellow to dark blue (Figure 3A). Similarly, the neutral state of C-Sty3x displayed an absorbance maximum around 375 nm, which gradually decreased when voltages from 0 to 0.85 V were applied, with concomitant formation of new absorptions around 477 nm and above 1000 nm. A further increase in voltage from 0.85 to 1.5 V, resulting in a broad absorption peak in the visible–near-IR

range with absorbance maxima around 830 and 987 nm. The color of the C-Sty3x film has varied due to differences in absorbance in a manner similar to that of C-Sty2x, with a significantly deeper blue during the second oxidation (Figure 3B). The transmittance changes of the films in the colored (1.5 V) and bleached (0 V) states showed a contrast difference ( $\Delta T$  %) of 65% at 890 nm for C-Sty2x and 78% at 850 nm for C-Sty3x on FTO substrates (Figure 3C,D). The coloration efficiency of the films was calculated using the formula for the coloration efficiency,  $\eta = \log(T_b/T_c)/Q_d$ , where  $T_b$  and  $T_c$  are the transmittances of the films in the bleached and colored states at a particular wavelength, respectively, and  $Q_d$  is the amount of charge transfer per unit area. The coloration efficiency was determined to be 162 cm<sup>2</sup>/C for C-Sty2x at 890 nm and 248 cm<sup>2</sup>/C for C-Sty3x at 850 nm. The double-potential-step chronoamperometry of the films was conducted in order to find the charge (area under the curve) and is shown in Figure S14. Despite having a thinner film than C-Sty2x (film thickness = 245 ± 10 nm), C-Sty3x (film thickness = 230 ± 10 nm) produced a high contrast of transmittance changes with the highest degree of coloration efficiency at 850 nm, demonstrating the impact of charge transfer in different kinds of cross-linked films.

EC devices were fabricated by following the architecture FTO/electrolyte/EC layer/FTO, as shown in Figure 4.

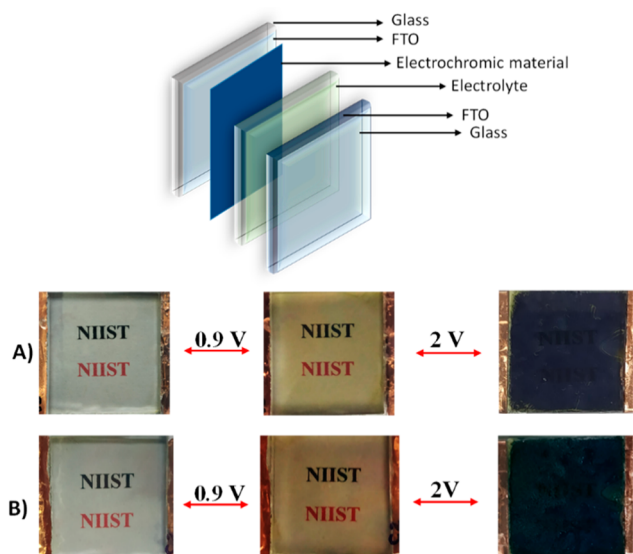


**Figure 4.** Device architecture and images of the devices (A) C-Sty2 and (B) C-Sty3 at applied potentials of 0, 0.9, and 2 V.

Materials were spin-coated onto electrodes, thermally cross-linked, and then used as the EC layer. The thickness of the C-Sty2x and C-Sty3x films used for device fabrication were 245 ± 10 and 230 ± 10 nm, respectively. Figures 4A and 4B show photographs of the devices at 0, 0.9, and 2 V, and the corresponding transmittance spectra demonstrated a change in transmittance of 61% for the C-Sty2x device and 70% for the C-Sty3x devices at 890 and 850 nm, respectively (Figure S15A,B). The color of the devices changed from transparent (0 V) to transmissive yellow (0.9 V) to dark blue (2 V) in both cases with  $L^*a^*b^*$  values for the colors under different applied voltages as follows. The C-Sty2x device showed  $L^* = 86.74$ ,  $a^* = -1.46$ , and  $b^* = 9.07$  at 0 V,  $L^* = 86.95$ ,  $a^* = -6.14$ , and  $b^* = 20.6$  at 0.9 V, and  $L^* = 42.73$ ,  $a^* = -7.6$ , and  $b^* = -11.97$  at

2 V, whereas the C-Sty3x device showed  $L^* = 86.36$ ,  $a^* = -1.23$ , and  $b^* = 9.1$ ,  $L^* = 86.68$ ,  $a^* = -6.02$ , and  $b^* = 20.78$ , and  $L^* = 38.03$ ,  $a^* = -8.9$ , and  $b^* = -15.20$  at 0, 0.9, and 2 V, respectively. The spectroelectrochemical response of the C-Sty2x and C-Sty3x devices to various applied potentials showed changes similar to those of the corresponding FTO films (Figure S15C,D). CV analysis of the devices exhibited two peaks around 0.9 and 2 V corresponding to monocation and dication formation (Figure S16). Multiple cyclic switching of the devices revealed the stability and switching time through transmittance measurements with respect to time at different pulse widths. The transmittance changes (%  $\Delta T$ ) at 20, 10, and 5 s pulse widths at 890 nm (C-Sty2x device) and 850 nm (C-Sty3x device) showed minor losses in transmittance. For example, the C-Sty2x device exhibited a transmittance loss of 3% from 20 to 10 s and 6% from 10 to 5 s pulse-width change (Figure 5A), and for the C-Sty3x device, 5% and 3% reductions were observed for from 20 to 10 s and from 10 to 5 s changes in the pulse width, respectively (Figure 5B). The C-Sty2x and C-Sty3x devices showed reasonably good stability and reversibility over 100 cycles at a switching pulse width of 20 s (Figure S17A,B). Both C-Sty2x and C-Sty3x devices demonstrated transmittance losses of 6% and 4% after 100 cycles at 890 and 850 nm, respectively. The coloration and bleaching time required for the C-Sty2x device at 890 nm were found to be 3.1 and 5.8 s (Figure 5C), and those of the C-Sty3x device at 850 nm were 2.8 and 4.4 s, respectively (Figure 5D). Further, the open-circuit memory of the devices was studied by monitoring the transmittance change of the oxidized state of both the C-Sty2x and C-Sty3x devices at 890 and 850 nm, respectively, for over 2 h and 20 min. The C-Sty2x and C-Sty3x devices retained 75% and 90% of the initial color even after many hours under open-circuit conditions, respectively (Figure S18A,B).

A comparison of the spectroelectrochemical and device properties of C-Sty2x and C-Sty3x showed that C-Sty3x, with three cross-linkable styrene units, forms smoother films with rigid and compact surface and exhibited better thermal stability, darker color in the oxidized state, higher coloration efficiency, and open-circuit memory. EIS can be employed to evaluate the electrical conductivity and ion transport of the cross-linked films. The Nyquist plots obtained via EIS show the impedance spectra for C-Sty2x and C-Sty3x measured in a conventional three-electrode configuration in the frequency range of 100 kHz to 10 mHz. The experimental and model-based Nyquist plots and equivalent circuit fitted are shown in Figure 6. The impedance spectra can be divided into two regions: a semicircle arc in the high-frequency zone and a straight line in the low-frequency region. The equivalent series resistance, or  $R_s$ , is given by the intercept on the real axis in the high-frequency range and consists of the inherent resistances of the electroactive material, the bulk resistance of the electrolyte, and the contact resistance at the electrode/electrolyte interface. The diameter of a semicircle in the high-frequency range can be used to determine the charge-transfer resistance ( $R_{ct}$ ), which results from electron diffusion. The slope of the EIS curve in the low-frequency region can be used to represent the Warburg resistance ( $W$ ), which represents the diffusion of redox species in the electrolyte.<sup>55,56</sup> The C-Sty2x and C-Sty3x circuit models obtained after the fitting of Nyquist plots using EC-Lab software is  $R_1 + Q_1/(R_2 + W) + Q_2/R_3$ , where  $Q_1$  and  $Q_2$  are the constant-phase elements representing the capacitance of the electrochemical double layer,  $R_1$  is the



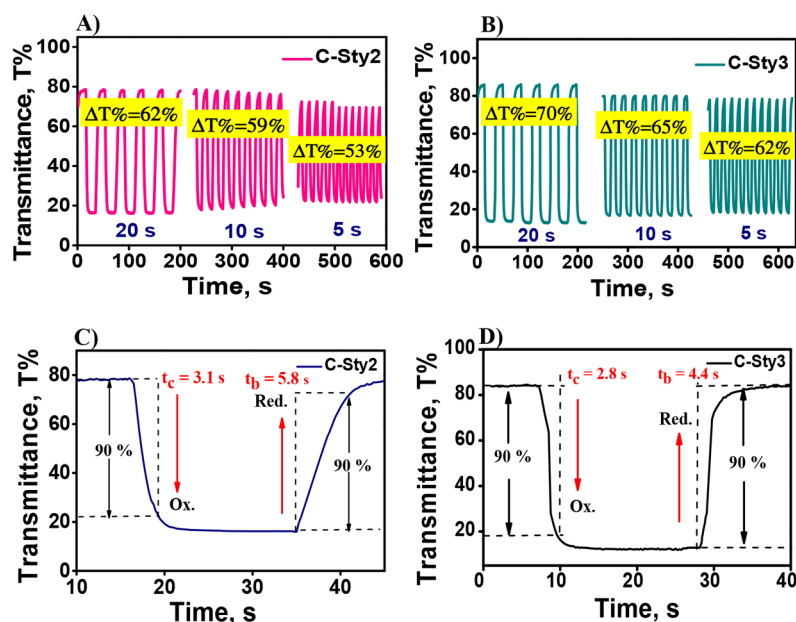


**Figure 5.** Transmittance spectra of the (A) C-Sty2 and (B) C-Sty3 devices at 890 and 850 nm, respectively, with pulse widths of 20, 10, and 5 s. EC switching of the (C) C-Sty2 and (D) C-Sty3 devices at 890 and 850 nm, respectively.

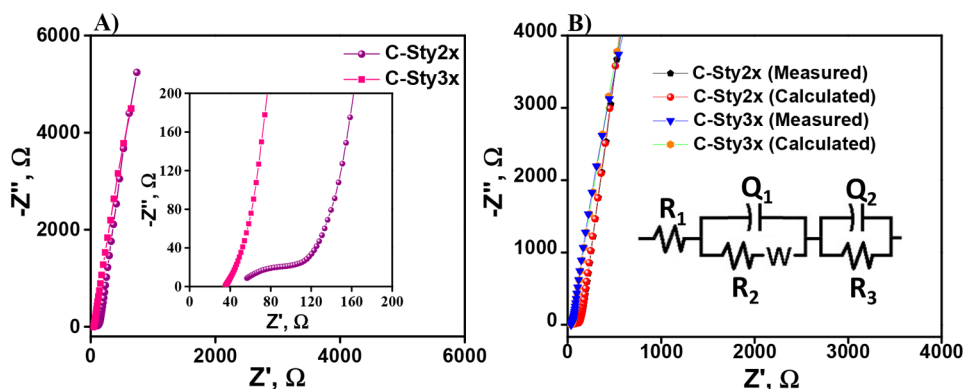


**Figure 6.** (A) Nyquist plots of the C-Sty2x and C-Sty3x films on FTO in 0.1 M TBAPF<sub>6</sub>/acetonitrile measured in a frequency range of 100 kHz to 10 MHz. (B) Experimental and model-based Nyquist plots and the equivalent circuit obtained from *EC-Lab* software (the active surface area of the film is 5 cm<sup>2</sup>).

solution resistance, and  $R_2$  is the charge-transfer resistance.<sup>57–59</sup> The high-frequency part gives  $R_s$  values of 44.02 and 34.55  $\Omega$  for C-Sty2x and C-Sty3x, respectively, and the fitted  $R_{ct}$  values for C-Sty2x and C-Sty3x are 101.7 and 62.99  $\Omega$ , respectively. The absence of a prominent semicircle arc in the high-frequency area and low charge-transfer resistance indicates fast charge transfer at the film/electrolyte interface, implying improved conductivity of C-Sty3x.<sup>60</sup>

A further comparison of the device properties of the carbazole–diphenylamine derivatives with previously reported D– $\pi$ –D derivatives with fluorene<sup>6</sup> and tetraphenylethylene<sup>7</sup>  $\pi$  cores revealed that the  $\pi$  core and nature of cross-linking have a significant influence on the EC device properties. For example, derivatives with a cross-linkable fluorene core (FDOMe-X)<sup>6</sup> showed transparent-to-dark-blue coloration upon oxidation, while TPOSt-X with a tetraphenylethylene core<sup>7</sup> exhibited a transparent-to-dark-gray electrochromism along with significant electrofluorochromism from a highly fluorescent neutral state to a dark oxidized state. Compared to these derivatives, C-Sty2x and C-Sty3x showed significantly

different coloration properties with a transparent-to-dark-blue EC change upon oxidation, with significant absorption spanning the visible range (Figure S19). Compared to all other derivatives, hyper-cross-linked C-Sty3x showed better coloration efficiency and optical contrast, with a significantly lower switching response time for coloration and bleaching. Thus, the D– $\pi$ –D design strategy with multiple cross-linking units and different  $\pi$  cores provides a series of organic EC materials with tunable properties (Table S2).

#### 4. CONCLUSIONS

In conclusion, we have developed and discussed the EC properties of two D– $\pi$ –D-type carbazole–diphenylamine derivatives, C-Sty2 and C-Sty3, incorporated with two and three styryl units, respectively, and compared the cross-linking effect on the EC properties. The cross-linking properties were examined thoroughly with different techniques like FT-IR, DSC, AFM, WAXD, etc. The CV and spectroelectrochemical studies of the C-Sty2x and C-Sty3x films and devices revealed mono- and dication formation with a color change from a

colorless, transparent initial state to a transmissive yellow and then to dark blue. The maximum color contrast obtained from the transmittance plot is 62% at 890 nm for the **C-Sty2x** device and 70% at 850 nm for the **C-Sty3x** device. The devices exhibited good switching stability with low switching voltages, relatively low switching time, and excellent open-circuit memory. In contrast to **C-Sty2**, **C-Sty3** with three styryl subunits forms films that are rigid, smooth, and compact with reduced thickness, regular morphology, and clear grains. **C-Sty3x** performed better in terms of coloration efficiency, optical contrast, and open-circuit memory. The EIS studies showed fast charge transfer at the **C-Sty3** film/electrolyte interface than **C-Sty2** films with  $R_{ct}$  values of 62.99 and 101.7  $\Omega$ , respectively, corroborating the enhanced EC properties of **C-Sty3** film-based devices. The EC performances of the **C-Sty3** polymer were compared to those of previously reported D- $\pi$ -D systems with fluorene and tetraphenylethylene as  $\pi$  cores and two cross-linkable styrene moieties, demonstrating the strategy to aid a new material design for obtaining EC materials with higher coloration efficiency, contrast, and optical memory. Thus, the derivatives with their easy synthesis, solution processability, extensive cross-linked and stable film formation having increased solvent resistance, good coloration efficiency, and optical contrast, and open-circuit memory give the potential for these materials to turn out to be suitable for EC applications.

## ■ ASSOCIATED CONTENT

### SI Supporting Information

The Supporting Information is available free of charge at <https://pubs.acs.org/doi/10.1021/acsapm.3c00393>.

Information about the synthesis and characterization of the molecules (Scheme S1 and Figures S1–S4), compounds' absorption and emission maxima and their molar extinction coefficients and quantum yields (Table S1), absorption and emission spectra in different solvents (Figures S5 and S6), FT-IR and WAXD of **C-Sty2** before and after polymerization (Figure S7), UV-vis absorption spectra of **C-Sty2** before and after cross-linking and after rinsing with chlorobenzene (Figure S8), square-wave voltammograms of the **C-Sty2x** and **C-Sty3x** films on a FTO substrate (Figure S9), switching analyses of the **C-Sty2x** and **C-Sty3x** films (Figure S10), AFM images of the molecules before and after cross-linking (Figure S11), TGA and emission spectra of the monomers and polymers (Figures S12 and S13), chronoamperometry plots of the films (Figure S14), transmittance spectra and spectroelectrochemical response of devices in the colored and bleached states (Figure S15), CV analysis, switching stability, and open-circuit memory of the devices (Figures S16–S18, respectively), Figure S19 comprises of device photographs, spectroelectrochemical responses and molecular structures of **FDOMe**, **TPOSt**, and **C-Sty3** compounds, and a comparison of the EC properties (Table S2) (PDF)

## ■ AUTHOR INFORMATION

### Corresponding Authors

**Joshya Joseph** – *Photosciences and Photonics Section, Chemical Sciences and Technology Division, CSIR-National Institute for Interdisciplinary Science and Technology,*

*Thiruvananthapuram 695019 Kerala, India; Academy of Scientific and Innovative Research (AcSIR), Ghaziabad 201002, India; [orcid.org/0000-0002-4592-8991](https://orcid.org/0000-0002-4592-8991);* Email: [joshyja@gmail.com](mailto:joshyja@gmail.com), [joshy@niist.res.in](mailto:joshy@niist.res.in)

**Biswapriya Deb** – *Photosciences and Photonics Section, Chemical Sciences and Technology Division, CSIR-National Institute for Interdisciplinary Science and Technology, Thiruvananthapuram 695019 Kerala, India; Academy of Scientific and Innovative Research (AcSIR), Ghaziabad 201002, India; [orcid.org/0000-0001-7954-9386](https://orcid.org/0000-0001-7954-9386);* Email: [biswapriyadeb@gmail.com](mailto:biswapriyadeb@gmail.com)

### Authors

**Shibna Balakrishnan** – *Photosciences and Photonics Section, Chemical Sciences and Technology Division, CSIR-National Institute for Interdisciplinary Science and Technology, Thiruvananthapuram 695019 Kerala, India; Academy of Scientific and Innovative Research (AcSIR), Ghaziabad 201002, India*

**Ranjana Venugopal** – *Photosciences and Photonics Section, Chemical Sciences and Technology Division, CSIR-National Institute for Interdisciplinary Science and Technology, Thiruvananthapuram 695019 Kerala, India; Academy of Scientific and Innovative Research (AcSIR), Ghaziabad 201002, India*

**Aswathi Harikumar** – *Photosciences and Photonics Section, Chemical Sciences and Technology Division, CSIR-National Institute for Interdisciplinary Science and Technology, Thiruvananthapuram 695019 Kerala, India*

Complete contact information is available at: <https://pubs.acs.org/doi/10.1021/acsapm.3c00393>

### Author Contributions

J.J. and S.B. are responsible for the conceptualization and wrote the paper. A.H. helped with synthesis and characterization of the molecules while R.V. and B.D. were involved in device fabrication and characterization. All authors contributed to the general discussion.

### Notes

The authors declare no competing financial interest.

## ■ ACKNOWLEDGMENTS

We thank Dr. Rakhi R. B. for the impedance studies and discussions. We thank Dr. Bhoje Gowd for DSC and WAXD studies and discussions. Financial support from the Council of Scientific and Industrial Research (MLP 0049 and DST-Nanomission-GAP 162939) is gratefully acknowledged. B.D. is grateful to CRG-GAP 163029 and AMM-HCP 0030 for financial support. S.B. gratefully acknowledges CSIR, Government of India, for a research fellowship, and R.V. acknowledges the University Grant Commission, Government of India, for a research fellowship.

## ■ ABBREVIATIONS

AFM, atomic force microscopy; CV, cyclic voltammetry; DSC, differential scanning calorimetry; EC, electrochromic; EIS, electrochemical impedance spectroscopy; FT-IR, Fourier transform infrared spectroscopy; FTO, fluorine-doped tin oxide; TBAPF<sub>6</sub>, tetra-*n*-butylammonium hexafluorophosphate; TGA, thermogravimetric analysis; WAXD, wide-angle X-ray diffraction



## REFERENCES

- (1) Argun, A. A.; Aubert, P.-H.; Thompson, B. C.; Schwendeman, I.; Gaupp, C. L.; Hwang, J.; Pinto, N. J.; Tanner, D. B.; MacDiarmid, A. G.; Reynolds, J. R. Multicolored Electrochromism in Polymers: Structures and Devices. *Chem. Mater.* **2004**, *16* (23), 4401–4412.
- (2) Beaujuge, P. M.; Reynolds, J. R. Color Control in  $\pi$ -Conjugated Organic Polymers for Use in Electrochromic Devices. *Chem. Rev.* **2010**, *110* (1), 268–320.
- (3) Fang, H.; Zheng, P.; Ma, R.; Xu, C.; Yang, G.; Wang, Q.; Wang, H. Multifunctional hydrogel enables extremely simplified electrochromic devices for smart windows and ionic writing boards. *Materials Horizons* **2018**, *5* (5), 1000–1007.
- (4) Mortimer, R. J. Organic electrochromic materials. *Electrochim. Acta* **1999**, *44* (18), 2971–2981.
- (5) Yen, H.-J.; Liou, G.-S. Recent advances in triphenylamine-based electrochromic derivatives and polymers. *Polym. Chem.* **2018**, *9* (22), 3001–3018.
- (6) Abraham, S.; Ganesh, G. P. T.; Varughese, S.; Deb, B.; Joseph, J. Cross-Linkable Fluorene-Diphenylamine Derivatives for Electrochromic Applications. *ACS Appl. Mater. Interfaces* **2015**, *7* (45), 25424–25433.
- (7) Abraham, S.; Mangalath, S.; Sasikumar, D.; Joseph, J. Transmissive-to-Black Electrochromic Devices Based on Cross-Linkable Tetraphenylethene-Diphenylamine Derivatives. *Chem. Mater.* **2017**, *29* (23), 9877–9881.
- (8) Wałęsa-Chorab, M.; Skene, W. G. Visible-to-NIR Electrochromic Device Prepared from a Thermally Polymerizable Electroactive Organic Monomer. *ACS Appl. Mater. Interfaces* **2017**, *9* (25), 21524–21531.
- (9) Lv, X.; Li, J.; Xu, L.; Zhu, X.; Tameev, A.; Nekrasov, A.; Kim, G.; Xu, H.; Zhang, C. Colorless to Multicolored, Fast Switching, and Highly Stable Electrochromic Devices Based on Thermally Cross-Linking Copolymer. *ACS Appl. Mater. Interfaces* **2021**, *13* (35), 41826–41835.
- (10) Lv, X.; Shao, M.; Zhu, X.; Xu, L.; Ouyang, M.; Zhou, C.; Dong, J.; Zhang, C. Thermally Cross-Linked Copolymer for Highly Transparent to Multicolor-Showing Electrochromic Materials. *ACS Applied Polymer Materials* **2023**, DOI: 10.1021/acsapm.3c00250.
- (11) Sun, Y.; Zhu, G.; Zhao, X.; Kang, W.; Li, M.; Zhang, X.; Yang, H.; Guo, L.; Lin, B. Solution-processable, hypercrosslinked polymer via post-crosslinking for electrochromic supercapacitor with outstanding electrochemical stability. *Sol. Energy Mater. Sol. Cells* **2020**, *215*, 110661.
- (12) Frolov, D. G.; Makhaeva, E. E.; Keshotov, M. L. Electrochromic behavior of films and «smart windows» prototypes based on  $\pi$ -conjugated and non-conjugated poly(pyridinium triflate)s. *Synth. Met.* **2019**, *248*, 14–19.
- (13) Kamata, K.; Suzuki, T.; Kawai, T.; Iyoda, T. Voltammetric anion recognition by a highly cross-linked polyviologen film. *J. Electroanal. Chem.* **1999**, *473* (1), 145–155.
- (14) Wang, F.; Wilson, M. S.; Rauh, R. D.; Schottland, P.; Thompson, B. C.; Reynolds, J. R. Electrochromic Linear and Star Branched Poly(3,4-ethylenedioxythiophene–didodecyloxybenzene) Polymers. *Macromolecules* **2000**, *33* (6), 2083–2091.
- (15) Soganci, T.; Gumusay, O.; Soyleyici, H. C.; Ak, M. Synthesis of highly branched conducting polymer architecture for electrochromic applications. *Polymer* **2018**, *134*, 187–195.
- (16) Bhandari, S.; Deepa, M.; Srivastava, A. K.; Joshi, A. G.; Kant, R. Poly(3,4-ethylenedioxythiophene)–Multiwalled Carbon Nanotube Composite Films: Structure-Directed Amplified Electrochromic Response and Improved Redox Activity. *J. Phys. Chem. B* **2009**, *113* (28), 9416–9428.
- (17) Hsiao, S.-H.; Liou, G.-S.; Kung, Y.-C.; Yen, H.-J. High Contrast Ratio and Rapid Switching Electrochromic Polymeric Films Based on 4-(Dimethylamino)triphenylamine-Functionalized Aromatic Polyamides. *Macromolecules* **2008**, *41* (8), 2800–2808.
- (18) Navarathne, D.; Skene, W. G. Dynachromes – dynamic electrochromic polymers capable of property tuning and patterning via multiple constitutional component exchange. *Journal of Materials Chemistry C* **2013**, *1* (41), 6743–6747.
- (19) Gaupp, C. L.; Reynolds, J. R. Multichromic Copolymers Based on 3,6-Bis(2-(3,4-ethylenedioxythiophene))–N-alkylcarbazole Derivatives. *Macromolecules* **2003**, *36* (17), 6305–6315.
- (20) Sankaran, B.; Reynolds, J. R. High-Contrast Electrochromic Polymers from Alkyl-Derivatized Poly(3,4-ethylenedioxythiophenes). *Macromolecules* **1997**, *30* (9), 2582–2588.
- (21) Sapp, S. A.; Sotzing, G. A.; Reynolds, J. R. High Contrast Ratio and Fast-Switching Dual Polymer Electrochromic Devices. *Chem. Mater.* **1998**, *10* (8), 2101–2108.
- (22) Schwendeman, I.; Hickman, R.; Sönmez, G.; Schottland, P.; Zong, K.; Welsh, D. M.; Reynolds, J. R. Enhanced Contrast Dual Polymer Electrochromic Devices. *Chem. Mater.* **2002**, *14* (7), 3118–3122.
- (23) Österholm, A. M.; Shen, D. E.; Kerszulis, J. A.; Bulloch, R. H.; Kuepfert, M.; Dyer, A. L.; Reynolds, J. R. Four Shades of Brown: Tuning of Electrochromic Polymer Blends Toward High-Contrast Eyewear. *ACS Appl. Mater. Interfaces* **2015**, *7* (3), 1413–1421.
- (24) Wang, S.; Cai, S.; Cai, W.; Niu, H.; Wang, C.; Bai, X.; Wang, W.; Hou, Y. Organic-inorganic hybrid electrochromic materials, polysilsesquioxanes containing triarylamine, changing color from colorless to blue. *Sci. Rep.* **2017**, *7* (1), 14627.
- (25) Zeng, J.; Yang, H.; Zhong, C.; Rajan, K.; Sagar, R. U. R.; Qi, X.; Deng, Y.; Jiang, H.; Liu, P.; Liang, T. Colorless-to-black electrochromic devices based on ambipolar electrochromic system consisting of cross-linked poly(4-vinyltriphenylamine) and tungsten trioxide with high optical contrast in visible and near-infrared regions. *Chemical Engineering Journal* **2021**, *404*, 126402.
- (26) Xu, T.; Walter, E. C.; Agrawal, A.; Bohn, C.; Velmurugan, J.; Zhu, W.; Lezec, H. J.; Talin, A. A. High-contrast and fast electrochromic switching enabled by plasmonics. *Nat. Commun.* **2016**, *7* (1), 10479.
- (27) Zhang, Q.; Tsai, C.-Y.; Li, L.-J.; Liaw, D.-J. Colorless-to-colorful switching electrochromic polyimides with very high contrast ratio. *Nat. Commun.* **2019**, *10* (1), 1239.
- (28) Topal, S.; Savlug Ipek, O.; Sezer, E.; Ozturk, T. Electrochromic-Hybrid energy storage material consisting of triphenylamine and dithienothiophene. *Chemical Engineering Journal* **2022**, *434*, 133868.
- (29) Wałęsa-Chorab, M.; Muras, K.; Filiatrault, H. L.; Skene, W. G. Suitability of alkyne donor- $\pi$ -donor- $\pi$ -donor scaffolds for electrofluorochromic and electrochromic use. *Journal of Materials Chemistry C* **2022**, *10* (10), 3691–3703.
- (30) Yu, T.; Theato, P.; Yao, H.; Liu, H.; Di, Y.; Sun, Z.; Guan, S. Colorless Electrochromic/Electrofluorochromic Dual-Functional Triphenylamine-Based Polyimides: Effect of a Tetraphenylethylene-Based  $\pi$ -Bridge on optoelectronic properties. *Chemical Engineering Journal* **2023**, *451*, 138441.
- (31) Gao, L.; Schloemer, T. H.; Zhang, F.; Chen, X.; Xiao, C.; Zhu, K.; Sellinger, A. Carbazole-Based Hole-Transport Materials for High-Efficiency and Stable Perovskite Solar Cells. *ACS Applied Energy Materials* **2020**, *3* (5), 4492–4498.
- (32) Leijtens, T.; Ding, I. K.; Giovenzana, T.; Bloking, J. T.; McGehee, M. D.; Sellinger, A. Hole Transport Materials with Low Glass Transition Temperatures and High Solubility for Application in Solid-State Dye-Sensitized Solar Cells. *ACS Nano* **2012**, *6* (2), 1455–1462.
- (33) Liu, H.; He, B.; Lu, H.; Tang, R.; Wu, F.; Zhong, C.; Li, S.; Wang, J.; Zhu, L. Carbazole-based D–A type hole transport materials to enhance the performance of perovskite solar cells. *Sustainable Energy & Fuels* **2022**, *6* (2), 371–376.
- (34) Teh, C. H.; Daik, R.; Lim, E. L.; Yap, C. C.; Ibrahim, M. A.; Ludin, N. A.; Sopian, K.; Mat Teridi, M. A. A review of organic small molecule-based hole-transporting materials for meso-structured organic–inorganic perovskite solar cells. *Journal of Materials Chemistry A* **2016**, *4* (41), 15788–15822.
- (35) Xu, B.; Sheibani, E.; Liu, P.; Zhang, J.; Tian, H.; Vlachopoulos, N.; Boschloo, G.; Kloo, L.; Hagfeldt, A.; Sun, L. *Carbazole-Based Hole-*

*Transport Materials for Efficient Solid-State Dye-Sensitized Solar Cells and Perovskite Solar Cells* **2014**, *26* (38), 6629–6634.

(36) Ledwon, P. Recent advances of donor-acceptor type carbazole-based molecules for light emitting applications. *Org. Electron.* **2019**, *75*, 105422.

(37) Li, G.; Zheng, J.; Klimes, K.; Zhu, Z.-Q.; Wu, J.; Zhu, H.; Li, J. Novel Carbazole/Fluorene-Based Host Material for Stable and Efficient Phosphorescent OLEDs. *ACS Appl. Mater. Interfaces* **2019**, *11* (43), 40320–40331.

(38) Tao, Y.; Yang, C.; Qin, J. Organic host materials for phosphorescent organic light-emitting diodes. *Chem. Soc. Rev.* **2011**, *40* (5), 2943–2970.

(39) Wex, B.; Kaafarani, B. R. Perspective on carbazole-based organic compounds as emitters and hosts in TADF applications. *Journal of Materials Chemistry C* **2017**, *5* (34), 8622–8653.

(40) Ates, M.; Uludag, N. Carbazole derivative synthesis and their electropolymerization. *J. Solid State Electrochem.* **2016**, *20* (10), 2599–2612.

(41) Zhou, P.; Wan, Z.; Liu, Y.; Jia, C.; Weng, X.; Xie, J.; Deng, L. Synthesis and electrochromic properties of a novel conducting polymer film based on dithiafulvenyl-triphenylamine-di(N-carbazole). *Electrochim. Acta* **2016**, *190*, 1015–1024.

(42) Zhang, Y.; Liu, F.; Hou, Y.; Niu, H. Soluble high coloration efficiency electrochromic polymers based on (N-phenyl)carbazole, triphenylamine and 9,9-dioctyl-9H-fluorene. *Synth. Met.* **2019**, *247*, 81–89.

(43) Cansu-Ergun, E. G. Covering the More Visible Region by Electrochemical Copolymerization of Carbazole and Benzothiadiazole Based Donor-Acceptor Type Monomers. *Chin. J. Polym. Sci.* **2019**, *37* (1), 28–35.

(44) Akbayrak, M.; Cansu-Ergun, E. G.; Önal, A. M. Synthesis and electro-optical properties of a new copolymer based on EDOT and carbazole. *Des. Monomers Polym.* **2016**, *19* (7), 679–687.

(45) Liu, Y.; Chao, D.; Yao, H. New triphenylamine-based poly(amine-imide)s with carbazole-substituents for electrochromic applications. *Org. Electron.* **2014**, *15* (7), 1422–1431.

(46) Liu, Y.; Pang, L.; Liu, T.; Guo, J.; Wang, J.; Li, W. Novel triphenylamine polyazomethines bearing carbazole and trifluoromethyl substituents: Preparation and electrochromic behavior. *Dyes Pigm.* **2020**, *173*, 107921.

(47) Karon, K.; Lapkowski, M.; Dabulienė, A.; Tomkevičienė, A.; Kostiv, N.; Grazulevičius, J. V. Spectroelectrochemical characterization of conducting polymers from star-shaped carbazole-triphenylamine compounds. *Electrochim. Acta* **2015**, *154*, 119–127.

(48) Data, P.; Zassowski, P.; Lapkowski, M.; Domagala, W.; Krompiec, S.; Flak, T.; Penkala, M.; Swist, A.; Soloduch, J.; Danikiewicz, W. Electrochemical and spectroelectrochemical comparison of alternated monomers and their copolymers based on carbazole and thiophene derivatives. *Electrochim. Acta* **2014**, *122*, 118–129.

(49) Cansu-Ergun, E. G.; Önal, A. M. Carbazole based electrochromic polymers bearing ethylenedioxy and propylenedioxy scaffolds. *J. Electroanal. Chem.* **2018**, *815*, 158–165.

(50) Daskeviciute-Geguziene, S.; Magomedov, A.; Daskeviciene, M.; Genevicius, K.; Nekrašas, N.; Jankauskas, V.; Kantminiene, K.; McGehee, M. D.; Getautis, V. Cross-linkable carbazole-based hole transporting materials for perovskite solar cells. *Chem. Commun.* **2022**, *58* (54), 7495–7498.

(51) Joseph, V.; Justin Thomas, K. R.; Yang, W. Y.; Kumar Yadav, R. A.; Kumar Dubey, D.; Jou, J.-H. *Tetra-substituted Dipolar Carbazoles: Tuning Optical and Electroluminescence Properties by Linkage Variation* **2018**, *7* (8), 1654–1666.

(52) Palayangoda, S. S.; Cai, X.; Adhikari, R. M.; Neckers, D. C. Carbazole-Based Donor–Acceptor Compounds: Highly Fluorescent Organic Nanoparticles. *Org. Lett.* **2008**, *10* (2), 281–284.

(53) Zhang, L.; Zhan, W.; Dong, Y.; Yang, T.; Zhang, C.; Ouyang, M.; Li, W. Liquid/Liquid Interfacial Suzuki Polymerization Prepared Novel Triphenylamine-Based Conjugated Polymer Films with Excellent Electrochromic Properties. *ACS Appl. Mater. Interfaces* **2021**, *13* (17), 20810–20820.

(54) Fu, W.; Chen, H.; Han, Y.; Wang, W.; Zhang, R.; Liu, J. Electropolymerization of D–A–D type monomers consisting of triphenylamine and substituted quinoxaline moieties for electrochromic devices. *New J. Chem.* **2021**, *45* (40), 19082–19087.

(55) Rakhi, R. B.; Chen, W.; Cha, D.; Alshareef, H. N. Substrate Dependent Self-Organization of Mesoporous Cobalt Oxide Nanowires with Remarkable Pseudocapacitance. *Nano Lett.* **2012**, *12* (5), 2559–2567.

(56) Rakhi, R. B.; Ahmed, B.; Anjum, D.; Alshareef, H. N. Direct Chemical Synthesis of MnO<sub>2</sub> Nanowhiskers on Transition-Metal Carbide Surfaces for Supercapacitor Applications. *ACS Appl. Mater. Interfaces* **2016**, *8* (29), 18806–18814.

(57) Wang, W.; Guo, S.; Lee, I.; Ahmed, K.; Zhong, J.; Favors, Z.; Zaera, F.; Ozkan, M.; Ozkan, C. S. Hydrrous Ruthenium Oxide Nanoparticles Anchored to Graphene and Carbon Nanotube Hybrid Foam for Supercapacitors. *Sci. Rep.* **2014**, *4* (1), 4452.

(58) Liu, C.; Luo, H.; Xu, Y.; Wang, W.; Liang, Q.; Mitsuzaki, N.; Chen, Z. Cobalt–phosphate-modified Mo:BiVO<sub>4</sub> mesoporous photoelectrodes for enhanced photoelectrochemical water splitting. *J. Mater. Sci.* **2019**, *54* (15), 10670–10683.

(59) Jayabalan, A. D.; Din, M. M. U.; Indu, M. S.; Karthik, K.; Ragupathi, V.; Nagarajan, G. S.; Panigrahi, P.; Murugan, R. Electrospun 3D CNF–SiO<sub>2</sub> fabricated using non-biodegradable silica gel as prospective anode for lithium–ion batteries. *Ionics* **2019**, *25* (11), 5305–5313.

(60) Gupta, B.; Singh, A. K.; Prakash, R. Electrolyte effects on various properties of polycarbazole. *Thin Solid Films* **2010**, *519* (3), 1016–1019.

## Recommended by ACS

### Sulfonate-Group-Containing Polymeric Polyamide for Simultaneous Transparency and Flame Retardancy of Polycarbonate

Zi-Xun Chen, Yu-Zhong Wang, *et al.*

JUNE 09, 2023

ACS APPLIED POLYMER MATERIALS

READ 

### Waste to Treasure: Preparation of Functional Polymeric Particles from Waste Olefins in Carboic Oil by Self-Stabilized Precipitation Polymerization

Tianxiao Chang, Wantai Yang, *et al.*

MARCH 07, 2023

ACS APPLIED POLYMER MATERIALS

READ 

### Poly(lactic Acid/Calcium Stearate Hydrocharging Melt-Blown Nonwoven Fabrics for Respirator Applications

Rui Hu, Bin Ding, *et al.*

MAY 05, 2023

ACS APPLIED POLYMER MATERIALS

READ 

### Poly(phenylene oxide) Films with Hydrophilic Sulfonated Amorphous Phase and Physically Cross-Linking Hydrophobic Crystalline Phase

Baku Nagendra, Gaetano Guerra, *et al.*

APRIL 14, 2023

ACS APPLIED POLYMER MATERIALS

READ 

Get More Suggestions >